UNIVERSITÀ DEGLI STUDI MILANO BICOCCA
Facoltà di Scienze MM. FF. NN.

Scuola di Dottorato di Scienze Corso di
Dottorato di Ricerca in Fisica ed Astronomia

Search for a heavy gauge boson W′ in the final state with electron and large E_{T}^{miss} in pp collisions at $\sqrt{s} = 7$ TeV

Coordinatore: prof. **Giuseppe Chirico**
Relatore: prof. **Tommaso Tabarelli de Fatis**

Tesi di Dottorato di
Federico De Guio
Matricola: 048574

Ciclo XXIV
Anno Accademico 2011-2012

CONTENTS

EXECUTIVE SUMMARY

The Standard Model of particle physics (SM) is a successful theory developed in the second half of the 20^{th} century and it provides a framework capable to describe with great precision the interactions of the fundamental particles and the forces carriers, at the energy scale below 1 TeV. The Higgs boson, an hypothetical spin 0 particle responsible for the mass of all the other particles (by the means of the electroweak spontaneous symmetry breaking mechanism), is foreseen by the theory and after the discovery of the top quark in 1995, it is the last missing piece of the SM. The search for the Higgs boson is therefore one of the main goals of the experiments operating at the Large Hadron Collider (LHC). However there are experimental evidences that the Standard Model can not be the ultimate theory in describing the particle physics: according to cosmological precision measurements the Universe is made by yet unknown components without a counterpart in the Standard Model (Dark energy and Dark Matter). Moreover it is proven that the mass of the neutrinos differs from 0. On the theoretical side, extensions of the SM try to explain unsolved questions such as hierarchy problem between the electroweak and the Planck scales, the radiative stability of the Higgs boson mass or the unbalance between matter and antimatter. In several extensions of the SM, the existence of additional gauge bosons is foreseen. In the Left-Right-Symmetric Model, for instance, the SM gauge group is extended by the introduction of an additional $SU(2)$ gauge group which restores the Lagrangian's intrinsic exact parity symmetry. The extension by a right-handed sector has not only aesthetic reasons, but it provides a mechanism for parity violation in weak interactions whose origin stays unexplained within the Standard Model. The extension of the gauge group postulates the existence of new gauge bosons W′ and Z′, heavy partners of the SM W and Z.

In this thesis the search for an hypothetical W′ decaying in electron and neutrino performed with the Compact Muon Solenoid (CMS) detector is presented. The W′ properties are derived from the Reference Model by Altarelli, which represents a generalization of the Left-Right-Symmetric Model. The Reference Model is obtained by simply introducing ad hoc new heavy gauge bosons: two charged W′ vector bosons and one

neutral Z′ as a carbon copy of the Standard Model ones. The couplings are chosen to be the same as for the ordinary W and Z bosons. The only parameters are the masses of the new vector bosons. Interactions with the Standard Model gauge bosons are excluded, as the interactions with other heavy gauge bosons. This suppression arises in extended gauge theories in a natural manner: if the new gauge bosons and the SM ones belong to different gauge groups, vertices of the kind $Z'Z^0Z^0$ or $W'W^{\pm}Z^0$ are forbidden. They can only occur after symmetry breaking due to mixing of the gauge group eigenstate to mass eigenstate. With this assumption, the Reference Model and the Left-Right-Symmetric Model have comparable branching ratios. Assuming the former for a direct search is then a reasonable approach. The W′ decay modes and branching fractions are similar to those of the W boson, with the notable exception of the $t\bar{b}$ channel, which opens for W′ masses beyond 180 GeV.
The proton-proton Large Hadron Collider built at CERN, with 7 TeV of energy in the center of mass, represents a powerful tool for the investigation of theories beyond the Standard Model. The Compact Muon Solenoid is one of the two multi-purpose experiments located at the LHC and it is designed not only to search for the Higgs boson, but even for new physics signatures searches. In this analysis, the clear decay signature contains one isolated electron of very high energy. The neutrino can not be detected, but its transverse momentum is measured as an energy unbalance in the transverse plane of CMS and arises through the missing transverse energy ($E_{\mathrm{T}}^{\mathrm{miss}}$). The invariant mass of the W′ can not be reconstructed, then the search for an excess in the data with respect to the Standard Model background expectations is performed in the transverse mass spectrum (analogous of the invariant mass built in the transverse plane). In order to reject the background processes, the transverse momenta of the two leptons are required to be balanced both in direction and in magnitude. The main background in the final sample is due to the SM $W \to e\nu$ process which is irreducible because its signature is identical to the signal albeit peaked at lower transverse masses. Other backgrounds with an electron and a neutrino in the final state are $W \to \tau\nu$, WW, WZ, ZZ, $t\bar{t}$. In addition, in processes such as the $multi-jet$ and the $Z \to ee$, an electron can be mis-reconstructed due to instrumental effects.
Since this analysis relies on electrons and the $E_{\mathrm{T}}^{\mathrm{miss}}$ observable, high electron reconstruction and identification efficiencies, the capability in rejecting fake electrons from the $multi-jet$ background and a good energy resolution on the $E_{\mathrm{T}}^{\mathrm{miss}}$ are aspects of primary importance. In this endeavor the role of the electromagnetic calorimeter (ECAL) of the CMS detector is central. ECAL is an hermetic homogeneous electromagnetic calorimeter made of 75848 lead tungstate ($PbWO_4$) scintillating crystals organized in a central region, the barrel, and in two endcaps. The response uniformity across the detector and the stability in time are severe challenges to achieve the most accurate

energy resolution for electrons and photons. While a channel-to-channel calibration (inter-calibration) precision of 0.5% is desired to achieve the best sensitivity to the postulated $H \to \gamma\gamma$ decay, an inter-calibration at the percent level is sufficient for the W$'$ search and for most of the CMS physics programme. The main sources of channel-to-channel response variation are the crystal light yield variation in the barrel, about 13% at construction, and the gain spread of the photodetectors in the endcaps, about 25%. To reduce the initial spread and provide a reasonable detector performance already at startup, different calibration procedures have been adopted during the construction (pre-calibration) and commissioning phase of ECAL. In the context of this thesis, data from cosmic ray muons and beam induced muon events collected with the CMS detector in his final position before the LHC startup, were used to perform an in situ check of the pre-calibration constants. The precision of these measurements, which are made at the level of 1-2% for the barrel and better than 5% in the endcaps provided the initial inter-calibration constants for the calibration methods using LHC beam events.
During the last part of 2010 and during 2011 runs, variations of order 1% (10%) in the transparency of the barrel (endcap) crystals have been observed, as expected from the radiation damage and recovery cycles of the $PbWO_4$ crystals. A monitoring system, based on the injection of laser light into the crystals has been exploited to derive corrections to compensate for the transparency variations. Electrons from W decays, the main background in the W$'$ search, have been used to cross check the monitoring corrections and improve the stability of the ECAL response.
The LHC running condition evolved rapidly during 2011 and the instantaneous luminosity, measure of the collision rate, grew up to 3.5×10^{33} cm^{-2}s^{-1} from an initial value of 10^{32} cm^{-2}s^{-1} in 2010. Since it is not possible to record on tape all the collision events with a rate of 40 MHz (20 MHz in 2011), an online selection system (the trigger of CMS), is necessary to recognize and discard the non-interesting events. The trigger system consists of two main steps: a Level1 Trigger which consists of custom-designed, largely programmable electronics allows to reduce the rate from 40 MHz to 100 kHz, and a High Level Trigger (HLT) software system implemented in a filter farm of about one thousand commercial processors to reduce the rate from 100 kHz to 300 Hz. The HLT is based on fast reconstruction algorithms. In the W$'$ analysis context, the HLT parameters were tuned in order to save as much W events as possible. The Jacobian peak in the transverse mass distribution stemming from the W decay is used for the validation of the Monte Carlo simulation and the $multi-jet$ estimate which is extracted from data, whereas the tail of the transverse mass distribution is searched for a possible W$'$ signal. Moreover the electrons coming from the decay of the W events are employed for the monitoring of the performance of the ECAL during

the data taking.
The analysis of the data collected between March and July 2011, corresponding to an integrated luminosity of 1.13 fb^{-1}, did not evidence any excess over the expected background. This allowed us to set an upper limit on the production cross section for heavy charged gauge bosons decaying into electron and neutrino, $\sigma_{W'} \times Br(W' \to e\nu)$ which translate into a lower limit on the invariant mass of the W′ of 2.15 TeV at 95% confidence level by means of the Reference Model already described. This is the best exclusion limit to date. The result is currently being updated with the full 2011 dataset corresponding to 4.7 fb^{-1}.

The discussion is organized as follows. The first Chapter briefly illustrates the main theoretical problematics to which the Standard Model does not give answer then the model which would justify the existence of the W′ is presented: the Left-Right Symmetric model and the Reference Model are illustrated in detail. In Chapter 2 a partial list of the results obtained with the CMS detector in the context of non-supersymmetric searches beyond the Standard Model is given. After an overview of the LHC system and the CMS detector, given in Chapter 3, Chapter 4 is devoted to the optimization of the event reconstruction in ECAL, as performed with the first collision data, and to the tuning of the detector simulation. Particular emphasis will be given to the study and understanding of the Nuclear Counter Effect (NCE), related to the direct ionization of the readout photodetectors of the ECAL barrel. The NCE events could fake high energy signals and had to be properly identified and rejected. In Chapter 5 the description of the techniques adopted to calibrate the ECAL and the results of the calorimeter performance monitoring during the whole 2011 data taking are reported. In Chapter 6 and Chapter 7 the W′ search strategy and the search results are discussed: the study of the kinematic of the signal with the Monte Carlo simulation, the strategies to describe, select and reduce the background in the final sample and the implementation of a combined electron+M_T trigger path used both for the W′ analysis and for detector purposes are reported.
Prospects for the evolution of the W′ and new gauge bosons searches at the LHC will be given as concluding remarks of this work.

CHAPTER 1

W' SEARCH

A large number of experimental tests performed over many years has given us confidence that the Standard Model of particle physics (SM) is the correct effective theory of elementary particles at energies up to the weak scale. These tests include a wide range of direct particle searches as well as high-precision tests of quantum effects. Since the Standard Model, including the Higgs boson, is based on a renormalizable gauge field theory, the model can also be consistently extrapolated to energies many orders of magnitude above what has been directly probed. Despite these successes, the central ingredient of electroweak symmetry breaking is not fully understood: the Higgs boson, responsible for the breakdown of the electroweak symmetry to the $SU(2) \times U(1)$ subgroup within the Standard Model, still has to be discovered. The search for the source of electroweak symmetry breaking has been the major motivation for experimental searches as well as theoretical model building for the past 25 years.
Besides our ignorance of the cause of electroweak symmetry breaking, there are many reasons to expect that new particles and interactions beyond the Standard Model will be discovered in the near future. These include:

- If the Higgs boson is a fundamental scalar boson, its mass parameter, which is closely tied to the scale of electroweak symmetry breaking, is extremely sensitive to quantum corrections. As a result, attempts to extrapolate the Standard Model to energies much above the electroweak scale lead to the gauge hierarchy problem, where an extreme fine tuning of the underlying model parameters is required to maintain the electroweak scale at its observed value. This is not inconsistent theoretically, but it is at the very least extremely puzzling.

- There is no explanation why charged weak currents are strictly left-handed and why there are three fermion generations. Their mixing and the masses given through the Yukawa coupling stays arbitrary in the SM. The hierarchical pattern of quark masses, but also for charged leptons, might be hint for additional hidden symmetries.

- In the Standard Model neutrinos have exactly zero mass, but, even if today's experiments only yield upper limits for neutrino masses, the observed neutrino oscillations require neutrinos to have a non vanishing mass.

- The Standard Model is unable to account for the dark matter in the universe. On the other hand, dark matter can be explained by a new stable weak-scale particle with weak couplings. Stable new weakly-interacting states also arise in many theories that attempt to protect the scale of electroweak symmetry breaking.

- The Standard Model cannot explain the asymmetry of visible matter over anti-matter. New physics near the electroweak scale can potentially give rise to this baryon asymmetry.

- Gravitation is still far outside the Standard Model since its addition spoils the feature of the renormalisability. Theories beyond the SM, such as String Theories, try to perform this unification.

Thus evidences of several new physics phenomena beyond the Standard Model have been searched for in the data acquired by the experiments operated at the Large Hadron Collider (LHC) [1].

1.1 New charged gauge bosons beyond the Standard Model

Several theoretical models predict, in addition to the well known electroweak vector bosons γ, W, Z, further heavy gauge bosons. These additional particles are postulated for example in Left-Right-Symmetric Models [2–5], based on the gauge group $SU(3)_C \times SU(2)_L \times SU(2)_R \times U(1)_{B-L}$ (B, L: baryon-, lepton-number) or in theories predicting a substructure of the known elementary particles.
In this thesis the detection capabilities for a hypothetical heavy partner of the W, a charged spin-1 boson W$'$, are investigated with the Compact Muon Solenoid (CMS) [6] detector. None of the specific models mentioned above is assumed, but, similarly to several earlier experimental searches, the W$'$ properties are derived from the Reference Model by Altarelli [7] so that the resulting limits can be compared easily.
The Left-Right-Symmetric Model and the Reference Model are described in detail in section 1.1.1 and 1.1.2 respectively. The former direct and indirect W$'$ searches are

instead discussed in section 1.1.3. For completeness, other complementary or supplementary extensions of the standard model tested at the LHC are reviewed in the next chapter.

1.1.1 LEFT-RIGHT SIMMETRIC EXTENSIONS OF THE STANDARD MODEL

In the Standard Model, the origin of parity violation in weak interactions stays unexplained. A priori the multiplets are explicitly designed to break parity in the weak sector. The left-handed particles are assigned to doublets, whereas the right-handed particles do not participate to weak interactions since they are $SU(2)_L$ singlets. The introduction of parity violation has nothing to do with the spontaneous symmetry breaking of the gauge groups, but has been included by hand.
Left-Right-Symmetric Models (LRSM) address this problem and provide an attractive extension of the Standard Model. The general feature of these models is the intrinsic exact parity symmetry of the Lagrangian and an additional $SU(2)$ gauge group, resulting in an observable W′ and Z′. To match the low energy behavior of maximum parity violation in weak interaction, the symmetry is spontaneously broken by a scalar Higgs field.
In addition Left-Right-Symmetric Models incorporate full quark-lepton symmetry and identify the hypercharge Y quantum number of the $U(1)$ symmetry group with the value of barion-minus-lepton number $B-L$. Finally the theory gives a natural explanation for the smallness of the neutrino masses, by relating it to the observed suppression of $V+A$ currents.

TECHNICAL REALIZATION

In order to remedy the apparent arbitrariness of Nature to have only strictly left-handed couplings in weak interactions, the electroweak gauge group of the Standard Model is extended by a right-handed sector (the strong sector remains unchanged). The simplest realization is a Left-Right-Symmetric Model. It is based on the gauge group:

$$SU(2)_L \times SU(2)_R \times U(1)_{\tilde{Y}}. \tag{1.1}$$

The SM fermion doublets are mirrored by arranging the right-handed singlets together from another $SU(2)$ doublet. In the lepton sector this can only be done by predicting a neutrino singlet ν_R for each generation, which is a massive Majorana particle

$$u_R, d_R \rightarrow \begin{pmatrix} u_R \\ d_R \end{pmatrix}; \quad \nu_R, l_R \rightarrow \begin{pmatrix} \nu_R \\ l_R \end{pmatrix}. \tag{1.2}$$

Both doublets can not be assigned to the same $SU(2)$ gauge group, since this would result in a vector current instead of the observed $V-A$ current in weak interactions. Because of the right-handness of the fermions the group is indexed by an “R". The according quantum numbers are reported in table 1.1.

The quantum number of the $U(1)_{\tilde{Y}}$ can be determined by taking into account that the right- and left-handed fermions are assigned to different $SU(2)$ transformations, but have the same electric charge. Thus the $U(1)$ acts on both of them in the same manner. This results in the modified Gell-Mann-Nishijima formula

$$Q = T_{3L} + T_{3R} + \frac{1}{2}(B-L) \tag{1.3}$$

with $T_{3L,3R}$ as third component of the right and left isospin and Q as the charge matrix. Upon computation of $\tilde{Y}$ for right- and left-handed quarks and leptons:

$$\text{Quarks:} \quad \begin{pmatrix} \frac{1}{2} & 0 \\ 0 & -\frac{1}{2} \end{pmatrix} + \begin{pmatrix} \frac{1}{2}\tilde{Y}_l & 0 \\ 0 & \frac{1}{2}\tilde{Y}_l \end{pmatrix} = \begin{pmatrix} q_{\nu_{R,L}} & 0 \\ 0 & q_{l_{R,L}} \end{pmatrix} = \begin{pmatrix} 0 & 0 \\ 0 & -1 \end{pmatrix} \tag{1.4}$$

$$\text{Leptons:} \quad \begin{pmatrix} \frac{1}{2} & 0 \\ 0 & -\frac{1}{2} \end{pmatrix} + \begin{pmatrix} \frac{1}{2}\tilde{Y}_q & 0 \\ 0 & \frac{1}{2}\tilde{Y}_q \end{pmatrix} = \begin{pmatrix} q_{u_{R,L}} & 0 \\ 0 & q_{d_{R,L}} \end{pmatrix} = \begin{pmatrix} \frac{2}{3} & 0 \\ 0 & -\frac{1}{3} \end{pmatrix} \tag{1.5}$$

$$\Rightarrow \tilde{Y}_l = -1 \quad \text{and} \quad \tilde{Y}_q = 1/3 \tag{1.6}$$

and after comparison of this result with the difference of baryon B and lepton number L, one ends up with the equation:

$$\tilde{Y} = B - L \tag{1.7}$$

Thus the quantum number of the $U(1)$ generator can be identified with a physically meaningful quantity, compared to the hypercharge Y in the Standard Model.

Similarly to the Standard Model the fermionic Lagrangian is uniquely fixed by gauge invariance. It can be separated in right-handed and left-handed part by collecting the right- and left-handed fields in spinors ψ_R and ψ_L, respectively:

$$\mathcal{L}_{fermion} = i\bar{\psi}_L\gamma^{\mu}D_{L\mu}\psi_L + i\bar{\psi}_R\gamma^{\mu}D_{R\mu}\psi_R \tag{1.8}$$

with left- and right-handed covariant derivative

$$D_{L\mu} = \partial_{\mu} + ig_L\frac{\vec{T}_L}{2}\cdot\vec{W}_{L\mu} + ig'\frac{B-L}{2}B_{\mu} \tag{1.9}$$

Fermions (Spin 1/2)						
	Multiplets	Quantum Number				
		T_L	T_{3L}	T_R	T_{3R}	$\tilde{Y} = B - L$
Quarks	$\begin{pmatrix} u \\ d' \end{pmatrix}_L$	1/2 1/2	1/2 -1/2	0 0	0 0	1/3 1/3
	$\begin{pmatrix} u \\ d' \end{pmatrix}_R$	0 0	0 0	1/2 1/2	1/2 -1/2	1/3 1/3
Leptons	$\begin{pmatrix} \nu \\ l \end{pmatrix}_L$	1/2 1/2	1/2 -1/2	0 0	0 0	-1 -1
	$\begin{pmatrix} \nu \\ l \end{pmatrix}_R$	0 0	0 0	1/2 1/2	1/2 -1/2	-1 -1

Table 1.1.: Particles of the Left-Right-Symmetric Model with their quantum numbers. The left-handed doublets transform trivial under the right-handed $SU(2)$ and vice versa. For the sake of clearness the flavor index as well as the color index of the quark doublets have been dropped.

$$D_{R\mu} = \partial_\mu + ig_R \frac{\vec{T}_R}{2} \cdot \vec{W}_{R\mu} + ig' \frac{B-L}{2} B_\mu \tag{1.10}$$

The Lagrangian is completely invariant under the interchange $L \longleftrightarrow R$. The introduction of a Higgs sector is necessary to give mass to the fermions and thus add terms proportional to $\bar{\psi}\phi\psi$ to the Lagrangian. The simplest solution within LRSM is provided by a Higgs field ϕ given by a 2×2 matrix, whose transformation properties are dictated by ψ_L, ψ_R. The Higgs field ϕ, as well as $\tilde{\phi} T_2 \phi * T_2$, transforms as doublets under $SU(2)_R$ and $SU(2)_L$ and trivial under $U(1)_{B-L}$, so that the most general coupling of the fermions to ϕ is given by

$$\mathcal{L}_{Yukawa} = -\sum_{i,j} \{ \bar{\psi}_{Li} \Gamma^{\psi}_{ij} \phi \psi_{Rj} + \bar{\psi}_{Li} \Delta^{\psi}_{ij} \tilde{\phi} \psi_{Rj} + h.c. \} \tag{1.11}$$

where i and j denote the flavor indices and Γ^{ψ}_{ij} and Δ^{ψ}_{ij} describe the Yukawa coupling to the Higgs i.e. the mass of the particles.

The charge of the Higgs fields can be determined from the modified Gell-Mann-

Nishijima formula 1.3

$$Q\phi = \left[\frac{1}{2}T_3, \phi\right] = \begin{pmatrix} 0\cdot\phi_{11} & \phi_{12} \\ -\phi 21 & 0\cdot\phi_{22} \end{pmatrix} \tag{1.12}$$

using

$$\phi = \begin{pmatrix} \phi_{11} & \phi_{12} \\ \phi 21 & \phi_{22} \end{pmatrix} \quad \text{and} \quad \tilde{Y}(\phi) = 0 \tag{1.13}$$

Therefore ϕ_{11} and ϕ_{22} are electrically neutral scalars.

SPONTANEOUS PARITY BREAKING

Before discussing the spontaneous symmetry breaking of parity, a sufficient definition for parity within Left-Right-Symmetric Model is given. There is an obvious symmetry: every left-handed field in the fermion sector have a right-handed counterpart and also the gauge bosons $\vec{W}_L$ and $\vec{W}_R$ correspond to each other. A mathematical formulation of this transformation, interpreted as parity transformation, is:

$$\vec{W}^{\mu}_{L,R}(x) \longrightarrow \varepsilon(\mu)\vec{W}^{\mu}_{R,L}(\hat{x}) \tag{1.14}$$

$$B^{\mu}(x) \longrightarrow \varepsilon(\mu)B^{\mu}(\hat{x}) \tag{1.15}$$

$$\psi_{L,R}(x) \longrightarrow V^{\psi}_{R,L}\gamma^0\psi_{R,L}(\hat{x}) \tag{1.16}$$

$$\phi(x) \longrightarrow \phi^{\dagger}(\hat{x}) \tag{1.17}$$

using the definitions

$$\hat{x} = \begin{pmatrix} x^0 \\ -\vec{x} \end{pmatrix} \quad \text{and} \quad \varepsilon(\mu) = \begin{cases} 1 & \text{for} \quad \mu = 0 \\ -1 & \text{for} \quad \mu = 1,2,3 \end{cases} \tag{1.18}$$

To conserve the invariance of the Lagrangian under this parity transformation the same coupling constants to both $SU(2)$ groups and an additional constraint involving the arbitrary unitary matrices $V^{\psi}_{L,R}$ are required.

$$g_R = g_L, \quad \left(V^{\psi}_R\right)^{\dagger}\Gamma_{psi}V^{\psi}_L = \Gamma^{\dagger}_{\psi}, \quad \left(V^{\psi}_R\right)^{\dagger}\Delta_{psi}V^{\psi}_L = \Delta^{\dagger}_{\psi}. \tag{1.19}$$

The simplest choice assumes $V^{\psi}_{L,R} = 1$.

Since the Higgs field ϕ, which has been introduced to give mass to the fermions, is neither able to break the gauge group of the LRSM to the Glashow Wimberg Salam (GWS) gauge groups $SU(2)_L \times U(1)_Y$ nor to $U(1)_{em}$, the Higgs sector has to be enlarged for this purpose. Since the Higgs fields, which are required to break down the symmetry, are not unique, there are several interesting realizations. We limit the discussion to the simplest model referred to as minimal LR-model, with three scalar multiplets ϕ, Δ_L, Δ_R [2] and refer the reader to the literature for alternative realizations [3]. The latter Higgs fields are complex $SU(2)$ triplets with lepton number $L = -2$, which can be written as:

$$\Delta = \frac{1}{\sqrt{2}}\sigma_a \delta_a = \begin{pmatrix} \delta_3 & \delta_1 - i\delta_2 \\ \delta_1 + i\delta_2 & -\delta_3 \end{pmatrix} \tag{1.20}$$

where σ_a denotes the Pauli matrices.

The charge of the Higgs is obtained by

$$Q\Delta = \left[\frac{1}{2}\sigma_3, \Delta\right] + 1 \cdot \Delta = \begin{pmatrix} \Delta_{11} & 2 \cdot \Delta_{12} \\ 0 \cdot \Delta 21 & \Delta_{22} \end{pmatrix} \tag{1.21}$$

and thus leading to doubly charged as well as single charged and neutral Higgs scalars.

The vacuum expectation values are chosen so that both $SU(2)$ and the $U(1)_{B-L}$ are broken, but the $U(1)_{em}$ symmetry remains:

$$\langle \phi \rangle_0 = \frac{1}{\sqrt{2}} \begin{pmatrix} v & 0 \\ 0 & w \end{pmatrix}, \quad \langle \Delta_{L,R} \rangle = \frac{1}{\sqrt{2}} \begin{pmatrix} 0 & 0 \\ u_{L,R} & 0 \end{pmatrix} \tag{1.22}$$

In addition the assumption of the order of magnitude relation

$$|u_L|^2 \ll |v|^2 + |w|^2 \ll |u_R|^2 \tag{1.23}$$

is motivated by the breaking scheme, which has been established in the SM. The difference in the symmetry of the Higgs potential, reflected by the vacuum expectation values and the symmetry of the Lagrangian, results in the following spontaneous symmetry breaking:

$$SU(2)_L \times SU(2)_R \times U(1)_{L-B} \times P \xrightarrow{u_R} SU(2)_L \times U(1)_Y \xrightarrow{v,w} U_{em} \tag{1.24}$$

P symbolically denotes the parity symmetry which is broken in the first step.

EXPERIMENTAL CONSEQUENCES AND THE W′

During the symmetry breaking, described by 1.24, the first stage gives mass to the W_R and Z_R, which are bosons in the right-handed sector. The properties of the W_R are different compared to the SM and thus match with the given definition of a W′. At this intermediate stage one obtains the Standard Model with additional Higgs bosons related to ϕ and the Δ's. In addition right-handed neutrinos occur which have to be very heavy (see below). The parity symmetry of the Lagrangian is broken by the Δ-Higgs bosons whose vacuum expectation value is not parity conserving. Then the appealing feature of the LRSM is the recovered parity conservation at energies at the scale of the W_R.

The masses of the other boson fields, W_L and Z_L, result from the subsequent symmetry breaking. The step is in principle equivalent to the Higgs mechanism in the Standard Model and the arising bosonic fields can therefore be identified with the SM W and Z^0.

The symmetry breaking pattern dictates that the vacuum expectation value for Δ_R is greater then those for Δ_L and ϕ. Since the former is related to the W_R field and the latter to W_L, the mass of the W_R boson is larger than the W_L. The fields W_R and W_L do not correspond to physical mass eigenstates $W^{\pm}_{1,2}$ one to one, but are a mixing of both fields:

$$\begin{pmatrix} W_1^{\pm} \\ W_2^{\pm} \end{pmatrix} = \begin{pmatrix} cos\xi & -sin\xi e^{i\lambda} \\ sin\xi e^{-i\lambda} & cos\xi \end{pmatrix} \begin{pmatrix} W_L^{\pm} \\ W_R^{\pm} \end{pmatrix} \tag{1.25}$$

The mixing angle and the (CP-violating) phase can be calculated as a function of the vacuum expectation values

$$e^{i\lambda} = -\frac{vw^*}{|vw|}, \qquad \xi \simeq \frac{2|vw|}{|v|^2+|w|^2}\left(\frac{M_1}{M_2}\right)^2 \tag{1.26}$$

The masses of the two eigenstates are then given by:

$$M_1^2 \simeq \frac{1}{4}g^2(|v|^2+|w|^2), \quad M_2^2 \simeq \frac{1}{4}g^2(|v|^2+|w|^2+2|u_R|^2) \tag{1.27}$$

The mass of the W_1 is the Standard Model mass of the W, whereas the mass of the W_2 is dictated by the breaking scale u_R of $SU(2)_R$. Since the mass scale has not been observed, u_R has to be sufficiently large and thus the mixing can be assumed to be zero as it is done in this work.

Besides the additional vector bosons and numerous Higgs scalars, an important feature of Left-Right-Symmetric models is the generation of neutrino masses. Due to the existence of right-handed neutrinos, the neutrinos obtain Majorana masses through the symmetry breaking. Through the see-saw mechanism the Standard Model neutrinos obtain small masses, while the right-handed neutrinos N obtain masses in the order of the breaking mass scale u_R

$$m_N \sim u_R \sim M_2, \quad m_{\nu_l} \sim m_l^2/m_N. \tag{1.28}$$

1.1.2 THE W′ REFERENCE MODEL AS A GENERAL APPROACH

Given the large number of models which predict new heavy charged gauge bosons, it is a natural approach to use a simplified ansatz for such a search. After a discovery of signatures related to a new boson, detailed studies can be performed to distinguish between these models and to determine whether the boson belongs to a Little Higgs model, a Left-Right Symmetric or a totally different one. Following the traditions of direct searches at colliders, this study is based on the Reference Model first discussed by Altarelli [7].

The Reference Model is obtained by simply introducing ad hoc new heavy gauge bosons: two charged W′ vector bosons and one neutral Z′ as a carbon copy of the Standard Model ones. The couplings are chosen to be the same as for the ordinary W and Z^0 bosons. The only parameters are the masses of the new vector bosons. While the coupling of the so constructed bosons with leptons is comparable to those obtained in extended gauge theories, the coupling to the massive Standard Model gauge boson are enlarged. For W′ masses larger than 500 GeV this leads to a W′ width larger than its mass. Since such a state is not interpreted as a particle anymore, the couplings of W′ and Z′ to the Standard Model W and Z^0 are suppressed manually in the Reference Model. This results in a moderate width for the new gauge bosons.

This suppression arises in extended gauge theories in a natural manner: if the new gauge bosons and the SM ones belong to different gauge groups, vertices of the kind $Z'Z^0Z^0$ or $W'W^{\pm}Z^0$ are forbidden. They can only occur after symmetry breaking due to mixing of the gauge group eigenstate to mass eigenstate. The vertices are then suppressed by a factor of the order of $(W^{\pm}/\mathrm{W}')^2$. With this assumption, the Reference Model and the Left-Right-Symmetric Model have comparable branching ratios. Assuming the former for a direct search is then a reasonable approach. Additional neutrinos are not taken into account within the model.

PRODUCTION OF A W′ BOSON

The production of a W′ in a proton-proton collision is comparable to that of a W boson. From constraints of Lorentz-invariance and renormalisability the matrix element for a coupling of a W′ to two fermions i and j has the form:

$$\mathcal{M} = -\frac{1}{\sqrt{2}} i g W'_{\mu} \bar{\psi}_i \gamma^{\mu} (a + b\gamma_5) \psi_j U_{ij}. \tag{1.29}$$

As mentioned before, the coupling constant g is assumed to be identical with the SM one. Therefore also the constants a and b describing the vector and the axial-vector fraction of the interaction are set in coincidence to the SM ($a = 1$, $b = -1$). U_{ij} is the Cabibbo-Kobajashi-Maskawa matrix connecting fermions i and j.

The partial width of a W′ resulting from the coupling to a quark q_i and an antiquark $\bar{q}_j$ is:

$$\Gamma_{ij} = \frac{N_C G_F M_W^2 M_{W'}}{6\sqrt{2}} |U_{ij}| \tag{1.30}$$

with the colour factor N_C and the Fermi coupling constant G_F. Due to the close relation of the W′ to the W of the Standard Model, the full W′ width $\Gamma_{W'}$ can be expressed in terms of the W width Γ_W

$$\Gamma_{W'} \simeq \begin{cases} \frac{M_{W'}}{M_W}\Gamma_W & \text{for} \quad M_{W'} < 180 \text{ GeV} \\ \frac{4}{3}\frac{M_{W'}}{M_W}\Gamma_W & \text{for} \quad M_{W'} \gg 180 \text{ GeV}. \end{cases} \tag{1.31}$$

For the W′ masses below the top mass ($\sim$ 180 GeV) the kinematically allowed decay channels are identical for the SM W and the W′. For W′ masses above 180 GeV the decay $W' \rightarrow tb$ opens. Since the phase space is enlarged it results in an increase of the width by a factor of 4/3 passing from $N_C = 9$ to $N_C = 12$.

From the tree level Feynman diagram (fig. 1.1) the differential production cross section at leading order for a W′ results in [7]:

$$\frac{d\sigma}{dy}(pp \rightarrow W' + X) = \frac{4\pi^2}{3M_{W'}^3} \sum_{ij} \int dx_i dx_j f_i(x_i, M_{W'}^2) f_j(x_j, M_{W'}^2) \Gamma_{ij} \tag{1.32}$$

with $f_i(x_i, M_{W'}^2)$ is the probability to find a parton i with a proton's momentum fraction x_i at the energy scale of the W′ mass.

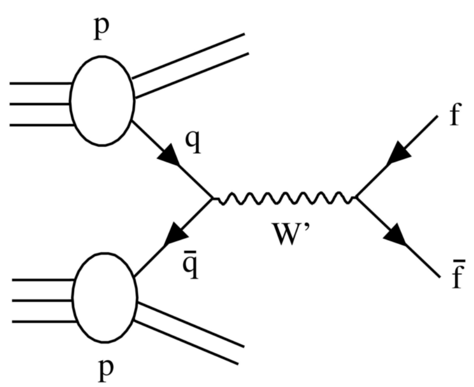

Figure 1.1.: Feynman diagram of the W′ production at the lowest order. A quark-antiquark pair annihilates into a W′ and decays into a fermion pair.

1.1.3 PREVIOUS SEARCHES

There are two basic strategies for testing a new model: the direct search for the production and decay of new particles, and the indirect search. In the latter case, the new physics is identified via additional contributions in Feynman diagrams. These may enhance or suppress a given process. In direct searches the new particles are produced for example at colliders. In the resonant process the center-of-mass energy is required to be equal to the production threshold for on-shell production.

DIRECT SEARCHES

Thanks to the higher luminosity and higher center of mass energy with respect to the Tevatron, the LHC allowed to improve the pre-existent exclusion limit for the W′ already with 36 pb^{-1} collected during the 2010 run. The W′ with an invariant mass below 1.58 TeV has been excluded at the 95% confidence level in the combined electron plus muon channel by the CMS collaboration, improving the previous limit of 1 TeV from the CDF experiment. The limit was further improved during 2011 thanks to the increasing amount of collected data and the results with 1.13 fb^{-1} of data is presented in Chapter 7.

INDIRECT SEARCHES

Because of the variety of indirect searches, which make different assumptions about the coupling of the new gauge bosons, the Higgs sector and the neutrino sector, only some ideas for experiments resulting in W′ mass limit are given.

- $K_L - K_S$ mass difference: The $K_L - K_S$ mass difference can receive important contributions from box diagrams including the exchange of new heacy charged gause bosons as shown in figure 1.2.
  Since the mass difference in the $K_L - K_S$ system is known from experiments to be $\Delta m = m_{K_L} - m_{K_S} = (3.483 \pm 0.006)\dot{1}0^{-12}$ MeV [8] a mass limit of the order of $M_{W_R} > 1.6$ TeV can be derived depending on the assumed couplings [9].
- Neutrinoless Double β decay: The existence of a new heavy right handed gauge boson coupling to massive Majorana neutrinos, gives rise to additional Feynman graphs for the neutrino β-decay. The most important contribution arise from the graph reported in figure 1.2 right. Two neutrons both decay into a right-handed W′. If one W′ decays into a lepton and a Majorana neutrino, the other W′ can absorbe it since the neutrino is its own antiparticle and create a lepton. Up to now there have not been any observations of this kind of neutrinoless β-decay. From the upper bound on the cross section, a limit on the W′ mass of 310 GeV can be derived [10].

Further constraints on the W′ mass have been derived from cosmological considerations concerning supernovae, neutrino-electron and electron-hadron interactions and more [8].

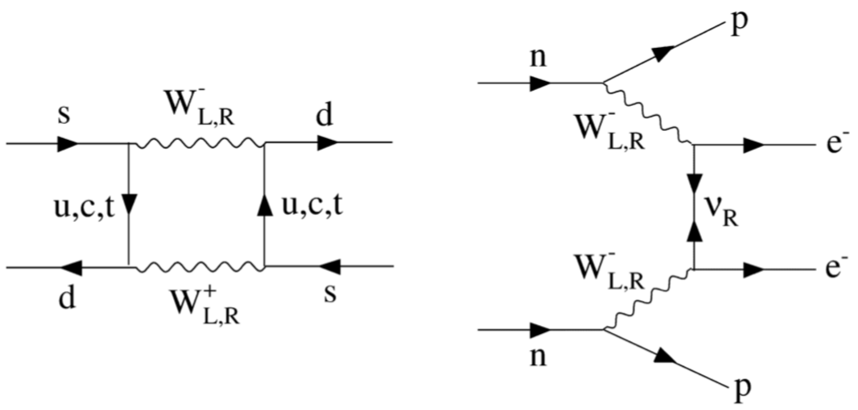

Figure 1.2.: Additional Feynman diagrams arising in case of an existing W′ in $K_L - K_S$ oscillations (left) and neutrinoless double beta decay (right).

1.2 W′ SIGNATURE AND BACKGROUNDS

From the analysis point of view, only two objects are needed in order to identify the W′ final state: one electron with high p_{T} and one neutrino balanced with the electron both in direction and in module. Additional objects could be present in the inclusive final state like jets, other neutrinos or leptons. Since the neutrino is not detectable, his transverse momentum is measured as an energy unbalance in the transverse plane perpendicular to the beam direction (where the parton momentum fraction before the collision is negligible) and arises via the missing transverse energy $E_{\mathrm{T}}^{\mathrm{miss}}$ in the detector. The search is accomplished by comparing the data with simulated events from the expected Standard Model backgrounds. Due to the unknown momentum of the neutrino in the direction along the beam line, the invariant mass of the boson could not be accessed. The presence of a W′ signal would be reflected in an excess of events in the high transverse mass region. The transverse mass is defined in analogy with the invariant mass using only transverse quantities:

$$M_T = \sqrt{2E_T^e E_{\mathrm{T}}^{\mathrm{miss}}(1 - \cos\Delta\phi_{e,\nu})} \tag{1.33}$$

The following Standard Model processes which can contribute to the inclusive final state under investigation ($e + E_{\mathrm{T}}^{\mathrm{miss}} + X$) are considered:

- $W \rightarrow e\nu + X$
- $W \rightarrow \tau\nu + X \rightarrow e\nu + X$
- $WW \rightarrow e\nu + X$
- $WZ \rightarrow e\nu + X$
- $ZZ \rightarrow e\nu + X$
- $t\bar{t} \rightarrow Wb + X \rightarrow e\nu + X$

where X could be an object like lepton, neutrino, one or more jets from initial/final state radiation. Due to the identical final state and same kinematics, the $W \rightarrow e\nu$ is the main and irreducible background.
In addition to the backgrounds already listed, also drell-yan and multijet events can be a source of instrumental background:

- $Z \rightarrow ee$ events can lead to a final state with electron and $E_{\mathrm{T}}^{\mathrm{miss}}$ if one of the two electrons falls in a non instrumented region. Soft radiation such as jets opposite to the boson (hadron recoil), could further contribute to the missing transverse energy.
- QCD multijet events have to be considered due to the high cross section at hadron colliders despite the rate of jets faking an electron is fairly low (2-3%). Di-jet events in which one jet mimics an electron and the other is mis-measured, creating missing transverse energy, could be mistaken as genuine $ele + E_{\mathrm{T}}^{\mathrm{miss}}$ events. The fake rate method, described in 7.4, is a data-driven approach used to estimate both shape and normalization of the multijet background. The choice of a data-driven technique is desirable for this background given the difficult to model the process due to large theoretical uncertainties and given the few statistics available in the generated MC samples.

In the following chapters, when referring to Standard Model backgrounds, the full list of physics or instrumental backgrounds is taken into account.
The detailed discussion of the simulation and the cross section calculation for background and signal processes is presented in section 7.1.

Since this analysis relies on electrons and missing transverse energy, the role of the electromagnetic calorimeter is central. High electron reconstruction and identification efficiencies, the capability in rejecting fake electrons from the multi-jet background as well as a good energy resolution on the $E_{\mathrm{T}}^{\mathrm{miss}}$ are aspects of primary importance.

The main subdetectors of CMS involved in the analysis, other then the electromagnetic calorimeter, are the internal tracking system for the measurement of the electron momentum and for the charge assignment and the hadronic calorimeter mainly used to veto the energy deposition from hadrons in order to minimize the contamination of non-leptonic particles in the final sample. The details about the CMS detector are discussed in Chapter 3 with particular emphasis on the description of the electromagnetic calorimeter of CMS. The discussion of the electron and $E_{\mathrm{T}}^{\mathrm{miss}}$ reconstruction processes is presented in Chapter 6.

CHAPTER 2

REVIEW OF SEARCHES FOR (NON-SUSY) PHENOMENA BEYOND THE STANDARD MODEL

In the last decades, several theories have been built to extend the Standard Model allowing for different models of electroweak symmetry breaking, while still in agreement with the current experimental data. In the complex panorama of the beyond the SM models, a rough classification discerns the supersymmetric theories from the rest.

Supersymmetry (SUSY) [11] is one proposed solution to the hierarchy problem, ensuring a finite Higgs boson mass by loop cancellation. It doubles the number of elementary particles in nature: it postulates that there are new particles with similar mass and equal couplings to those in the SM. The SUSY and the SM particles are related by an operator Q, such that $Q|\text{fermion} >= |\text{boson} >$ and $Q|\text{boson} >= |\text{fermion} >$, and therefore the superpartners differ from their standard model counterparts by a half-unit of spin. Thus, all fermions have bosonic SUSY partners, and vice-versa. The electroweak symmetry breaking problem is still solved through a Higgs mechanism, though in this case instead of a single Higgs scalar field, at least two Higgs doublets have to be introduced. Experimental signatures of these supersymmetric particles should be observed at the energies that the LHC will reach.

In the non-SUSY context, an extension of the SM are Grand Unified Theories (GUTs) [12, 13] describing the symmetry in the Standard Model ($SU(3)_C \times SU(2)_L \times U(1)_Y$) as if it would be originated from a larger symmetry group relating quarks and leptons. This addresses the unification problem: the symmetry is unbroken at some higher energy where all interactions are described by a local gauge theory with one running coupling. A general problem with most GUT theories is the prediction of proton de-

cay, which has not yet been observed.
Also the existence of Extra Dimensions is considered. In the ADD model [14, 15] the SM fields are confined to a four-dimensional membrane in a higher-dimensional space. Gravity travels in additional spatial dimensions, making it seem much weaker than the other fundamental forces in four dimensions. The theory thus offers a solution to the hierarchy problem. It also contributes with a Dark Matter candidate: the graviton travels in all the spatial dimensions, giving rise to several Kaluza-Klein resonances on the four-dimensional brane.
Compositeness [16] is a possible explanation for the source of the mass hierarchy of quarks and leptons. It proposes a composite structure for them and postulates the existence of excited fermions. Many different models of excited fermions and fermion substructure studies via contact interactions have been carried out.

In the data recorded during 2011 no sign of new physics has been found at the LHC, but many search analyses have set more stringent limits to the existence of new particles. A partial list of the results obtained in the searches for new particles foreseen in non-SUSY extensions of the SM is reported in the next section.
Since the search for a new heavy gauge boson W′ is the main argument of this thesis, the description of the analysis strategy and the results are presented in detail in Chapter 6 and 7 and they are deliberately omitted from the current chapter.
All the results already published by the CMS collaboration can be found in [17].

2.1 The status of the art of the exotica searches with the CMS detector

The results of beyond the SM searches presented in this section are known with the name of “exotica searches” by the particle physicists. The analysis make use of the proton-proton collision data delivered by the LHC and collected with the CMS detector and are based on an integrated luminosity which varies from 1 fb^{-1} to 2 fb^{-1}. All the results are currently being updated with the full statistics of 4.7 fb^{-1} collected in 2011.

2.1.1 Heavy resonances

Di-lepton and di-photon resonances

Several theoretical models beyond the SM predict the existence of narrow resonances, possibly at the mass scale of O(1) TeV, that decay to a pair of charged leptons [18]. Also the Randall-Sundrum (RS) model of extra dimensions [19, 20] foresees the existence of Kaluza-Klein graviton excitations (GKK) decaying to a pair of charged leptons or pair of photons. The CMS collaboration has searched for such narrow resonances in the invariant mass spectrum of di-muon, di-electron [21] and di-photons [22] final states.

$Z' \to l^+ l^-$ events are characterized by two high transverse momentum leptons with opposite charge. For both di-muon and di-electron final states, two isolated same flavour leptons. The main SM process that contributes to the di-muon and di-electron invariant mass spectra is Drell-Yan production (Z/γ^*); there are also contributions from the $t\bar{t}$, tW, WW, and $Z \to \tau\tau$ channels. Especially for the electron channel, jets may be misidentified as leptons and contribute to the dilepton invariant mass spectrum through multi-jet and vector boson+jet final states.

The spectra are consistent with standard model expectations in both the bulk and the tails of the invariant mass distribution. Figure 2.1 shows the 95% confidence level (CL) upper limits on the cross section of Z' production, obtained combining the di-electron and di-muon channels. These limits exclude at 95% confidence level a Z' with standard-model-like couplings below 1.94 TeV, the superstring-inspired Z'_ψ [18] below 1.62 TeV, and, for values of the coupling parameter $k/\bar{M}_{Pl}$ of 0.05 (0.1), Kaluza-Klein gravitons below 1.45 (1.78) TeV.

In the di-photon channel, limits are derived on the cross section for the production of RS gravitons, and hence on the parameters of the warped extra dimension model. For values of the coupling parameter ranging from 0.01 to 0.1, graviton masses below 0.86 to 1.84 TeV are excluded at the 95% CL.

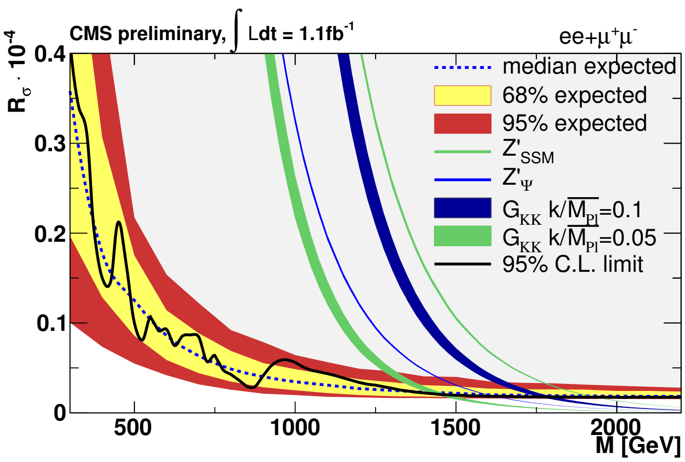

Figure 2.1.: The upper limits as a function of resonance mass M, on the production ratio R_σ of cross section times branching fraction into lepton pairs for Z'_{SSM} and G_{KK} production and Z'_ψ boson production (see text). The limits are shown from the combined di-lepton result. The predicted cross section ratios are shown as bands, with widths indicating the theoretical uncertainties.

LEPTOQUARKS SEARCH

The standard model has an intriguing but ad hoc symmetry between quarks and leptons. In some theories beyond the SM, such as $SU(5)$ gran unification [12], Pati-Salam $SU(4)$ [5], technicolor [23–25] and others, the existence of a new symmetry relates the quarks and leptons in a fundamental way. These models predict the existence of new bosons, called leptoquarks. The leptoquark (LQ) is colored, has fractional electric charge, and decays to a charged lepton and a quark with unknown branching fraction β, or a neutrino and a quark with branching fraction (1 - β). Searches for pair-production of first and second generation scalar LQs have been performed in the eejj [26], eνjj [27], and $\mu\mu$jj or $\mu\nu$jj [28] final states. The dominant backgrounds for these searches arise from the SM production of Z/γ+jets, W+jets and $t\bar{t}$ events. Figure 2.2 shows the exclusion limits at 95% CL on the second generation leptoquark hypothesis with $\beta = 1$ for the $\mu\mu jj$ and $\mu\nu jj$ channels separately. Second generation scalar LQ masses below 632 GeV (523 GeV) are excluded at 95% CL for β = 1 (β = 0.5). From analysis of the electronic final state, based on a statistics of 36 pb^{-1}, the first generation of LQs is excluded below a mass of 350 GeV with $\beta = 0.5$.

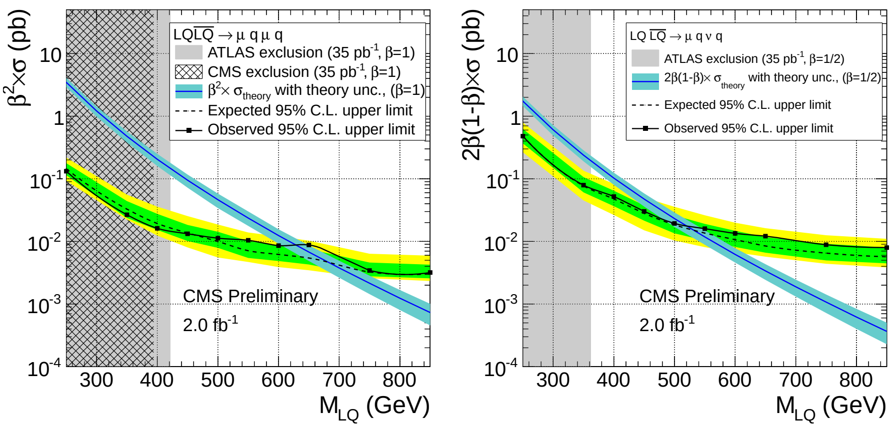

Figure 2.2.: Exclusion limits at 95% CL on the second generation LQ hypothesis in $\mu\mu jj$ and $\mu\nu jj$ final state.

DI-JET FINAL STATE

In the standard model, point like parton-parton scatterings in high energy proton-proton collisions can give rise to final states with energetic jets. At large momentum transfers, events with at least two energetic jets (di-jets) may be used to confront the predictions of perturbative Quantum Chromodynamics (QCD) and to search for signatures of new physics. The new physics could manifest itself via the direct production of a new massive particle decaying into a di-jet final state (quark-quark, quark-gluon, or gluon-gluon resonances). Figure 2.3 (left) shows the 95% CL upper limits on signal cross section versus di-jet resonance mass, compared to theoretical predictions for various new physics models. String resonances [29, 30], excited quarks [31], axigluons [32], colorons [33], and E6 diquarks [34], in specific mass intervals, have been excluded at 95% CL [35].

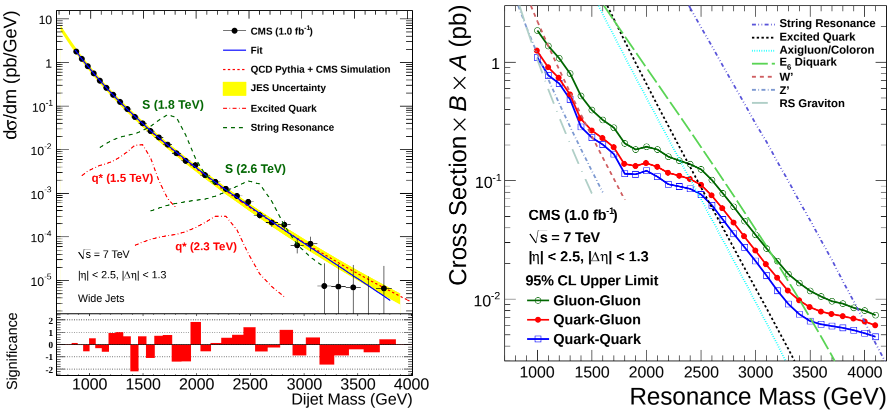

Figure 2.3.: (Left) Dijet Mass spectrum from wide jets (points) compared to a smooth fit (solid) and to predictions including detector simulation of QCD (short-dashed), excited quark signals(dot-dashed), and string resonance signals(long-dashed). The bin by bin significance of the data-fit difference is shown at bottom. (Right) The 95% CL upper limits on $\sigma \times B \times A$ for dijet resonances of type gluon-gluon (open circles), quark-gluon (solid circle), and quark-quark (open boxes), compared to theoretical predictions for string resonances, E6 diquarks, excited quarks, axigluons, colorons, new gauage bosons W$'$ and Z$'$, Randall-Sundrum gravitons (see text).

FOURTH GENERATION OF FERMIONS

Recently, there has been renewed interest in extensions of the SM predicting a fourth generation of massive fermions [36–38]. Theoretical studies have shown that indirect bounds on the Higgs boson mass can be relaxed, and an additional generation of quarks may possess enough intrinsic matter and anti-matter asymmetry to be relevant for the baryon asymmetry of the Universe. Driven by this motivation, a search for final states with b' and t' fourth generation quarks produced singly or in pair is performed with the CMS detector. The main backgrounds derive from $t\bar{t}$, $W/Z + jets$ and single top processes. In a simplified CKM4 model [39], based on one coupling parameter $A = |V_{tb}|^2 = |V_{t'b'}|^2$ in a unitary model, the masses of the fourth generation quarks are assumed to be degenerated: $m_{t'} = m_{b'}$. For minimal off-diagonal mixing ($A \simeq 1$) between the third and the fourth generation, the exclusion limit $m_{t'} = m_{b'} > 490$ GeV at 95% CL is observed.

2.1.2 Compositeness models

A fundamental question in the standard model of particle physics is the source of the mass hierarchy of the quarks and leptons. A commonly proposed explanation for the three generations is a compositeness model [16, 40] in which the known leptons and quarks are bound states of either three fermions, or a fermion-boson pair. The underlying substructure of these new bound states implies a large spectrum of excited states. Novel strong contact interactions (CI) couple excited fermions ($f*$) to ordinary quarks and leptons (f) and can be described with the effective Lagrangian $\mathcal{L}_{CI} \propto (j^{\mu} j_{\mu})/\Lambda^2$, where Λ is the compositeness scale, and j_{μ} is the fermion current.

Excited leptons

The excited lepton decays into one photon and one SM lepton in the analysis considered here. The associated production of a lepton and an oppositely charged excited lepton resulting in a final state with an isolated photon and an isolated pair of charge conjugated same-flavor leptons is searched [41]. The maximum reconstructed invariant mass among the two possible lepton-photon combination, $M_{l\gamma}^{max}$, is used to discriminate between signal and SM backgrounds. 95% CL upper limits on the scale Λ as a function of the excited lepton mass in the O(1) TeV range are set.

Excited quarks

The CMS experiment has performed a search for anomalous production of highly boosted Z bosons in the dimuon decay channel arising from the decays of new heavy particles [42]. The search is optimized for the detection of excited quark production and decay via $q^* \to qZ \to q\mu\mu$, with no explicit requirement on the jet recoiling against a high transverse momentum Z. The results are consistent with background-only expectations. Limits are derived on excited quark production in the plane of compositeness scale Λ versus mass for two scenarios of production and decay [40]: one assuming excited quark transitions via SM gauge bosons only, and one including also novel contact interaction transitions from new strong dynamics. The $q*$ mass limits at 95% CL with contact interactions are more sensitive than previous searches in scenarios where the coupling to gluons is suppressed relative to the electroweak gauge bosons, ruling out masses below 1.17 TeV in the extreme case when this coupling is zero.

2.1.3 EXTRA DIMENSIONS

In the ADD model[14, 15] framework, the fundamental Planck scale can be lowered to the electroweak scale making possible the production of gravitons at the LHC. Searches for virtual-graviton contributions in the di-photon [22] and di-muon [43] final states have been performed. Figure 2.4 (Left) displays the di-photon invariant mass distribution for the observed data, the backgrounds, and the ADD signal. The ADD signal would appear as a broad excess of events at high values of invariant mass differently from the case of searches for heavy resonances with the same final state. The data are found to be consistent with SM expectations. Lower limits are set on the effective Planck scale in the range of 2.3-3.8 TeV at the 95% confidence level.

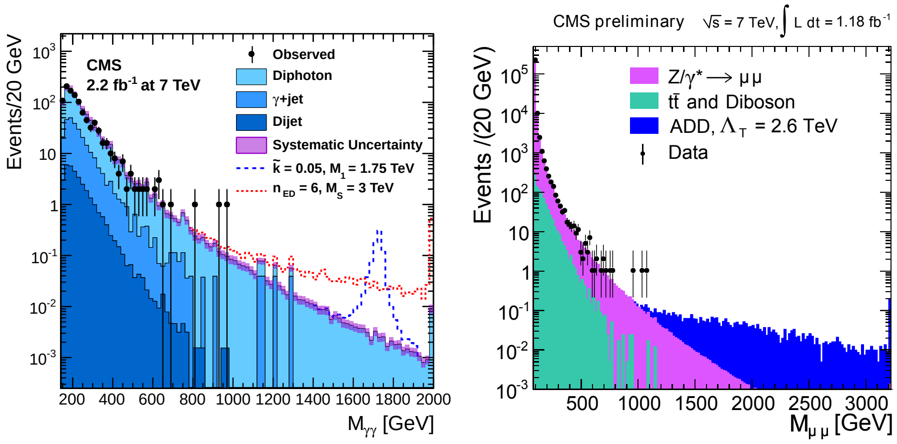

Figure 2.4.: (Left) Observed data (points with error bars) and background expectations (filled solid histograms) as a function of the di-photon invariant mass. Photons are required to be isolated, with ET > 70 GeV. (Right) Dimuon invariant mass spectrum compared with the SM prediction and a simulated ADD signal with $\Lambda_T = 2.6$ TeV.

2.1.4 MASSIVE LONG LIVED PARTICLES

Historically, the strange, long-lived kaons heralded a revolution in particle physics, in terms of new fundamental matter, and also in the shape of a new conserved quantum number. Today, states classifiable as Stable Massive Particles (SMPs) recur in many theoretical extensions of the Standard Model [44]. The most obvious possibility for an SMP is that one or more new states carry a new conserved, or almost conserved, global quantum number. The already cited SUSY with R-parity, extra dimensions with KK-parity fall into this category.

Heavy long-lived particles with hadronic nature, such as gluinos or stops, hadronize in

flight, forming meta-stable bound states with quarks and gluons (so called R-Hadrons). If the lifetime of R-Hadrons produced at LHC is longer than a few nanoseconds, these particles will travel over distances which are comparable or larger than the size of a typical particle detector, and hence might be detected and identified via their direct interaction with the detector. The CMS experiment uses two complementary strategies to identify such long-lived particles. A significant fraction of these massive particles (assuming masses greater than 100 GeV) will have a velocity $\beta = v/c$, smaller than 0.9. A first approach is to identify R-Hadrons through the distinctive signature of a high momentum track with an anomalously large rate of energy loss through ionization in the silicon tracker. Searches have been also performed for very slow ($\beta < 0.4$) R-hadrons containing a gluino, for which the electromagnetic and nuclear energy loss is sufficient to bring a significant fraction of the produced particles to rest inside the CMS detector volume. These stopped R-hadrons would decay into an hadronic jet and a neutralino only seconds, days, or weeks later (accordingly to their unknown lifetime), and out-of-time with respect to the LHC collisions. The online selection of events requires the firing of a single jet trigger with an explicit veto on the beam presence. In both cases no significant excess above background (mainly instrumental noise) was observed.
A 95% CL lower limit of 899 (839) GeV on the mass of pair-produced $\tilde{g}$, hadronizing into stable R-gluonballs with 10% (50%) probability, is set with the tracker-only selection. The tracker-plus-muon selection gives a lower limit of 885 (829) GeV for the same signal model (figure 2.5). The analogous limit on the $\tilde{t}_1$ mass is 620 GeV with the tracker-only selection and 608 GeV with the tracker-plus-muon selection.

In summary no evidence for physics beyond the standard model has been observed in several signatures complementary or supplementary to the search for charged heavy gauge bosons W$'$. Results consistent with those presented in this section have been obtained by the ATLAS collaboration with the same amount of data.

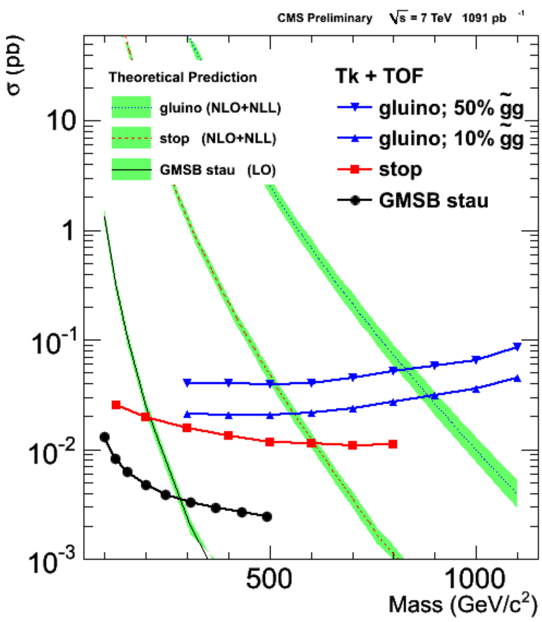

Figure 2.5.: Predicted theoretical cross section and observed 95% CL upper limits on the cross section for the different combinations of models and scenarios considered: pair production of supersymmetric stop and gluinos; different fractions, f, of R-gluonball states produced after hadronization.

CHAPTER 3

THE CMS EXPERIMENT AT THE LARGE HADRON COLLIDER

Today's world largest particle physics laboratory, CERN, situated on the border between France and Switzerland, was founded on September 29, 1954. Since its foundation, CERN made the way to breakthroughs in the understanding of fundamental particles and their interactions: the discovery of W and Z bosons in 1983, the high precision measurements of weak interactions ad the LEP and lately the exploration of a new state of matter (quark-gluon-plasma) are just some of the historical highlights. In the following sections a description of the Large Hadron Collider and the CMS experiment is outlined.

3.1 THE LARGE HADRON COLLIDER

The LHC [1] is the most powerful particle collider built up to now and is operational at CERN, hosted in the former Large Electron-Positron Collider (LEP) [45] tunnel. Both protons and heavy ions can be accelerated.
In the initial phase, the LHC collides protons at a centre of mass energy of $\sqrt{s} = 7$ TeV, which is the highest presently reached. The centre of mass energy will then rise in the coming years to the design value of $\sqrt{s} = 14$ TeV.

The LHC proton-proton synchrotron is part of the CERN accelerator complex (figure 3.1). Machines like the SPS (Super Proton Synchrotron) and PS (Proton Synchrotron), are used to pre-accelerate protons to 400 GeV before their injection into the LHC. Two beams circulate simultaneously in the machine in opposite directions and they are crossed at four interaction points where the main experiments are located. The accelerator is 27 km long and in total composed of more than one thousand magnets, all employing superconductive wirings. It comprises superconductive radio frequency cavities to accelerate the protons and ions and dipole magnets able to generate a 8.3 T magnetic field to bend them. Moreover, other magnet types are employed for the machine optics, participating in the focussing and squeezing of the beams. The superconductivity regime is reached in the magnets at an operational temperature of about $-271°$C, which makes the LHC one of the coldest objects in the Universe. Such extreme conditions are reached with an advanced cryogenic system.

The LHC is a machine conceived to give access to a large range of physics opportunities, from the precise measurement of the properties of known objects to the exploration of high energy frontiers. Energies greater than a few 100 GeV are prohibitive for electrons with the current acceleration technology due to the synchrotron radiation. On the contrary protons, which have a much larger mass than electrons, give rise to a much smaller significant synchrotron radiation, which allows to reach higher energies (up to several TeV). Moreover, given their composite nature, the proton total momentum is distributed according to the parton distribution functions among partons, which in the energy regime of the LHC are the scatterers taking part in the collisions. The centre of mass energy of the fundamental scatterers is therefore not known a priori, like for an electron-positron collider, allowing to explore every possible region of the phase space without varying the energy of the beams. At last, at the LHC proton-proton are chosen instead of proton-antiproton because it is extremely difficult producing antiprotons and reach high luminosity with them. Thinking at the physics processes there are no advantages in choosing a proton-antiproton reaction instead of a proton-proton one at the energies reached at the LHC.

Beyond the energy of the particles circulating in the machine, another relevant parameter to consider is the luminosity which is the factor of proportionality between the event rate and the interaction cross section. Hence, to accumulate the maximum number of events in a given amount of running time, a high luminosity is of crucial importance. The design luminosity of the LHC is unprecedented for a proton machine: 10^{34} cm^{-2}s^{-1}. This quantity can be calculated as a first approximation by the formula:

$$\mathcal{L} = \frac{N^2 k f \gamma}{4\pi \varepsilon_n \beta^*} F \tag{3.1}$$

where N is the number of particles in each of the k circulating bunches, the “packages” of protons into which the beam is divided, f the revolution frequency, β^* the value of the betatron function at the crossing point and ε_n the emittance corresponding to one σ

contour of the beam, contracted by a Lorentz factor γ. F is a reduction factor due to the crossing angle between the beams. Thus, to achieve high luminosity, the LHC beam is made of a high number of bunches, filled with $\sim 10^{10}$ protons, which collide at an extremely high frequency (the nominal value is 40 MHz) with well focussed beams. The main machine parameters (design values) are listed in table 3.1.

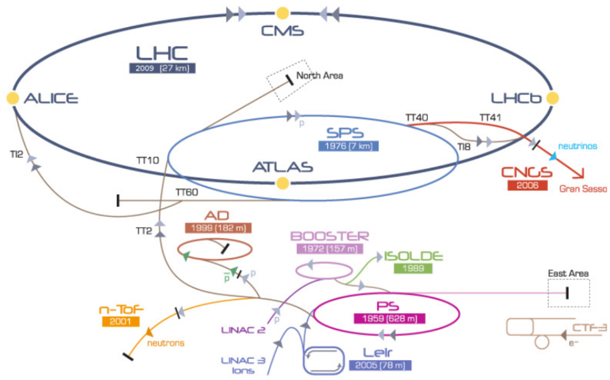

Figure 3.1.: The CERN accelerator complex. The names of the machines are accompanied by the starting year of their operation. Several machines are used to pre-accelerate the protons before the injection into the LHC.

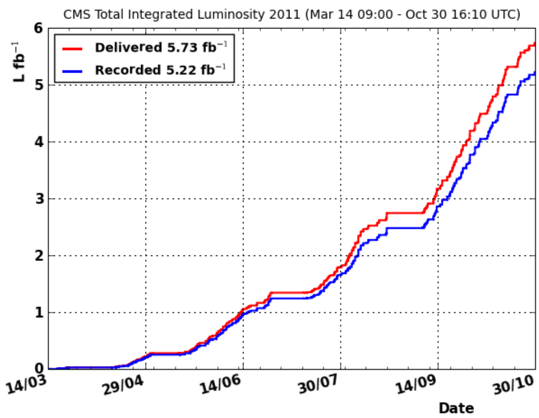

Figure 3.2.: Integrated luminosity delivered by LHC and recorded by CMS as a function of the time (from March to October).

Parameter	pp	$Pb-Pb$	Dimensions
Energy per nucleon	7	2.76	TeV
Dipole field at 7 TeV	8.33	8.33	T
Design luminosity	10^{34}	10^{27}	cm^{-2}s^{-1}
Bunch separation	25	100	ns
Num of bunches	2808	592	–
Particles per bunch	1.15×10^{11}	7×10^{7}	–
β value at IP	0.55	0.5	m
RMS beam radius at IP	16.7	15.9	µm
Luminosity lifetime	15	6	h
Number of collisions/crossing	~ 20	–	–

Table 3.1.: Some of the nominal machine parameters relevant for the LHC detectors.

3.1.1 Detectors at the LHC

Along the course of the accelerator ring, there are four big detectors which measure the outcome of the collisions. These include two general purpose experiments (ATLAS, CMS) and two specialized detectors (ALICE, LHCb). These detectors allow to study the physics at the energy which has not been accessible before. Here is the brief description of LHC experiments:

- ATLAS (A Large Toroidal ApparatuS) [46] and CMS (Compact Muon Solenoid) [6]: are general purpose detectors designed to exploit the full LHC potential. ATLAS is larger than CMS but is less dense. The two detector are featured by complementary characteristics and detector choices. The main lines of research are: the search for the Higgs boson or any other mechanism of the electroweak symmetry breaking, the precise measurement of mass of heavy particles like top quark or W boson, the search for supersymmetric particles, the study on non-SUSY physics beyond the Standard Model, the study of heavy ion collisions and of the formation of the quark-gluon plasma, emulating thus the very first moments after the Big Bang.

- ALICE: (A Large Ion Collider Experiment) is a detector specially designed to study the collisions of heavy ions [47]. Experiments at CERN in 1990's and at the Brookhaven National Laboratory in 2000's showed that at very high temperatures the quarks are probably not confined inside hadrons but they are rather free in a state which was called the quark-gluon plasma (QGP). It is expected that this state of matter exists naturally inside heavy neutron stars and that it was also one of the initial stages of the Universe.

- LHCb: (Large Hadron Collider beauty) is an experiment devoted to the measurement of CP violation, especially in the B mesons decay. It is expected that it could be most clearly seen in the difference between the decay of B_d meson ($d\bar{b}$) to J/ψ ($c\bar{c}$) and K_0 ($d\bar{s}$) and the decay of $\bar{B}_d$ meson to respective antiparticles. By studying the difference in the decay times, it will be possible to determine the complex phase of CKM matrix [48].

The construction of two detectors with similar goals fulfils the natural requirement on experimental physics – that any result should be independently confirmed. Also, thanks to the combined statistics from both experiments, it is possible to obtain more precise results. The CMS experiment will be described in detail in the following section.

3.2 THE CMS DETECTOR

CMS is a general purpose detector that is installed at the interaction point number five along the LHC tunnel. The detector has a cylindrical shape, symmetric around the beam and is divided in two endcaps and a barrel. The overall dimensions of CMS are a length of 21.6 m, a diameter of 14.6 m and a total weight of 12500 tons. It is characterized by a layered structure: starting from the beam pipe its subdetectors are a silicon tracking device, an electromagnetic calorimeter, a hadronic calorimeter and an advanced muon detection system. In every particle detector, the magnetic field plays a fundamental role, since it is necessary for the momentum measurement of charged particles. An important aspect driving the detector design and layout is the choice of the magnetic field configuration. At the heart of CMS sits a 13 m long, 5.9 m inner diameter, 3.8 T superconducting solenoid. Such a high magnetic field aligned to the beam axis was chosen in order to achieve good momentum resolution with a compact spectrometer. The core of the magnet coil is large enough to accommodate the inner tracker and the calorimetry subsystems, with the exception of its very-forward part. An iron return yoke routes back the magnetic field generated by the solenoid, avoiding its spread into the cavern. The return field is so intense (1.5 T) to saturate three layers of iron, in total 1.5 m thick. Each of these layers is installed between two layers of muon detectors. The redundancy ensured by the muon measurements therewith obtained, ensures robustness as well as full geometric coverage. The overall layout of CMS is shown in figure 3.3 and a slice of it can be inspected in figure 3.4.

The coordinate frame used to describe the detector is a right handed Cartesian system with the x axis pointing toward the centre of the LHC ring, the z axis directed along the beam axis and the y axis directed upward. Given the cylindrical symmetry of CMS, a convenient coordinate system is given by the triplet (r, ϕ, η), being r the distance from the z axis, ϕ the azimuthal coordinate with respect to the x axis and η

the pseudorapidity, which is defined as $\eta = -\ln(\tan(\theta/2))$, where θ is the polar angle with respect to the z axis. The pseudorapidity is used as the angle of a particle relative to the beam axis.

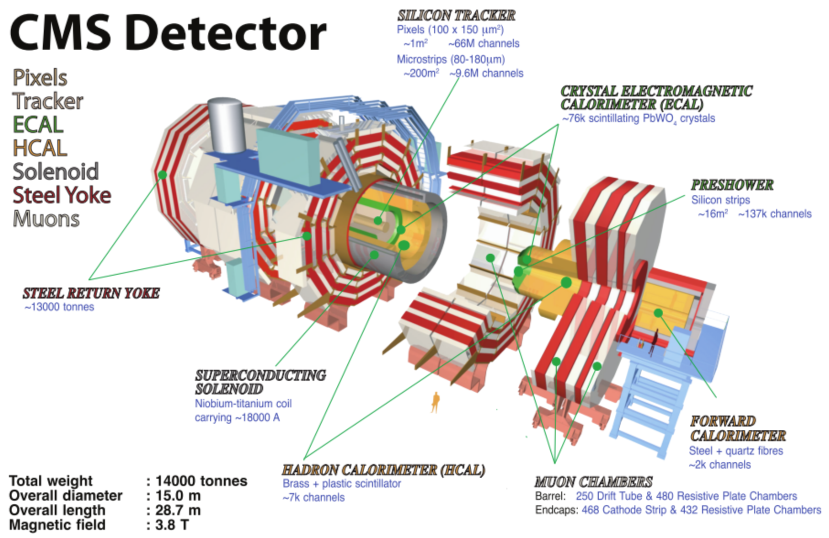

Figure 3.3.: An overall view of CMS. The detector is symmetrical around the beam line and designed to be hermetic.

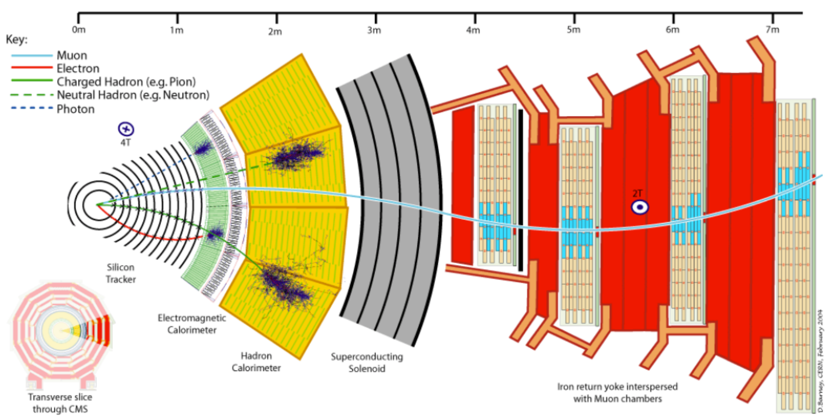

Figure 3.4.: Slice of the CMS detector with the tracks of an electron, a photon, a hadron (e.g. a pion) and a muon. The electron and the photon deposit their whole energy in the electromagnetic calorimeter generating an electromagnetic shower. The hadron reaches the hadron calorimeter where it is stopped. Only muons are able to escape the whole detector. Their momentum is measured by the tracker and the muon system.

3.2.1 THE INNER TRACKING SYSTEM

The CMS tracker [49] is the subdetector closer to the interaction point, placed in the 3.8 T magnetic field of the superconductive solenoid. It is designed to determine the interaction vertex, measure with good accuracy the momentum of the charged particles, identify the presence of secondary vertices. The tracker must be able to operate without degrading its performances in the hard radiation environment of LHC and it has to comply with severe material budget (see figure 3.6) constraints, in order not to degrade the excellent energy resolution of the electromagnetic calorimeter. The CMS collaboration has adopted silicon technology for the whole tracker.

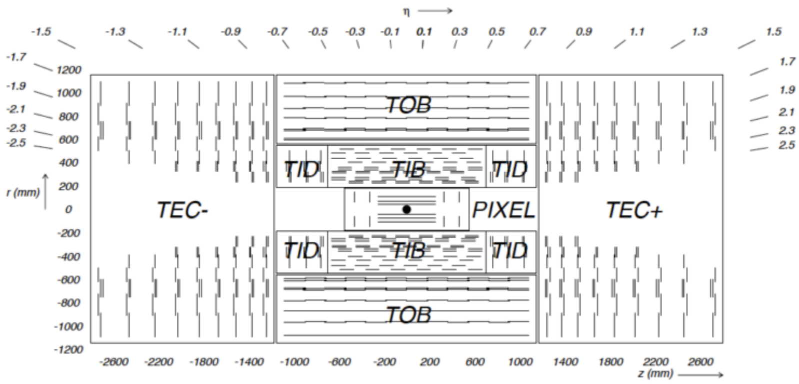

Figure 3.5.: CMS inner tracker.

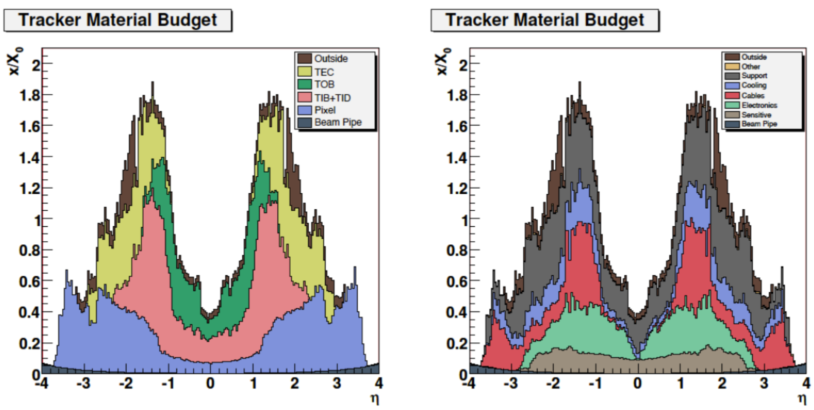

Figure 3.6.: Material budget of the CMS tracker as a function of pseudorapidity. Different contributions to the tracker material budget are showed in the two figures.

Three regions can be delineated, considering the charged particle flux at different radii at high luminosity:

- Closest to the interaction vertex where the particle flux is highest (about 10^7 Hz at $r \sim 10$ cm) pixel detectors are placed. The size of the pixels is approximately $100 \times 150\,\mu m^2$, leading to an occupancy of 10^{-4} per pixel per LHC crossing.

- In the intermediate region with 20 cm < r < 55 cm the particle flux becomes low enough to allow the use of silicon microstrip detectors, with a minimum $z \times R\phi$ cell size of approximately 10 cm $\times$ 80 µm, giving an occupancy of 2-3% per LHC crossing.

- The outermost region is characterized by sufficiently low fluxes that enable to adopt larger-pitch silicon microstrips with a maximum cell size of approximately 25 cm $\times$ 80 µm, keeping the occupancy to about 1%.

The pixel detector consists of three barrel layers and two endcap disks at each side. The barrel layers are located at 4.4 cm, 7.3 cm and 10.2 cm and are 53 cm long. The two endcap disks, extending from 6 to 15 cm in radius, are placed on each side at |z|= 34.5 cm and |z|= 46.5 cm. This design allows to obtain at least two points per track in the $|\eta| < 2.2$ region, for tracks originating within $2\sigma_z$ from the central interaction point. The total number of channels is about 66 millions, organized in about 16000 modules of 52 columns and 80 rows. The total active area is close to 0.92 m^2. The presence of high magnetic field causes a noticeable drift of the electrons (and a smaller drift for the holes) from the ionization point along the track with a Lorentz angle of about 32°. This leads to a charge sharing between pixels which, using an analog readout, can be exploited to considerably improve the resolution, down to about 10 µm. In the endcap the modules of the detector are arranged in a turbine-like shape with a 20° tilt, again in order to enhance the charge sharing.
The inner and outer tracker detector are based on silicon strips. They are p^+ strips on a n-type bulk whose thickness is close to 300 and 500 µm respectively in the inner and outer tracker. In the barrel the strips are parallel to the beam axis while for the endcaps they have a radial orientation. The inner tracker is made of 4 barrel layers, the two innermost are double sided, and the endcaps count 3 disks each. The outer tracker consists of 6 layers in the barrel (the two innermost are double sided) while the endcaps are made of 9 layers (the first, the second and the fifth are double sided). On the whole the silicon trackers is made of about 10 millions of channels for an active area close to 198 m^2. The performance of the tracker is illustrated in figure 3.7, which shows the transverse momentum and impact parameter resolutions in the r-ϕ and z planes for single muons with a pt of 1, 10 and 100 GeV, as a function of pseudorapidity.
High energy electrons are reconstructed with efficiency higher than 90%. The recon-

struction efficiency for isolated muons with $p_T > 1$ GeV is close to 100% in the $|\eta| < 2$ region.

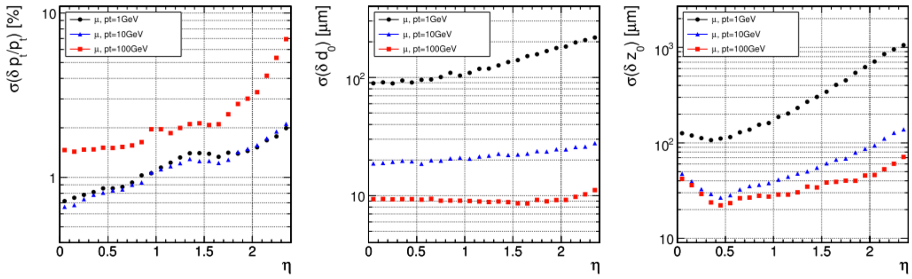

Figure 3.7.: Resolution of several track parameters for single muons with transverse momenta of 1, 10 and 100 GeV: (left) transverse momentum, (center) transverse impact parameter, and (right) longitudinal impact parameter.

3.2.2 THE ELECTROMAGNETIC CALORIMETER

The electromagnetic calorimeter (ECAL) measures the energy of the electrons and photons. The design of the CMS ECAL [50] was driven by the requirements imposed by the search of the Higgs boson in the channel $H \to \gamma\gamma$, where a peak in the di-photon invariant mass placed at the Higgs mass, has to be distinguished from a continuous background [51]. A good resolution and a fine granularity are therefore required: both of them improve the invariant mass resolution on the di-photon system by improving respectively the energy and angle measurement of the two photons. The fine granularity also helps to obtain a good π^0/γ separation.
In order not to deteriorate the energy resolution the ECAL is placed inside the solenoid, hence a compact calorimeter is required. ECAL is a hermetic, homogeneous calorimeter made of lead tungstate ($PbWO_4$) crystals, 61200 crystals mounted in the central barrel part, and 7324 crystals in each end-cap (see figure 3.8). The choice of lead tungstate scintillating crystals was driven by their characteristics: they have a short radiation length ($X_0 = 0.89$ cm) and a small Moliere radius ($R_M = 2.2$ cm); they are fast, as the 80% of the scintillation light is emitted within 25 ns and radiation hard. The use of $PbWO_4$ crystals has thus allowed the design of a compact calorimeter to be placed inside the solenoid with fine granularity and radiation resistant. However the relative low light yield (30 photons/MeV) requires the use of photodetectors with intrinsic gain that can operate in a magnetic field. In the barrel, silicon avalanche photodiodes (APDs) are used as photodetectors, while vacuum phototriodes (VPTs) have been chosen for the endcaps because of their high radiation hardness. In addition, the sensitivity of both the crystals and the APDs response to temperature changes requires

temperature stability. A water cooling system guarantees a long term stability at the $0.1°C$ in order to preserve the ECAL energy resolution performances.
The desired ECAL performance requires that the front end signals are digitized to almost 16-bit accuracy. Rather than develop a radiation hard 16-bit analogue-to-digital converter (ADC), the approach has been to use multiple gain ranges in the pre-amplifier, digitizing and transmitting the signals to the off-detector electronics only for the highest non-saturated range. Thus a 12-bit ADC is sufficient, but a decision must be made on the detector at the very front end (VFE). The choice of three gain ranges achieves the physics performance both in the ECAL barrel and in the ECAL endcap.
The barrel region has a pseudorapidity coverage up to $|\eta| < 1.479$. It has an inner

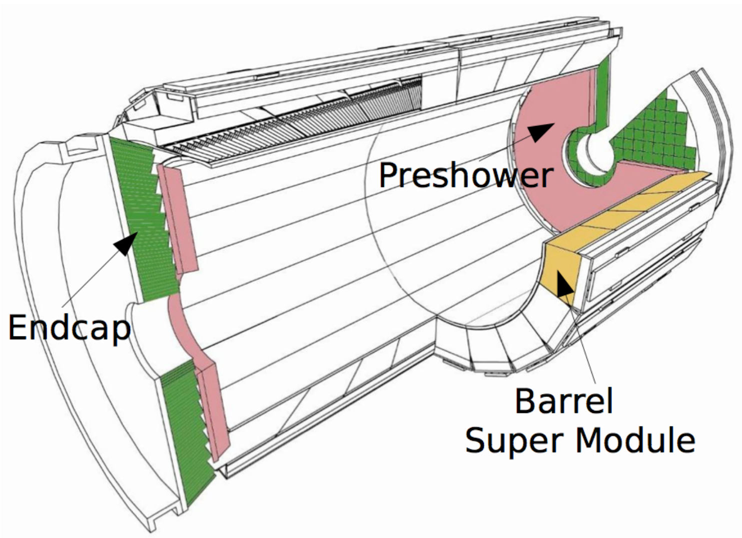

Figure 3.8.: Scheme of the barrel and the endcaps of the CMS ECAL.

radius of 129 cm and is structured in 36 supermodules, containing 1700 crystals each, covering half the barrel length and subtending a 20° angle in ϕ. Each supermodule is divided along η into four modules which in their turn are made of submodules, the basic assembling alveolar units, containing 5×2 crystals each. The barrel crystals have a front face cross-section of about 22×22 cm^2 and have a length of 230 cm, corresponding to 25.8 X_0. The crystal axes are oriented with a 3° tilt with respect to the pointing geometry to avoid that the particles can directly escape into the non instrumented regions between the crystals. The granularity of the barrel is $\Delta\phi \times \Delta\eta = 0.0175 \times 0.0175$ and the crystals are grouped, from the readout point of view, into 5×5 arrays corresponding to the trigger towers. The endcaps cover the pseudorapidity region $1.48 < |\eta| < 3.0$, ensuring precision measurements up to $\eta < 2.5$. The endcap crystals have dimensions of $28.6 \times 28.6 \times 220$ cm^2. Each endcap is structured in two "Dees" con-

sisting of semi-circular aluminum plates from which are cantilevered structural units of 5×5 crystals, known as "super-crystals".
A preshower device, whose principal aim is to identify neutral pions in the endcaps within $1.653 < |\eta| < 2.6$, is placed in front of the crystal calorimeter. The active elements are two planes of silicon strip detectors which lie behind disks of lead adsorber at depths of $2\ X_0$ and $3\ X_0$.

One of the relevant parameter in evaluating the performances of the electromagnetic calorimeter is its energy resolution. In the relevant energy range between 25 GeV and 500 GeV, the energy resolution is usually parametrized as the sum in quadrature of three different terms:

$$\frac{\sigma_E}{E} = \frac{a}{\sqrt{E}} \oplus \frac{b}{E} \oplus c \tag{3.2}$$

where a, b and c are named respectively stochastic, noise and constant term, and E is the energy expressed in GeV.

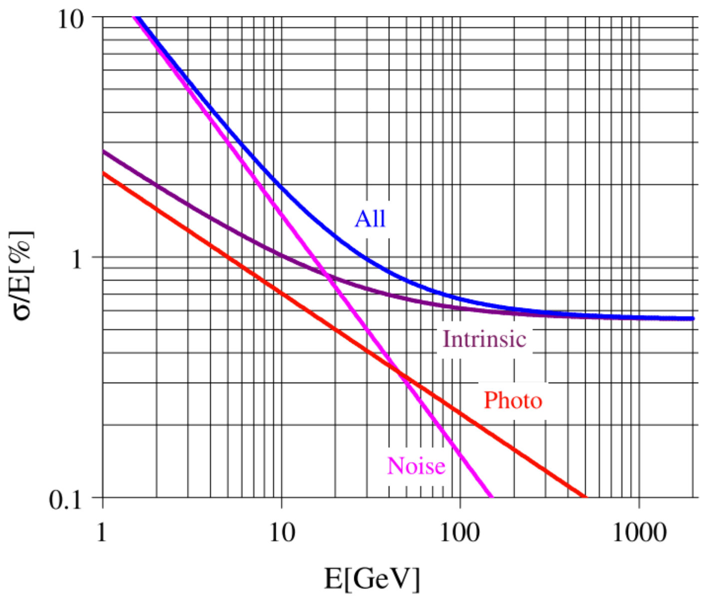

Figure 3.9.: The expected ECAL energy resolution versus the energy of the impacting electron. The different contributions are superimposed separately. The term "Intrinsic" includes the shower containment contribution and a constant term (0.5%).

The target values for CMS are 2.7% for a, 200 MeV when adding the signal of 5×5 crystals for b, and 0.5% for c. Their relative contributions are reported in figure 3.9. It can be noticed that above 50 GeV the resolution is dominated by the constant term (in the figure the term "Intrinsic" includes the shower containment contribution and a constant term of 0.5%). Different effects contribute to the different terms in equation 3.2:

- the stochastic term a receives a contribution from the fluctuations in the number of electrons which reaches the preamplifier (n_e). These fluctuations are proportional to $\sqrt{n_e}$ and therefore proportional to the square root of the deposited energy. Contributions to this term come from the light yield of the crystals, from the efficiency in collecting light onto the photodetector surface and from the quantum efficiency of the photodetector. The fluctuations in the electrons multiplication process also contribute to this term, as an excess noise term F.

- The noise term b accounts for all the effects that can alter the measurements of the energy deposit independently of the energy itself. This term receives contributions from the electronic noise and from the pile-up events, whose contribution are different in the barrel and in the endcaps and can vary with the luminosity of LHC. The target values for the barrel (at $\eta = 0$) and the endcaps (at $\eta = 2$) in the low luminosity running are respectively 155 MeV and 205 MeV.

- The constant term determines the energy resolution at high energy. Many different effects contribute to this term: the stability of the operating conditions such as the temperature and the high voltage of the photodetectors; the rear and lateral leakage of the electromagnetic shower and the presence of the dead material of the supporting structure between the crystals; the light collection uniformity along the crystal axis; the inter-calibration between the channels which contributes almost directly to the overall energy resolution since the most of the energy is contained into few crystals; the radiation damage of the $PbWO_4$ crystals.

Given the relevance for the work presented in this thesis, the ECAL calibration procedure will be described in chapter 5.

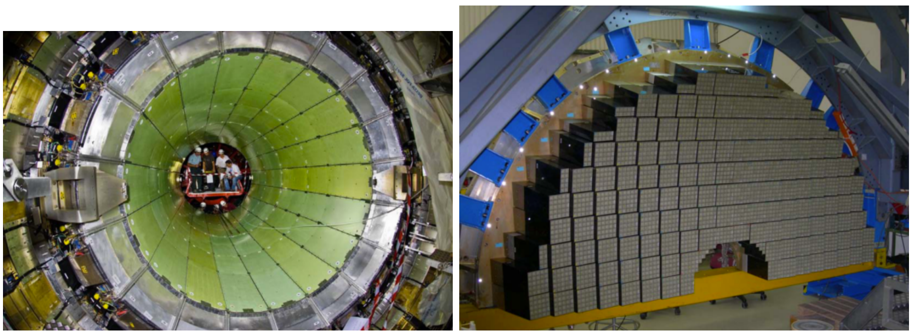

Figure 3.10.: The electromagnetic calorimeter: barrel section after installation in CMS (left) and half of one endcap section during the assembly (right).

3.2.3 THE HADRONIC CALORIMETER

The hadron calorimeter (HCAL) [52], placed just ouside the electromagnetic calorimeter, plays a major role in the reconstruction of jets and missing energy. Its resolution must guarantee a good reconstruction of the di-jets invariant mass and an efficient measurements of the missing energy which represent an effective signature in many channels of physics beyond the Standard Model. Similarly to the other subdetectors, HCAL has to provide a good hermeticity, which is critical for determining the missing energy, and a quite fine granularity to allow a clear separation of di-jets from resonance decays and improve the resolution in the invariant mass of the di-jets. Moreover it has to provide a number of interaction lengths sufficient to contain the energetic particles from high transverse momentum jets. The dynamic range has to be large to to detect signals ranging from the signal of a single minimum ionizing muon up to an energy of 3 TeV.

The pseudorapidity region $|\eta| < 3$ is covered by the barrel (up to $|\eta| < 1.74$) and the two endcaps. The HCAL is composed by brass layers as absorbers interleaved by plastic scintillator layers, 4 cm thick, used as active medium. The absorber layers thickness is between 60 cm thick in the barrel and 80 cm in the endcaps, while the scintillators layers are 4 cm thick. In terms of interaction lengths λ, the barrel ranges from 5.46 λ at $|\eta| = 0$ up to 10.82 λ at $|\eta| = 1.3$; the barrel corresponds on average to 11 λ. The scintillator in each layer is divided into tiles with a granularity matching the granularity of the ECAL trigger towers ($\Delta\eta \times \Delta\phi = 0.0875 \times 0.0875$) and the light is collected by wavelength shifters.

The two hadronic forward calorimeters improve the HCAL hermeticity, covering the pseudorapidity region $3 < |\eta| < 5$. It is placed at 11.15 m from the interaction point outside the magnetic field. Due to the extremely harsh radiation environment a different detection technique is used: a grid of quartz (radiation hard) fibers is embedded in a iron absorber.

3.2.4 THE MUON SPECTROMETER

In CMS the muon detectors are placed beyond the calorimeters and the solenoid. The muon system [53] consists of four active stations interleaved by the iron absorber layers which constitute the return yoke for the magnetic field. The return field is large enough to saturate 1.5 m of iron, allowing the muon stations to be integrated to ensure robustness and full geometric coverage. Each muon station consists of several layers of aluminium drift tubes (DT) in the barrel region, where the neutron induced background is small, the muon rate is low and the residual magnetic field in the chambers is low, and cathode strip chambers (CSCs) in the endcap region, where the muon rate as well as the neutron induced background rate is high, and the magnetic field is also high,

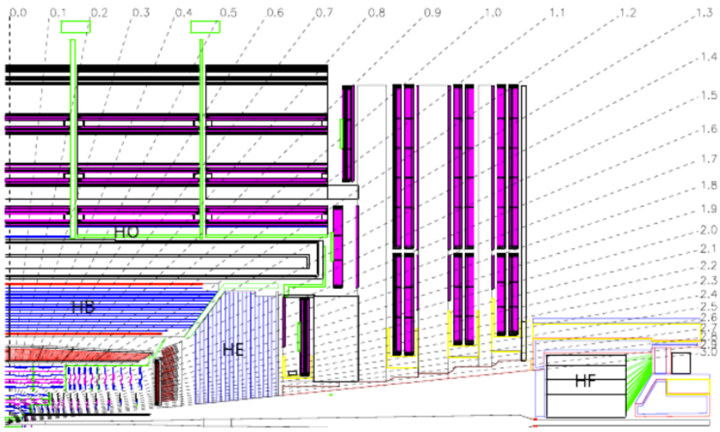

Figure 3.11.: Schematic view of the HCAL components in CMS, including the barrel section (HB), the endcap section (HE), the tail catcher outside the solenoid (HO) and the forward section (HF).

complemented by resistive plate chambers (RPCs) in both the barrel and the endcap regions. The DT and CSC detectors are used to obtain a precise measurement of the position and thus the momentum of the muons, whereas the RPC chambers are dedicated to providing fast information for the Level1 trigger. The layout of one quarter of the CMS muon system for initial low luminosity running is shown in figure 3.12. In the Muon Barrel (MB) region, 4 stations of detectors are arranged in cylinders interleaved with the iron yoke. The segmentation along the beam direction follows the 5 wheels of the yoke. In each of the endcaps, the CSCs and RPCs are arranged in 4 disks perpendicular to the beam, and in concentric rings, 3 rings in the innermost station, and 2 in the others. In total, the muon system contains of order 25000 m^2 of active detection planes, and nearly 1 M electronic channels. The muon momentum resolution is shown in figure 3.13.

3.2.5 The trigger system

At the nominal LHC luminosity, the expected event rate is about 10^9 Hz. Given the typical size of a raw event ($\sim$ 1 MB) it is not possible to record all the informations for all the events. Indeed, the event rate is largely dominated by soft $p-p$ interactions with particles of low transverse momentum. The triggering system must have a large reduction factor and mantain at the same time an high efficiency on the potential interesting events, reducing the rate down to 100 Hz, which is the maximum sustainable rate for storing events. The trigger system consists of two main steps: a Level1 Trigger which consists of custom-designed, largely programmable electronics, and a

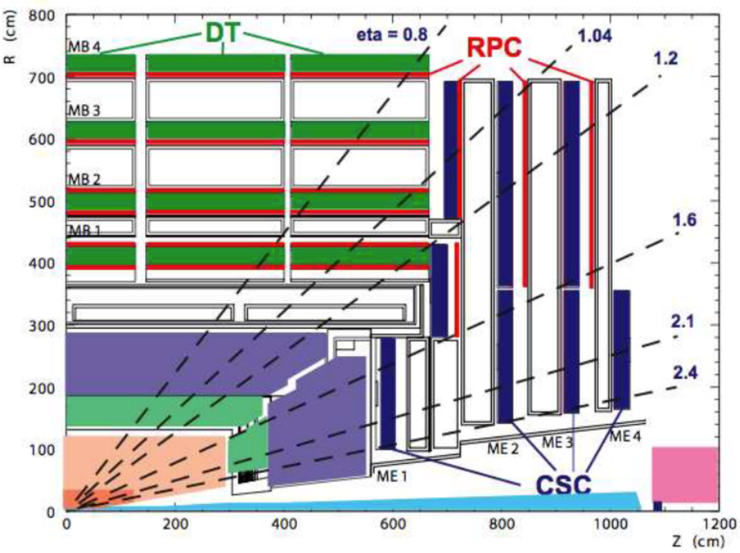

Figure 3.12.: Layout of one quarter of the CMS experiment. The Muon Barrel system extends r > 350 cm and |z| < 700 cm (chambers are shown in green color). In the endcap part CSC chambers (noted as ME) are clearly visible (blue color). RPCs are displayed in red color in the barrel and endcap parts.

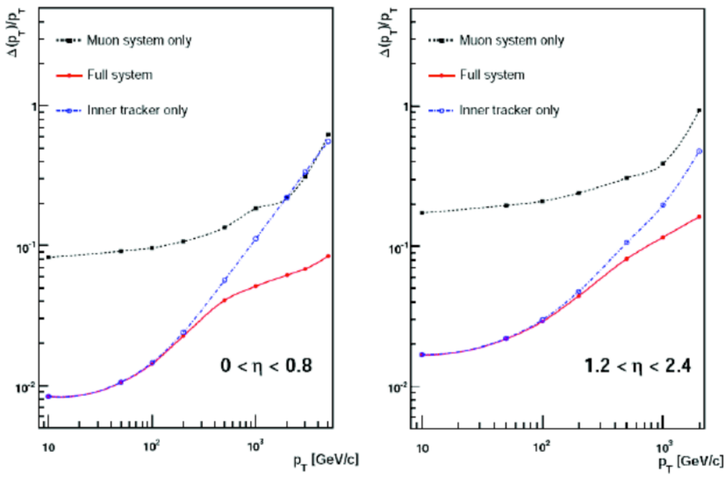

Figure 3.13.: Muon transverse momentum resolution as a function of p_T in the barrel (left) and endcap (right) region obtained using only the tracker or the muon system information and combination of both.

High Level Trigger software system implemented in a filter farm of about one thousand commercial processors. The basic concepts will be described in the following. A complete description can be found in [54].

LEVEL1 TRIGGER

The Level 1 trigger (L1) reduces the rate of selected events down to 50 (100) kHz for the low (high) luminosity running. The full data are stored in pipelines of processing elements, while waiting for the trigger decision. The L1 decision about taking or descarding data from a particular bunch crossing has to be taken in 3.2 μs. If the L1 accepts the event, the data are moved to be processed by the High Level Trigger. To deal with the 25 ns bunch crossing rate, the L1 trigger has to take a decision in a time too short to read data from the whole detector, therefore it employs the calorimetric and muons informations only, since the tracker algorithms are too slow for this purpose. The Level-1 trigger is organized into a Calorimeter Trigger and a Muon trigger whose informations are transferred to the Global Trigger which takes the accept-reject decision.

The Calorimeter Trigger is based on trigger towers, arrays of 5 crystals in ECAL , which match the granularity of the HCAL towers. The trigger towers are grouped in calorimetric region of 4×4 trigger towers. The Calorimeter Trigger identifies, from the calorimetric region information, the best four candidates of each of the following classes: electrons and photons, central jets, forward jets and τ-jets identified from the shape of the deposited energy. The information of these objects is passed to the Global Trigger, together with the measured $E_{\mathrm{T}}^{\mathrm{miss}}$. The Muon trigger is performed separately for each muon detector. The information is then merged and the best four muon candidates are transferred to the Global Trigger. The Global Triggers takes the accept-reject decision exploiting both the characteristic of the single objects and of combination of them.

HIGH LEVEL TRIGGER

The High Level Trigger reduces the ouput rate down to 300 Hz. The idea of the HLT trigger software is the regional reconstruction on demand, that is only those objects in the useful regions are reconstructed and the uninteresting events are rejected as soon as possible. This leads to the development of three “virtual trigger” levels: at the first level only the full information of the muon system and of the calorimeters is used, in the second level the information of the tracker pixels is added and in the third and final level the full event information is available. The use of a processor farm for all selections beyond Level1 allows maximal benefit to be taken from the evolution of computing technology. Flexibility is maximized since there is complete freedom in the selection of the data to access, as well as in the sophistication of the algorithms.

More details about the electron trigger are reported in section 6.3.

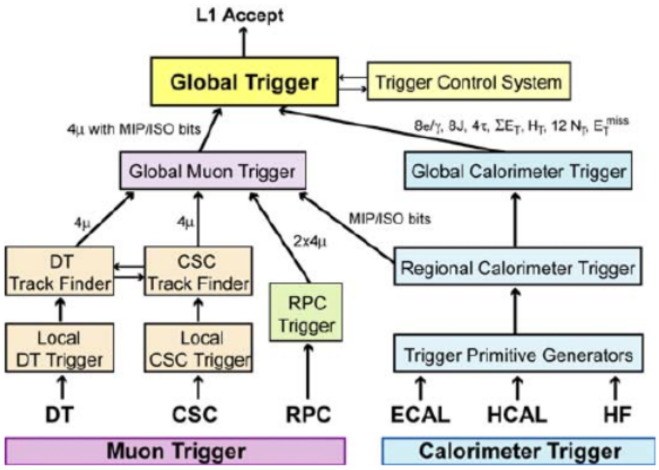

Figure 3.14.: Schematic representation of the CMS L1 trigger system.

3.2.6 DATA IN CMS

The first $p-p$ collisions took place at the end of 2009 starting with a pilot commissioning run with collisions at centre of mass energy of 900 GeV and 2.36 TeV in November and December. Finally, the LHC operation at $\sqrt{s}=7$ TeV started on March 30th, 2010. After two full years of data taking, the integrated luminosity recorded by CMS is 5.2 fb^{-1}. The results presented in this thesis are based on an integrated luminosity of 1.13 fb^{-1} which is the amount of data collected until June 2011. The LHC machine performed smoothly during the whole 7 TeV operation increasing progressively the instantaneous luminosity up to $L = 3.54 \times 10^{33}$ cm^{-2}s^{-1} reached in October 2011 (see figure 3.15).

The quality of the data used in all CMS analyses is guaranteed by the Data Quality Monitoring (DQM) system, which controls the detector conditions and the reconstruction chain and objects. It consists of a catalogue of one and two dimensional histograms that allows to have access to information from the performance of the hardware to high level objects variables. This information is scrutinized by a team of experts to asses the quality of the data recorded and to certify its goodness to be analysed. According to these quality tests, 4.7 fb^{-1} of data were certified as optimal out of the 5.2 fb^{-1} recorded by CMS during 2011.

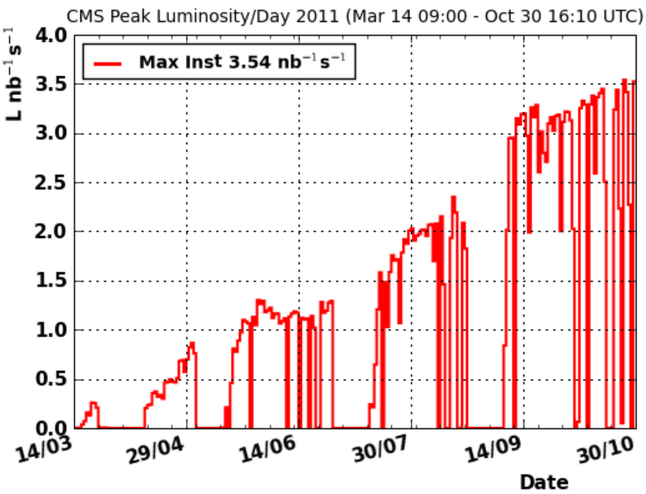

Figure 3.15.: Maximum Instantaneous luminosity per day delivered to CMS during stable beams for pp running at 7 TeV centre-of-mass energy.

CHAPTER 4

ECAL COMMISSIONING WITH EARLY COLLISIONS

The accurate observation and interpretation of the first data has been a mandatory step in the understanding of the detector response. In this chapter the data-MC comparison and the necessary tunings to the MC simulation for the low level observables of ECAL is discussed.
The study and understanding of the Nuclear Counter Effect (NCE), related to the direct ionization of the readout photodetectors of the ECAL barrel is also presented. The NCE events could fake high energy signals and had to be properly identified and rejected. The criteria to individuate and reject them are presented in detail.

4.1 ECAL LOW LEVEL OBSERVABLES

When the first proton–proton collision data came in 2010, one of the first steps in understanding the detector response was the validation of the data-Monte Carlo comparison and the necessary tunings to the MC simulation for low level observables. This translates into the tuning of the MC parameters trying to understand and reproduce the shape of the key variables from data with the highest accuracy as possible. For the electromagnetic calorimeter validation, distributions such as the single channel energy, timing, the channel occupancy over the barrel and the endcap and the profiles versus the η and ϕ coordinates were investigated in samples of minimum bias events. Four different Monte Carlo samples with different tuning were compared to the data. A delicate point is the reproduction of the noise associated to each single channel. The detailed simulation of the digitization step and of the energy equivalent noise in each single channel explains the excellent agreement between data and Monte Carlo distributions. Also the distributions of higher level observables, such as the energy of clusters of crystals, showed an overall good agreement between data and simulation, demonstrating the maturity of the understanding of the detector and reconstruction algorithms. The distributions mentioned are reported in appendix A.

4.2 Anomalous signals in the calorimeter

The following section describes the observation and the characterization of anomalous energy deposits in the CMS electromagnetic calorimeter during proton-proton collision data taking in 2009-2010. The anomalous signals are observed to occour in the channels of the calorimeter's barrel with a rate proportional to the intensity of the proton beams. The anomalous signals have to be rejected to avoid the risk of large biases in the number and in the energy of the reconstructed electron, photon and jets. The missing transverse energy reconstruction is also affected by definition (see section 6.2). In figure 4.1 the impact of anomalous signals on the tail of the missing transverse energy is reported. After the anomalous signals rejection the data and the simulation agree.
The anomalous signals are understood to be produced by the direct ionization of the Avalanche Photodiode (APD) active volumes by particles that are produced in pp collisions. This hypothesis has been checked by studying the APD response via laboratory and test beam studies, and the development of Monte Carlo simulations where the APDs are treated as active volumes.

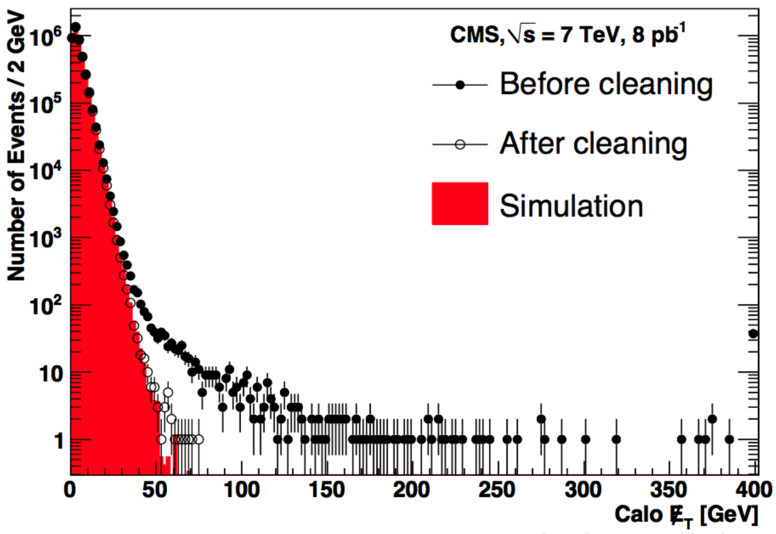

Figure 4.1.: Calo E_T^{miss} distributions in a minimum-bias data sample without (black dots) and with (open circles) cleaning and filters, compared to simulation. Overflows are included in the highest bin.

4.2.1 ANOMALOUS SIGNALS PROPERTIES

The general properties of the anomalous signals are as follows:

- Isolated, high energy deposits that are only observed in the ECAL barrel. They have a shower shape that is inconsistent with that expected from an average electromagnetic shower.

- The reconstructed time distribution for these signals is peculiar. They are reconstructed as "early" signals. In addition, the timing distribution has a long positive tail, extending beyond +40 ns.

- Their pulse shape is inconsistent with the expected response measured using a 120 GeV electron beam.

The technics developed to identify and reject the anomalous signals are based on the three properties listed above and they are presented in section 4.2.5.
Figure 4.2 shows a typical anomalous signal energy deposit in the ECAL Barrel. The event was recorded during pp collisions with $\sqrt{s} = 7$ TeV. Here there is significant energy in a single crystal ($E_T = 184$ GeV) with very little surrounding activity. In addition, the reconstructed time of the hit is significantly different from zero ($t \sim -10$ ns) while the expected timing resolution for such a high energy rechit is less than 1 ns.

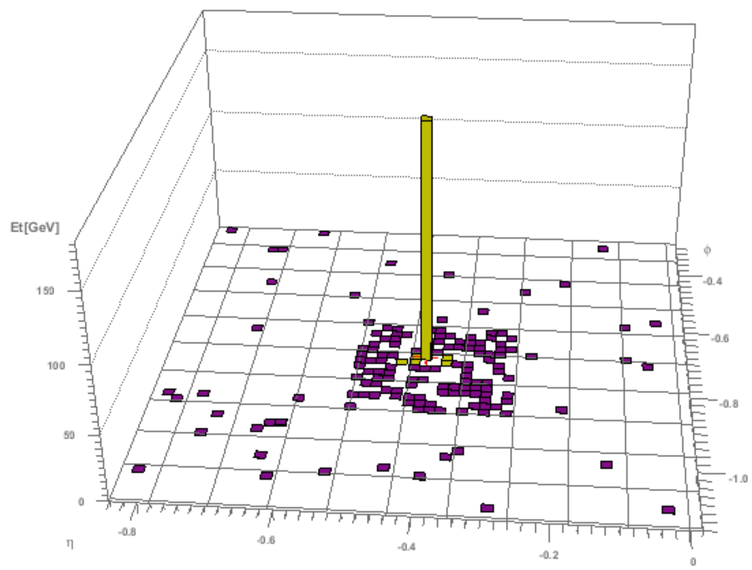

Figure 4.2.: Typical anomalous signal energy deposit in the ECAL barrel. Event details: run 133874, event 66775940, RecHit transverse energy: 184 GeV, Rechit reconstructed time: -10.5 ns.

4.2.2 Anomalous signals production mechanism

The anomalous energy deposits are caused by direct ionization of the avalanche photodiode (APD) sensitive volumes by highly ionizing particles, mainly protons, neutrons and heavy ions, produced during proton-proton collisions. This is supported by the results of Monte Carlo simulations and laboratory measurements during which the APD was exposed to neutrons from Am-Be and Cf sources. In addition, anomalous signals related to the barrel APDs have been observed in test beam measurements in 2006 and 2010, as well as a dedicated test in which a neutron source was placed in a spare barrel supermodule.

APD construction

A detailed description of the APD construction can be found in [50]. The salient features are as follows: each crystal is read out by two Hamamatsu S1848 APDs read out in series. Each APD has an active area of $5 \times 5\ \mathrm{cm}^2$ and operates at a nominal gain of 50. The internal construction of the APD, illustrated in figure 4.3, consists of a 5 µm thick "low-gain" silicon layer before the amplification region and a 45 µm thick "high-gain" silicon layer after the amplification region. A protective epoxy layer of roughly 400 µm covers the front of the APD. The simulation results and laboratory measurements indicate that a significant fraction of the anomalous signals are produced by np scattering in the epoxy region closest to the APD, and the resulting proton producing direct ionization in the APD active volume.

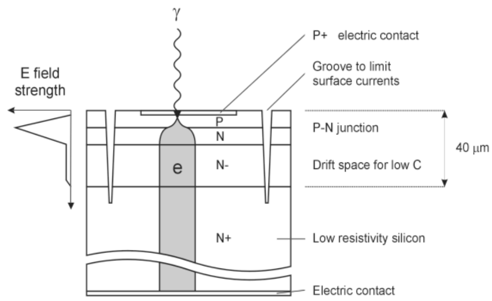

Figure 4.3.: Schematic diagram of an avalanche photodiode (APD) used in CMS.

4.2.3 Rates of the anomalous signals

Analysis of the rate of anomalous signals during early proton-proton running at 900 GeV in December 2009 established a direct correlation between the rate of anomalous signals and the pp collisions rate.

Table 4.1 shows the rate of anomalous signals per Minimum Bias event as a function of the LHC centre-of-mass energy (0.9, 2.36, 7 TeV). The increase in anomalous signals rate between 0.9 and 7 TeV is directly related to the increase in charged-particle multiplicity between these two datasets, again confirming the relationship between event activity and anomalous signals rate. Several collisions runs were taken at $\sqrt{s} = 7$ TeV

C.M. energy (TeV)	Anomalous Signals/Minimum Bias event
0.9	$(1.666 \pm 0.089) \times 10^{-3}$
2.36	$(1.811 \pm 0.342) \times 10^{-3}$
7.0	$(2.697 \pm 0.005) \times 10^{-3}$

Table 4.1.: Average anomalous signals rates per Minimum Bias event (technical bit 41) as a function of LHC centre-of-mass energy. Anomalous Signals are defined as RecHits with 3 GeV and (1-E4/E1)>0.95.

with the CMS magnetic field at zero tesla. For these runs, the number of anomalous signals per Minimum Bias event was observed to increase by 35%. This indicates the importance of low-momentum (~ 1 GeV/c) charged tracks in the production of anomalous signals since these particles are swept away from the ECAL barrel region in the nominal magnetic field of CMS.

4.2.4 Impact and consequences on the data acquisition

Since the characteristics of the anomalous signals are localized high energy deposits, they will tend to dominate the rate of the electron and photon trigger at high transverse energy. Given that the rate of anomalous signals is directly proportional to the minimum bias collisions rate, it is clear that at high luminosity, the rate of anomalous signals will be a significant (dominant) component of the 100 kHz Level-1 trigger rate bandwidth. The identification of the anomalous energy deposits is possible by exploiting the functionalities of the front-end electronics. If a trigger tower contains an anomalous deposit, it is vetoed from participating in the global trigger decision and hence reduce the Level-1 rate from anomalous signals. The rejection criteria at the Level-1 trigger based on the topology of the event are online since the beginning of 2011. However, even if the protection at trigger level is enough to keep the rate under control, it does not prevent the contamination of anomalous signals in the acquired data. A more accurate cleaning, based on higher level variables not available at the Level-1, is applied offline in the event reconstruction process. The offline rejection of the anomalous signals is discussed in the next session.

4.2.5 Rejection of the anomalous signals

The "Swiss cross" variable

Several cluster topological variables have been adopted to distinguish between anomalous signals, where the energy is generally confined to a single crystal, and EM energy deposits, where energy is shared between crystals in a 3×3 or 5×5 crystal array. One such example is the so-called "Swiss-cross" variable, which compares the energy of a single crystal ($E1$) to the summed energy of the four adjacent crystals in η and ϕ ($E4$). From these quantities, the Swiss-cross variable $(1 - E4/E1)$ is constructed. Figure 4.4 shows the distribution of this variable for Minimum Bias data and Monte Carlo, with $\sqrt{s} = 7$ TeV, plotted for the highest energy rechit in each event, requiring a minimum rechit transverse energy of 3 GeV. For a EM shower that is well-centered on a crystal, one expects approximately 80% of the shower energy in the central crystal, and about 20% of the energy in the four adjacent crystals. The Monte Carlo distribution (hatched) therefore shows a peak at approximately 0.8 in the Swiss-cross variable, with a tail extending to low values and a relatively sharp cut-off above 0.95.
The data distribution (points), which is normalised to the same number of events as the Monte Carlo below a Swiss-cross value of 0.9, shows good agreement with the shape of the Monte Carlo distribution below this value. However, there is a significant second peak at 1.0, due to anomalous signals, that is not present in the default Monte Carlo simulation. A cut on the Swiss-cross variable at a value of 0.95 is therefore efficient at removing a large fraction of these anomalous signal induced hits in data.

The timing variable

Time reconstruction of ECAL pulses is performed by analysing the pulse shape of the ten 25 ns ADC samples that are recorded for each hit. The estimation of the RecHit time is determined by comparing the ratios of consecutive samples. The time of the pulse maximum can be precisely determined by comparing these ratios to those expected from the ECAL pulse shape that is directly measured from test beam data [55]. Figure 4.5 shows the distribution of the RecHit timing for Minimum Bias data and Monte Carlo, with $\sqrt{s} = 7$ TeV, plotted for the highest energy rechit in each event, requiring a minimum rechit transverse energy of 3 GeV. RecHit timing is calibrated for each channel such that a relativistic particle produced at the interaction point at the centre of CMS will be reconstructed with an average time of zero. The timing resolution, which is energy-dependent, is approximately 1 ns for a RecHit of 1 GeV in EB, and 4 GeV in EE [56].
The timing distribution for Minimum Bias data (represented by the data points in figure 4.5) is clearly inconsistent with the Monte Carlo distribution (hatched). The peak at

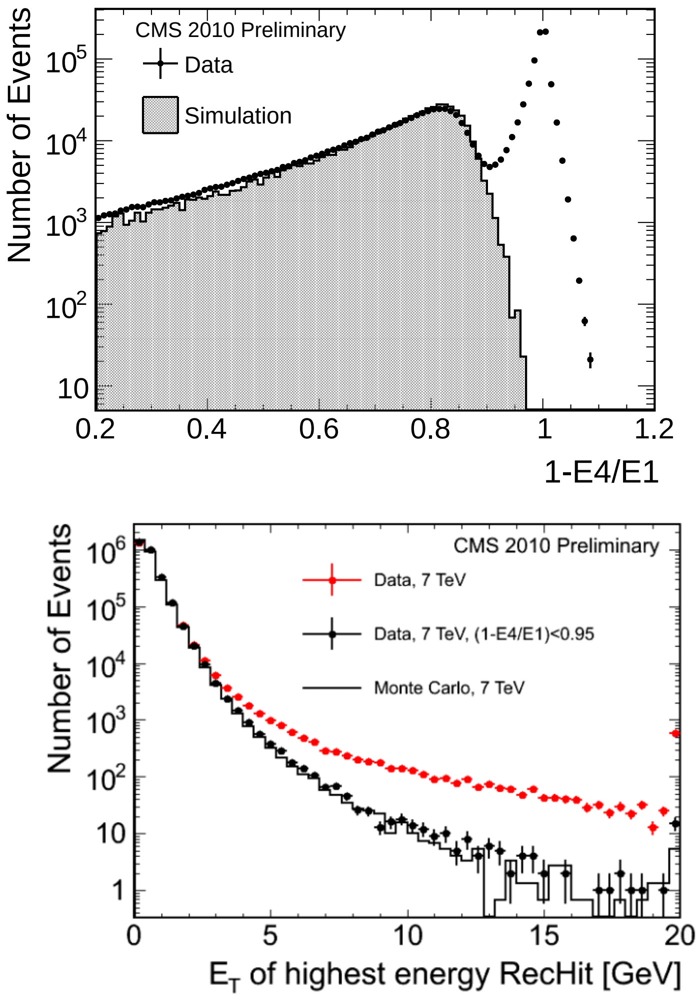

Figure 4.4.: Distribution of the "Swiss Cross" topological variable $(1 - E4/E1)$ for the highest energy deposit in each event for data and simulation ($\sqrt{s} = 7$ TeV). Only events with an energy deposit with $E_T > 3$ GeV are plotted. The two distributions are normalized to the same total number of minimum bias events below (1-E4/E1)<0.9 (top). Distribution of the transverse energy for the same event subsample (bottom). The Swiss cross cleaned sample is in good agreement with the MC simulation.

zero is due to prompt electromagnetic showers, and is modelled by the Monte Carlo. The secondary peak at about -10 ns is due to anomalous signals. The origin of the 10 ns difference can be understood by comparing the pulse shape of 'normal' (Swiss-cross < 0.95) and 'anomalous' (Swiss-cross> 0.95) RecHits (figure 4.6.) The faster pulse rise time for the anomalous signal RecHits is due to the lack of a scintillation

component (80% of light emitted in 25 ns), since the anomalous signals are produced by particles directly interacting in the APD. Since the time reconstruction algorithm compares this pulse to the expected shape, this faster rise time results in an apparent ‘early’ reconstructed time for the pulse. There is also a long tail in the anomalous signal timing distribution extending out to +60 ns in the figure. These are understood to be caused by non-prompt particles striking the APD and producing delayed anomalous signals.The bumps at +15 and +40 ns, which are spaced at +25 (1 clock cycle) and +50 (2 clock cycles) from the peak at -10 ns, and are a consequence of the quantization of the ECAL time samples.
It is clear from figure 4.5 that RecHit timing is a powerful additional tool to reject anomalous signals, and it is exploited in offline reconstruction by requiring that reconstructed hits are consistent with the expected timing of an prompt EM shower produced at the interaction vertex.

The rejection criteria based on the swiss Swiss-cross and the timing variables were

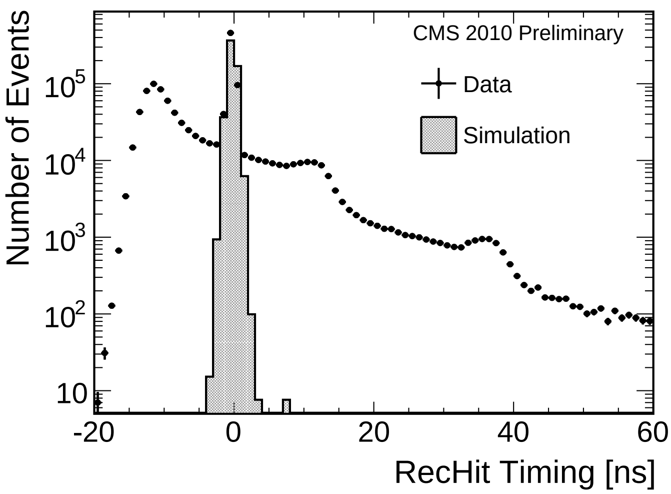

Figure 4.5.: Distribution of the reconstructed time of the highest energy deposit in each event for data and simulation ($\sqrt{s} = 7$ TeV). Only events with an energy deposit with $E_T > 3$ GeV are plotted. The two distributions are normalized to the same total number of minimum bias events below (1-E4/E1)<0.9.

considered mature enough to be activated in the online sequence at the High Level Trigger. Few uncleaned control HLT paths allow to monitor the effectiveness of the described criteria in rejecting the anomalous signals.

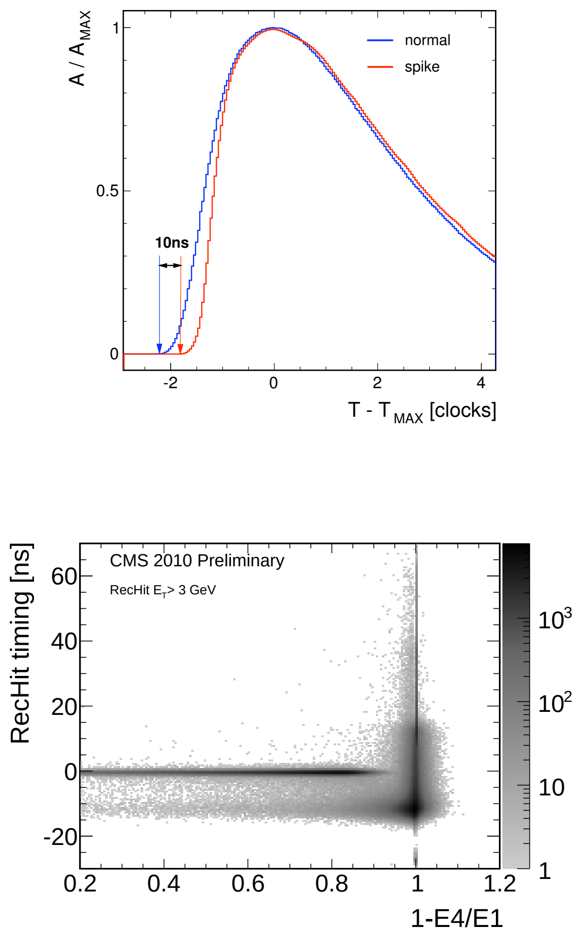

Figure 4.6.: Pulse shapes of normal and anomalous RecHits, aligned such that the pulse maxima occur at the same value of T_{max} (top). Swiss cross versus RecHit timing for MinimumBias data (bottom).

OTHER REJECTION CRITERIA

In addition to the topological Swiss cross selection and timing selection, other discriminants have been studied in order to improve the anomalous signal rejection especially in the case of anomalous signals embedded in physics objects. Instead of using the rechit timing only, an option is to build a discriminant based on the difference of the full pulse shape in the case of a scintillation signal or an anomalous signal. The first shape is known from data with a 1 ns sampling precision and it is the convolution of scintillation and electronics response; for the second, given that the electronics components are known, it is possible to calculate the analytical form [57] which is:

$$f(t) = A\frac{(t-t_0)}{\tau}e^{\frac{1-(t-t_0)}{\tau}} \tag{4.1}$$

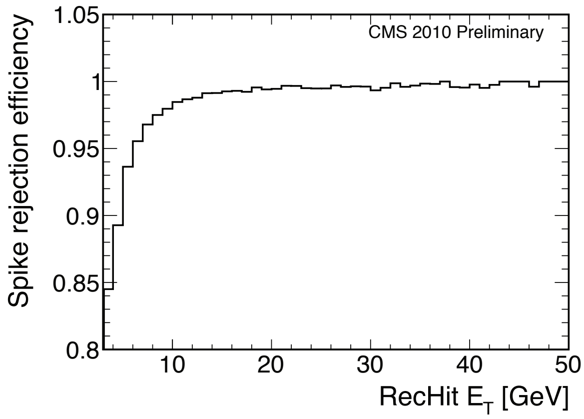

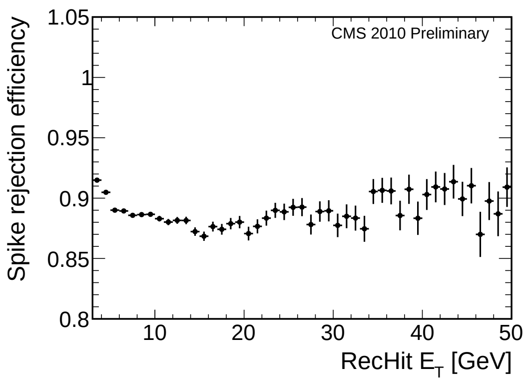

Figure 4.7.: Efficiency of the Swiss Cross cut (1-E4/E1 < 0.95) and the timing cut (|t| < 3 ns) as a function of the RecHit transverse energy in MinimumBias data.

where τ is a channel dependent parameter which varies in the range $40-43$ ns (average $\tau = 41.5$ ns for the ECAL barrel) and t_0, A are free parameters.
The t_0 can be derived analitically for each pair of samples (t_i e $t_i + \Delta t_i$) above the pedestal:

$$t_0 = t_i + \frac{\gamma \Delta t}{1-\gamma} \quad \text{where} \quad \gamma = \frac{A_2}{A_1} e^{\frac{\Delta t}{\tau}} \tag{4.2}$$

Is then possible to compute the amplitude A:

$$A = \frac{\sum_i f(t_i) A_i}{\sum_i f(t_i)^2} \tag{4.3}$$

It is now possible to fit the 10 samples with the scintillation and electronic pulse shapes and build a discriminant based on the likelihood ratio of the two hypotheses.

LIKELIHOOD RATIO: THE DISCRIMINANT D

Assuming that the amplitude of each sample is distributed according to a Gaussian for both the scintillation and the electronic signal, the Likelihood corresponding to the two hypotheses are:

$$L_1 = \frac{1}{\sigma^{N_1}(2\pi)^{\frac{N_1}{2}}} e^{-\chi_1^2} \tag{4.4}$$

$$L_2 = \frac{1}{\sigma^{N_2}(2\pi)^{\frac{N_2}{2}}} e^{-\chi_2^2} \tag{4.5}$$

where $N_1 = N_2$.
Then discriminant can be defined as follows:

$$D = \frac{L_1}{(L_1 + L_2)} = \frac{1}{1 + \frac{L_2}{L_1}} = \frac{1}{1 + e^{-\Delta\chi^2}} \tag{4.6}$$

$$D > 0.5 \rightarrow Signal \tag{4.7}$$

$$D < 0.5 \rightarrow Background \tag{4.8}$$

The likelihood ratio is then univocally related to the $\Delta\chi^2$. In figure 4.8 (top) is reported the distribution of the discriminant for the good signals in green and the anomalous signals in red where the latter are defined as recHits with Swiss cross > 0.95. The performance of the method, tested with $\tau = 41$ ns, gives nearly a 100% efficiency on the signal and 38% efficiency on the anomalous signal sample.
The anomalous signal rejection power has been also tested on the data recorded during the so called ECAL readout phase scan. During the phase scan, the pulse shape is shifted by introducing a positive/negative time phase. The main goal is to minimize the fraction of the trigger pre/post firing and to improve the bunch crossing assignment for each channel. The efficiency results, as a function of the ECAL readout phase, are shown in fig. 4.8 (Bottom). The anomalous signals rejection power of the discriminant is maximum for a time shift of +2 ns.

ANOMALOUS SIGNALS IN TIME

Since the timing and the likelihood ratio are not independent variables, in the following is presented the anomalous signals rejection power in the special case of in time anomalous signals with the discriminant D defined in the previous section. The study is particularly interesting because gives an idea on the ability to reject anomalous signals if they are embedded in a physics object and they are in time. In the following the performance are tested on an isolated anomalous signals sample defined by: Swiss

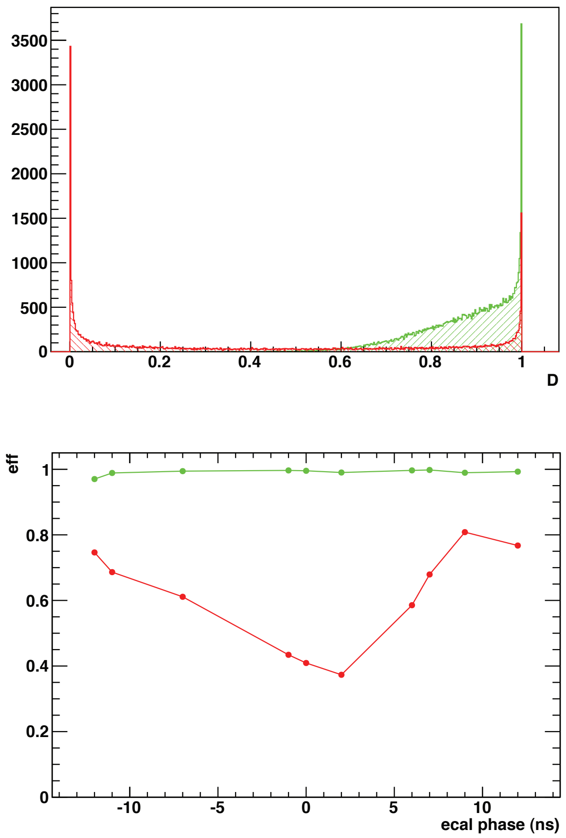

Figure 4.8.: (Top) Distribution of the discriminant D for the scintillation signals (green) and for the anomalous signals (red). The latter are defined as recHits with Swiss cross > 0.95. (Bottom) Efficiency of the D selection as a function of the ECAL phase.

cross > 0.95 and -4 ns < time < 4ns. The ecal phase is 0 ns.
In fig. 4.9 (top) the pulse shape for good signals and anomalous signals are reported in green and red respectively. The two shapes differ especially in the 4^{th} and 10^{th} samples as enlighted by the two blue circles. In fig. 4.9 (bottom) the performances of the discriminant D are compared in two different configuration: considering all the samples in the χ^2 calculation or considering only the 4^{th} and 10^{th} samples. The rejection power which corresponds to a signal efficiency of 95% is 70% and 87% respectively.

The results presented show that it is possible to improve slightly the anomalous signals rejection power by adding a third criterion based on the likelihood ratio in the scintillation signal and anomalous signal hypotheses, to the criteria based on the topology of the energy deposit and on the timing of the reconstructed rechit. This helps especially in the case of embedded anomalous signals (condition that will become more frequent with the increasing of the pile-up) where the topological criteria are

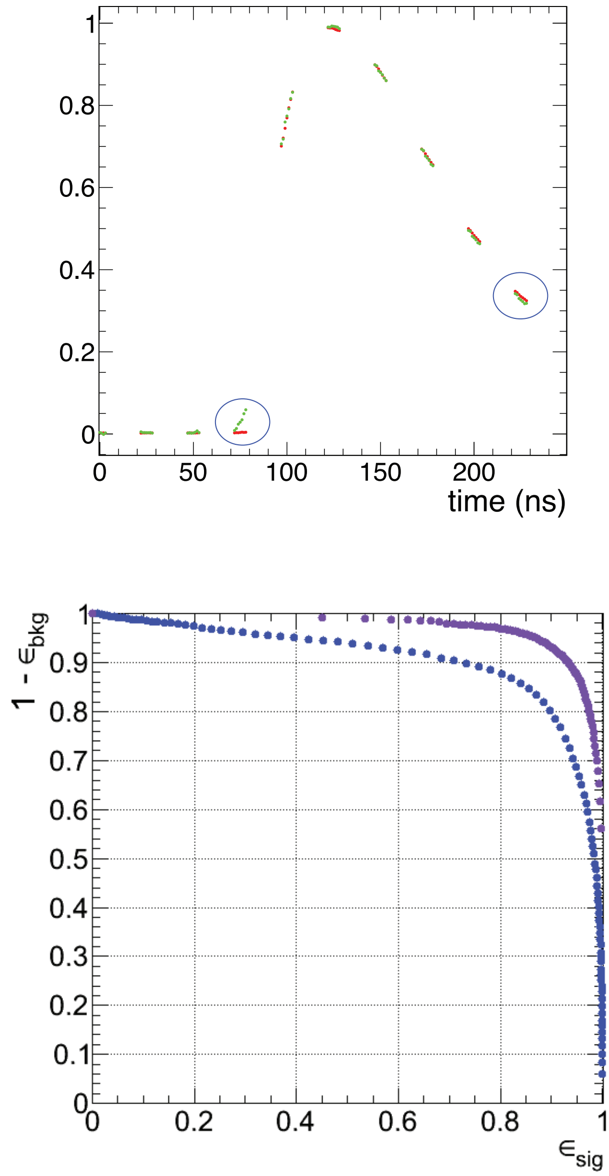

Figure 4.9.: Top: pulse shape for a good signal (green) and an anomalous signal (red). Bottom: the performance of the discriminant D are compared in two different configuration (see text).

not reliable. However the performances of the method are strongly dependent on the ECAL phase and on the τ value and it was not included by default in the CMSSW [58] framework.

4.3 Detector and reconstruction effects affecting the ele+$E_{\mathrm{T}}^{\mathrm{MISS}}$ signature

As illustrated in section 1.2, only two objects are involved in the reconstruction of the final state of the W′ search. Given that the one electron plus missing transverse energy is a very clean signature, the electron spectrum at high E_{T} and the M_{T} spectrum have been used as a reference in a weekly monitoring of the data quality. A few problems of instrumental origin have been identified and fixed.

4.3.1 Residual anomalous signals contamination

With a center of mass energy of 7 TeV the anomalous signals rate is about 1 every 1000 MinBias events. In the hypothesis that an anomalous signal survives all the cleaning steps, the reconstruction of an object such as a photon or an electron is triggered by the anomalous signal. By definition a momentum contribution of the same magnitude and opposite direction will be summed in the $E_{\mathrm{T}}^{\mathrm{miss}}$ reconstruction. Then a single anomalous signal can result in an electron + $E_{\mathrm{T}}^{\mathrm{miss}}$ signature. Of course the event should survive also the electron quality selections to reach the final step of the analysis, but it can not be classified as a bad event by using kinematic criteria.
Since the anomalous signals are not yet simulated in the default Monte Carlo samples, any residual contamination in the final data sample would result in an excess of the data with respect to the Standard Model MC prediction and it has to be carefully subtracted. The event by event monitoring of the transverse mass tail ($M_{\mathrm{T}} > 400$ GeV) of the first 2 fb^{-1}, did not evidenced any contamination in the final sample. The matching probability between a track in the tracker and an anomalous signal in the calorimeter is marginal. The description of the electron reconstruction procedure is reported in section 6.1.

4.3.2 Electronic slew rate

As already mentioned in section 4.1, the timing distribution in minimum bias events is well understood and well reproduced with the Monte Carlo. However, during 2010, as the number of events with high energy deposits in the electromagnetic calorimeter increased, there was growing evidence that the time reconstruction was biased for large pulses (see figure 4.10). This is an effect related to the slew rate limit of the electronic. In electronics, the slew rate represents the maximum rate of change of a signal in a circuit. Limitations in slew rate capability can give rise to non linear effects in electronic amplifiers and pulse shape distortion. The slew rate can be defined as follows:

$$SR = max\left(\left|\frac{dv_{out}(t)}{dt}\right|\right) \tag{4.9}$$

where $v_{out}(t)$ is the output produced by the amplifier as a function of time t. For en-

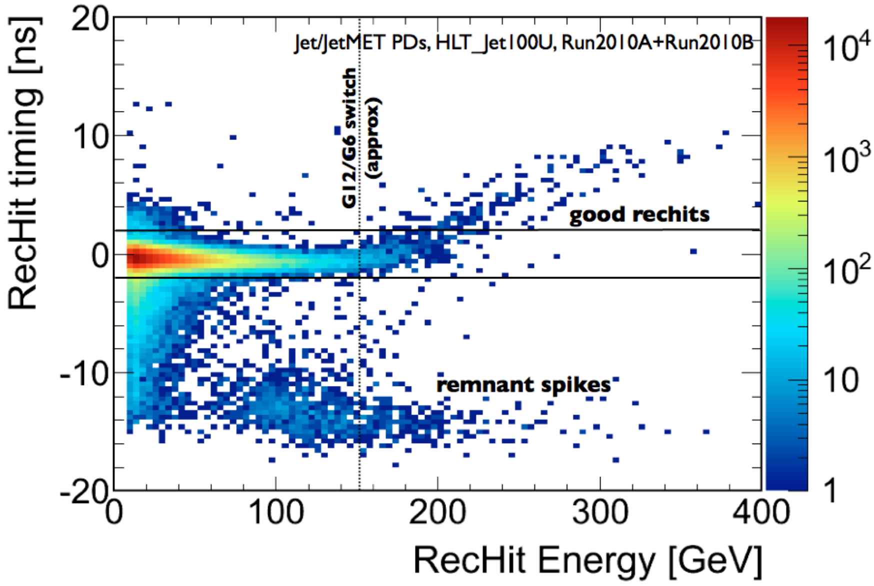

Figure 4.10.: The timing of the seed of electron objects is plotted versus the channel amplitude. The positive timing bias is visible above ~ 150 GeV which is the saturation threshold of the gain 12 regime. The recHits included between the two horizontal lines are flagged as in time recHits; the others as out-of-time.

ergies above 150 GeV in a single channel, the electronic gain switches from 12 to 6. The last sample before the gain switch suffers from the slew rate limit of the electronic resulting in a distorsion of the pulse shape in correspondence with that sample. This effect is visible for the fifth sample, the last at gain 12, of the pulse shape in figure 4.12. The black and red lines are the shapes in case of scintillation and anomalous signal hypothesis respectively. From the eta-phi map in figure 4.11 is also visible that the timing of the inspected channel is not compatible with the timing of the surrounding channels in the 5×5 crystal matrix. The time bias can be as large as 10 ns for good pulses, and this affects anomalous signal cleaning based on timing, which is included by default in the reconstruction chain. The direct effect could be the exclusion of good caloTowers during the $E_{\mathrm{T}}^{\mathrm{miss}}$ reconstruction resulting in a bias that affects the missing transverse energy in that event.

The bias is visible in the ECAL barrel as showed in figure 4.10: all the channels with

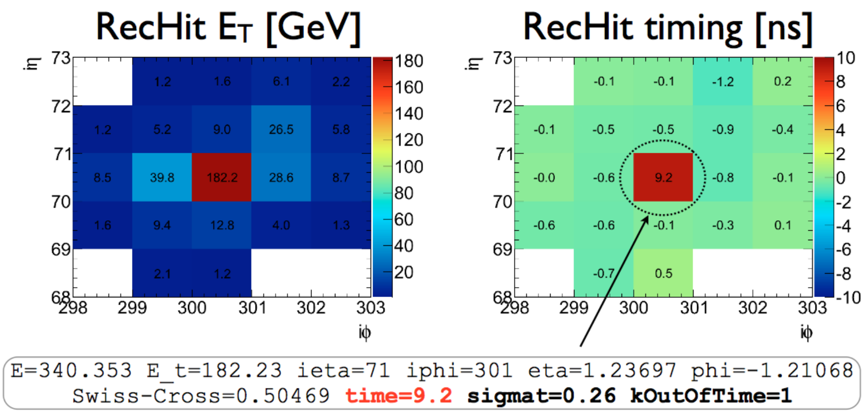

Figure 4.11.: Transverse energy values (left) and timing values (right) for the recHits in the 5×5 matrix centered around the seed of an electron. The 50% of the energy of the object is contained in the central channel. The timing of the seed is not consistent with the timing values from the other recHits in the matrix.

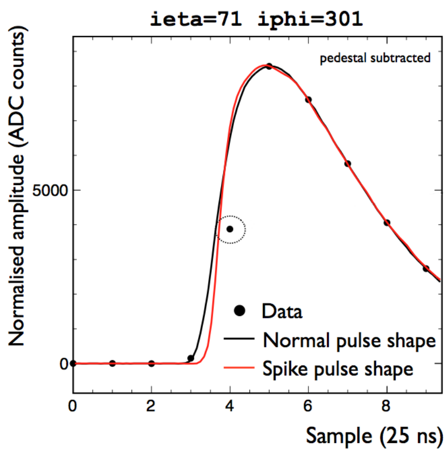

Figure 4.12.: Pulse shape for the seed of the electron showed in figure 4.11. The black dots (data) are not compatible with the anomalous signal pulse shape in red (see the fourth sample). The amplitude of the fifth sample is underestimated due to the slew rate limit of the electronic in gain 12. The sixth sample is the first after the gain switch.

timing not included between the two horizontal lines are flagged as out-of-time channels and then excluded from the supercluster seeding.

For a proper time reconstruction in pulses with amplitude larger than 150 GeV, the fith sample is disregarded in the time reconstruction [59].

4.3.3 SATURATION

The dynamical range of the Multi-Gain-Pre-Amplifier is limited and for very energetic electrons and photons the saturation could occur in the ECAL electronics [60]. This is a critical aspect especially for heavy resonances with masses of several TeV/c^2 decaying in electrons and photons in the context of searches for new physics.
From 2004 test beam data analysis, the saturation threshold at the lowest MPGS gain has been established to be at 1.7 TeV in the barrel and 3.0 TeV in the endcaps. In case of saturation several techniques to extract the energy of the saturated channels from the study of the energy deposition in the 5×5 matrix around it have already been developed using test beam and Monte Carlo data. It was shown in [61] that it is possible to parameterize with good precision the energy ratio E_1/E_{25} in the form of functions $F(X,Y;E,\eta)$. Routines to calculate the energy deposited in the saturated channel based on the E_1/E_{25} parametrization are already included in the CMSSW framework.
In the first 2 fb^{-1} the channel saturation occurred only in events with anomalous signals. No saturation have been observed in ECAL due to genuine electrons or photons.

CHAPTER 5

CALIBRATION OF THE ELECTROMAGNETIC CALORIMETER

Precision calibration is a severe technical challenge for the operation of the CMS electromagnetic calorimeter. It can be seen as composed of a global component, giving the absolute energy scale, and a channel-to-channel relative component, which is referred to as inter-calibration. The final goal of the calibration strategy is to achive the most accurate energy measurement for electrons and photons. Schematically, the reconstructed energy can be factorized into several terms:

$$E_{e,\gamma} = F_{e,\gamma}(E_{\mathrm{T}}, \eta) \cdot \sum_i G(ADC/\,\mathrm{GeV}) \times S_i(T,t) \times c_i \times A_i \tag{5.1}$$

where the sum is over the crystals in a super-cluster. A_i are the reconstructed amplitudes in ADC counts, c_i is the inter-calibration constant, S_i the transparency correction factor, while G is the ECAL energy scale. The factor $F_{e,\gamma}$ is defined as an additional energy correction which depends on the type of the particle, its energy and pseudorapidity and in particular takes into account shower leakage and bremsstrahlung losses.

While an inter-calibration precision of 0.5% is desired to achieve the best sensitivity to the postulated $H \to \gamma\gamma$ decay, an inter-calibration at the percent level is sufficient for the W$'$ search and for most of the CMS physics programme. This can be evinced from figure 5.1 where the width of the Z boson peak is shown as a function of the ECAL residual miscalibration (to be compared with figure 5.2 for the $H \to \gamma\gamma$ process). The vertical arrows show the evolution of the inter-calibration precision for the barrel (orange) and the endcaps (blue). The main inter-calibration procedures used to calibrate the ECAL and the precision reached with each method will be outlined in the following sections together with the strategies to monitor the performance of the detector.

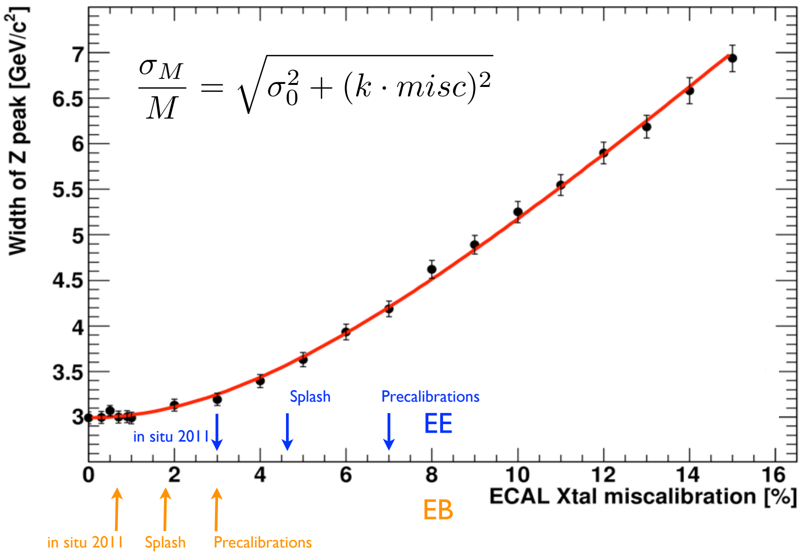

Figure 5.1.: Width of the Z boson peak ($Z \to e^+e^-$ process) as a function of the inter-calibration precision.

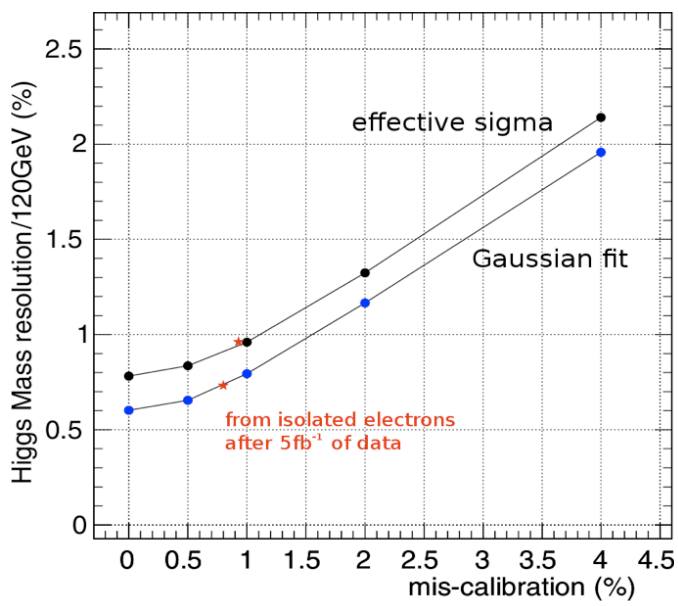

Figure 5.2.: Width of the H boson peak ($H \to \gamma\gamma$ process) as a function of the inter-calibration precision.

5.1 ECAL CALIBRATION PROCEDURES

While the ECAL calibration target precision has been achieved in the central part of the barrel with physics events within the first year of data taking, pre-calibration procedures with test beam data, exposure to cosmic rays and laboratory measurements of the crystal light yield and photodetector gains, provided good performances for the initial data taking. In particular, 9 supermodules of the ECAL barrel have been inter-calibrated using 120 GeV electrons from test beam with an accuracy of 0.3% [62]. The remaining 27 supermodules were inter-calibrated with a precision of 1.5%-2.5%, obtained by exposure to cosmic rays. For the ECAL endcaps, the inter-calibration constants were determined from laboratory measurement of the light yield and of the VPT gain, with an accuracy of 7.4%. A set of 460 crystals in EE-[1] was also exposed to electrons in test beams and inter-calibrated with a precision better than 1%. This inter-calibration coefficient set was derived at B = 0 T. Transportation at B = 3.8 T, corresponding to the nominal operation conditions in CMS is done with small additional uncertainty ($\sim$0.5%).
The data from cosmic ray muons and beam induced muon events collected with the CMS detector in his final position before the LHC startup, were used to perform an *in situ* check of the pre-calibration constants described above. The precision of these measurements, which are made at the level of 1-2% for the barrel and better than 5% in the endcaps, are comparable to the laboratory measurements. They also provided the initial calibration constants for the calibration methods using LHC beam events, which will ultimately achieve the final calibration goal of 0.5%. In the light of what has been shown, the W$'$ search was never limited by the calibration accuracy of the ECAL.

Some of the aforementioned pre-calibration procedures will be presented in detail in the following sections. The channel-by-channel calibration techniques with physics events are briefly listed here for completeness:

- the ϕ-symmetry inter-calibration is a fast calibration method, i.e. it requires a low amount of statistics ($\sim 102\,\text{nb}^{-1}$) and it is based on the invariance around the beam axis of energy flow in minimum bias events; it allows to inter-calibrate crystals in a ring at the same pseudorapidity. Inhomogeneities in the detector material limit the precision of the method to about 1.5%-3% depending on the channel pseudorapidity [63, 64];

- the π^0 and η calibration exploits the mass peak of photon pairs selected as

[1]The two ECAL endcaps are labeled EE+ and EE- if z>0 or z<0 according to the CMS coordinate system that is defined in such a way that the x-axis points to the center of the LHC ring, the y-axis points vertically upwards and the z-axis is arranged to produce a right handed coordinate system.

$\pi^0(\eta) \to \gamma\gamma$ candidates; it is useful at the start-up also to investigate the ECAL energy scale [65];

- isolated electrons from $W \to e\nu$ and $Z \to e^+e^-$ decays can be used to compare the energy measured in ECAL to the track momentum measured in the silicon tracker. This will be the primary channel-to-channel calibration tool for several fb^{-1} of collected integrated luminosity [66];

In parallel, di-electron resonances such as $J/\Psi \to e^+e^-$ and $Z \to e^+e^-$ can be used to monitor and correct the absolute ECAL energy scale. On a longer term, other physics events such as $Z \to \mu\mu\gamma$ can be used for this purpose.

5.2 Validation of the barrel response with cosmics rays muon

During October-November 2008 the CMS Collaboration performed a month-long data taking exercise, known as the Cosmic Run At Four Tesla (CRAFT) [67], with the goal of commissioning the experiment for an extended operating period. With all the subdetectors participating, CMS recorded about 270 millions of cosmics ray triggered events with the solenoid at its nominal axial magnetic field strength of 3.8 T. An event display of a cosmic muon crossing CMS is shown in Fig. 5.3.
CRAFT data were exploited to measure the muon specific energy loss in lead tungstate as a function of the muon momentum. This measurement allowed to check the global energy scale and local energy scale in the ECAL barrel.

5.2.1 Data Set

The muon stopping power dE/dx has been measured for muons in a momentum range between 5 GeV and 1 TeV. Single muons reconstructed in the inner tracker with an associated energy deposit in both the upper and lower half of ECAL barrel were considered. The sixteen supermodules located at the top and bottom of the ECAL, which have the highest acceptance to the vertical cosmic-ray muon flux, were selected for this analysis. The typical muon energy release in ECAL is about 300 MeV. In order to increase the sensitivity to low energy deposits the APD gain was raised from the nominal gain 50 to 200. In this condition the equivalent energy noise corresponds to 9.5 MeV per readout channel. Events with small angle ($< 30°$) between the muon track and the crystals axis were selected. This reduces systematic biases on the energy scale due to crystal energy deposits falling below the clustering or zero suppression thresholds, which is more probable for large angle tracks which pass through multiple crystals. A total of 250 000 events remained after all selection cuts.

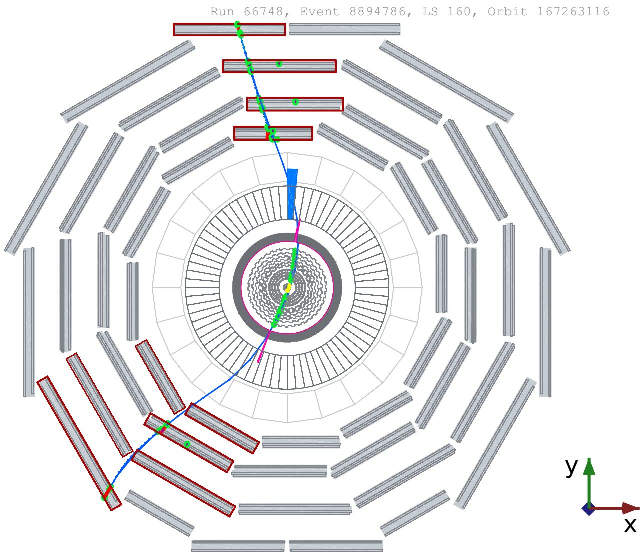

Figure 5.3.: An event display of a cosmic muon crossing CMS. ECAL hits are in magenta, HCAL in blue, tracker and muon hits in green.

5.2.2 Validation of the global energy scale in the ECAL barrel

The muon stopping power measure as a function of the muon momentum is shown in figure 5.4. Absolute measured values of energy loss are in agreement with expectations [68] within an overall uncertainty of about 2%. The result is dominated by the precision of the measurements in the momentum region below 20 GeV/c, where radiation losses are negligible and shows that the energy scale set with 120 GeV electrons in test beam still holds in the sub-GeV ($\sim$300 MeV) region.
The curve

$$(\mathrm{d}E/\mathrm{d}x)_{meas} = \alpha \left[\left(\frac{\mathrm{d}E}{\mathrm{d}x} \right)_{coll} + \beta \times \left(\frac{\mathrm{d}E}{\mathrm{d}x} \right)_{rad} \right] \tag{5.2}$$

where *coll* and *rad* label the predicted energy losses in $PbWO_4$ due to collisions with atomic electrons and radiative processes respectively [69], is fitted to experimental stopping power data using a binned maximum likelihood. The parameters α and β account for the overall normalization of the energy scale and for the relative normalization of radiation and collision losses. With the adopted parameterization the overall energy scale measurement is completely absorbed in the α parameter. The fit results in:

$$\alpha = 1.004^{+0.002}_{-0.003}\,(\text{stat.}) \pm 0.019\,(\text{syst.}) \tag{5.3}$$

$$\beta = 1.07^{+0.05}_{-0.04}\,(\text{stat.}) \pm 0.6\,(\text{syst.}). \tag{5.4}$$

Adding statistical and systematic contributions in quadrature, it may be concluded from the above results that the energy scale is consistent with expectations within an uncertainty of about 2 %.

The dE/dx measurement is in agreement with expectations over the full momentum range and a comparison of collision losses with radiative losses allows to derive the muon critical energy in $PbWO_4$.

A more exaustive discussion about the systematics, the extraction of the muon critical energy in lead tungstate and the statistical analysis can be found in the paper that we have published on this topic [70];

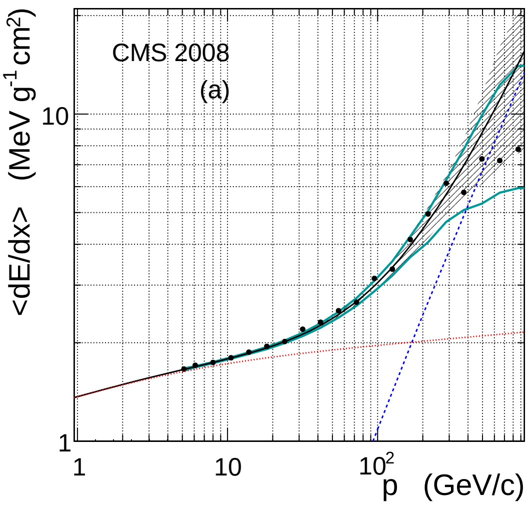

Figure 5.4.: Muon stopping power measured in $PbWO_4$ (dots) as a function of muon momentum compared to expectations [68] (continuous black line). The expected contributions from collision and radiative processes are plotted as well (red dotted line and blue dashed line respectively).

5.2.3 Validation of the local energy scale in the ECAL barrel

A check of the pre-calibration constants for 14 of the 36 barrel supermodules was performed by comparing the stopping power ($\mathrm{d}E/\mathrm{d}x$) distributions for cosmic ray muons after the constants were applied.

The momentum selection of the cosmic-ray muons is performed after the muons have passed through the upper hemisphere but before they pass through the lower hemisphere of ECAL. This causes a difference in the energy deposits in the two hemispheres of about 0.5%, due to the dependence of $\mathrm{d}E/\mathrm{d}x$ on the muon momentum. In order to compare the ECAL response in the upper and lower hemispheres, this effect is corrected for in the analysis.

The average pre-calibration constants for each supermodule, $\langle \mathrm{IC} \rangle$, vary by up to 30%, due to differences in crystal light yield (Fig. 5.5). The measured $\mathrm{d}E/\mathrm{d}x$ distributions for the 14 supermodules were compared after applying the pre-calibration constants to equalise the light yield response. Figure 5.6(a) shows the mean stopping power for each supermodule, plotted as a function of $\langle \mathrm{IC} \rangle$. Each point is normalised to the average $\mathrm{d}E/\mathrm{d}x$ value for all 14 supermodules, and the values of $\langle \mathrm{IC} \rangle$ are normalised to a reference supermodule. The most probable value of $\mathrm{d}E/\mathrm{d}x$ in this momentum range is measured to be approximately 1.75 MeV $\mathrm{g}^{-1}\mathrm{cm}^2$ [70]. This corresponds to an energy loss of 335 MeV for a particle traversing the full length of a crystal. A truncated mean is used in the determination of the average $\mathrm{d}E/\mathrm{d}x$ value in order to remove statistical fluctuations from high energy deposits in the upper 5% of the $\mathrm{d}E/\mathrm{d}x$ distributions. The spread of these measurements, which indicates the level of uniformity of the detector response, is about 1.1% (RMS). This is comparable to the statistical precision of the measurements (typically 0.4%) combined with the following systematic uncertainties: a) the dependence of the muon energy scale on the angle between the crystal axis and the muon direction (estimated to be 0.5%); b) the variation in average muon momentum for different supermodules, since they have different angular acceptance to cosmic-ray muons and hence sample different regions of the cosmic-ray muon flux (estimated to be 0.4%). The total systematic uncertainty of 0.6% is indicated by the shaded band in Fig. 5.6(a). All estimates of systematic error are derived from data. A full description of their evaluation is provided in Ref. [70]. The calibration procedures in ϕ that utilise LHC data will yield precise inter-calibration of crystals at a given η value. The pre-calibration constants will provide the relative scale for crystals at different η values at LHC startup. The cosmic-ray muon data taken during CRAFT were therefore used to validate in situ the pre-calibration constants as a function of η. Figure 5.6(b) shows the (truncated) mean $\mathrm{d}E/\mathrm{d}x$ as a function of the crystal index in the η coordinate. These measurements are normalised to the average $\mathrm{d}E/\mathrm{d}x$ integrated over all η values. The distribution is plotted over the range $-0.7 < \eta < 0.7$, where most of the muons that pass through both the tracker and the ECAL are located. The spread of the measurements, indicating the precision to which the η-dependent pre-calibration scale is verified, is 0.8% (RMS). The statistical precision of the measurements, indicated by the error bars on the points, is typically 0.4%. The total systematic uncertainty, which is represented by the shaded region, is 0.5%. The main contribution to the systematic error is the energy scale dependence on the angle between the muon trajectory and the crystal axis (0.5%). Since each data point integrates over all values of ϕ, the systematic uncertainty on the muon momentum scale due to the variation in acceptance to the cosmic-ray muon flux is reduced, and is estimated to be 0.1% in Fig. 5.6(b).

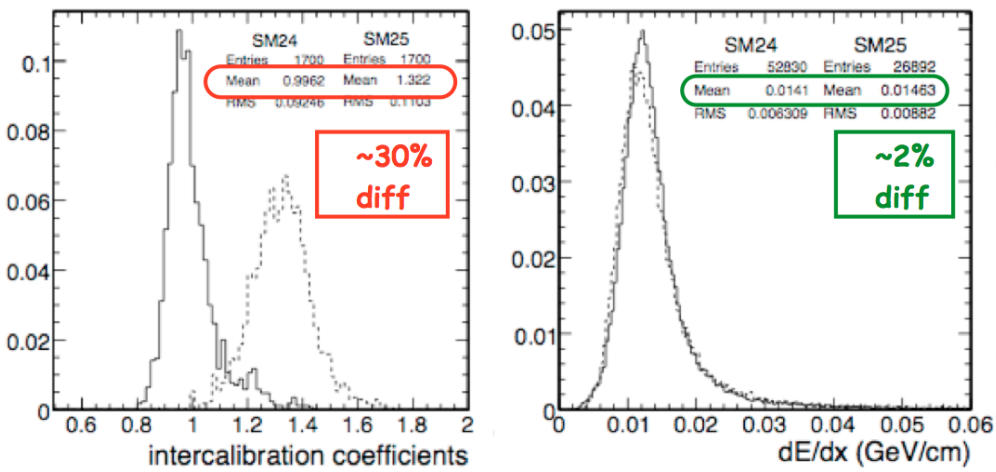

Figure 5.5.: Distribution of the inter-calibration coefficients (left) and the dE/dx measurement from cosmic muons (right) for two adjacent supermodules. The average light yeld value varies up to 30% between different supermodules.

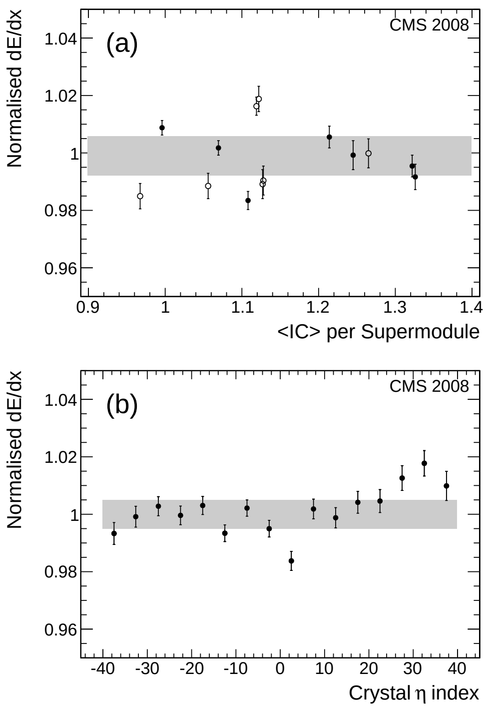

Figure 5.6.: (a) Mean stopping power, dE/dx, versus the mean pre-calibration constants, $\langle$IC$\rangle$, for 14 supermodules. Each point is normalised to the average value of dE/dx calculated using all 14 supermodules. The filled circles indicate supermodules located in the upper hemisphere of the ECAL and the open circles represent supermodules located in the lower hemisphere. (b) Mean stopping power, dE/dx, versus the crystal index in the η coordinate. Each data point is integrated over five crystals in η and all values of ϕ. In both plots, the shaded region represents the systematic uncertainty on the measurement of dE/dx.

5.3 Pre-calibration of the ECAL with beam dump events

The pre-calibration techniques described in this section exploit the beam dump data, usually referred to as "beam splash events", collected from LHC beam dumps in collimators located about 150 m from the detector. In these events, a bunch of muons, produced in the hadronic cascade initiated by protons in the collimator, reaches the detector illuminating all the active channels. The event display for one of the beam dump events is reported in Fig. 5.7.

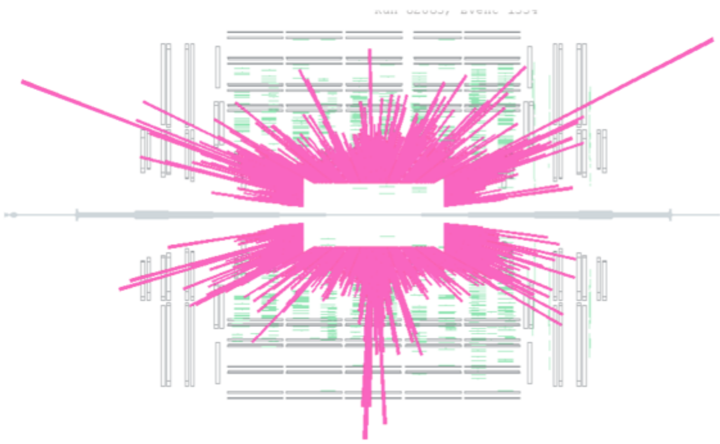

Figure 5.7.: Event display for a beam dump event coming from EE+. The energy deposits in ECAL are visible in pink.

5.3.1 Data Set

Beam dump events were collected at B = 0 T in 2008 and at B = 3.8 T in 2009. The first set consists of 41 events in total, of which 22 events with the beam coming from the EE+ side and 19 events coming from the EE- side. The second one consists of 1253 events with the beam coming only from one side (EE-). For sake of simplicity, in the following I will refer to "BS08" for the 2008 beam splash dataset and to "BS09" for the 2009 dataset.

The average energy deposition per crystal per event in each endcap is shown in Fig. 5.8 for one run in the 2009 dataset. The beam comes from the EE- side. The shielding effect of the ECAL barrel explains the lower energy deposition in the external region of the endcap downstream to the beam direction. The squarish region visible in the central part of the endcaps is due to the shielding structure of the CMS cavern. Long range modulations of the energy deposits across the detector barrel (fig. 5.9) are ascribed to the inhomogeneity of the muon flux in the $i\phi$ coordinate, ultimately related to the geometry of the beam and of the experimental setup, and to muons absorption along $i\eta$ (with $i\eta$ and $i\phi$ are the crystal indexes along η and along ϕ, respectively). Only muons with more than about 5 GeV have sufficient energy to entirely cross the ECAL barrel. From the decrease in the energy deposition along $i\eta$, it is possible to estimate that about 15% of the incoming muons are below 5 GeV. In figures 5.8 and 5.9, white squared areas correspond to towers of crystals masked from the readout.

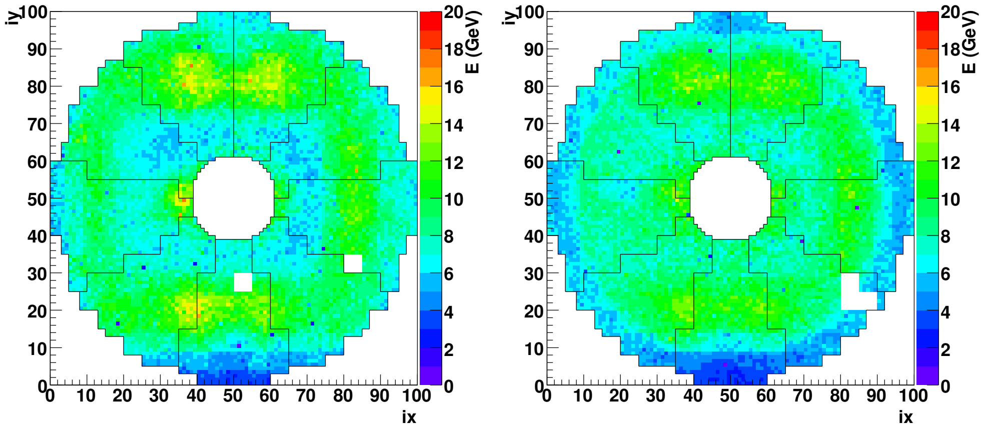

Figure 5.8.: Maps of the average energy deposited by splash events (2009 data) in EE- (left) and EE+ (right). Inter-calibration coefficients from laboratory measurements are applied.

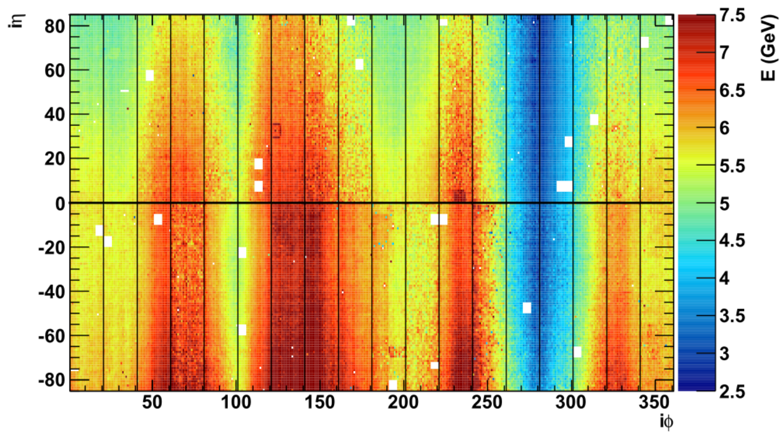

Figure 5.9.: Map of the average energy deposited by splash events in the ECAL barrel (2009 data). Each bin is one crystal identified by a pair of indices ($i\phi$, $i\eta$). Inter-calibration coefficients from pre-calibrations are applied.

5.3.2 ECAL BARREL

In a typical beam splash event, the average energy per channel varies between 6 and 8 GeV with an estimate muon fluence of about 5 muons/ cm ^{2} at the entrance of ECAL. With O(1000) beam dump events, the total energy integrated by each crystal is about 6 TeV. The stochastic and noise fluctuations on the measured mean energy are below 0.1%, and all the difference in the energy deposits must be ascribed to systematic effects.
Under the assumption of the muon flux conservation through the crystals volume, a technique to calibrate the ECAL barrel with beam dump events and the validation of the results against inter-calibration methods based physics events is presented.

INTER-CALIBRATION PROCEDURE

Besides long range modulations as a function of $i\phi$ and $i\eta$ in the energy map of figure 5.9, reflecting the inhomogeneity of the muon flux versus $i\phi$ and the decrease of flux versus $i\eta$, there is evidence of definite structures, which are inconsistent with the assumption that the energy profile should vary with continuity across the detector. Some noteworthy features are indeed identified with poorly calibrated regions during the commissioning phase of the detector. Notably, there are a few isolated trigger towers (regions of 5×5 crystals) which appears somewhat off calibrated as compared to their neighbors. Moreover, by visual inspection of the map, it is possible to identify "I - L" structures, reminders of the way the monitoring light from a laser source is injected in the crystals (see e.g. the supermodule EB-10 at negative $i\phi$ and $i\eta$ ranging from 180 and 200).
These observations suggest that local inhomogeneities in the single channel response can be measured and re-equalized with the beam dump sample, by simply assuming that the muon flux should vary with continuity as a function of $i\eta$ and $i\phi$. This is formalized in the equation:

$$E = D(i\phi)D(i\eta)c(i\phi,i\eta)E(i\phi,i\eta) \tag{5.5}$$

where $E(i\phi,i\eta)$ is the measured average energy in a single channel, $c(i\phi,i\eta)$ is its intercalibration coefficient, E is the average energy in all the channels and $D(i\phi)$ and $D(i\eta)$ are empirical correction factors to compensate for the variations of the energy depositions across the detector. The intercalibration constants can be further factorized as:

$$c(i\phi,i\eta) = c_{pre}(i\phi,i\eta) \times [1+\delta(i\phi,i\eta)] \tag{5.6}$$

where $c_{pre}(i\phi,i\eta)$ are the pre-calibration constants applied in the data reconstruction and $f(i\phi,i\eta) = [1+\delta(i\phi,i\eta)]$ is a correction factor to be derived from the analysis.

At zero-th order, the $D(i\phi)$ and $D(i\eta)$ corrections are defined by the projections of energy map of figure 5.9 on the $i\eta$ and the $i\phi$ coordinates, as shown in figure 5.10. The "bump" around $i\eta = 0$ (left plot) superimposed to a constant decrease of flux is understood as the sum of different effects: the volume of the crystals is not constant, the projective geometry of ECAL modifies the self-shielding effect of ECAL along $i\eta$. The zero-th order D functions average out the local fluctuations due to the residual

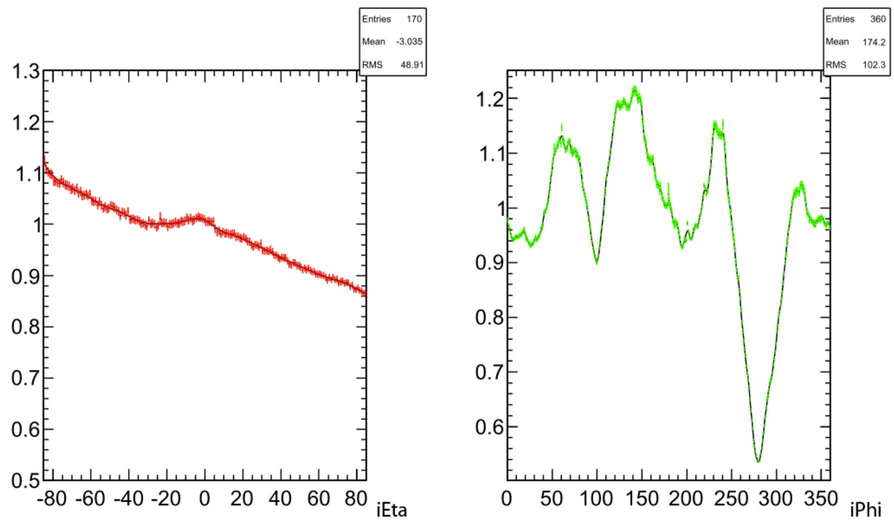

Figure 5.10.: The zero-th order D correction functions derived from the projection of the energy map on $i\eta$ (left) and $i\phi$ (right).

miscalibration of the individual channels, and would provide an (almost) exact correction if the muon energy spectrum was the same at all $i\phi$. Because of the ϕ-symmetry of the detector, the stopping power of ECAL is the same at all $i\phi$, thus the relative variation of the muon flux along $i\eta$ would be the same at all $i\phi$, for the same energy spectrum.

The assumption of ϕ-invariance of the muon energy spectrum is only approximate. Violations of a few percent are observed *a-posteriori*, as the correction factors to pre-calibration derived from these D-functions turn out to be not flat along $i\eta$, with an $i\phi$ pattern. The effect is more pronounced in the region around $i\phi = 270$, closer to the cavern floor, where the intensity of the muon flux is lower than elsewhere.

Assuming that the pre-calibration constants are not differently biased along $i\eta$ in the different supermodules, we compensated this effect through by means of local corrections to $D(i\eta)$, to make the energy profile versus $i\eta$ flat in each SM. These correction are derived from second order polinomial fits to the energy profile in each SM after the zero-th order correction were applied. In this step $D(i\eta)$ is also normalized locally so that the inter-calibration constants are averaged to 1 in each SM.

VALIDATION OF THE INTER-CALIBRATION

The comparison of the obtained inter-calibration coefficients with the corresponding coefficients in the nine super-modules exposed to test beam gives an estimate of the precision of the method. Given the precision of test beam pre-calibrations, in fact, the RMS spread 1.7% (see fig. 5.11) is totally dominated by the calibration with beam splashes.

A direct comparison of the correction factors derived in this analysis to the ones de-

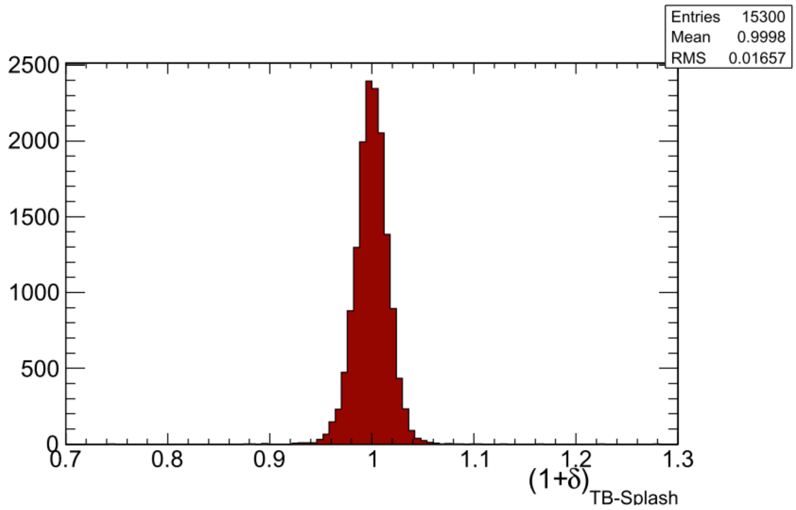

Figure 5.11.: Distribution of the correction factor to pre-calibrations defined in equation 5.6 for the nine super-modules exposed to test beam. The RMS spread is measure of the inter-calibration precision with beam splashes.

rived by the other methods show that the results are consistent. One such example is shown in figure 5.12 for all the channels at $|i\eta| < 50$, which indicates the level of agreement between the correction factors determined by the π^0 inter-calibration method and from beam dump data. The RMS spread of 2.5% of the difference between the correction factors derived in the two methods is consistent with the estimated precision of each method alone. Similar results are obtained by comparing to ϕ-symmetry results.These results consolidate the assumption that the claimed precision of inter-calibration derived at test beams has been conserved in P5 after four years from the test beams.

5.3.3 ECAL ENDCAP

In the ECAL endcaps (EE), the main source of variations in the channel-to-channel response are the the scintillation light yield of the individual crystals, and the variations in the VPT signal due to differences in the gain, quantum efficiency and photocathode

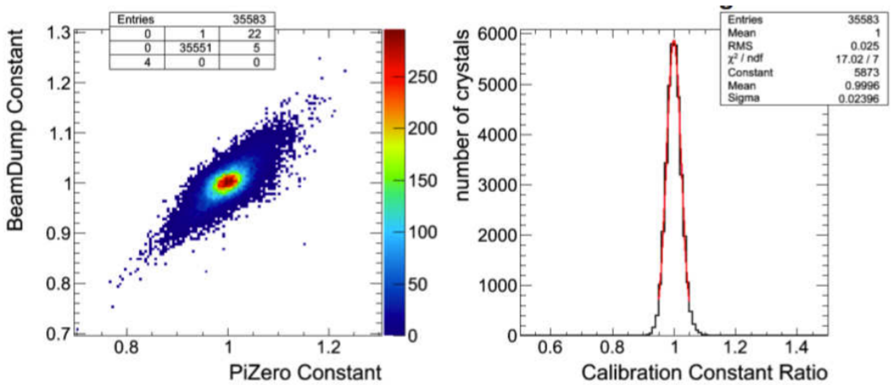

Figure 5.12.: Comparison of the correction factor to pre-calibration derived from beam dump data and from π^0 calibration in the $|i\eta| < 50$ region. The correlation (left) and the distribution of the ratio between the two results (right) are shown.

area.
Beam dump data are used to obtain a new set of inter-calibration constants under the assumption of local uniformity of the energy deposition in the ECAL endcaps. A complementary procedure exploiting the ECAL preshower to get an estimate of the energy flux in each endcap is moreover discussed in this chapter. It has been applied to data collected in 2009 when the preshower was in the data taking. Both methods are validated against measurements from test beam data and from laboratory. The combination of all the available sets of measurements provides an inter-calibration set with a precision better than 5%, which is comparable to the precision expected with other approaches after 10 pb^{-1} of collision data.

INTER-CALIBRATION WITH LOCAL UNIFORMITY

The inter-calibration relies on the assumption of local uniformity of the energy deposition is divided in two steps: using the local uniformity hypothesis, an inter-calibration within a 5×5 crystals matrix is performed and then pre-calibration coefficients are used to inter-calibrate between matrices, to account for the radial dependence of the EE inter-calibration constants. This results in the following definition of inter-calibration coefficient:

$$\mathrm{c_{splash}} = \frac{<\mathrm{E_i}>_{5\times5}}{\mathrm{E_i}} < c_{pre} >_{5\times5} \tag{5.7}$$

where $\mathrm{E_i}$ is the energy deposit in each crystal, $<\mathrm{E_i}>_{5\times5}$ is the average energy in the 5×5 matrix centered around the crystal i and $< c_{pre} >_{5\times5}$ is the average value on a 5×5 matrix of the pre-calibration coefficients. The uncertainty on the term $< c_{pre} >_{5\times5}$ should contribute to the final inter-calibration precision for about 1.5%, if c_{pre} are taken from laboratory measurements that are known to a 7.4% level. The matrices are selected with the sliding windows criterion, which means that the crystal matrices are always built centered on the crystal for which the inter-calibration coefficient is derived. With this approach, discontinuities at super-crystals boundaries due to variations in the incident flux over some super-crystal regions are largely reduced and the local uniformity improved, with a consequent improvement of the precision of the method.

INTER-CALIBRATION USING THE PRESHOWER

During the 2009 data taking, both the calorimeter and the endcaps preshowers were active. This allowed to exploit the informations from the preshower in order to get an independent measurement of the energy flux in the ECAL endcaps. As described in section 3.2.2, the active planes of silicon detectors are built of identical modules each subdivided into 32 strips with 1.9 mm pitch and they cover the rapidity interval $1.653 < \eta < 2.6$.
Assuming that the bunch of muons crosses the detector parallel to the beam pipe, the flux in each endcap crystal can be estimated from the energy deposited in the preshower strips lying in the the crystal shadow (see the scheme in Fig. 5.13). The flux

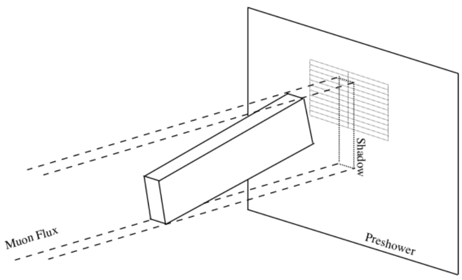

Figure 5.13.: The schematic representation of the setup shows the crystal's shadow on the preshower plane.

through the i-th crystal is therefore evaluated as

$$F_i = \frac{\sum_k E_k^{strip}}{N} \tag{5.8}$$

where the k index runs over the strips in the crystal shadow and N is the number of active strips in the shadow. The inter-calibration coefficient for the crystal is then extracted as

$$c_i = \frac{F_i}{E_i} \tag{5.9}$$

where E_i is the energy in GeV measured in the i-th crystal and F_i is the flux estimated from the average flux in the two preshower planes where they are both active.
The flux measurement using the preshower is reliable in the region $22 < \mathrm{R} < 38$, where R is the radius measured in crystal units. At smaller and larger radii the combination of several effects, as the incomplete coverage of the crystals shadows by the preshower strips and the flux gradient as a function of the radius, leads to an underestimation and an overestimation of the flux respectively. This is illustrated in Fig. 5.14, where the ratio between the energy flux estimated from the preshower and the energy measured in each crystal, after the application of inter-calibration constants from laboratory measurements, is shown as a function of the radius.

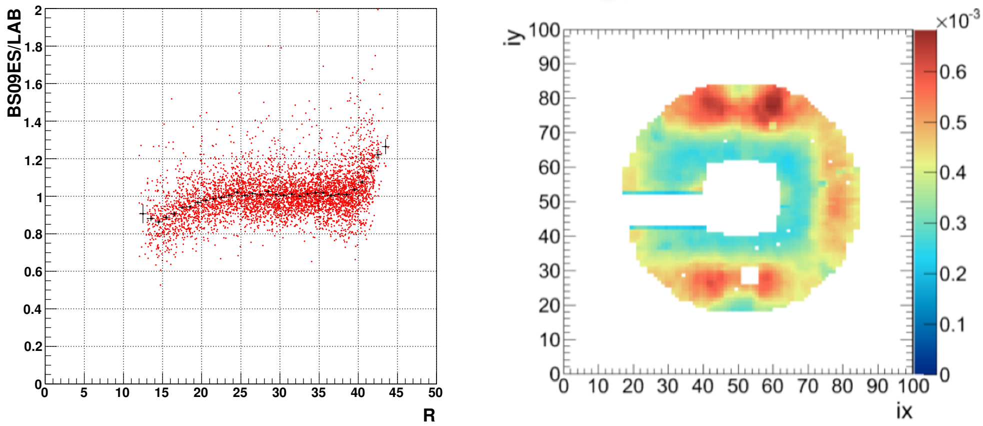

Figure 5.14.: Ratio between the energy flux estimated from the preshower (see Eq. 5.8) and the energy measured in each endcap crystal as a function of the radius (left).Map of the average flux in GeV/strip for EE- (right).

VALIDATION OF INTER-CALIBRATIONS FROM 2008 BEAM DUMP DATA (*local uniformity)*

Inter-calibration constants have been derived using 2008 beam dump data and applying the definition given in Eq. 5.7, where coefficients from laboratory measurements are used to inter-calibrate between 5×5 crystals matrices.

The inter-calibration constants derived from splashes are validated against the coefficients (c_{TB}) from the 2007 test beam on the 162 crystals reference crystals in EE-. The agreement between c_{splash} and c_{TB} is 9.6% RMS (Fig. 5.15). In order to validate the coefficients over the entire endcaps, we compared the inter-calibration coefficients from BS08 data to those from laboratory measurements. The width of the distribution $c_{\mathrm{splash}} - c_{\mathrm{pre}}$ is about 12% (Fig. 5.16), which is in agreement with the combination of

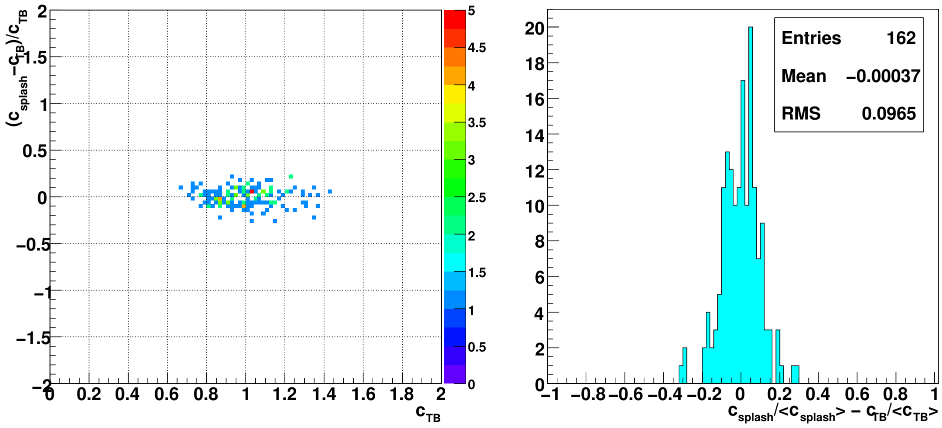

Figure 5.15.: Relative difference between the inter-calibration coefficients derived from 2008 splash events and the inter-calibration coefficients from test beam versus the inter-calibration coefficients from test beam (left). The agreement is about 9.6% (right).

the precisions on c_{splash} ($\sim$ 9.6%) and c_{pre} ($\sim$ 7.4%). The map of the ratio between the two sets is also reported in Fig. 5.16-bottom and shows a uniform behaviour over the entire endcaps.

VALIDATION OF INTER-CALIBRATIONS FROM 2009 BEAM DUMP DATA (*local uniformity)*

The method based on the local uniformity assumption is applied on 2009 data. In this case, the set of coefficients obtained from the weighted average of coefficients from laboratory and from BS08 data is used to inter-calibrate between crystals matrices. Inter-calibration constants from the combination of laboratory and BS08 data have a precision of about 6%.
The comparison of beam splash 2009 coefficients with test beam coefficients corrected for the magnetic field shows an agreement of about 6.4% on the 162 reference crystals. The improvement with respect to beam splash 2008 data is due to the larger statistics available and to the use of laboratory measurments combined with BS08 data to inter-calibrate matrices.

The set of coeffcicients from BS09 is validated against laboratory measurements over the entire endcaps. The width of the distribution of the difference between BS09 and laboratory is consistent with the precisions of the individual sets (Fig. 5.18).

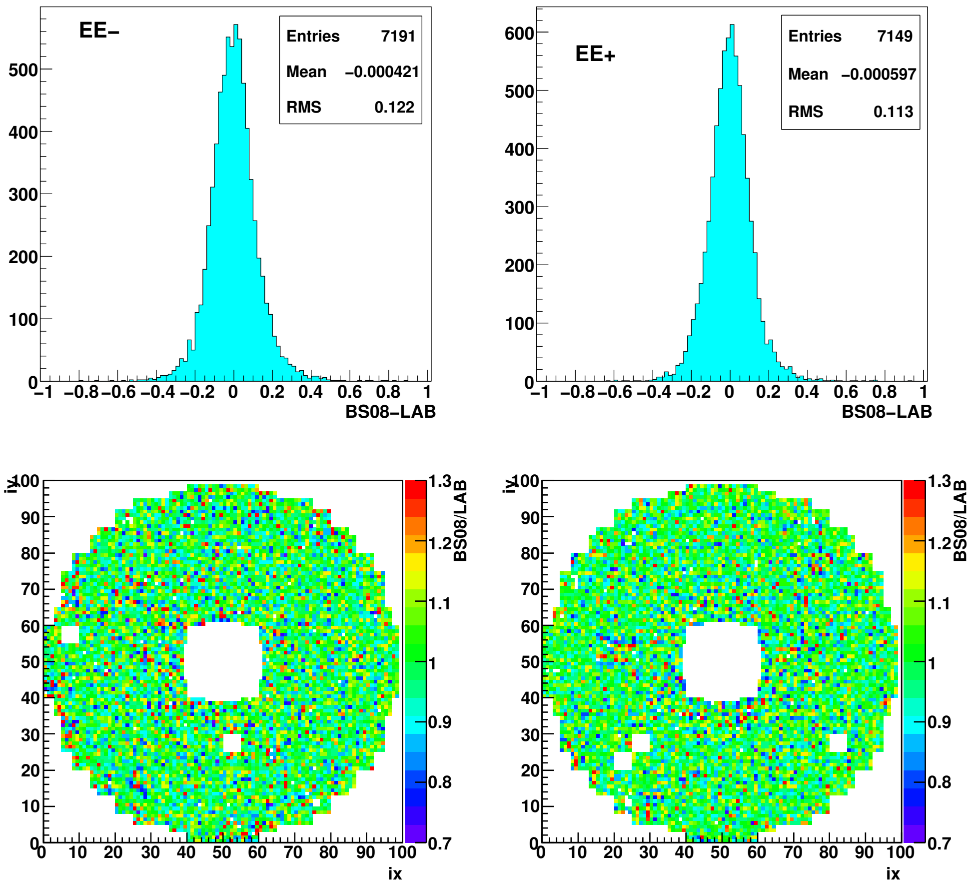

Figure 5.16.: Top: difference between the inter-calibration coefficients derived from 2008 splash events and the inter-calibration coefficients from laboratory measurements in EE-(left) and EE+(right). Bottom: map of the ratio between coefficients from beam splashes and laboratory measurements.

VALIDATION OF INTER-CALIBRATIONS FROM 2009 BEAM DUMP DATA (*preshower*)

The coefficients derived on BS09 data usisng the preshower are compared to coefficients from test beam with magnetic field corrections. The comparison is done for 329 crystals: only channels within $22 < R < 38$ for which the flux measurement from the preshower is reliable and both preshower planes were active have been considered. From this comparison, a precision of about 7% (RMS) is deduced for this method.

COMBINATION OF INTER-CALIBRATION COEFFICIENTS

Inter-calibration constants from the different sets have been combined, by means of a weighted average, deriving a final set of inter-calibration constants with improved

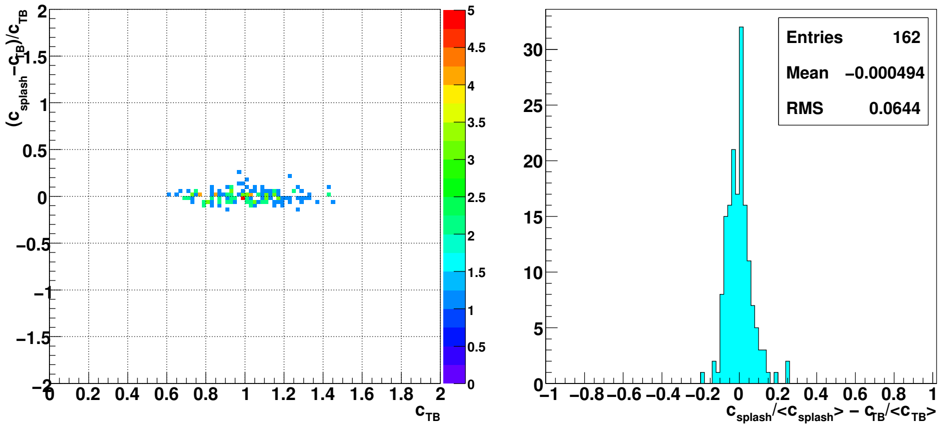

Figure 5.17.: Relative difference between the inter-calibration coefficients derived from 2009 splash events and the inter-calibration coefficients from test beam versus the inter-calibration coefficients from test beam (left). The agreement is about 6.4% (right).

precision.

For the encap region with $22 < R < 38$ where the estimation of the flux from the preshower is reliable, the combination is done using coefficients from all available measurements: laboratory, BS08 and BS09 data treated with the local uniformity method and BS09 with preshower. The resulting set has a precision of about 4.6%, estimated on the subsample of 162 reference crystals exposed to test beam (Fig. 5.20).

For all the other channels, the combination is performed using laboratory measurements and all beam dump data analysed with the local uniformity approach. The precision is still better than 5% as shown in figure 5.21, where the coefficient derived in this way are compared to test beam results on the same set of reference crystals. Figure 5.22 summarizes the final inter-calibration precision produced combining all the available pre-calibration sources (2007 test beam, laboratory measurements, 2008 and 2009 beam dump data). Different regions are visible: in blue the region where test beam measurements are available, in light blue the region corresponding to the combination of laboratory and all beam dump data, in green from the combination of laboratory measurements and beam dump data analyzed using the local uniformity technique, and in red regions where only laboratory data are available.

In summary the inter-calibration precision at startup was better than about 5% in the entire endcaps. This figure has been improved in 2011 to about 3% using di-photon resonances. Although this is not the ultimate precision, it is more than sufficient for

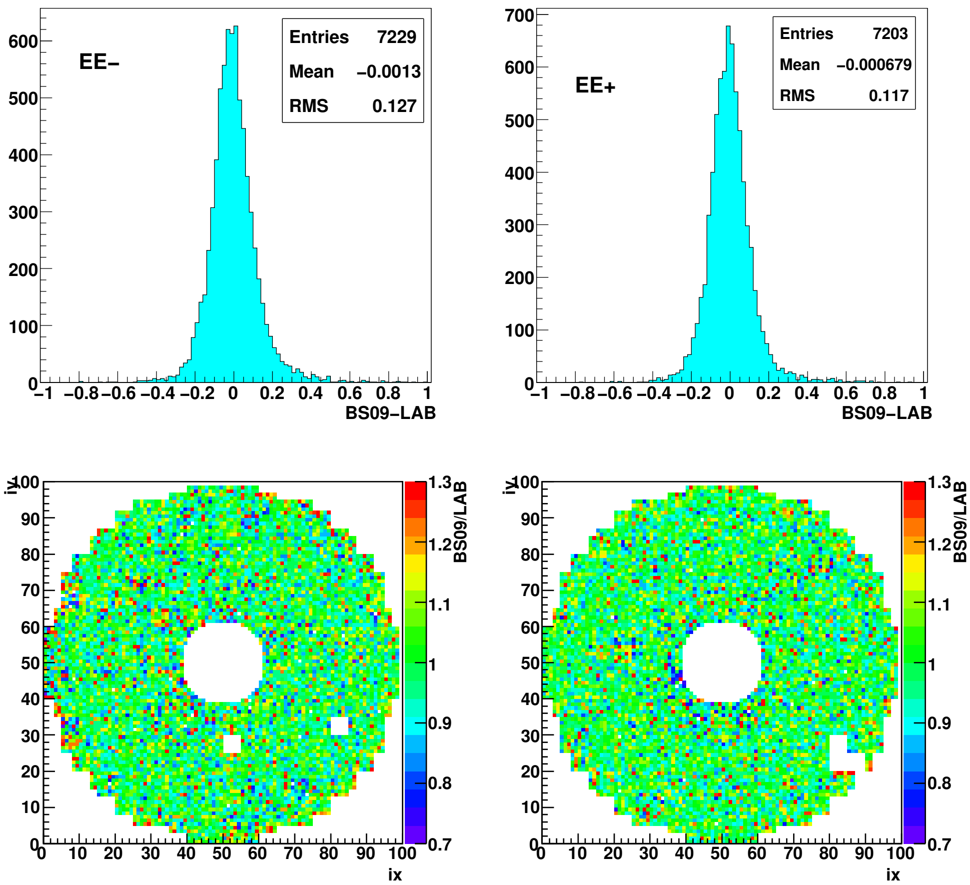

Figure 5.18.: Top: difference between the inter-calibration coefficients derived from 2009 splash events and the inter-calibration coefficients from laboratory measurements in EE-(left) and EE+(right). Bottom: map of the ratio between coefficients from beam splashes and laboratory measurements.

the purposes of the research discussed in this thesis.

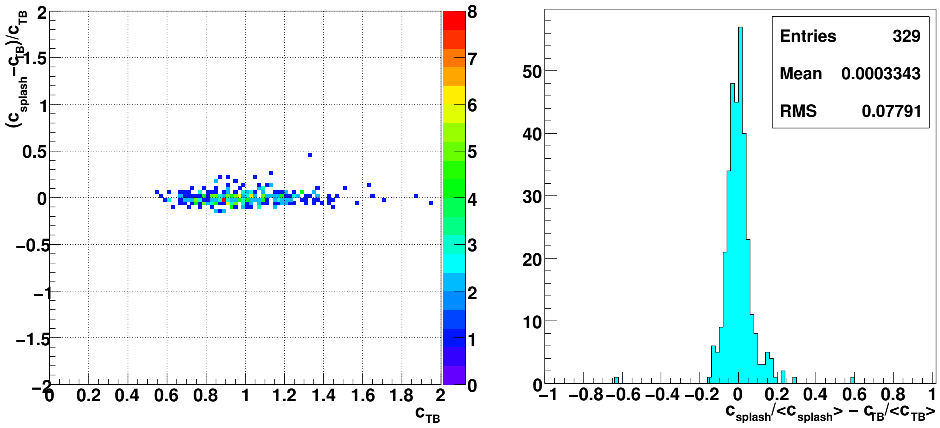

Figure 5.19.: Relative difference between the inter-calibration coefficients derived from 2009 splash events using the preshower estimation of the energy flux and the inter-calibration coefficients from test beam versus the inter-calibration coefficients from test beam (left). The agreement is at the 7% (RMS) level (right).

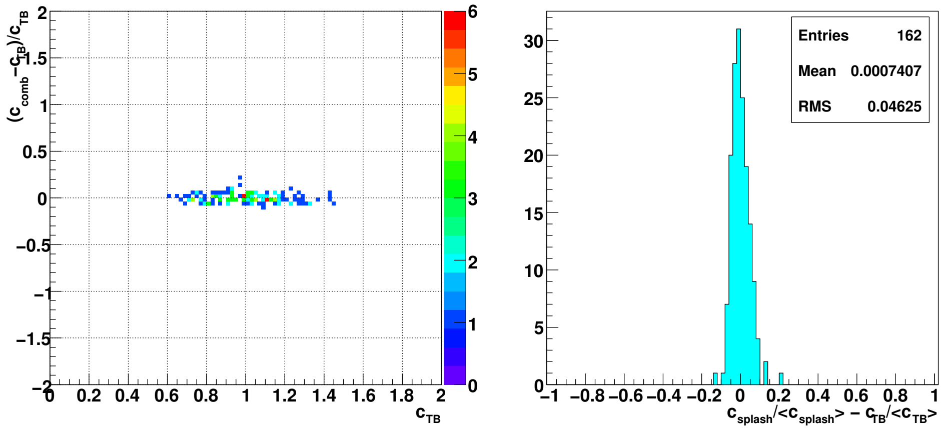

Figure 5.20.: Relative difference between the inter-calibration coefficients derived from the combination of all available measurements (laboratory, 2008 and 2009 beam dump data) and the inter-calibration coefficients from test beam versus the inter-calibration coefficients from test beam (left). The agreement is about 4.6% (right).

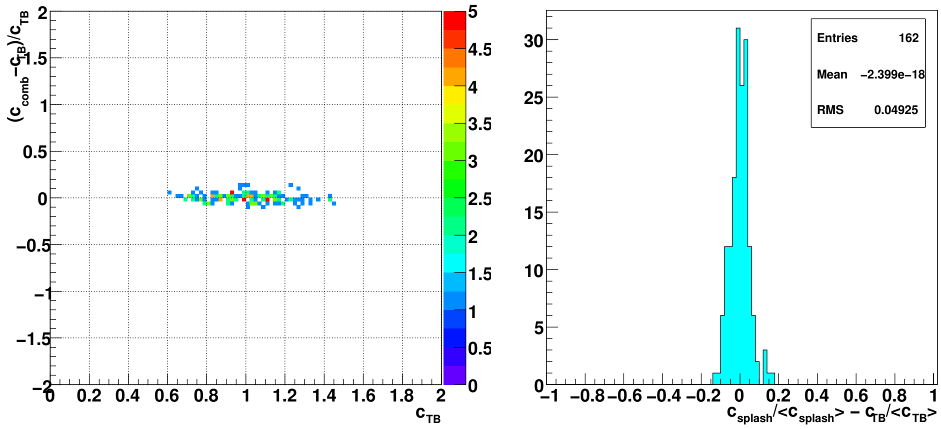

Figure 5.21.: Relative difference between the inter-calibration coefficients derived from the combination of all available measurements (laboratory, 2008 and 2009 beam dump data) and the inter-calibration coefficients from test beam versus the inter-calibration coefficients from test beam (left). The agreement is about 5% (right).

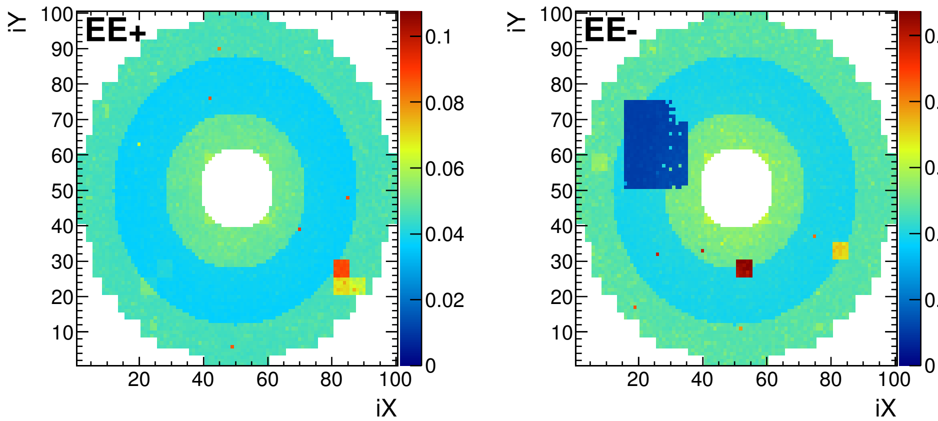

Figure 5.22.: Map of inter-calibration precision for EE+ (left) and EE-(right) produced combining all the pre-calibration sources.

5.4 Stability of the ECAL performance

Besides the precision of the inter-calibration, also the monitoring of the working conditions of the ECAL plays a fundamental role in the final calorimeter performance. The energy resolution of the ECAL (equation 3.2), which is a direct measurement of the calorimeter performances, is indeed sensitive to the calorimeter design (see section 3.2.2), the inter-calibration precision and the stability of the operating conditions. Among the different contributions to the latter are the temperature stability of the crystals and photodetectors and the crystal transparency, which can decrease with radiation.

The temperature stability over two months has been measured to be about $0.008°C$ and $0.015°C$ for the Barrel and the Endcaps respectively [71]. These values are well within specifications, which allow for maximum variations of $0.05°C$ in the Barrel and $0.1°C$ in the Endcaps.

During LHC cycles, the ECAL response varies depending on irradiation conditions, which modify the transparency of each individual $PbWO_4$ crystal depending on its radiation hardness. The radiation damage, related to colour center creation, during LHC fills is recovered during interfills and technical stops. These effects take place on a time scale of hours and cause transparency changes of a few percent in the ECAL barrel. In the ECAL endcap at large $|\eta|$, where the dose rate is considerably higher, the observed loss is on the average 10%, but has reached 30% at $|\eta| \sim 2.5$, the most forward electron acceptance in CMS. The transparency changes are monitored every 40 minutes by means of laser light injected into each crystal through optical fibres. The capability of this system to correct for transparency changes was proved with test beam data on a small set of crystals.

5.4.1 Monitoring with isolated electrons

The ratio of the super-cluster energy of an electron measured by ECAL to the momentum measured in the tracker has been exploited to monitor the stability and uniformity of the ECAL response. The analysis gives an unbiased answer on the electron energy measurement, if the measurement of the electron momentum is stable.
In this analysis the electron objects are exploited as instruments to monitor the stability of the ECAL performance. The efficiency of the electron reconstruction and identification process is not of primary importance here. For this reason the detailed description of the electron reconstruction and selection criteria are described in chapter 6 in the context of the W′ analysis.
A low threshold trigger on isolated electrons was not viable at the luminosities achieved

in 2011, as the rate due to the contamination of hadrons misidentified as electrons was too high. To keep the trigger rate at an acceptable level, and still select low p_{T} electrons from $W \to e\nu$ decays, a cross trigger strategy has been adopted. The presence of one isolated electron and $E_{\mathrm{T}}^{\mathrm{miss}}$ can be used to reduce the rate without affecting the trigger efficiency on signal events. This cross trigger ele+M_{T} has been developed and used also in the W$'$ analysis and it is presented in detail in section 6.3.

As we are interested in relative variations of the response rather than in the absolute response – fixed in ECAL via the invariant mass of $Z \to e^{+}e^{-}$ – the analysis strategy relies on the construction of a reference distribution (often referred to as 'template') describing the E/p observable at a given time, or position. This distibution is then scaled to best-fit to subsets of data, properly partitioned in time or position, to measure the relative response in each subset. The reference distribution has been in general sampled from the data themselves, to avoid intriducing biases related to an impefect description of the data by MC.
The generic fit function adopted in the analysis is defined as:

$$f(x;k) = kh(kx) * G(0,N,\sigma); \tag{5.10}$$

where $x = E/p$, k is a scaling factor linked to the energy scale by $s = 1/k$; $h(x)$ is a reference distribution of unit area, and $G(0,\sigma)$ is a Gauss distribution centered in zero, of width σ and integral N convoluted with the reference distribution. The parameter k is left floating in the fits, while normalization N is fixed to the integral of the events in the dataset. The gaussian term allows the function to describe distributions with different resolutions than the reference distribution. This is useful when MC samples are used to fit data, or when data in regions where electrons are poorly reconstructed (for example intermodule cracks) are analyzed. In general, however, we have collapsed the function at (5.10) to a Dirac's delta.
The shape of the E/p distribution can vary with varying datasets and selections. It is thus important that reference distribution is built using a consistent set of selection, and that its shape is representative of the whole set of sub-samples being analysed. The analysis has been typically split in ECAL barrel and ECAL endcap, as the energy and the momentum resolution are noticeably different in the two regions. Examples of inclusive E/p distributions in the ECAL barrel and endcap fitted to sub-sets of data are shown in figure 5.23.
The result of the stability monitoring in time is shown in figure 5.24 where the E/p ratio for the electron candidates is reported as a function of the event timestamp. The electrons are selected from $W \to e\nu$ decays and error bars on the x-axis show the time span over which events have been accumulated. The history plots are shown before (red

dots) and after (green dots) corrections to ECAL crystal energy due to transparency loss are applied. For each dot a number of electrons of the order of 10 thousands for the barrel and 5 thousands for the endcaps close in time is used to build and fit the E/p distribution at a given instant. The plots show that, despite the loss of transparency is significant both in the barrel and in the endcaps, the energy response is under control at the level of 0.14% in EB and 0.88% in EE which is better than what is required to maintain the constant term in the ECAL energy resolution at the level of 0.5%.

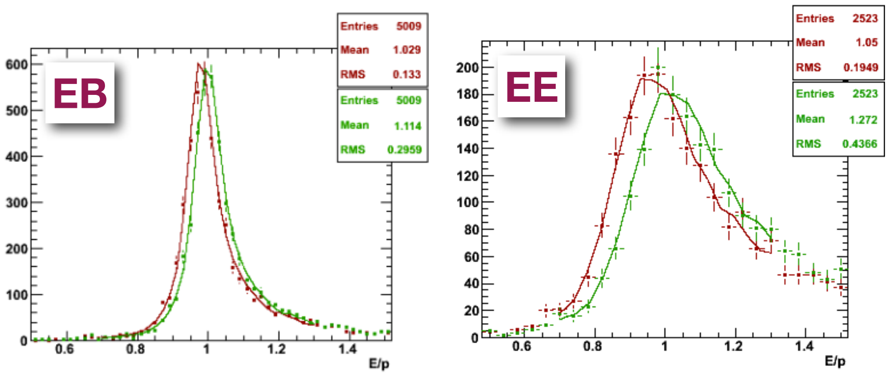

Figure 5.23.: Examples of E/p distributions in ECAL barrel (left) and ECAL endcap (right) with the best-fit reference distribution superimposed (line). In this examples, the reference distribution was sampled from a calibrated set of data and fitted to a subset of the same data before calibration (red) and after calibration (green).

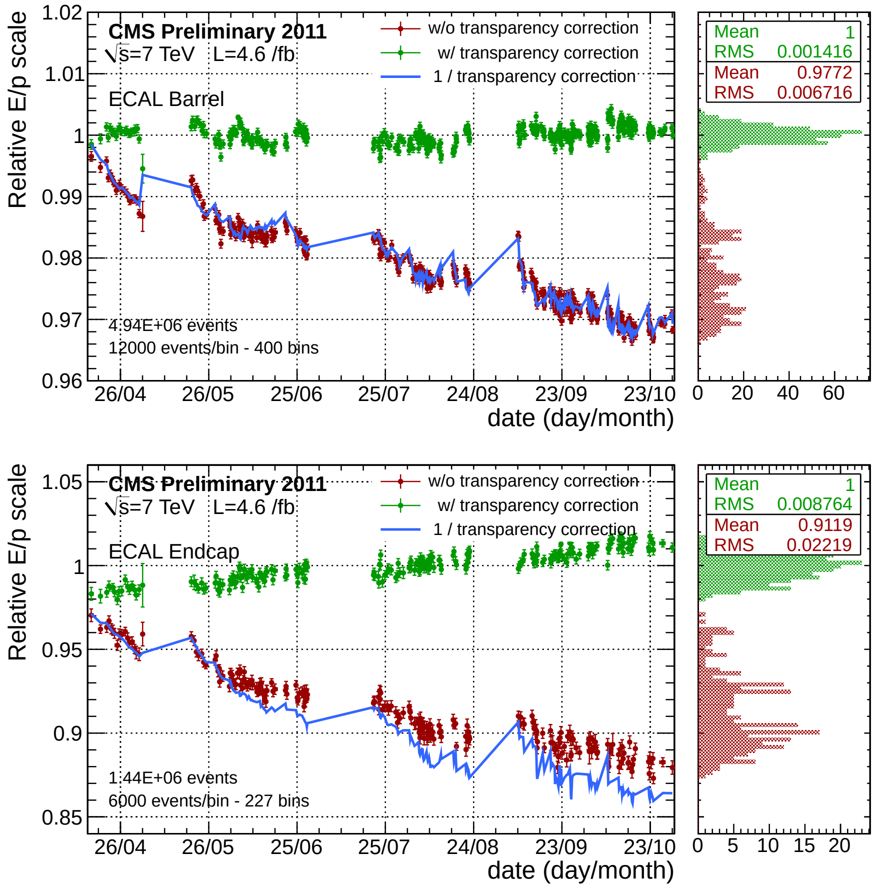

Figure 5.24.: E/p history for electrons reconstructed in the ECAL barrel (top) and ECAL endcap (bottom) during the 2011 run. Uncorrected data (red dots), data corrected for the observed transparency loss (green dots) and the inverse of the correcton derived from monitoring data (blue line) are displayed.

CHAPTER 6

OBJECT RECONSTRUCTION AND HIGH LEVEL TRIGGER

In the following chapter the electron reconstruction and the missing transverse energy reconstruction (related to the presence of a neutrino in the final state) are treated. Moreover the discussion about the developing of a combined High Level Trigger path which involves electron and $E_{\mathrm{T}}^{\mathrm{miss}}$ at trigger level, is presented.

6.1 ELECTRONS IN CMS

From the detector point of view to detect and identify an electron, two main subdetectors are needed: the tracker for the momentum measurement and the charge assignment and the electromagnetic calorimeter for the energy measurement. Electrons are then reconstructed as energy deposits in the electromagnetic calorimeter linked to a track in the tracker. The goal of the electron reconstruction algorithms is to combine all the information in order to assess the characteristics of each electron candidate. The electron reconstruction in CMS occurs through several steps: the electron clustering, the track reconstruction and the cluster-track matching. The objects reconstruction is part of the standard CMSSW reconstruction sequence which combines and elaborates the RAW information event by event to make available a list of high level particle ready for the analysis. The quality selections, often called electron identification and isolation selections, may vary analysis by analysis depending on the characteristics of the final state under study and are applied offline to the reconstructed candidate. The goal of the quality requirements is to reduce the contamination from fake electrons, mainly from the QCD multi-jet background, in the final collection of electron candidates. Even if the probability for a jet to fake an electron is fairly low (2-3%), the contamination from

QCD background needs to be taken into account due to its large cross section.

6.1.1 Electron reconstruction

Electron clustering

For a single electron (or photon) reaching the ECAL, most of the energy is collected in a small number of crystals. At the test beam [72], for a supermodule of the ECAL barrel, electrons with an energy of 120 GeV impinging at the centre of a crystal for instance deposit about 97% of their incident energy in a 5×5 crystal window.
The pattern is in general more complicated for the average electron. Electrons traversing the tracker material radiate photons and, due to the magnetic field, the energy reaches the ECAL after spraying along the ϕ direction. Integrated along the electron trajectory the effect can be very large. To obtain a measurement of the electron energy at the primary vertex and minimize the energy containment variations, it is essential to collect bremsstrahlung photons. This is the purpose of the super-clustering algorithms. Two different clustering algorithms have been designed for the barrel and endcap region, due to the different mechanical layout of the two sections. The algorithm used in the barrel region is called Hybrid clustering algorithm and exploits the $\eta - \phi$ geometry of this part of the detector. For the endcap region, a different algorithm, called $Multi - 5 \times 5$ clustering algorithm is used, which employs 5×5 crystal matrices to gather energy deposits. The Hybrid algorithm can be summarised in the following list of steps [73, 74]:

- At each step, all crystals not already belonging to a cluster are tested in decreasing energy order. To avoid noise contamination and low energy backgrounds, the crystal transverse energy E_{T} is required to be above a minimum threshold $E_T^{seedthr}$. If $E_{\mathrm{T}} > E_T^{seedthr}$ the crystal can seed the clustering process. Otherwise the next crystal is examined.
- A 5×1 domino of crystals in $\eta - \phi$ direction around the seed crystal is built.
- The second step is repeated for all crystals with the same η as the seed one that satisfy $|\phi_{crystal} - \phi_{seed}| < \Delta\phi$ road (search road). The domino is included in the cluster if $E_{domino} > E_{domthr}$.
- The dominoes with $E_{domino} > E_{domthr}$ that were not aggregated to the main clusters are then searched for local energy maxima and secondary clusters are formed around maxima where the highest crystal energy is above a second threshold E_{locthr}.
- The algorithm continues until all crystals have been examined. The result of the procedure are super-clusters made up by several showers at constant η but

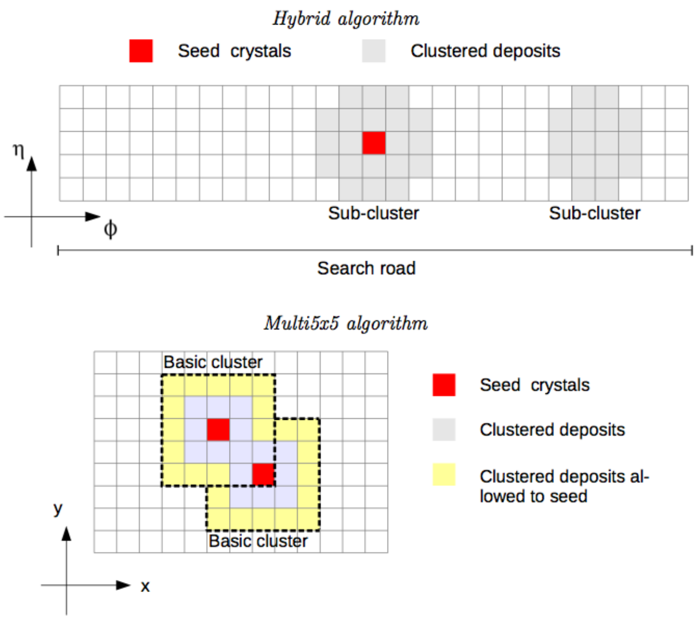

Figure 6.1.: Illustration of the clustering algorithms used in the barrel (top) and endcap (bottom) regions.

spread in the ϕ-direction, like in the example reported figure 6.1.

The $Multi-5\times5$ algorithm proceeds as follows:

· At each step unclustered crystals are examined in decreasing transverse energy order. If the transverse energy $E_{\mathrm{T}} > E_T^{seedthr}$, the crystal can seed the clustering process. Otherwise, the next crystal is examined.

· The crystal is tested for being a local maximum by comparing its energy to its four neighbors by side in a Swiss Cross pattern. If the crystal is not a local maximum, the algorithms goes back to the first step.

· A basic cluster is created including crystals in the 5×5 window around the seed that not already assigned to other basic clusters.

· The algorithms continues until all crystals have been examined.

To recover the energy of secondary showers, a rectangular window along η and ϕ is opened around basic clusters with transverse energy above a threshold E_{bcthr}. Other basic-clusters falling within the window are added to form the super-cluster. All basic clusters are examined in descending transverse energy order, with the constraint that

each basic cluster can be assigned to only one super-cluster. In the region covered by the preshower detector, the energy detected in the latter is added to the super-cluster energy. The association is performed extrapolating the super-cluster position towards the interaction point. Figure 6.1 shows, schematically, examples of super-clusters resulting from the two clustering algorithms. The parameters of the algorithms that were used in the reconstruction software for this thesis are reported in table 6.1.
Regardless of the algorithm, the SC position is estimated through a weighted average of the position of all the crystals, where each crystal enters with a weight $w_i = max(0, 4.7 + log(E_i/E_{SC}))$.

Hybrid algorithm (*Barrel*)		Multi5x5 algorithm (*Endcap*)	
$E_T^{seedthr}$	1 GeV	$E_T^{seedthr}$	180 MeV
E_{domthr}	350 MeV	E^{bcthr}	1 GeV
E_{locthr}	100 MeV		
$\Delta\phi_{road}$	17 crystals	$\Delta\phi_{road}$	0.14
		$\Delta\eta_{road}$	0.6

Table 6.1.: Parameters of the clustering algorithms as used in this thesis.

ENERGY CORRECTIONS

Once the super-cluster is built, an object dependent correction factor, tuned on the Monte Carlo and adjusted with data, is applied. The goal is to correct the energy of the cluster by taking into account geometry and material effects. The effectiveness of the correction is verified by looking at the width of the Z invariant mass peak. Recalling equation 5.1, the energy of the electron/photon candidate can be factorized as follows:

$$E_{e,\gamma} = F_{e,\gamma}(E_{\mathrm{T}}, \eta) \cdot \sum_i G(ADC/\,\mathrm{GeV}) \times S_i(T,t) \times c_i \times A_i \tag{6.1}$$

where the super-cluster corrections are included in $F_{e,\gamma}(E_{\mathrm{T}}, \eta)$.
Three types of effect are taken into account in this term:

- Variations of the shower containment as a function of the position in the detector are parametrised by a function labelled $C_{EB}(\eta)$. Such an effect is important only in the barrel region, where the non-uniformities in the lateral shower leakage due to the off-pointing geometry of the crystals need to be corrected. This correction is obtained from MC simulations and has been found to be in good agreement with test-beam data. Overall, the C_{EB} correction is $\leq$ 1% [55];

- Variations in the algorithm response to different super-cluster topologies are corrected through a function called $f(brem)$. The brem variable is defined as:

$$brem = \frac{\sqrt{\Sigma(\eta_i - \bar{\eta})^2 c_i A_i}}{\sqrt{\Sigma(\phi_i - \bar{\phi})^2 c_i A_i}} \tag{6.2}$$

where the sum runs over all crystals in the super-cluster and $\bar{\eta}, \bar{\phi}$ refers to the super-cluster position. This function is insensitive, within certain limits, to the amount of material in front of the calorimeter and can be obtained from MC simulations. The size of the $f(brem)$ term is $< 7\%$ in the barrel region and $\leq 20\%$ in the endcap region.

· Residual variations due to the non-uniform distribution of material in the detector and the energy dependence of the energy collection efficiency are corrected through a function $f(E_{\mathrm{T}}, \eta)$. Since this function depends on the details of the material distribution in the detector its determination has to be performed in-situ. In the case of electrons, $f(E_{\mathrm{T}}, \eta)$ can be measured using $Z \to ee$ events. Differences between electrons and photons are expected to be small and can be modelled using MC simulation, until a sufficient sample of prompt high energy photons is accumulated using events with associated $Z\gamma$ production.

TRACK RECONSTRUCTION

The track reconstruction procedure in CMS is the result of several seps. Firstly a seed is created whenever two hits compatible with a given beam spot are found in the pixel detector then, starting from the seed, a trajectory is created. Compatible hits on the next silicon layers are searched for and an extrapolation is performed using a Bethe Heitler modeling of the electron losses and a Gaussian Sum Filter (GSF) in the forward fit [75]. This procedure is iterated until the last tracker layer, unless no hit is found in two subsequent layers. A minimum of five hits is finally required to create a track.

When using the GSF to fit the track, the knowledge of the track momentum at the outermost state gives the possibility of estimating from the track fit the fraction of energy lost by bremsstrahlung. The difference between the magnitude of the momentum at the vertex and at the layer of the outermost hit is a measurement of the integral amount of bremsstrahlung and it is used in the definition of electron classes. The total amount of bremsstrahlung could be defined as follows:

$$f_{brem} = (p_{in} - p_{out})/p_{in} \tag{6.3}$$

THE HIGH-LEVEL ELECTRON OBJECT

Once the clustering and tracking sequence are completed the following steps are performed in order to build and characterize the list of electron candidates in the event:

- the electron candidates are preselected by requiring a loose track-cluster geometrical matching so to preserve the highest possible efficiency while removing part of the QCD background;
- a cleaning is performed to resolve cases where several tracks are reconstructed from the conversion legs of radiated photons;
- the electron charge is determined by comparing different charge measurement observables to better cope with the mis-identification that arises from early conversions of radiated photons;
- electrons are classified using observables sensitive to the pattern of bremsstrahlung emission and showering in the tracker material. The classes are: "golden", or electrons with small bremsstrahlung emission with a reconstructed track well matching the supercluster; "big brem", or electrons with high bremsstrahlung fraction but no evidence of energy loss effects; "showering", or electrons with an energy pattern highly affected by bremsstrahlung losses;
- the electron energy E_{ele} is deduced from a combination of the supercluster energy and tracker momentum measurements based on the electron classes. The electron direction is that of the reconstructed electron track at the interaction point.

6.1.2 ELECTRON IDENTIFICATION AND ISOLATION

For the identification of the electrons, dedicated sets of selections have been designed to ensure high efficiency for genuine electrons and a high rejection of fake electrons. The performance of the electron identification depends on the nature of the considered background. The tuning of the parameters is based on criteria such as the identification efficiency and purity for electrons from the signal sample and it is usually performed by running over the Monte Carlo. Details of the selections and arguments for their optimization are described in [76].
For the W$'$ analysis the so called Working Point 80 (WP80), tuned to have an efficiency around 80% over electrons from a pure sample of W, has been chosen. The main reason of this choice is related to the characteristics of the High Level Trigger path used in the analysis. A detailed description of the selections at HLT level and their tuning are discussed in section 6.3.

The energy deposition and the shower shape in the calorimeters are required to be consistent to the characteristics of an electron. An isolation criterion is also applied, as electrons from the W decay are expected to be well isolated from possible hadron deposits in the event. This is accomplished through the set of selections reported in table 6.2. The distributions of the same electron identification and isolation variables are collected in figure 6.2 for the electron with highest p_{T} in the event. The genuine electrons from W MC candidates are showed in red, the fakes from multi-jet MC background are in blue. Only electron candidates with $E_{\mathrm{T}} > 30$ GeV and with $|\eta| < 1.5$ (ECAL barrel) are considered.

These variables, relying on the differences between the energy deposit from a genuine electron and from a jet, are expected to be effective in the rejection of the fake electrons and are defined as follows:

Quantity	WP80 EB	WP80 EE
E_{T}	35 GeV	35 GeV
η_{SC}	$\|\eta\| < 1.442$	$1.560 < \|\eta\| < 2.5$
$\Delta\eta_{in}$	0.004	0.007
$\Delta\phi_{in}$	0.06	0.03
$\sigma_{i\eta i\eta}$	0.01	0.03
H/E	0.04	0.025
Relative Track Iso	0.09	0.04
Relative ECAL Iso	0.07	0.05
Relative HCAL Iso	0.1	0.025

Table 6.2.: List of the electron identification and isolation selections for the WP80 working point.

- E_T: Defined as the $E_{ele} \times \sin\theta_{trk}$ where θ_{trk} is the polar angle of the electron track measured at the inner tracker layer and then extrapolated to the interaction vertex.

- η_{SC}: Defined as the pseudo rapidity of the electron's supercluster. Note this is with respect to the point $(0,0,0)$ and not with respect to the position of the actual collision vertex where the electron originates from. Thus its use is for fiducial cuts due to detector acceptance and should not be used to calculate four-momenta in physics results such as mass calculations.

- η: Defined as the pseudo rapidity of the electrons track as measured at the inner layer of the tracker and then extrapolated to the interaction vertex. This should be used for calculating the electrons four-momentum and for all physics results, but it is not used for detector fiducial cuts.

- $\Delta\eta_{in}$ and $\Delta\phi_{in}$: The difference in η and ϕ between the track position as measured in the inner layer tracker, extrapolated to the interaction vertex and then extrapolated to the calorimeter and the η and ϕ of the super-cluster.

- H/E: The ratio of the hadronic energy of all the HCAL Rec Hits in a cone of radius $\Delta R = \sqrt{\Delta\eta^2 + \Delta\phi^2} = 0.1$ centered on the electron position in the calorimeter to the electromagnetic energy of the electron super-cluster. This is expected to be close to zero for genuine electrons.

- $\sigma_{i\eta i\eta}$: A measure of the spread in η in units of crystals of the electrons energy in the 5x5 block centred on the seed crystal. This variable is expected to be broader for candidates from the QCD background (typically π^0 with an associated track) with respect to the case of genuine electrons.

- ECAL Isolation: It is defined as the transverse EM energy of all the rec-hits with $|E| > 0.08$ GeV in the ECAL barrel ($|E| > 0.1$ GeV in the ECAL endcap) in a cone of 0.3 radius centered on the electron's position in the calorimeter excluding those in an inner cone of radius 3 crystals and η stripe of total width of 3 crystals.

- Hadronic Depth Isolation: It is defined as the transverse depth hadronic energy of all the HCAL CaloTowers in a cone of 0.3 radius centred on the electron's position in the calorimeter, excluding CaloTowers in a cone of 0.15 radius. Different depths are defined for the barrel towers 1-17 (no depth segmentation), the forward ones 18-29 and the very forward towers 27-29 (see also Fig.5.1 in Ref.[72]). Exploiting the segmented depth in the forward towers gives better performance at high E_{T}.

- Track Isolation: It is defined as the sum p_{T} of the CTF tracks in a ΔR cone of 0.04 - 0.3 with $p_{\mathrm{T}} > 0.7$ GeV/c and z0 with ± 0.2 of the z0 of the electrons GsfTrack. The variable z0 is minimum distance in z from the point (0, 0, 0).

- Relative Isolation: Defined as the ECAL Isolation or the HCAL Isolation or the Track Isolation divided by the E_{T} of the electron candidate.

In the context of the searches with high-p_{T} electrons in the final state, the electron-ID and isolation selections have to be efficient in the p_{T} region above 150 GeV and have

to guarantee a low rate of jets faking electrons in the same p_{T} range.
The energy resolution improves with the energy according to the formula 3.2 and the momentum resolution gets worse with the momentum. As a general criterion, the electron-ID variables are chosen to exploit the energy measurement in the calorimeters without involving the track momentum which is not reliable for high-p_{T}. The tracking information is only used to calculate the electron direction and it does not affect the estimate of the energy of the candidate.
The measurement of the efficiency of the reconstruction and the identification step is usually performed using data with a tag-and-probe technique with Z bosons [77, 78]. The results are presented in section 6.4 together with the efficiency measurement for the High Level Trigger paths used in the analysis.

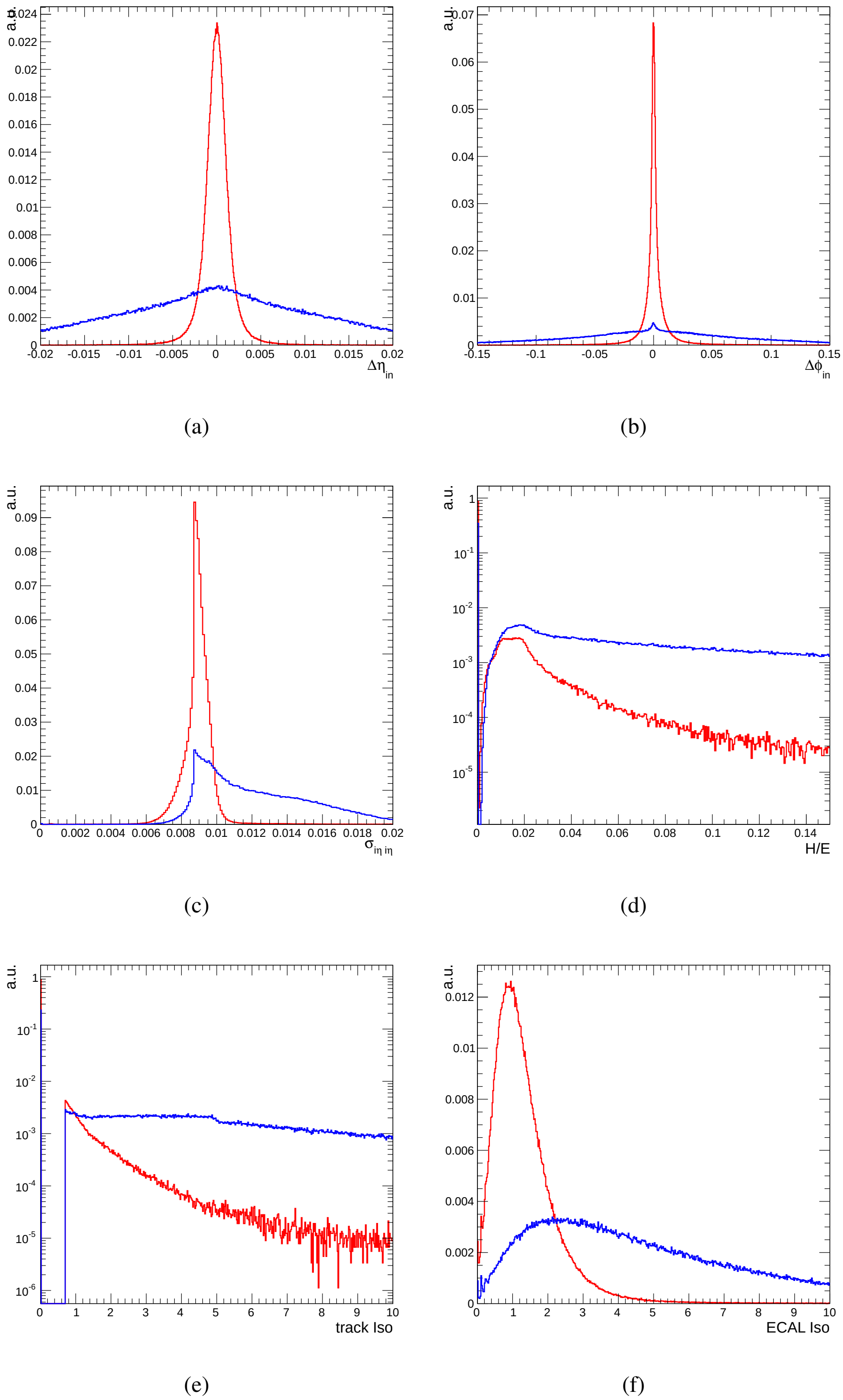

Figure 6.2.: The main ele-ID distributions for genuine electrons from W and fake electrons from a multi-jet sample are compared. Only electron candidates with $E_{\mathrm{T}} > 30$ GeV and with $|\eta| < 1.5$ are considered. (a) distribution of the $\Delta\eta_{in}$; (b) distribution of the $\Delta\phi_{in}$; (c) distribution of the $\sigma_{i\eta i\eta}$; (d) distribution of the H/E; (e) distribution of the track isolation; (f) distribution of the ECAL isolation.

6.2 $E_{\mathrm{T}}^{\mathrm{MISS}}$ DEFINITION

As described in the Introduction, we are interested in events with large missing transverse energy ($E_{\mathrm{T}}^{\mathrm{miss}}$). Currently, there are three algorithms that are used by the CMS experiment: calorimeter based $E_{\mathrm{T}}^{\mathrm{miss}}$ (calo$E_{\mathrm{T}}^{\mathrm{miss}}$), track-corrected calorimeter $E_{\mathrm{T}}^{\mathrm{miss}}$ (tc$E_{\mathrm{T}}^{\mathrm{miss}}$), and particle-flow $E_{\mathrm{T}}^{\mathrm{miss}}$ (pf$E_{\mathrm{T}}^{\mathrm{miss}}$).

Calo$E_{\mathrm{T}}^{\mathrm{miss}}$ [79] is the negative vector sum of the transverse energy deposited in calorimeter towers that are above the noise threshold. On top of this, one can employ corrections (designated as type-I) to account for clustered energy and muon deposits. Muons will deposit a small fraction of their energy (~ 2 GeV) in the calorimeters. The muon correction removes the muon p_{T} and adds back the energy deposition. In order to incorporate the nonlinear and non-compensating behavior of the hadron calorimeter, the jet energy corrections are propagated to calo$E_{\mathrm{T}}^{\mathrm{miss}}$. Finally other correction (designated as type-II) correct all unclustered towers (jets) for this nonlinearity.

$$E_{\mathrm{T}}^{\mathrm{miss}} = -\sum_{CaloTowers} \vec{E}_{\mathrm{T}} - \sum_{muons} \vec{p}_{\mathrm{T}}{}^{\mu} + \sum_{muons} \vec{E}_{\mathrm{T}}{}^{\mu} \tag{6.4}$$

The track-corrected $E_{\mathrm{T}}^{\mathrm{miss}}$ algorithm [80] starts from calo$E_{\mathrm{T}}^{\mathrm{miss}}$. From there, tracking information is incorporated by adding the p_{T} of reconstructed tracks and subtracting the expected calorimetric energy deposited by that track. For this, tracks are treated as pions, and the expected energy deposit is determined from MC. Tracks with $p_{\mathrm{T}} < 2$ GeV (they deposit no energy in the calorimeters) or $p_{\mathrm{T}} > 100$ GeV (their energy is well measured by the electromagnetic calorimeter) are not included in this correction.

$$E_{\mathrm{T}}^{\mathrm{miss}} = -\sum_{CaloTowers} \vec{E}_{\mathrm{T}} - \sum_{muons} \vec{p}_{\mathrm{T}}{}^{\mu} + \sum_{muons} \vec{E}_{\mathrm{T}}{}^{\mu} - \sum_{goodTracks} \vec{p}_{\mathrm{T}}{}^{track} + \sum_{goodTracks} \vec{E}_{\mathrm{T}}{}^{track} \tag{6.5}$$

The particle-flow technique [81] aims at reconstructing a complete, unique list of particles in each event using the entire CMS detector: muons, electrons, photons, and charged and neutral hadrons. The pf$E_{\mathrm{T}}^{\mathrm{miss}}$ is the negative vector sum of all reconstructed particles in the event. Type-I corrections to pf$E_{\mathrm{T}}^{\mathrm{miss}}$ to propagate particle-flow jet energy corrections to $E_{\mathrm{T}}^{\mathrm{miss}}$ are currently being investigated, but they will not be used for this analysis.

$$E_{\mathrm{T}}^{\mathrm{miss}} = -\sum_{PF-particles} \vec{p}_{\mathrm{T}} \tag{6.6}$$

In order to compare the different $E_{\mathrm{T}}^{\mathrm{miss}}$ algorithms for our selection, we investigated the $E_{\mathrm{T}}^{\mathrm{miss}}$ distributions and the differences between $E_{\mathrm{T}}^{\mathrm{miss}}$ algorithms in events dominated by real $E_{\mathrm{T}}^{\mathrm{miss}}$ (e.g. $W \to e\nu$ events). Figure 6.3 shows the $E_{\mathrm{T}}^{\mathrm{miss}}$ distributions for the three different algorithms. Notice that the three $E_{\mathrm{T}}^{\mathrm{miss}}$ algorithms have a qualitatively similar behavior for large values of missing transverse energy, but they display different behaviors for small values of missing transverse energy. The Monte Carlo simulation predicts that calorimeter $E_{\mathrm{T}}^{\mathrm{miss}}$ has a much larger contribution from the multi-jet and γ+jets background than the other $E_{\mathrm{T}}^{\mathrm{miss}}$ algorithms. Figure 6.4 shows the differences between the three $E_{\mathrm{T}}^{\mathrm{miss}}$ algorithms for two different selections: requiring events have one WP80 electron (dominated by multi-jet background), and requiring events have one WP80 electron and $0.4 < E_T^{ele}/E_{\mathrm{T}}^{\mathrm{miss}} < 1.5$ (dominated by $W \to e\nu$). On average, calorimeter $E_{\mathrm{T}}^{\mathrm{miss}}$ is larger than either track-corrected or particle-flow $E_{\mathrm{T}}^{\mathrm{miss}}$ in a selection dominated by multi-jet events. In particular the pf$E_{\mathrm{T}}^{\mathrm{miss}}$ and tc$E_{\mathrm{T}}^{\mathrm{miss}}$ have similar performances: the distribution of pf$E_{\mathrm{T}}^{\mathrm{miss}}$- tc$E_{\mathrm{T}}^{\mathrm{miss}}$ is well described by a Gaussian distribution with a mean of 1.1 GeV and a sigma of 3.7 GeV. In addition, there are only a handful of events where the difference between the two algorithms is greater than 20 GeV.

CMS has studied the performance of these different types of $E_{\mathrm{T}}^{\mathrm{miss}}$ in events containing electroweak bosons [82]. Good agreement has been observed between data and Monte Carlo simulation for each of the three $E_{\mathrm{T}}^{\mathrm{miss}}$ algorithms. However, it was noted that the inclusion of charged-particle tracking (e.g. for pf$E_{\mathrm{T}}^{\mathrm{miss}}$ and tc$E_{\mathrm{T}}^{\mathrm{miss}}$) significantly improves the $E_{\mathrm{T}}^{\mathrm{miss}}$ resolution, especially in events with genuine $E_{\mathrm{T}}^{\mathrm{miss}}$ (as is the case for $W \to e\nu$ events). In order to use the $E_{\mathrm{T}}^{\mathrm{miss}}$ with the best resolution the particle-flow $E_{\mathrm{T}}^{\mathrm{miss}}$ is chosen for this analysis. The same choice was made in CMS for the analysis of the $\mathrm{W}' \to \mu\nu$ search.

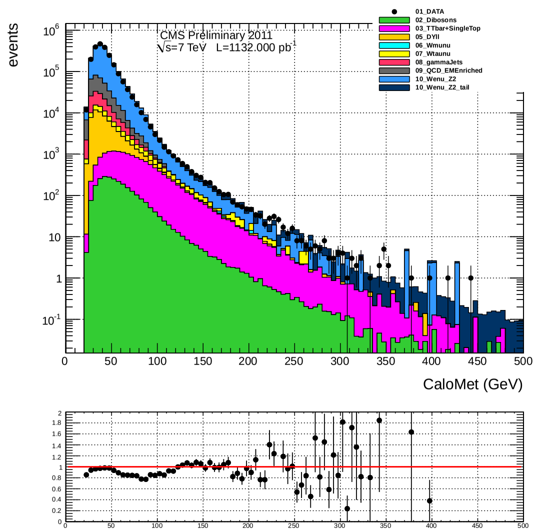

(a)

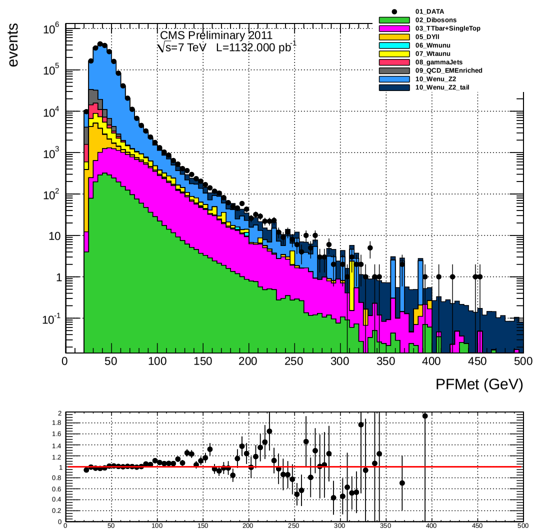

(b)

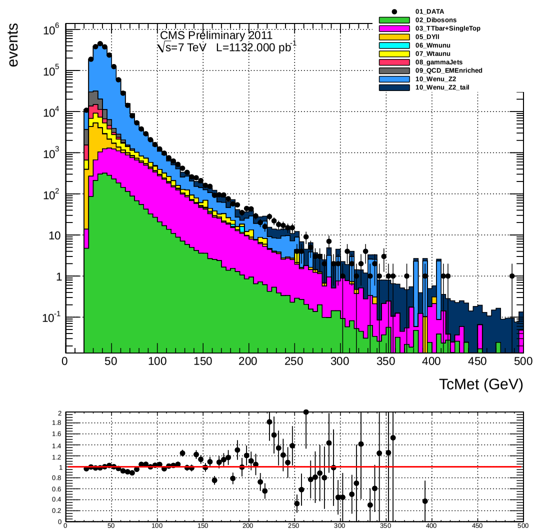

(c)

Figure 6.3.: Distribution of $E_{\mathrm{T}}^{\mathrm{miss}}$ as reconstructed by the three different algorithms discussed in the text. Events are selected by requiring one WP80 electron, $E_{\mathrm{T}}^{\mathrm{miss}} > 20$ GeV, and $0.4 < E_T^{ele}/E_{\mathrm{T}}^{\mathrm{miss}} < 1.5$. Left: Calorimeter $E_{\mathrm{T}}^{\mathrm{miss}}$. Center: Particle-flow $E_{\mathrm{T}}^{\mathrm{miss}}$. Right: Track-corrected $E_{\mathrm{T}}^{\mathrm{miss}}$.

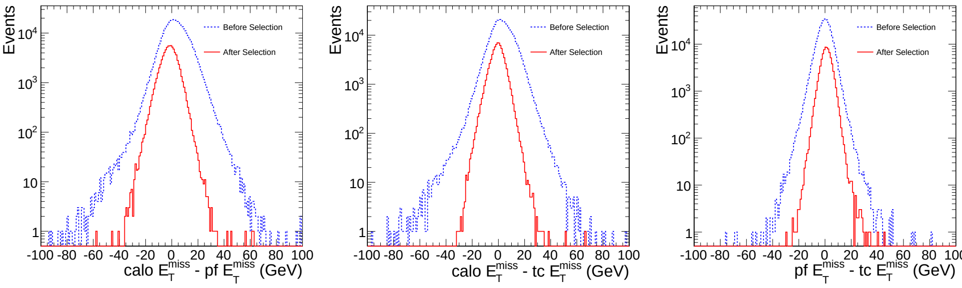

Figure 6.4.: Distributions of $E_{\mathrm{T}}^{\mathrm{miss}}$ as measured by three different algorithms in data for events with one WP80 electron. Distributions are shown before (dashed line) and after (solid line) requiring $0.4 < E_T^{ele}/E_{\mathrm{T}}^{\mathrm{miss}} < 1.5$. Left: Calorimeter $E_{\mathrm{T}}^{\mathrm{miss}}$- Particle-flow $E_{\mathrm{T}}^{\mathrm{miss}}$. Center: Calorimeter $E_{\mathrm{T}}^{\mathrm{miss}}$- Track-corrected $E_{\mathrm{T}}^{\mathrm{miss}}$. Right: Particle-flow $E_{\mathrm{T}}^{\mathrm{miss}}$- Track-corrected $E_{\mathrm{T}}^{\mathrm{miss}}$.

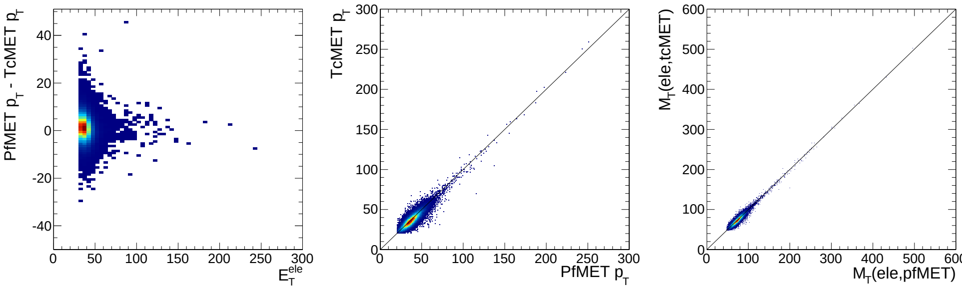

Figure 6.5.: Comparison of the tc and pf-$E_{\mathrm{T}}^{\mathrm{miss}}$ algorithms for our analysis. The bulk of the differences are at small E_{T}, $E_{\mathrm{T}}^{\mathrm{miss}}$, and transverse mass. The differences between algorithms decrease rapidly at higher energy scales Left: Difference between pf and tc-$E_{\mathrm{T}}^{\mathrm{miss}}$ as a function of the electron E_{T}. Center: pf-$E_{\mathrm{T}}^{\mathrm{miss}}$ vs tc-$E_{\mathrm{T}}^{\mathrm{miss}}$. Right: pf vs tc transverse mass.

6.3 ELE+M_T HIGH LEVEL TRIGGER PATH

As described in section 3.2.5 the High Level Trigger is the second level of the CMS trigger system and it is based on the software analysis of online event reconstruction. A high Level Trigger selection loosely identifying electrons (“SingleElectron path”) would be the most obvious choice to keep high trigger efficiency for the W′ search. However, due to the QCD background contaminating the electron sample (see discussion in section 6.1), a trigger selection with loose electron identification and a threshold of 25 GeV would have resulted in a contribution to the HLT trigger rate of nearly 10 Hz at $5 \times 10^{32}\,\mathrm{cm}^{-2}\,\mathrm{s}^{-1}$. As the total trigger rate of CMS should not exceed about 300 Hz, a compromise has to be found to keep the rate under control and within the limits of the bandwidth allotted to this search. Since the W′ manifest itself in the high E_T tail of the electron transverse momentum distribution, there is no risk to cut off the signal peak at the trigger level and a the usage of a very high E_T threshold, a naturally low rate selection, could have been adopted. However, as a general criteria, it is not advisable to develop an analysis working on the tail of a distribution which could be affected by large statistical fluctuation. For this reason a combined ele+M_T HLT path which involves the E_T^{miss} object at trigger level in addition to the electron object has been developed. To cut on the M_T variable event by event already at trigger level is the optimal choice to record Standard Model W events and keep the rate under control at the same time. The W jacobian peak can then be exploited as a control region to check the data-MC agreement and test data-driven methods for the backgrounds.
The isolated electrons coming from the decay of W events are also used for the monitoring of the stability of the ECAL performance as illustrated in section 5.4.

6.3.1 IMPLEMENTATION OF THE ELE+M_T PATH

The ele+M_T HLT trigger path is seeded by electromagnetic objects with a minimum E_T of 15 GeV. The rate of the Level-1 object is expected to be around 16 kHz for an instantaneous luminosity of $5 \times 10^{32}\,\mathrm{cm}^{-2}\,\mathrm{s}^{-1}$. At this stage the trigger choice is based only on the transverse energy of the deposit and the ratio of the energies recorded in the electromagnetic and hadronic calorimeter.
In the High Level Trigger a fast version of the offline reconstruction sequences, already described, allows to build high level objects such as electrons and E_T^{miss}. It is then possible to tune the selection on the reconstructed objects and reject non-interesting events. In the case of the ele+M_T trigger, the subdetector involved are the calorimeters and the tracker.
First of all, the reconstruction of an electron object is seeded by clusters in ECAL, in regions centered around the Level-1 EG seeds in the event and of a size sufficient to

ensure complete collection of energy. Super-clusters are constructed then the super-cluster transverse energy (E_T) is required to exceed a threshold. Subsequently the energy deposited in HCAL is reconstructed. At this step, a cut on both the ECAL and HCAL isolation variables, as well on the ECAL cluster shape is applied. The working point chosen for the electron identification and isolation is already described in table 6.2.
Secondly, the energy and the position of the super-cluster are used to back-propagate the electron through the magnetic field to search for compatible hits in the first or second layer of the pixel detector, within a search area restricted to 40 mrad in ϕ. It is required that an additional hit in the second or third pixel layer is found, satisfying tight requirements on its compatibility with the position of the first pixel hit and the position and energy of the super-cluster. The pixel seeding is followed by electron tracking using a Kalman Filter technique. Once the track is calculated, additional selection can be applied on the electron candidate, both on the matching between the track and the super-cluster and on the track isolation, according to table 6.2.
After the electron reconstruction, the E_T^{miss} is reconstructed as the simple vector sum of the towers above a threshold of 500 MeV. The angles of the towers are calculated with respect to the nominal interaction vertex $z = 0$. The particle flow E_T^{miss} is also implemented at HLT level and gives a slightly higher efficiency with respect to the standard reconstruction algorithms. For this reason it is chosen for the implementation of the HLT path.

RATE

The rate of the ele+M_T trigger is estimated with data collected at the beginning of 2011 when the instantaneous luminosity was approaching $5 \times 10^{32}\,\text{cm}^{-2}\,\text{s}^{-1}$. The tuning of the cuts on the electron transverse energy and the M_T is performed in order to keep the rate within the allotted bandwidth (5 Hz at $5 \times 10^{32}\,\text{cm}^{-2}\,\text{s}^{-1}$) and maximize the efficiency of the selection. The measurement of the rate of the new path is performed in comparison to a reference trigger already available for which the rate was already measured in data. In figure 6.6 the rate of the ele+M_T path ($z-$axis) is showed as a function of the increasing threshold on the electron E_T and the M_T. The chosen working point, E_T = 25 GeV and M_T = 40 GeV, allows to save most of the W bosons and a rate around 5 Hz at the same time.
Once the trigger was deployed online it was possible to measure the effective rate of the combined path from data. The rate turned out to be consistent with the prediction: 9 Hz with an instantaneous luminosity of $1.04 \times 10^{33}\,\text{cm}^{-2}\,\text{s}^{-1}$ (see figure 6.7).

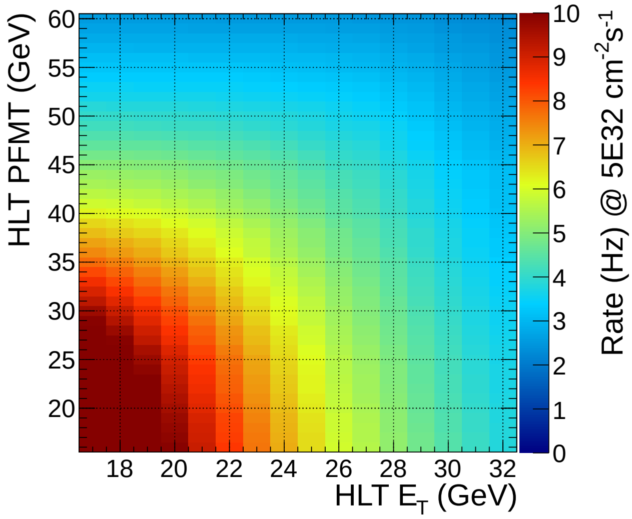

(a)

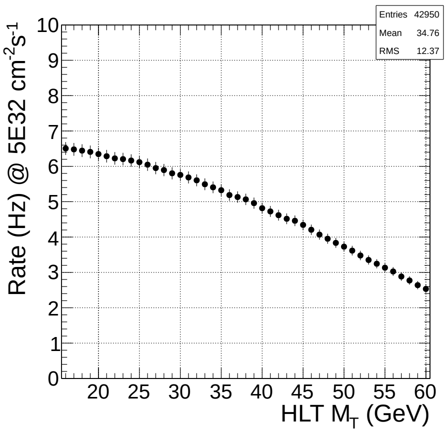

(b)

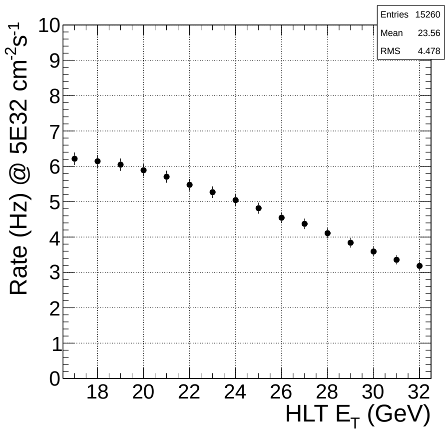

(c)

Figure 6.6.: Electron plus M_{T} HLT rate as a function of the increasing selection on the electron transverse energy and transverse mass.

EFFICIENCY

The measurement of the overall efficiency for the path under study has been performed from data with a tag and probe technique and will be presented in the next section. In figure 6.8 instead is reported the turn-on curve for the $E_{\mathrm{T}}^{\mathrm{miss}}$ selection versus the transverse mass. It shows that there is not an additional inefficiency due to the $E_{\mathrm{T}}^{\mathrm{miss}}$ with respect to the single electron HLT path used as reference. On the other hand it is clear that the turn-on of the M_{T} efficiency curve is slow due to the $E_{\mathrm{T}}^{\mathrm{miss}}$ energy resolution. The value of the cut on the M_{T} is 40 GeV; the plateau starts at 60 GeV. The

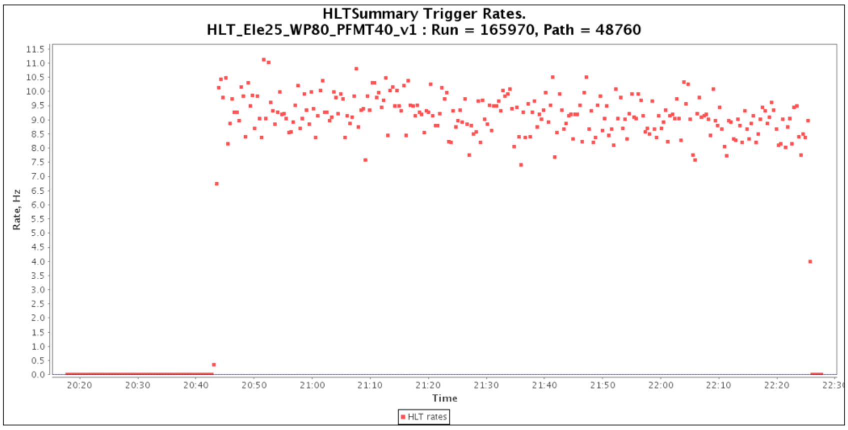

Figure 6.7.: Monitoring of the rate of the ele+M_{T} HLT path during the run 165970. The instantaneous luminosity is $1.04 \times 10^{33}\,\mathrm{cm}^{-2}\,\mathrm{s}^{-1}$.

trigger efficiency is defined as:

$$\varepsilon_{E_{\mathrm{T}}^{\mathrm{miss}} component} = \frac{\#(\text{offline \& SingleEle+}E_{\mathrm{T}}^{\mathrm{miss}})}{\#(\text{offline \& SingleEle})} \tag{6.7}$$

Since the developed trigger path is not yet available in the simulated trigger menu from MC a single electron trigger is required in the simulation. This could translate into a few percent inefficiency in data with respect to the Monte Carlo prediction in the first bins of the transverse mass distribution on the left of the W jacobian peak when the ele+M_{T} path does not reach the plateau yet.

The described trigger path has been has been exploited in the W′ search discussed in this thesis, but it has been adopted also for other physics channels (namely for standard model studies of W event production). Moreover, as discussed in Chapter 5, this trigger has been fundamental for ECAL calibration and monitoring purposes. In fact the trigger was developed having all these goals in mind.

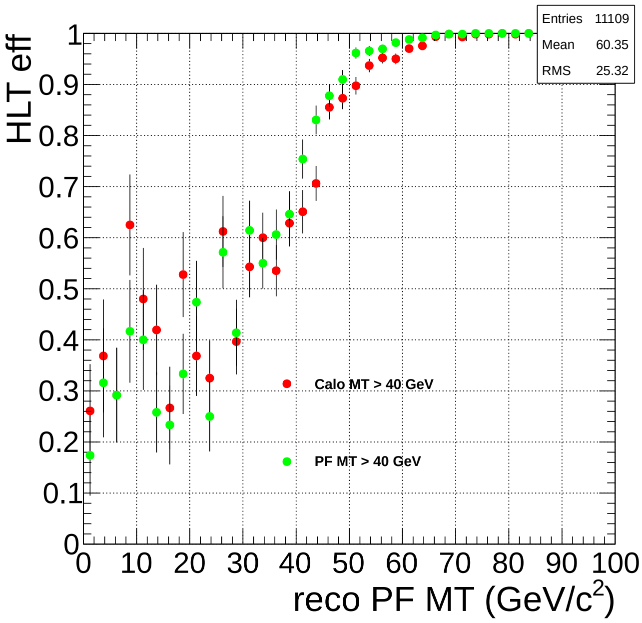

Figure 6.8.: Turn-on of the ele+M_T path as a function of M_T. The particle-flow algorithm for the E_T^{miss} ensures a slightly high efficiency with respect to the standard reconstruction algorithm.

6.4 EFFICIENCY MEASUREMENT WITH THE TAG AND PROBE TECHNIQUE

The electron reconstruction and identification efficiencies, as well as the trigger efficiency, are determined with a tag-and-probe technique with $Z \to ee$ events. The "tagging" lepton candidate has to satisfy the identification, isolation and trigger criteria as described in the previous sections. The "probe" candidate is required to pass the criterion under study.

Di-electron events with a reconstructed invariant mass around the Z-peak (80 GeV $< M_{inv} <$ 100 GeV) are selected for this study. The mass distributions before and after the selection under study are produced and fitted to evaluate the corresponding efficiency. The final efficiency can be factorized in three main contributions: electron reconstruction efficiency (from supercluster to gsfElectron), the electron identification and isolation efficiency and the high level trigger efficiency. In each step the probe selection is the outcome of the previous step so that:

$$\varepsilon_{tot} = \varepsilon_{SC \to gsf} \times \varepsilon_{gsf \to ID,ISO} \times \varepsilon_{ID,ISO \to HLT} \qquad (6.8)$$

The resulting efficiencies are summarized in table 6.3 based on 500 pb^{-1} of data and the $Z \rightarrow ee$ Monte Carlo sample. The contamination from non Drell-Yan events in the data sample is small due to the tight invariant mass window chosen to select the di-lepton candidates. In the plots of figure 6.9, the efficiency for each step as a function of the probe transverse energy is reported.
In the first step a few percent inefficiency is expected due to the track-cluster matching (pixel matching). The measured efficiency for the WP80 selection confirms that the electron identification and isolation selection have an efficiency of about 80% over a pure sample of electrons. The inefficiency of the third step ($\sim$2%) is due to the differences in the online reconstruction algorithms running at the HLT with respect to the offline ones (see section 3.2.5).

Efficiency	Simulation	Data	Ratio Data/MC
SC to gsfElectron	0.9691±0.0004	0.9683±0.0009	0.999
WP80 selection	0.8404±0.0009	0.8358±0.0019	0.994
HLT Ele25_PFMT40	0.9798±0.0004	0.9779±0.0009	0.998

Table 6.3.: Breakdown of the efficiencies for each electron reconstruction step measured in data and MC with a tag-and-probe method.

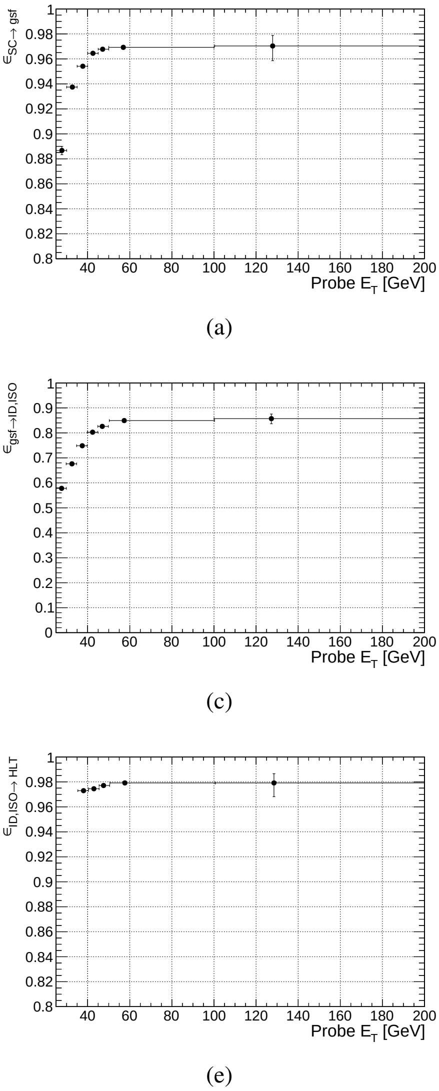

Figure 6.9.: Efficiency vs transverse energy of the probe for DATA (left column) and MC (right column). The steps SC to gsfElectron, WP80 selection, HLT Ele25_PFMT40 are showed from the top to the bottom.

CHAPTER 7

THE W′ ANALYSIS IN CMS

The search of the W′ is based on the comparison of the collected data with the Standard Model processes (background) and the expected signal both simulated with a Monte Carlo. An excess of events characterized by the presence of one electron and $E_{\mathrm{T}}^{\mathrm{miss}}$ is searched in the high tail of the transverse mass distribution. In the following chapter all the details concerning the event selection, the signal extraction, the estimate of the systematic uncertainties and the statistical analysis are discussed in detail. The analysis with a data sample corresponding to an integrated luminosity of 1.13 fb^{-1}, collected from March to July 2011, is presented.

7.1 DETECTOR SIMULATION, MONTE CARLO AND COLLISION DATASET

An accurate simulation of the physics processes and of the detector response is a crucial point in analyses which aims at discovering a new particle. An excellent understanding of the data, which translates into a good description with the MC samples, is fundamental to distinguish a hint of new physics from background processes. The simulation of the signal and the background processes is used in the analysis to estimate the relative efficiencies of each sample after each selection step. The selections are tuned to maximize the signal over background ratio and the significance for the W′ search.

7.1.1 SIMULATION OF MONTE CARLO SAMPLES

The first stage of a Monte Carlo simulation is the generation of elementary physics processes. The W′ signal under study, for example, is created from two proton constituents

and consequently it is forced to decay into an electron and neutrino pair. This task is performed by generators such as PYTHIA 6.4.9 [83] which is used for the signal production. The interaction of the particles with the matter is subsequently simulated with GEANT4 [84], but already at generator level it is possible to study the features of a process such as the momentum distribution of the W′ decay products.
The list of the signal and background samples with the generator used for the production, the process cross section and the available statistics is reported in table 7.1 and 7.2 respectively.

SIMULATION OF SIGNAL EVENTS

The W′ production and decay has been simulated with PYTHIA using the CTEQ6L1 [85, 86] parton distribution functions (PDF) according to the Altarelli Model described in section 1.1.2. Since in PYTHIA matrix elements are not computed at orders beyond the leading one, the leading order (LO) PDF is used for the event generation. A *k*-factor, defined as the ratio of the production cross section at NNLO and LO:

$$k_{NNLO} = \frac{\sigma_{NNLO}}{\sigma_{LO}} \tag{7.1}$$

is subsequently used to weight the event generation. The NLLO and LO cross sections are obtained using a package called Fully Exclusive W and Z Production (FEWZ) [87]. The *k*-factor is calculated and applied on the LO cross section value for each mass point. It ranges from 1.311 (for $M_{W'}$= 1.2 TeV) to 1.142 (for $M_{W'}$ = 2.5 TeV). The uncertainties on the production cross section have been derived with a method based on both PDF and α_s variation and are showed in figure 7.1a as a function of the W′ mass (more details on the method are available at [88]). The LO and NNLO cross section values are reported in table 7.1 along with the *k*-factor values for each mass point. The graphical representation of the same quantities is shown in figure 7.19. According to the theoretical discussion reported in Chapter 1, the W′ invariant mass distribution differs in shape depending on the generated mass value. As shown in figure 7.2, for low mass values, the W′ are almost all produced within the Breit-Wigner resonance around the nominal mass. The W′ production occurs via the scattering of a quark and an anti-quark. The effective centre of mass energy for this scattering is a small fraction of the proton-proton centre of mass energy and on the average lower than the W′ mass already for masses larger than 2.5 TeV. Hence W′ production at large masses occurs mostly off-shell, giving rise to a broad distribution rather than to the Breit-Wigner resonance.

As reported in figure 7.3, the transverse momentum of the W′ is determined by the transverse momentum of the colliding partons and the initial state radiation (momen-

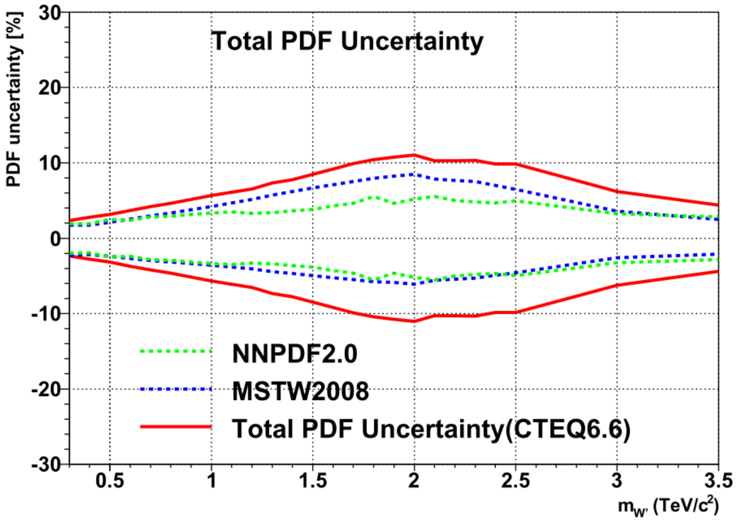

(a)

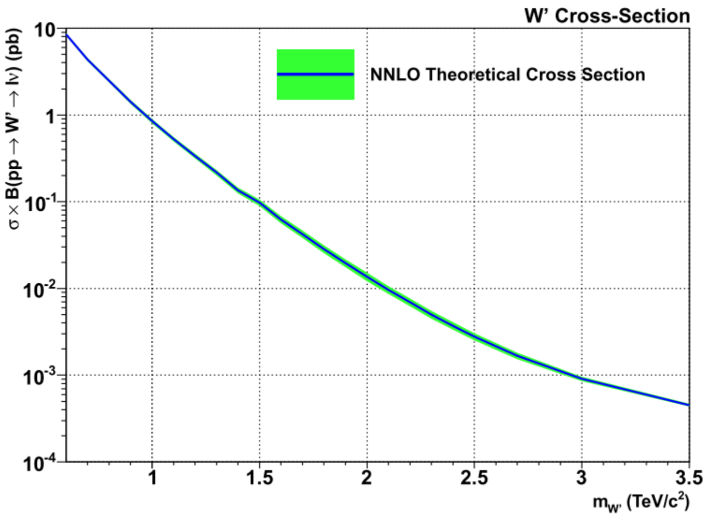

(b)

Figure 7.1.: (a) Uncertainites for various PDF sets with respect to CTEQ6L1 which was used to generate the signal samples, as a function of the W′ boson mass. The total PDF uncertainty used is shown with the red curve. (b) Cross section times branching fraction of W′ boson decaying into leptonic channel with PDF uncertainties.

tum of the particles emitted by the colliding partons before they create the W′). Independently of the W′ mass, the boson p_T is mainly below 100 GeV and thus small compared to the mass of the boson (fig. 7.3a). The longitudinal momenta, determined by the longitudinal momenta of the colliding partons, are significantly larger. While the longitudinal momentum distribution has its maximum at zero, often one of the partons

Generator	$m_{W'}$ (in GeV)	σ_{LO} (pb)	k-factor AN-11-273	σ_{NNLO} (pb)	# of events	PDF set
PYTHIA	1200	0.2640	1.311	0.34608	16.5K	CTEQ6L1
PYTHIA	1300	0.1711	1.298	0.22210	16.5K	CTEQ6L1
PYTHIA	1400	0.1126	1.279	0.14402	16.5K	CTEQ6L1
PYTHIA	1500	0.0750	1.265	0.09485	16.5K	CTEQ6L1
PYTHIA	1600	0.05058	1.255	0.06333	16.5K	CTEQ6L1
PYTHIA	1700	0.03434	1.234	0.04237	16.5K	CTEQ6L1
PYTHIA	1800	0.02354	1.211	0.02851	16.5K	CTEQ6L1
PYTHIA	1900	0.01629	1.191	0.01940	16.5K	CTEQ6L1
PYTHIA	2000	0.01136	1.184	0.01346	16.5K	CTEQ6L1
PYTHIA	2100	0.00800	1.172	0.00937	16.5K	CTEQ6L1
PYTHIA	2200	0.005686	1.162	0.00661	16.5K	CTEQ6L1
PYTHIA	2300	0.004077	1.157	0.00472	16.5K	CTEQ6L1
PYTHIA	2400	0.002963	1.147	0.00340	16.5K	CTEQ6L1
PYTHIA	2500	0.002175	1.142	0.00248	16.5K	CTEQ6L1
PYTHIA	2700	0.001224	1.166	0.00143	12.4K	CTEQ6L1
PYTHIA	3000	0.0005789	1.221	0.00071	16.5K	CTEQ6L1
PYTHIA	3500	0.0002100	1.335	0.00030	16.5K	CTEQ6L1
PYTHIA	4000	0.000106	1.375	0.00015	16.5K	CTEQ6L1

Table 7.1.: Summary of signal Monte Carlo samples. The NNLO cross sections for the various W′ mass points are calculated with a mass-dependent k-factor.

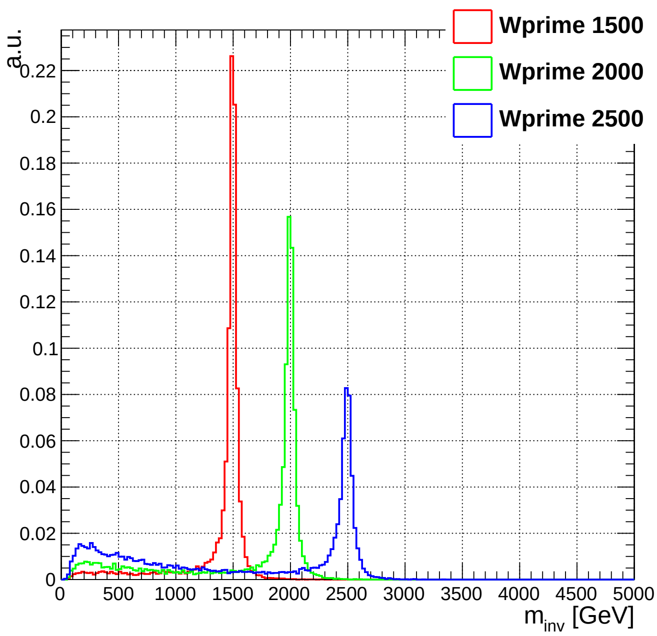

Figure 7.2.: The normalized mass distribution of W′ bosons with different masses show a Breit-Wigner resonance at the nominal mass (peak). For a 2.5 TeV W′ mass, the distribution has a significant off-shell part (left of the peak).

carries a significant larger momentum than the other (fig. 7.3b). Due to the large longitudinal momentum compared to the transverse one, the W′ bosons are flying mainly along the beam direction. This is clearly visible in figure 7.4

The properties of the W′ products are dominated by the properties of the W′ itself (fig. 7.5). The off-shell production of heavy bosons contributes to the low p_{T} tail in the electron and neutrino transverse momentum spectra. This tail is increasingly more

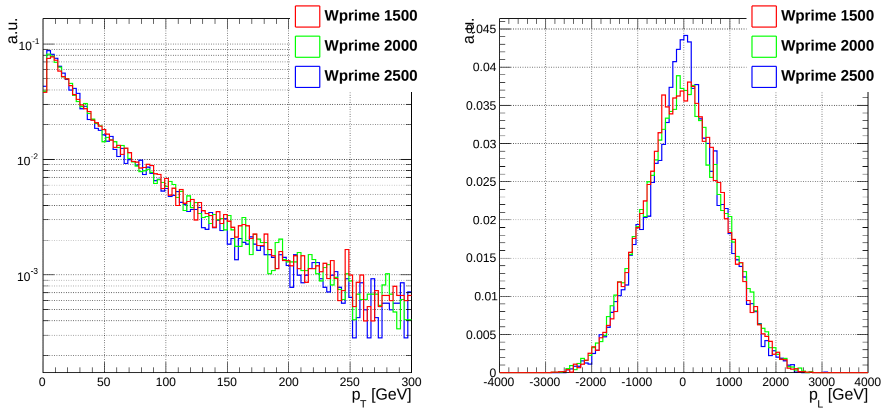

(a) (b)

Figure 7.3.: Transverse (left) and longitudinal (right) momentum of the W′. Only a slight dependence on the W′ mass is visible in the distributions. While the transverse momenta are smaller than the W′ mass, the longitudinal momentum reaches 3 TeV.

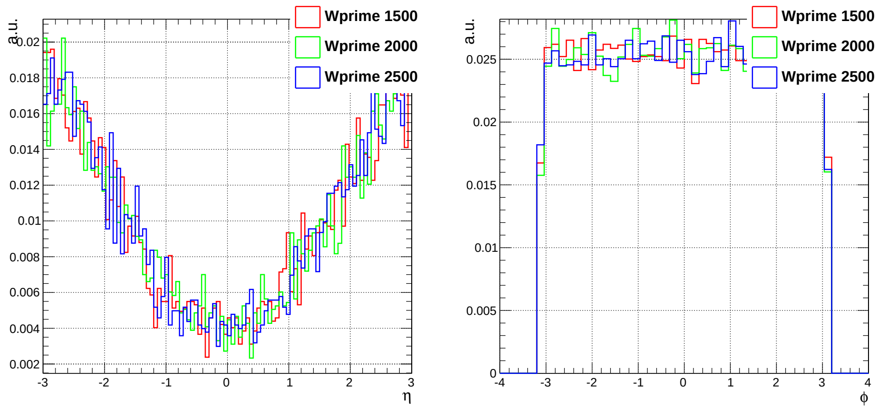

(a) (b)

Figure 7.4.: The angular distributions of the W′ momentum vector are shown for different masses.

important at larger W′ masses.

From the analysis point of view, it is not possible to reconstruct the invariant mass of the W′ by combining the information of its decay products because the momentum of the neutrino, which is not detectable, can only be determined in the transverse plane as an energy imbalance. This is a feature of hadron colliders where the amount of energy of the partons along the beam line is not known. Since in the W′ rest frame the

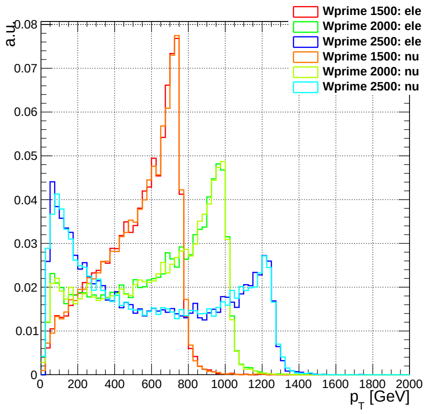

(a)

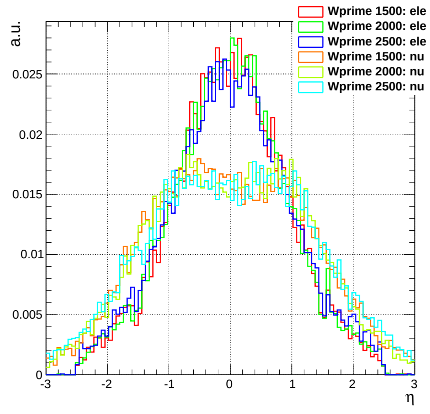

(b)

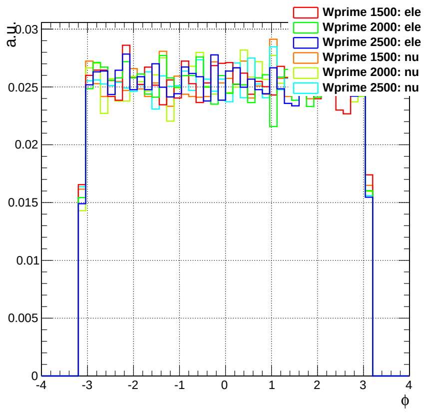

(c)

Figure 7.5.: Transverse momentum (a), pseudorapidity η (b), and azimuthal angle ϕ (c) distribution for the electron and the neutrino coming from the W′.

energy of each of the two leptons is one half of the W′ mass (two body back-to-back decay), in principle it is possible to perform the signal search in the tail of the electron energy distribution. However, to exploit the measurable properties of the neutrino and not only the electron information, can be defined the transverse invariant mass already discussed in section 1.2 and reported here for completeness:

$$M_T = \sqrt{2E_T^e E_{\mathrm{T}}^{\mathrm{miss}}(1 - \cos\Delta\phi_{e,\nu})} \tag{7.2}$$

with $\Delta\phi_{e,\nu})$ as the angle between the transverse momentum of the electron and the neutrino which are constrained to be in the transverse plane.
The distribution of the transverse mass for three W′ signals is reported in figure 7.6 where all the considerations made above remain valid.

Summarizing on the characteristics of the signal, the W′:

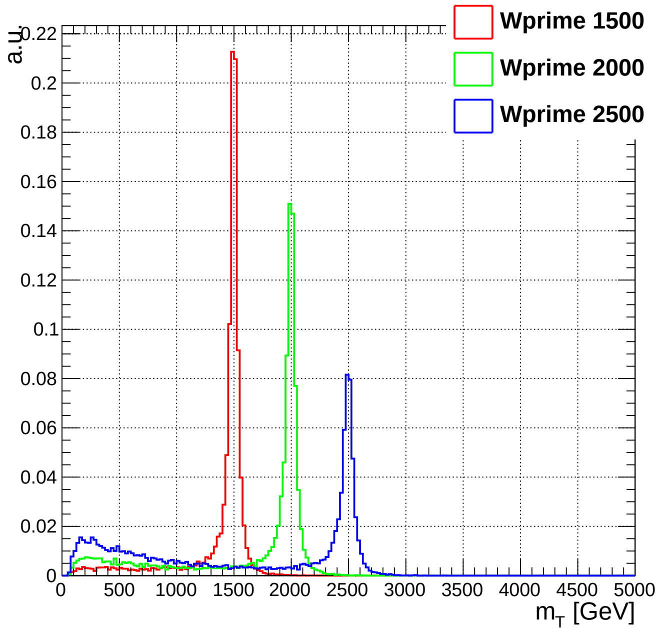

Figure 7.6.: The normalized transverse mass distribution of W′ bosons with different masses.

- has small cross sections;
- on-shell production is suppressed for high mass W′;
- decay products are balanced in terms of transverse momenta both in direction and in module;
- the electrons tend to be central and to have energies well above 100 GeV.

Based on these properties, the event selection presented in the next sections are introduced in order to reject the SM backgrounds and keep an high efficiency on the W′ signal. To separate the W boson irreducible background, a signal search region will be defined.

SIMULATION OF BACKGROUND EVENTS

Relevant background processes are qualified by a similar signature compared to the signal ($W \to l\nu$, di-boson, $t\bar{t}$, see discussion in section 1.2). For the simulation of the backgrounds, three generators (`POWHEG` [89–91], `PYTHIA` [83], `MADGRAPH` [92]) are used dependently on the process. The cross section [93] and the available number of

events for each sample are reported in table 7.2. For the multi-jet process (the so called QCD-events which dominate at hadron colliders) a data-driven approach to evaluate the contamination of fake electrons in the final sample is adopted (see section 7.4). A data-driven approach is desirable for all the processes for which the modeling is difficult or the cross section is too large and the generation of a sufficient number of events, compared to the collected statistics, requires too many computing resources. Since the analysis is based on the search for an excess over the SM prediction, the generated background has to faithfully reproduce the data in a region where the signal contamination is negligible. The region used for the validation of the MC is the jacobian peak of the W Standard Model bosons (which is the main irreducible background, see section 1.2) where the transverse mass spectrum is below 200 GeV. An accurate simulation of all the processes would reproduce correctly both the shape and the normalization of the data.
In order to avoid large statistical fluctuations in the M_{T} tail and to reduce the statistical error associated to the sample, the $W \to e\nu$ sample has been produced in bins by choosing special ranges for the transverse momentum $\hat{p}_T$ of the electron and the neutrino in the rest frame of the W. The various samples produced in disjoint $\hat{p}_T$ ranges, have been scaled according to their cross section and merged into one sample (see figure 7.7).
With the increasing of the instantaneous luminosity, the probability of multiple interactions in a beam crossing increases (pile-up). Minimum bias events are generated and reconstructed with the CMS framework and then added event by event to each Monte Carlo sample in order to reproduce the pile-up conditions in the data. The average number of pile-up events increased up to 15 at $3.5 \times 10^{33}\,\mathrm{cm}^{-2}\,\mathrm{s}^{-1}$.

7.1.2 The 2011 collision dataset

The results presented in the current chapter are based on the analysis of the *Run*2011*A* recorded between March and the end of June 2011 and corresponding to an integrated luminosity of 1.13 fb^{-1}. The High Level Trigger paths used and the corresponding run ranges are listed in table B.2. The condition of the LHC beam (bunch spacing, number of protons per bunch, beam size) evolved continuously during the course of the year with the aim to increase the instantaneous luminosity. The description of the running condition during 2011 has been presented in section 3.2.6.

Generator	Process	Kinematic cuts (in GeV, $c = 1$)	σ_{LO} (pb)	σ_{NNLO} (pb)	# of events	PDF set
		Background samples for the electron channel				
PYTHIA	W $\to \ell\nu$	$p_T < 100$ GeV	7899	10438	~5M	CTEQ6L
PYTHIA	W $\to \mu\nu$	$p_T > 100$ GeV	1.187	1.569	~4M	CTEQ6L
PYTHIA	W $\to e\nu$	$p_T > 100$ GeV	1.187	1.569	~1M	CTEQ6L
PYTHIA	W $\to \tau\nu$	no cuts	7899	10438	~5M	CTEQ6L
PYTHIA	Z $\to \ell\ell$	$m_{\ell\ell} > 20$	1300	1666	~1M	CTEQ6L
PYTHIA	Z $\to \ell\ell$	$m_{\ell\ell} > 200$	0.97	1.22	~ 55K	CTEQ6L
PYTHIA	Z $\to \ell\ell$	$m_{\ell\ell} > 500$	0.027	0.034	~55K	CTEQ6L
PYTHIA	Z $\to \ell\ell$	$m_{\ell\ell} > 800$	0.0031	0.0038	~55K	CTEQ6L
PYTHIA	Z $\to \ell\ell$	$m_{\ell\ell} > 1000$	9.735E-4	0.0012	~55K	CTEQ6L
Madgraph	$t\bar{t}$	no cuts	94	157.5 (NLO)	~4M	CTEQ6L
Powheg	$t \to bl\nu$ (s-Channel)	no cuts	-	3.19	~0.3M	CTEQ6L
Powheg	$t \to bl\nu$ (t-Channel)	no cuts	-	41.92	~4M	CTEQ6L
Powheg	$t \to bl\nu$ (tW-Channel DR)	no cuts	-	7.87	~0.8M	CTEQ6L
Powheg	$\bar{t} \to bl\nu$ (s-Channel)	no cuts	-	1.44	~0.1M	CTEQ6L
Powheg	$\bar{t} \to bl\nu$ (t-Channel)	no cuts	-	22.65	~2M	CTEQ6L
Powheg	$\bar{t} \to bl\nu$ (tW-Channel DR)	no cuts	-	7.87	~0.8M	CTEQ6L
PYTHIA	WW	no cuts	28	43	~2M	CTEQ6L
PYTHIA	WZ	no cuts	10.4	18	~2M	CTEQ6L
PYTHIA	ZZ	no cuts	4.3	5.9	~2M	CTEQ6L
PYTHIA	QCD EM enriched	$20 < \hat{p}_T < 30$	2454400	-	~37M	CTEQ6L
PYTHIA	QCD EM enriched	$30 < \hat{p}_T < 80$	3671200	-	~71M	CTEQ6L
PYTHIA	QCD EM enriched	$80 < \hat{p}_T < 170$	139500	-	~8M	CTEQ6L
PYTHIA	$\gamma + Jets$	$0 < \hat{p}_T < 15$	8.420e+07	-	~1M	CTEQ6L
PYTHIA	$\gamma + Jets$	$15 < \hat{p}_T < 30$	1.717e+05	-	~1M	CTEQ6L
PYTHIA	$\gamma + Jets$	$30 < \hat{p}_T < 50$	1.669e+04	-	~1M	CTEQ6L
PYTHIA	$\gamma + Jets$	$50 < \hat{p}_T < 80$	2.722e+03	-	~1M	CTEQ6L
PYTHIA	$\gamma + Jets$	$80 < \hat{p}_T < 120$	4.472e+02	-	~1M	CTEQ6L
PYTHIA	$\gamma + Jets$	$120 < \hat{p}_T < 170$	8.417e+01	-	~1M	CTEQ6L
PYTHIA	$\gamma + Jets$	$170 < \hat{p}_T < 300$	2.264e+01	-	~1M	CTEQ6L
PYTHIA	$\gamma + Jets$	$300 < \hat{p}_T < 470$	1.493e+00	-	~1M	CTEQ6L
PYTHIA	$\gamma + Jets$	$470 < \hat{p}_T < 800$	1.323e-01	-	~1M	CTEQ6L
PYTHIA	$\gamma + Jets$	$800 < \hat{p}_T < 1400$	3.481e-03	-	~1M	CTEQ6L
PYTHIA	$\gamma + Jets$	$1400 < \hat{p}_T < 1800$	1.270e-05	-	~1M	CTEQ6L
PYTHIA	$\gamma + Jets$	$\hat{p}_T > 1800$	2.936e-07	-	~1M	CTEQ6L
		Additional samples used for cross checks				
Powheg	$W^+ \to \ell^+\nu_\ell$	no cuts	5775	6152	~2M	CT10
Powheg	$W^- \to \ell^-\nu_\ell$	no cuts	3944	4286	~2M	CT10

Table 7.2.: Analysed Monte Carlo samples for various background processes (with $\ell = e, \mu$). In case only LO cross sections are known, the column for NNLO stays empty.

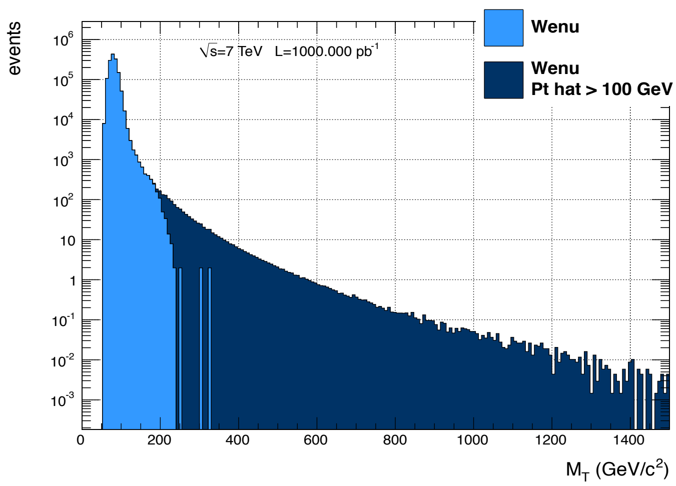

Figure 7.7.: Transverse mass of the different W samples. The matching is visible for values of the transverse mass around 200 GeV.

7.2 EVENT SELECTION

The goal of the event selection is to separate signal from background events. In order to maximize the signal to background ratio, events are selected according to the following set of requirements:

- at least one reconstructed electron with transverse energy greater than 35 GeV (preselection);
- exactly one electron surviving the electron identification and isolation criteria described in section 6.1.2. The electron is required to be within the ECAL acceptance in order to exclude non-instrumented regions;
- The ratio E_T/E_T^{miss} between the electron transverse energy and the E_T^{miss} for signal events should be around one given the two-body decay. The selected range is $0.4 < E_T/E_T^{miss} < 1.5$;
- The angle $\Delta\phi(e, E_T^{miss})$ between the direction of the electron and the E_T^{miss} should be close to π, since lepton and E_T^{miss} are expected to be almost back-to-back in the transverse plane for signal events. The used cut is $\Delta\phi(e, E_T^{miss}) > 2.5$ radiants.

Part of the characteristics of the events are already required at trigger level (see the discussion on the choice of the HLT path in section 6.3). The last two selection, instead, exploit the kinematic of the signal event by requiring a balance in momentum between the electron and the E_T^{miss}. As illustrated in figure 7.8, the distribution of E_T/E_T^{miss} shows a pronounced peak around 1. The $\Delta\phi(e, E_T^{miss})$ distribution peaks around π for the signal and for the $W \rightarrow e\nu$ background, while it is flatter for the main backgrounds (namely $t\bar{t}$, QCD, and Drell-Yan). No strong dependence of the signal selection efficiency on the exact value of the selection cut is observed from studies performed on simulated events.
The relative efficiency of these two selection on top of the electron quality cuts, is above 95% for any W′ signal in the mass range 1.5 TeV- 2.5 TeV and it is considerably lower for all the background except for the W due to the similar topology ($\varepsilon \sim 65\%$).

The data-MC comparison for the M_T distribution after the full selection chain is reported in figure 7.9a. The estimate of the background is from the Monte Carlo for all the considered processes. The agreement between data and background estimation in the high M_T region is good and the numbers of events are compatible within the errors. This is more evident from the cumulative distribution of figure 7.9b, where the number of selected events above a given transverse mass threshold is shown.

For large values of the W′ mass (M > 2 TeV) the fraction of the off-shell events in the tail on the left of the nominal mass peak increases. This is reflected in a decreased

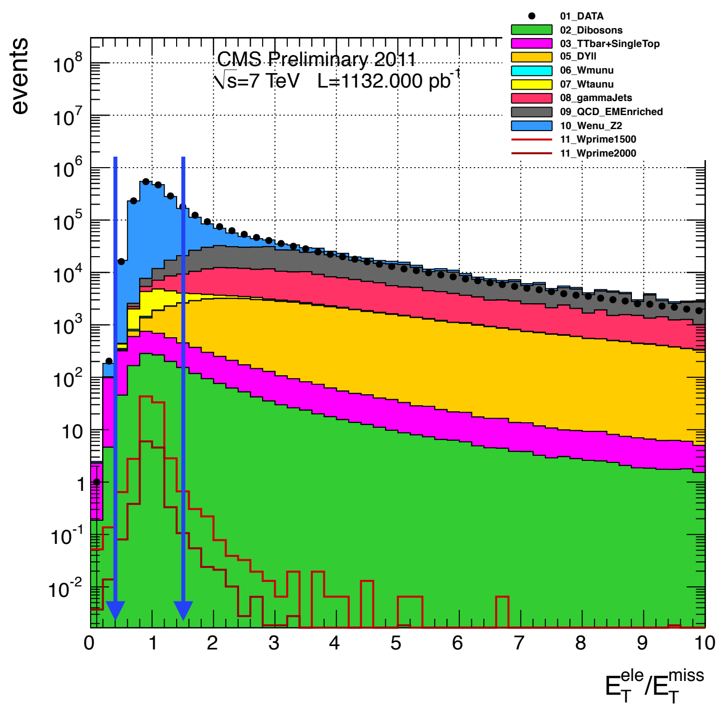

(a)

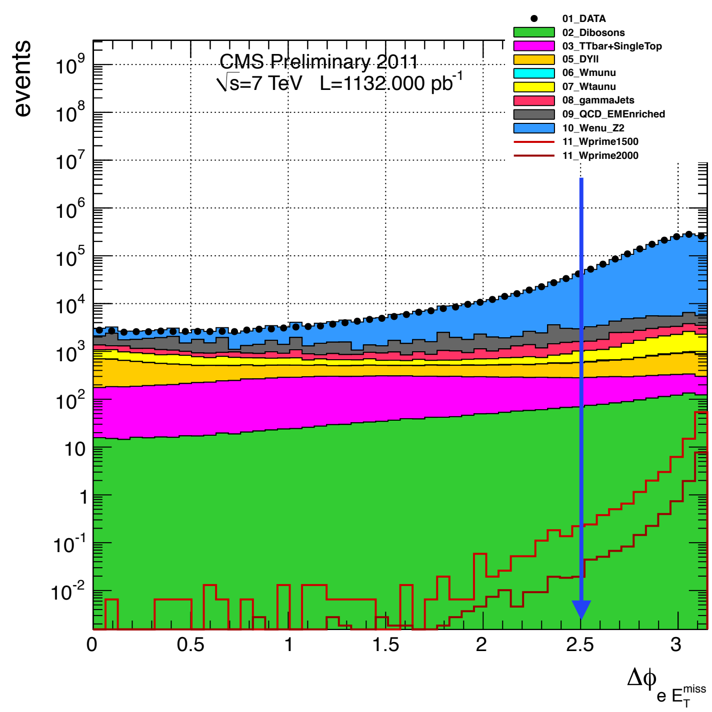

(b)

Figure 7.8.: Distributions of the E_T/E_T^{miss} (a) and azimuthal angle between electron and E_T^{miss} (b), which have been used to optimise the kinematic selection. All selection criteria are applied except from the discussed ones.

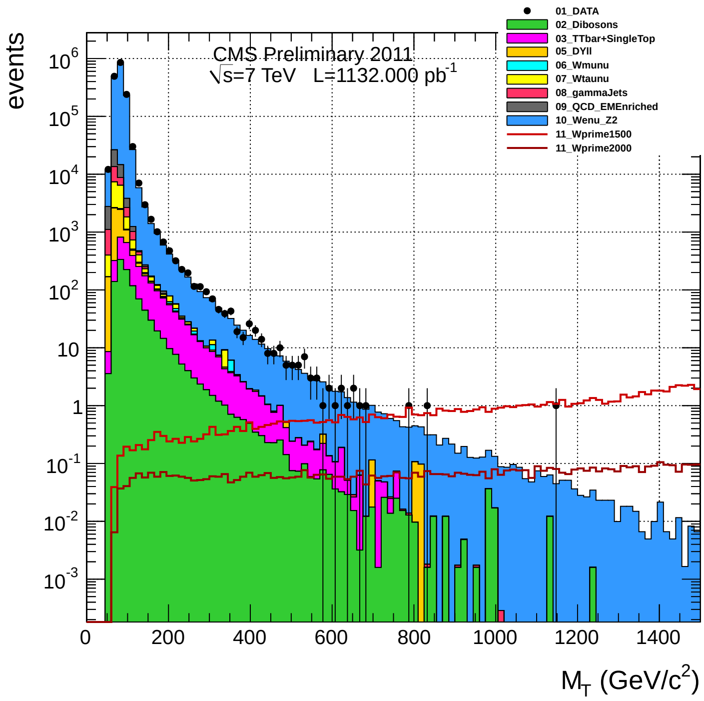

(a)

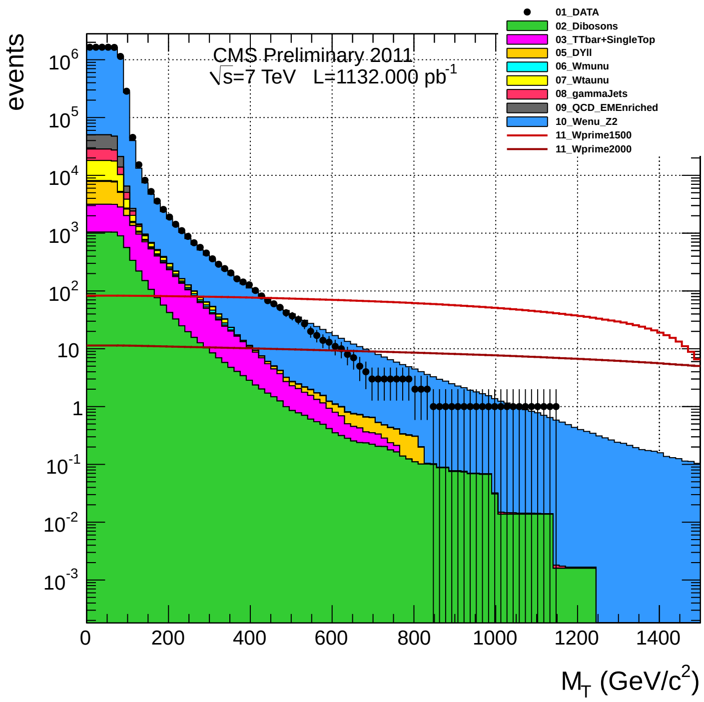

(b)

Figure 7.9.: Differential (a) and cumulative (b) distribution of the transverse mass for the data and the backgrounds from MC. The W′ signal with a mass of 1.5 TeV and 2.0 TeV is also shown.

efficiency as shown in fig. 7.10
The last selection, on top of the electron quality cuts and kinematic cuts, consists in the identification of the signal region in the M_T distribution. In order to maximize the significance, the M_T cut is optimized for each W′ mass signal. The discussion of the optimization of the selection is presented in section 7.9.

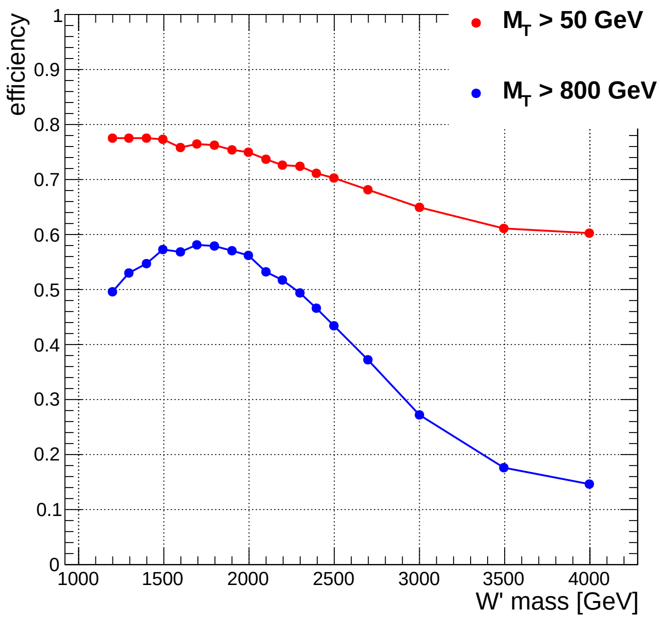

Figure 7.10.: With the increasing of the mass, the selection efficiency on the signal decreases due to the large fraction of off-shell W′. The efficiency is shown for each mass point for the full spectrum and for the signal region (M_T > 800 GeV).

The relative efficiencies for the major selection steps mentioned above (preselections, one good high E_T electron, angle and energy ratio between lepton and E_T^{miss}) along with the total efficiency after each cut are detailed in tab. 7.4 for the signal and the MC backgrounds.

Sample	Total events	Preselection & HLT	WP80 + 1 good ele	$\Delta\phi_{eE_T^{miss}} > 2.5$	$0.4 < E_T/E_T^{miss} < 1.5$
$W \to e\nu$	1.1818e+07	3.0020e+06	2.4574e+06	1.9617e+06	1.5934e+06
	(100%)	(25%,25%)	(82%,21%)	(79%,17%)	(81%,13%)
$W \to \mu\nu$	1.1816e+07	2.1566e+03	6.5046e+02	3.2741e+02	2.4229e+02
	(100%)	(0.02%,0.02%)	(30%,0.006%)	(50%,0.003%)	(74%,0.002%)
$W \to \tau\nu$	1.1816e+07	4.5794e+04	3.4406e+04	1.5220e+04	9.9832e+03
	(100%)	(0.4%,0.4%)	(75%,0.3%)	(44%,0.1%)	(66%,0.01%)
$t\bar{t}$, SingleTop	2.7444e+05	2.6865e+04	2.1350e+04	4.2546e+03	2.1165e+03
	(100%)	(9.7%,9.7%)	(80%,7.8%)	(20%,1.6%)	(50%,0.8%)
WW,WZ,ZZ	7.5957e+04	6.3239e+03	4.8471e+03	1.9102e+03	1.0424e+03
	(100%)	(8.3%,8.3%)	(77%,6.4%)	(39%,2.5%)	(55%,1.4%)
$Z/\gamma* \to e,\mu,\tau$	3.4503e+06	5.8927e+05	2.8125e+05	7.3983e+04	4.6835e+03
	(100%)	(17%,17%)	(48%,8.1%)	(26%,2.1%)	(6.3%,0.1%)
Multi-Jet	7.4072e+09	8.3564e+06	1.1418e+06	4.0412e+05	2.1798e+04
	(100%)	(0.1%,0.1%)	(14%,0.02%)	(35%,0.005%)	(5.4%,0.0003%)
$\gamma + jets$	2.1697e+08	8.1139e+05	5.3936e+05	1.9412e+05	1.0439e+04
	(100%)	(0.4%,0.4%)	(66%,0.2%)	(36%,0.09%)	(5.4%,0.005%)

Table 7.3.: Selection efficiencies for the electron channel background processes using 1.13 fb^{-1} of 2011 data.

W′ signal samples	Total events	Preselection & HLT	WP80 + 1 good ele	$\Delta\phi_{eE_{\mathrm{T}}^{\mathrm{miss}}} > 2.5$	$0.4 < E_{\mathrm{T}}/E_{\mathrm{T}}^{\mathrm{miss}} < 1.5$
$1.5\,TeV$	1.0737e+02	9.2104e+01	8.5727e+01	8.4204e+01	8.2981e+01
	(100%)	(86%,86%)	(93%,80%)	(98%%,78%)	(99%,77%)
$2.0\,TeV$	1.5237e+01	1.2732e+01	1.1782e+01	1.1584e+01	1.1395e+01
	(100%)	(84%,84%)	(93%,77%)	(98%,76%)	(98%,75%)
$2.5\,TeV$	2.8074e+00	2.2408e+00	2.0689e+00	2.0123e+00	1.9697e+00
	(100%)	(79%,79%)	(92%,74%)	(97%,72%)	(98%,70%)
$3.0\,TeV$	8.0372e-01	6.0742e-01	5.5929e-01	5.3844e-01	5.2169e-01
	(100%)	(76%,76%)	(92%,70%)	(96%,67%)	(97%,65%)
$3.5\,TeV$	3.3960e-01	2.4750e-01	2.2562e-01	2.1531e-01	2.0734e-01
	(100%)	(73%,73%)	(91%,66%)	(95%,63%)	(96%,61%)
$4.0\,TeV$	1.6980e-01	1.2281e-01	1.1213e-01	1.0663e-01	1.0203e-01
	(100%)	(72%,72%)	(91%,66%)	(95%,63%)	(96%,60%)

Table 7.4.: Selection efficiencies for the W′ signal in the electronic final state using 1.13 fb^{-1} of 2011 data.

7.3 Data-MC scaling factors

Correction factors are applied to account for different efficiencies between MC and data. For each observable taken into account, the tag-and-probe efficiency is calculated for both MC and data as presented in section 6.4. The total correction factor $\rho = \varepsilon_{data}/\varepsilon_{MC} = 0.99$ is then applied to the simulation samples for the evaluation of the expected number of background events. Since the statistical error on the correction factor is very small, a more conservative estimate of its uncertainty is obtained by repeating the tag-and-probe efficiency measurements with a larger invariant mass window for the di-lepton pairs (60 GeV < M_{inv} < 120 GeV) and quoting the difference on the final correction factor as a systematic. The uncertainty came out to be less than 2% and can be attributed to the different contamination of non Drell-Yan events in the data sample.
Since the scaling factor is estimated with electrons from the Z with momenta well below 200 GeV, in order to prove the validity of the MC scaling factor up to the signal region, the efficiency measurement is performed on the Monte Carlo with electrons from a W and a W′ samples and then the results are compared. A simple method based on the geometrical matching of the reconstructed electron candidate and the electron at generator level is used instead of the tag and probe technique. The efficiencies are found to be in agreement at the percent level. A 1% uncertainty is quoted as the systematic on the transportation of the scaling factor up to the 1 TeV region.

7.4 Data-Driven QCD multi-jet estimate

It is known that the shape and the normalization of the QCD multi-jet background are not well described by the MC simulation. This is critical especially in the electron channel where the probability for a jet to be reconstructed as an electron is not negligible.
The QCD multi-jet background then is determined from data. Events with exactly one isolated cluster of energy in the EM calorimeter (ECAL super-cluster) and large $E_{\mathrm{T}}^{\mathrm{miss}}$ that satisfy the selection criteria of the analysis (where the requirement of the electron are applied to the super-cluster) are selected. The number of QCD multi-jet events N_{ev}^{QCD} is estimated by

$$N_{ev}^{QCD} = \sum_{c\nu \text{ events in data}} P(e|c : E_{\mathrm{T}}) \quad , \tag{7.3}$$

where c is an ECAL super-cluster passing the criteria listed in Table 7.4, e is a reconstructed electron candidate passing the WP80 electron ID and isolation criteria described in Table 6.2, and $P(e|c)$ is the probability, or fake rate, that a cluster c is re-

constructed as and electron e estimated as a function of E_{T}. To simplify the procedure, events with 2 or more clusters c are not considered in Equation 7.3.
A combination of single photon HLT path with E_{T} threshold 30 GeV and 90 GeV is used for this study. Due to the high rate, both paths are pre-scaled. The prescale factor needs to be taken into account in the fake rate estimate.

Variable Name	Barrel Threshold	Endcap Threshold
H/E	< 0.15	< 0.15
$\sigma_{i\eta i\eta}$	< 0.024	< 0.040

Table 7.5.: Selection criteria for super-clusters employed in the QCD multi-jet background estimation. The selection is looser than the one applied in the WP80 electron-ID.

7.4.1 FAKE RATE CALCULATION

The fake rate, $P(e|c)$, is determined as the ratio between the number of electron candidates, N_e, and number of clusters, N_c, in a data sample enriched of QCD multi-jet events passing the following selection criteria:

- single-photon trigger, as described above;
- exactly one isolated super-cluster "c" with $p_{\mathrm{T}} > 35$ GeV;
- $E_{\mathrm{T}}^{\mathrm{miss}} < 10$ GeV.

The requirements of exactly one isolated super-cluster and low $E_{\mathrm{T}}^{\mathrm{miss}}$ reduce the contamination of real electrons in the sample from $Z \to ee$ and $W \to e\nu$ events, respectively. A residual contamination estimated from the MC of about 40% from real electrons and $\gamma + jets$ events needs to be subtracted from the numerator (see fig 7.11a).
The fake rates are calculated for the barrel and for the endcap separately. The fake probability is shown in Figure 7.12 as a function of the super-cluster E_{T}, separately for the barrel and the endcap regions. A first-degree and zero-degree polynomial fit are performed in two different E_{T} regions. The fit results are reported in Table 7.4.1. The shape and the normalization of the QCD multi-jet background can now be determined from at each step of the analysis.

Summarizing, the QCD multi-jet contamination in the final sample is the product of three terms:

- di-jet production cross section (multi-jet events with more than two jets are rejected by applying the requirements on the event kinematic);

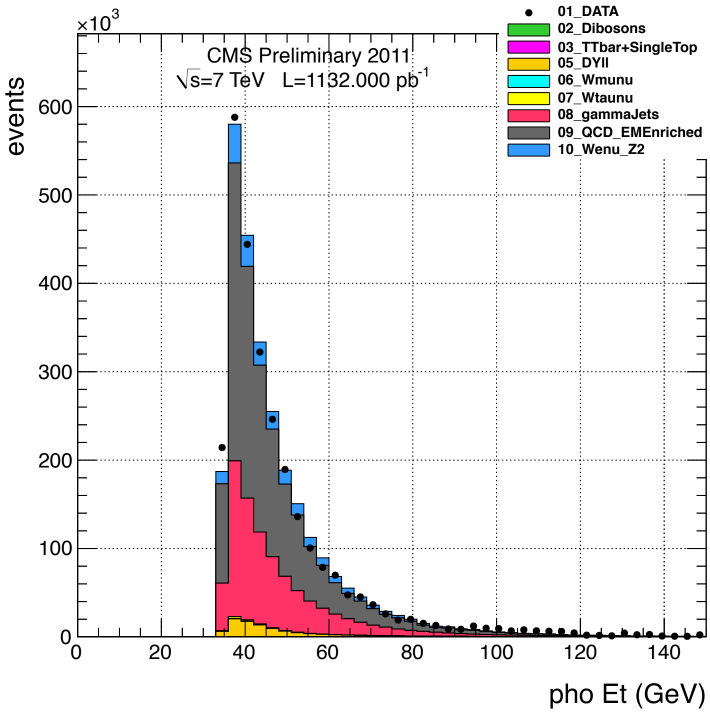

(a)

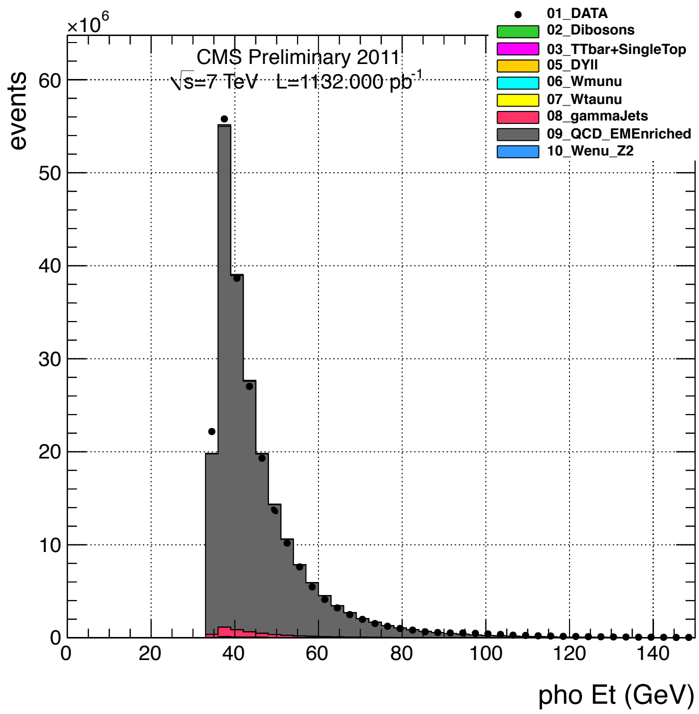

(b)

Figure 7.11.: Contamination of non-multi-jet events for the fake rate numerator (Left) and denominator (Right).

- probability for a jet to fake an electron (fake rate);
- probability for the other jet to be mis-measured creating missing transverse energy.

The fake rate is estimated as a function of E_T up to 250 GeV and then it is supposed to be constant and it is extrapolated up to 500 GeV. In a worst case scenario one can suppose that the fake rate grows linearly with E_T up to 1. However the cross section for di-jet events decreases rapidly with E_T and the only relevant background above $E_T = 250$ GeV or $M_T = 500$ GeV is the irreducible $W \to e\nu$ process. Anyhow, even if the QCD background contribution in the signal search region of the M_T spectrum is negligible, the illustrated method guarantees a good understanding of the data for the whole M_T spectrum down to the W jacobian peak.
The relevant distributions with the fake rate estimate of the multi-jet background are presented in section 7.6.

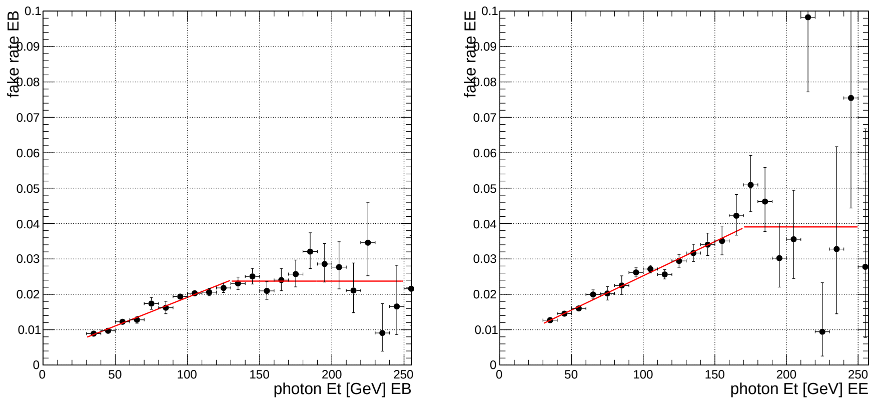

Figure 7.12.: The probability $P(e|c)$, fake rate, that an isolated ECAL super-cluster, c, is reconstructed as a WP80 electron, e, as a function of E_T of the super-cluster in the ECAL barrel (left) and ECAL endcap right, in data events with exactly one super-cluster and passing the selection criteria described in the text.

$P(e\|c)$	Barrel	Endcap
$pol1$	$E_{\mathrm{T}} < 130$ GeV	$E_{\mathrm{T}} < 170$ GeV
A	$(2.99 \pm 0.40) \times 10^{-3}$	$(5.92 \pm 0.49) \times 10^{-3}$
B	$(1.16 \pm 0.07) \times 10^{-4}$	$(1.93 \pm 0.09) \times 10^{-4}$
$pol0$	$E_{\mathrm{T}} > 130$ GeV	$E_{\mathrm{T}} > 170$ GeV
A	$(2.37 \pm 0.09) \times 10^{-2}$	$(3.90 \pm 0.41) \times 10^{-2}$

Table 7.6.: The fake rate functions, $P(e|c)$, of super-clusters reconstructed in ECAL barrel and endcaps are reported. Statistical uncertainties of the fit are shown.

7.5 Hadron recoil estimate as a check on the $E_{\mathrm{T}}^{\mathrm{MISS}}$ shape

The $W \to e\nu$ process is well understood from the theoretical side and it is well reproduced by the Monte Carlo generators. So the distributions predicted in simulation are expected to model successfully the data. The electron momentum scale and resolution determined in data are in very good agreement with the prediction of the MC simulation. One of the critical aspects is to reproduce in the simulation the pile-up conditions observed in data. An incorrect modeling of the pile-up has a direct impact on the missing energy distribution which is, by definition, related to the total amount of energy deposited in the calorimeters. To check the goodness of the $E_{\mathrm{T}}^{\mathrm{miss}}$ description in the simulation, the $E_{\mathrm{T}}^{\mathrm{miss}}$ is estimated on a event by event basis, starting from the measurement of the hadron recoil in $Z \to ee$ events profiting from the similar kinematics of W and Z events.

Z events have no physical source of $E_{\mathrm{T}}^{\mathrm{miss}}$ besides detector related resolution effects or mis-measured particles. So a clean $Z \to ee$ sample can be used to model the $E_{\mathrm{T}}^{\mathrm{miss}}$ response and resolution with data and then incorporate that information to the construction of the hadronic recoil for the W Monte Carlo events. The method has been employed in CMS in the measurement of the inclusive W cross section and is described in detail in reference [94].

Selected Z events consist in electron pairs of opposite charge with an invariant mass between 60 and 120 GeV/c^2; both electrons are required to pass the quality selections described in section 6.1.2. In Z events the momentum of the vector boson can be reconstructed by using the electron momenta. The hadronic recoil is defined as:

$$\vec{u}_T = -(\vec{E}_T^{miss} + \vec{p}_T^{V}) \tag{7.4}$$

where $\vec{p}_T^V$ is the vector associated to the transverse momentum of the W boson. The $\vec{u}_T$ depends on the hadronic activity associated to the vector boson and the pile-up. The procedure is the following: for a given value of the boson p_{T} an experimental missing transverse energy distribution from $Z \to ee$ data is obtained. This distribution is used to sample a realistic $E_{\mathrm{T}}^{\mathrm{miss}}$ value for a W Monte Carlo event of that boson p_{T}. The method samples the hadronic recoil into two components, parallel (u_1) and perpendicular (u_2) to the vector boson momentum. The parallel component is due to initial state gluons radiated from the quarks which produced the Z boson. This emission balances the p_{T} of the boson so the average $|u_1|$ is expected to increase with the Z boson momentum. The perpendicular component is caused by multiple interactions and remnants of the proton involved in the Z production. The distribution of u_2 is thus centered at zero, showing only resolution effects and being roughly constant as a function of Z p_{T}. Figure 7.13 shows the distributions of the parallel and perpendicular components as a function of Z p_{T} and the projection of each of them. The hadronic recoil in the W Monte Carlo simulation is replaced using the results derived from the Z events in data on an event-by-event basis. The transverse momentum of the W is estimated by accessing the neutrino information at generator level. The $E_{\mathrm{T}}^{\mathrm{miss}}$ can be extracted event by event: $\vec{E}_T^{miss} = -(\vec{u}_T + \vec{p}_T^V)$.

The new $E_{\mathrm{T}}^{\mathrm{miss}}$ calculated with the hadronic recoil method is in good agreement with the $E_{\mathrm{T}}^{\mathrm{miss}}$ from the MC within few percent as shown in figure 7.14. There is evidence that the pile-up is correctly modeled in the MC and, consequently, the $E_{\mathrm{T}}^{\mathrm{miss}}$ accurately describes the data.

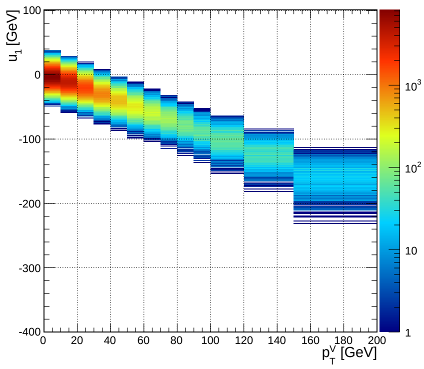

(a)

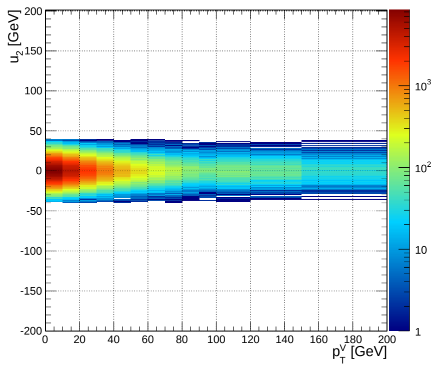

(b)

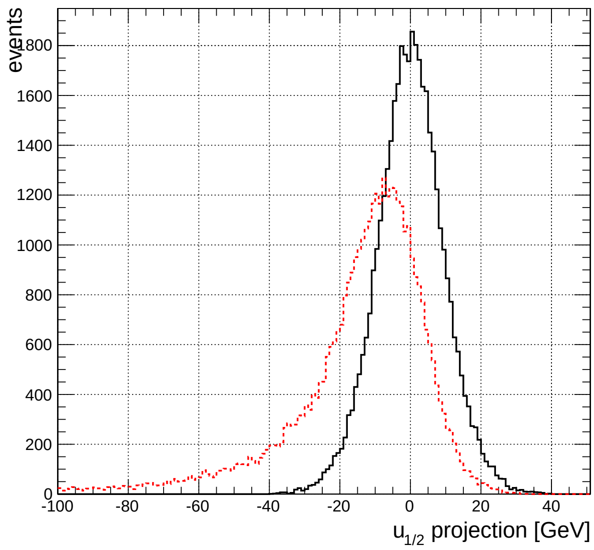

(c)

Figure 7.13.: Hadronic recoil component u_1 (a) and u_2 (b) as a function of the vector boson transverse momentum in $Z \to ee$ events. The projections of u_1 and u_2 are also shown in (c).

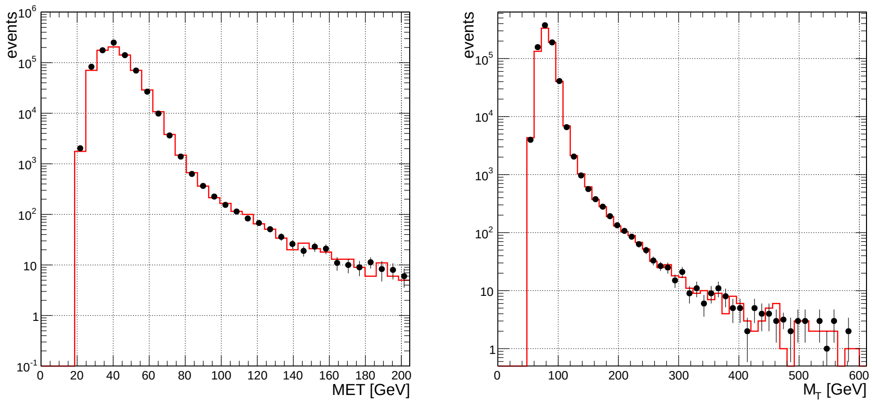

(a) (b)

Figure 7.14.: $E_{\mathrm{T}}^{\mathrm{miss}}$ (a) and M_{T} (b) distribution for $W \to e\nu$ events. The solid red line is the information from the Monte Carlo. For the black dots the $E_{\mathrm{T}}^{\mathrm{miss}}$ is estimated from the hadron recoil.

7.6 Data-Monte Carlo comparison

This section shows the comparison of the data to the simulated Monte Carlo samples for the key quantities of the analysis after the full selection chain. Here the data/MC scaling factors and the data driven estimate of the multi-jet background are applied. The distributions show a better agreement with data in the W peak region with respect to the ones in section 7.2. The full spectrum of the transverse mass M_{T}, reconstructed from the electron and the $E_{\mathrm{T}}^{\mathrm{miss}}$, is presented in figure 7.16 together with the cumulative distribution.

In figure 7.17 the highest transverse mass event in the dataset considered is displayed (M_{T} = 1150 GeV). The missing transverse energy is represented with a yellow arrow while the electromagnetic deposit is showed in red. A light blue track pointing to the energy deposit in ECAL is visible and it is almost straight in the transverse plane because of the high transverse momentum of the electron (597.2 GeV). The event is balanced and clean: only few jets with $p_{\mathrm{T}} > 20$ GeV are present.

The agreement between data and the expected background estimation from the Monte Carlo is good for all the key variables. The dominant background process is the $W \to e\nu$ in all the M_{T} range. For M_{T} values above 800 GeV the contamination from other processes is small.

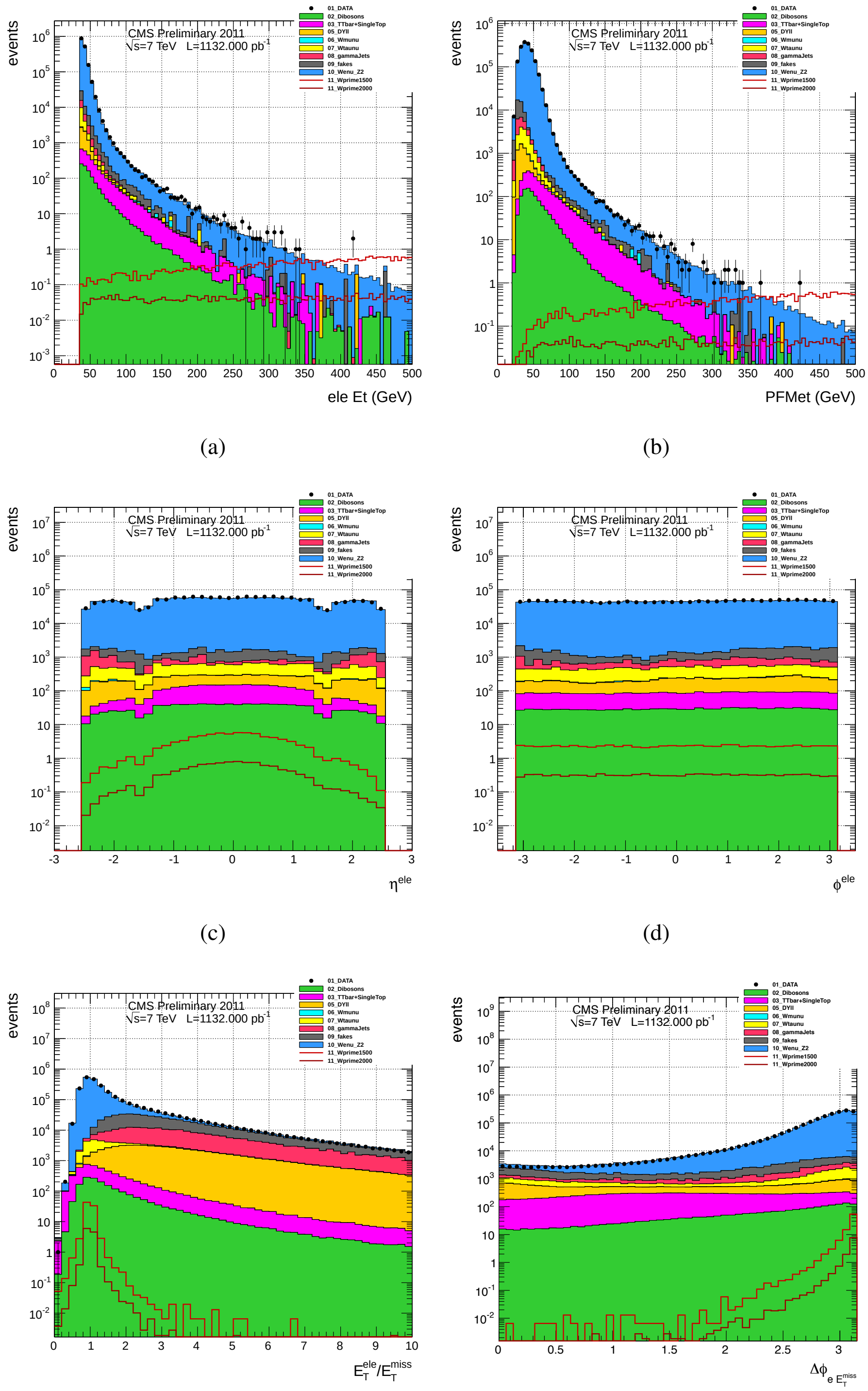

(a) (b)

(c) (d)

(e) (f)

Figure 7.15.: From the top to the bottom and from the left to the right: transverse energy of the electron, missing transverse energy, electron pseudorapidity (η), electron azimuthal angle (ϕ) and the kinematic variables related to the event (et$E_{\mathrm{T}}^{\mathrm{miss}}$, $\Delta\phi/E_{\mathrm{T}}^{\mathrm{miss}}$).

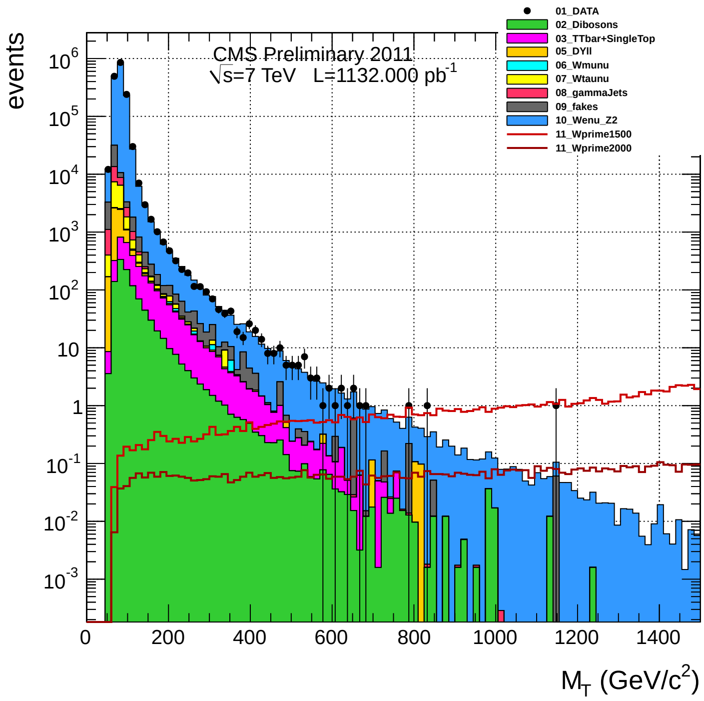

(a)

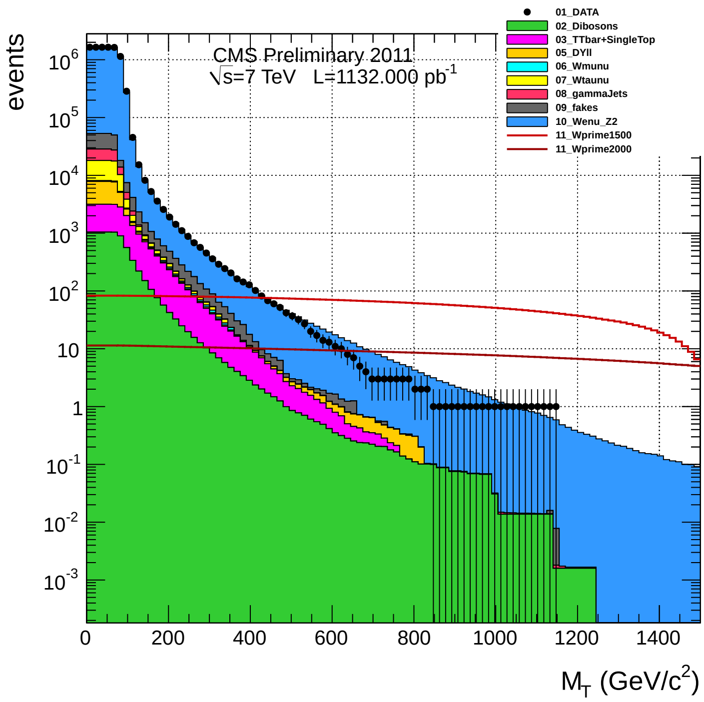

(b)

Figure 7.16.: Distribution of the transverse mass (a) and its cumulative (b) for the data and the backgrounds from MC after the corrections described above.

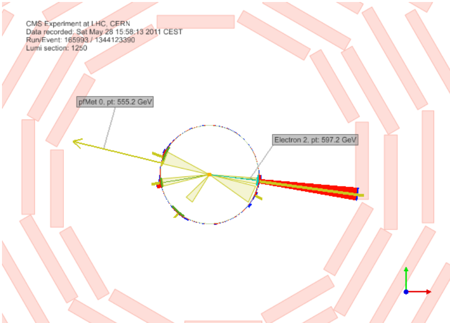

(a)

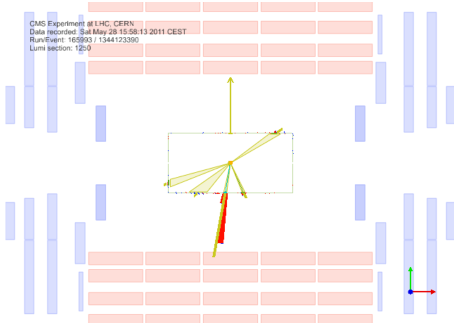

(b)

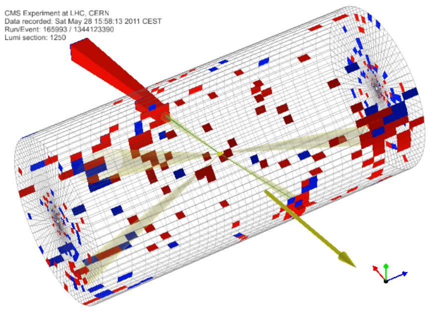

(c)

Figure 7.17.: Event with the highest transverse mass of 1150 GeV. $\rho - \phi$ view (a), $\rho - z$ view (b), $3D$ view (c).

7.7 SIGNAL EXTRACTION

A sideband fit approach is used to extract the background contamination in the signal region. The working assumption is that by doing a fit in a background dominated $M_{\rm T}$ region it is possible to model the shape of the background and, in a subsequent step, extrapolate the background fitting function to the “region of interest” ($M_{\rm T} > 800$ GeV) and estimate the number of background events without relying on the MC predictions in the tail of the $M_{\rm T}$ distribution. This is desirable to minimize the impact of the background modeling systematics, both theoretical and experimental, on the final result.
The total pp background contamination in the signal region is estimated using the 200 $< M_{\rm T} <$ 600 GeV/c^2 sideband region of the $M_{\rm T}$ spectrum. Many functions have been

tested and the following three ansatz functions are chosen based on the best χ^2:

$$\text{Function 1:} \quad \frac{a}{(x+b)^c} \tag{7.5}$$

$$\text{Function 2:} \quad \frac{a}{(x^2+bx+c)^d} \tag{7.6}$$

$$\text{Function 3:} \quad \frac{a(1+x)^b}{(x^{c+d\cdot logx})} \tag{7.7}$$

The choice of the parametric form of the functions to model the background has been performed on the Monte Carlo samples and tested on the data in the region dominated by $W \to e\nu$ events. The model has then be constrained to data, by fitting the model parameters in the side-band region from 200-600 GeV. The model parameters have enough flexibility to absorb a possible small difference in the data-MC comparison and, at the same time, prevent any risk of absorbing a genuine signal in the fit. The parameters of the fitting function are used to calculate the number of expected background events in the different bins of M_{T} outside the sideband. The choice of the sideband lower and upper limits is made in order to minimize the contribution from a hypothetical W$'$ signal and find a region that gives reliable extrapolations of the background in the signal region, based on MC studies. The comparison between the background prediction for several M_{T} ranges is reported in table 7.7 both for the sideband extrapolation and the Monte Carlo. The two predictions match each other showing that the sideband approach correctly predicts the number of background events in the MC. The robustness of the sidebands region fit and the uncertainty in the number of background events in the signal region obtained from the fit has been studied by varying the binning of the M_{T} distribution and the interval range (lower and upper limits) defining the sideband region. For each function, the lower edge of the sideband was varied between 170 and 210 GeV and the upper edge between 550 and 650 GeV. While the upper edge has little impact on the fit result, the lower edge has a stronger influence due to the steeply falling spectrum. The spread in the extrapolated results from the different fitting functions, as well as every sensitivity of the fit results to variations in the range of the sideband region are taken as systematic uncertainties (see column “spread” in table 7.7).

The sideband fit is showed in figure 7.18a with different colors for the three fitting functions. The spread between the function, in green in fig. 7.18b, correspond to the systematic on the method. In the same picture the MC prediction is also superimposed in red dots. The agreement of the MC with the sideband prediction is very good.

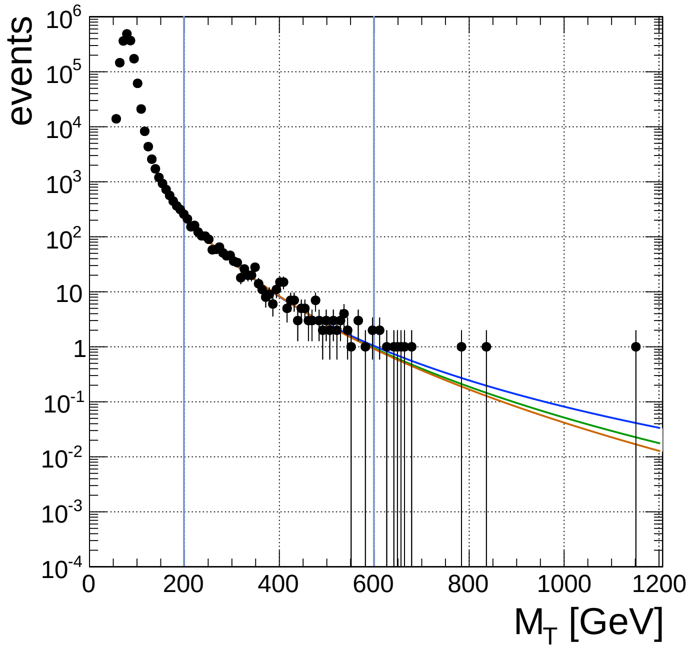

(a)

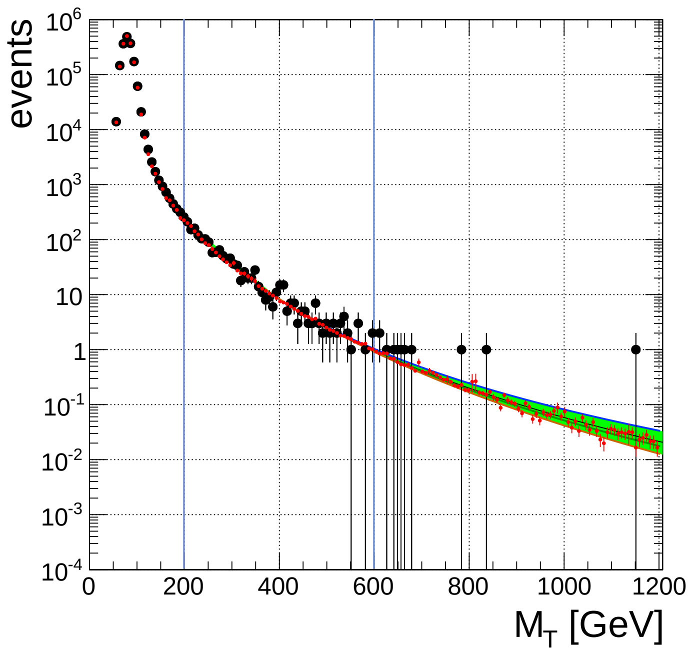

(b)

Figure 7.18.: (a) Transverse mass distribution with 1.13 fb^{-1} of 2011 data fitted with three different functions. The functions defined in the text as Function 1, Function 2 and Function 3 are reported in green, light blue and orange respectively. (b) the spread in the extrapolation of the fitting functions in the signal region defines the error band associated with the determination of the expected background. The fits are performed on the data points. The simulated points in red are superimposed for illustration.

Extrapolation	Number of events				Ratio
range in M_T	Mean Fit	Spread	MC Counted	Data	Data/Mean Fit
> 600	17.2	3.0	16.9	11	0.64
> 800	4.7	1.7	4.5	2	0.42
> 1000	1.8	0.9	1.4	1	0.57
> 1200	0.8	0.5	0.6	0	0
> 1400	0.4	0.3	0.3	0	0

Table 7.7.: Background predictions by extrapolation in various search windows for 1.13 fb^{-1} of 2011 data. Columns two and three correspond to fits of the data distribution with the three functions described in the text. Columns four and five contain the observed number of events in the simulation and the data, and column six the ratio of observed events to the average estimated background prediction in the same region for the different fits.

7.8 Systematic uncertainties

Two kinds of systematic uncertainties contribute in this analysis. The uncertainties on the effective luminosity, on the cross section, on the electron reconstruction and identification efficiencies and the trigger efficiency affect only the normalization. Uncertainties on the electron and E_T^{miss} energy scale and resolution lead to changes of the shape of the distributions. Since the estimate of the background is from a sideband fit of the data sample, the systematic uncertainties mentioned above have an effect on the signal prediction only. The uncertainty related to the background fitting function have already been presented in the previous section and it is summarized in table 7.7 (see column "spread"). The impact of this uncertainty varies depending on the M_T search window chosen. The uncertainty on the background integral above 600 GeV is about 17%.

The statistical error for the data sample with N events is given by $\sqrt{N}$ following a Poissonian statistics. For the Monte Carlo samples the number of generated events N^{GEN} and its error $\sqrt{N^{GEN}}$ are weighted with global event weights in order to scale the sample to the same luminosity available in the data sample.

7.8.1 Normalization uncertainties

Uncertainty on the luminosity

The uncertainty on the absolute value of the integrated luminosity was estimated in CMS to be 4.5% [95, 96]. The luminosity is obtained from the measurement of the event rate of a given process compared to the cross section corrected for the acceptance and efficiency. CMS uses signals registered by the forward hadronic (HF) calorimeters to determine the instantaneous luminosity in real time. This result is cross-checked with an offline analysis of the data.

CROSS SECTION

Uncertainties on the cross section of the signal sample are discussed in section 7.1.1. The uncertainty varies up to 10% for a W′ boson of mass equal to 2 TeV.

EFFICIENCIES

Electron reconstruction, identification and trigger efficiencies are measured with a tag-and-probe method with $Z \to ee$ events. A global scale factor of 0.99 is applied to the Monte Carlo samples in order to compensate for a slightly lower efficiency in data with respect to the simulation. A 2% systematic uncertainty on the scaling factor, coming from the uncertainty on the efficiency measurement method and from the transportation of the scaling factor up to the signal region, is considered.

7.8.2 SHAPE UNCERTAINTIES

ELECTRON ENERGY SCALE AND RESOLUTION

In order to study the effect of the electron energy scale and resolution on the event yield of the final M_{T} distribution, the electron energies E are varied within their uncertainties. The reconstructed electron energy E is replaced as follows:

$$\text{EM Scale:} \quad E \quad \to E \cdot (1 \pm \sigma_{scale}) \tag{7.8}$$

$$\text{EM Resolution:} \quad E \quad \to E^{true} \cdot (1 + G(\mu, \sigma \pm \sigma_{resolution})) \tag{7.9}$$

where σ_{scale} and $\sigma_{resolution}$ are the uncertainty on the energy scale and resolution respectively; E^{true} is the energy from the MC at generator level and $G(\mu,\sigma)$ is a Gaussian random number generated following the scale and the resolution of the electron object coming out from the simulation.

The energy scale uncertainty is about 1% in the ECAL Barrel and 3% in the ECAL endcaps [97]. The impact on the number of signal events above the threshold of $M_{\mathrm{T}} >$ 600 GeV varies between $\pm 0.4\%$ for $M'_{\mathrm{W}} = 1.5$ TeV and $\pm 1.0\%$ for $M'_{\mathrm{W}} = 3.0$ TeV.

The uncertainty on the energy resolution is 1.4% in EB and 3% in EE [97]. After the energy smearing, the impact on the signal is below 0.1% in the M_{T} search window above 600 GeV for a W′ mass ranging between 1.5 and 3.0 TeV.

$E_{\mathrm{T}}^{\mathrm{MISS}}$ ENERGY SCALE AND RESOLUTION

For the systematics associated to the $E_{\mathrm{T}}^{\mathrm{miss}}$, the procedure is similar as for the electron. A shift of 10% on an event by event basis to the hadronic component of the $E_{\mathrm{T}}^{\mathrm{miss}}$ value is applied. This results in a change of the signal event yield above $M_{\mathrm{T}} > 600$ GeV between about 2.3% for $M'_{\mathrm{W}} = 1.5$ TeV and about 4.8% for $M'_{\mathrm{W}} = 3.0$ TeV.
To estimate the impact of the resolution uncertainty, a 10% smearing in the x and y components of the hadronic $E_{\mathrm{T}}^{\mathrm{miss}}$ is applied. For the W′ signal (averaged over all masses), the impact on the number of events is found to be around 0.5%.

The quoted uncertainties on the energy scale and resolution of electrons and $E_{\mathrm{T}}^{\mathrm{miss}}$ are estimated in the energy range below 100 GeV. However the same values can be transported to the signal region if the linearity of the ECAL response is proven.
A method was developed to check the linearity of the ECAL energy response for energies larger than those reached in test beam measurements. Using Monte Carlo simulations, a relation is established between the energy deposit in the central, hottest crystal in a matrix of 5×5 crystals, and the surrounding 24 crystals. The algorithm describing this relation takes into account the effect of the distribution of the electron impact point position on the crystal face, estimated from asymmetries in η and ϕ of the energy deposits in the surrounding crystals [98]. To check the calorimeter response at high energy, distributions can be constructed as the difference between the measured energy (E_1) and the energy reconstructed with the algorithm (E_{rec}), divided by the mean of measured energy, in the hottest crystal.
Using high energy electrons from Drell-Yan candidate events, the mean of the distribution of the normalized difference $(E_1 - E_{rec})/ < E_1 >$ is observed to be at 0. The precision reached on this average is about 1%. These results indicate that the ECAL calibration in the barrel and endcaps parts is validated at high energy.

Summarizing, the sources of systematic uncertainty, the associated errors and their impact on the event yield of a 1.5 and 3.0 TeV W′ in the M_{T} region above 600 GeV, are reported in table 7.8.

Source of systematic error	Uncertainty	Signal (1.5 TeV) $M_T > 600$ GeV	Signal (3.0 TeV) $M_T > 600$ GeV
Luminosity	4.5%	4.5%	4.5%
Cross Section	< 10%	9%	8%
Efficiency (Reco*ID,ISO*HLT)	2%	2%	2%
Electron energy scale	1% (EB), 3% (EE)	0.4%	1%
Electron energy res	1.4% (EB), 3% (EE)	0.1%	0.1%
E_T^{miss} energy scale	10%	2.3%	4.8%
E_T^{miss} energy res	10%	0.5%	0.5%

Table 7.8.: Systematic uncertainties and their impact on the signal event yield above 600 GeV.

7.9 Statistical analysis and exclusion limit on the W′ production

Since there is no observed excess of data at the high M_T region beyond the Standard Model background prediction, the M_T distribution is used to set an upper limit on the W′ production cross section times branching fraction which can be translated into a lower limit on the mass of the potential W′.
The limit is set in the framework of the reference model described in chapter 1. Since the potential W′ signal would peak at large values of transverse mass, a threshold on the transverse mass is set to reduce the amount of background in the search window without significantly affecting the signal yield. The underlying statistical method is based on counting the number of data events above an optimized M_T threshold (the search window) and comparing it to the expected number of signal and background events including all systematic uncertainties. In other words, the aim is to quantify the level of agreement of the number of data events d with the sum of the different background processes b_i and a potential signal s with cross section σ. The upper limit on the production cross section for a W′ boson is calculated as a function of the W′ mass using a Bayesian approach. A brief review of the method follows.

The Poisson distribution specifies the probability to observe D events for a given mean value d

$$P(D|d) = \frac{e^{-d} \cdot d^D}{D!} \tag{7.10}$$

The mean d is given by the sum of the signal s and N background samples b_i

$$d = s + \sum_{i=1}^{N} b_i = \sigma \cdot \mathcal{L} \cdot \mathcal{A} + \sum_{i=1}^{N} b_i = \sigma \cdot a + \sum_{i=1}^{N} b_i = d(\sigma, a, \vec{b}) \tag{7.11}$$

with $\vec{b}$ replacing $b_1, b_2, ..., b_N$. The number of signal events s can be re-written using the cross section σ and the signal luminosity a which is equal to the product of the luminosity $\mathcal{L}$ and the signal acceptance $\mathcal{A}$.
In general a conditional probability $P(X|Y)$ can be inverted using the Bayes theorem:

$$P(Y|X) = \frac{P(X|Y)P(Y)}{P(X)} \tag{7.12}$$

The Likelihood function L is a conditional probability function considered as a function of its second argument with its first argument fixed, then:

$$L \ : \ y \mapsto P(X|Y = y) \quad \Rightarrow \quad L(y|X) \propto P(X|Y = y) \tag{7.13}$$

Now the Bayes theorem can be written using the Likelihood function:

$$P(Y|X) \propto L(y|X)P(Y) \tag{7.14}$$

and this can be applied in order to derive $P(d|D)$ from equation 7.10

$$P(d|D) = \frac{L(D|d) \cdot \pi(d)}{\mathcal{N}} = P(\sigma, a, \vec{b}|D) = \frac{L(D|\sigma, a, \vec{b}) \cdot \pi(\sigma, a, \vec{b})}{\mathcal{N}} \tag{7.15}$$

with $\mathcal{N}$ taking care of the proper normalization. The posterior probability density $P(\sigma|D)$ for the signal cross section σ given the observed number of events D is obtained by integration over the parameters a and $\vec{b}$

$$P(\sigma|D) = \frac{1}{\mathcal{N}} \int\int \cdots \int L(D|\sigma, a, \vec{b}) \cdot \pi(\sigma, a, \vec{b}) \mathrm{d}a \mathrm{d}\vec{b} \quad \text{with} \quad \mathcal{N} = \int P(\sigma|D) \mathrm{d}\sigma \tag{7.16}$$

The prior probability density $\pi(\sigma, a, \vec{b})$ can be disentangled under the assumption that any prior knowledge of a and $\vec{b}$ is independent of the signal cross section

$$\pi(\sigma, a, \vec{b}) = \pi(\sigma) \cdot \pi(a, \vec{b}) \tag{7.17}$$

The following flat prior is used for the signal cross section:

$$\pi(\sigma) = \begin{cases} \frac{1}{\sigma_{max}} & \text{for} \quad 0 < \sigma < \sigma_{max} \\ 0 & \text{otherwise} \end{cases} \tag{7.18}$$

The upper bound σ_{max} is chosen such that the posterior probability is negligible for $\sigma > \sigma_{max}$. Finally the Bayesian upper limit on the cross section σ_{CL} at a confidence level is obtained by solving the following expression (CL = 0.95 in this analysis):

$$CL = \int_0^{\sigma_{CL}} P(\sigma|D)\mathrm{d}\sigma \tag{7.19}$$

using the posterior probability

$$P(\sigma|D) \propto \int L(D|\sigma, a, \vec{b}) \cdot \pi(a, \vec{b})\mathrm{d}a\mathrm{d}\vec{b} \tag{7.20}$$

The technical implementation in this analysis is done by using the `RooStatsCl95` routine which is part of the package with the standard procedures for statistical inference in CMS physics analyses. Systematic uncertainties described in the previous chapter are incorporated in the limit setting procedure by treating them as nuisance parameters. A log-normal prior shape is used to integrate over these parameters. The number of expected and observed events, including all the systematic sources discussed are detailed in table 7.9, along with the search window, optimized for the best expected limit, and the observed limits.

Figure 7.19 presents the expected limit (with the one and two sigma bands showing its variation), the observed limit and the theoretical cross section for the production of a W′ boson decaying into electron and neutrino as a function of the W′ mass. The intersection between the observed limit and the theoretical cross section determines the lower limit on the W′ mass. Thus, the existence of a W′ boson with Standard Model-like couplings with a mass below 2.15 TeV/c^2 can be excluded at a 95% confidence level.

W′ mass (GeV)	M_T (GeV)	N_{sig} (Events)	N_{bkg} (Events)	N_{data} (Events)	σ_{theor} (pb)	Obs. Limit (pb)
1200	850	0.46 ± 0.07	3.62 ± 1.45	1	0.013	0.007
1400	950	0.46 ± 0.07	2.20 ± 1.07	1	0.010	0.008
1600	1050	0.46 ± 0.07	1.41 ± 0.81	1	0.009	0.008
1800	1075	0.48 ± 0.07	1.27 ± 0.75	1	0.009	0.008
2000	1200	0.44 ± 0.07	0.78 ± 0.54	0	0.009	0.007
2200	1200	0.41 ± 0.07	0.78 ± 0.54	0	0.009	0.008
2400	1200	0.37 ± 0.07	0.78 ± 0.54	0	0.010	0.008

Table 7.9.: For each W′ mass point, the optimized M_T search region, the expected numbers of signal and background events, the number of observed events, the corresponding cross-sections, and expected and observed limits for different W′ masses and search windows.

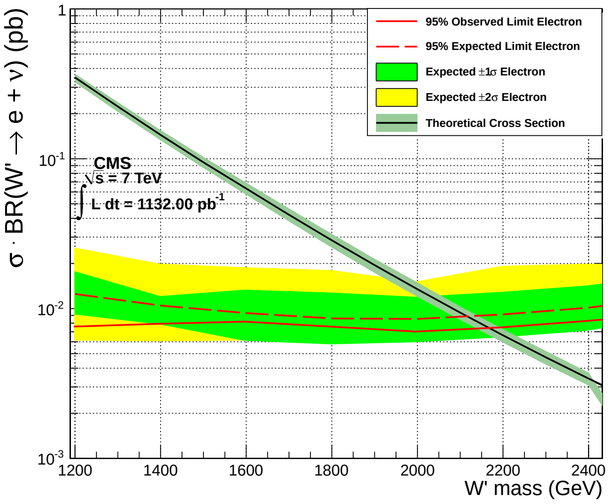

Figure 7.19.: Expected and observed limit on $\sigma\times$BR for the channel $W' \to e\nu$ using a Bayesian method for counting experiment. The background expectation is derived from the sideband method.

7.10 Updated limit in the $e+\mu$ combined channel

In this section the results of the W′ search in the combined channel with electronic or muonic final state are presented for completeness [99]. The problematics and the systematic uncertainties related to the reconstruction of high-p_T muons are not treated in this thesis, but the final result is reported.
The individual limit on the W′ invariant mass for the muon channel obtained with the same amount of statistics of 1.13 fb^{-1} is nearly 2.2 TeV at 95% CL and it is obtained as well with a Bayesian approach. The exclusion limit from the muon channel is slightly better than in the electron channel because there is a small excess in the MC background prediction with respect to the observed data in the high-M_T tail.
For the statistical combination of the two results, identical NNLO signal cross sections are used for both channels assuming lepton universality. Systematic uncertainties are assumed to be fully uncorrelated between both analysis while uncertainty on the luminosity is assumed to be fully correlated. Under these assumptions, the existence of a W′ boson with Standard Model-like couplings with masses below 2.25 TeV 95% has been excluded (figure 7.20).

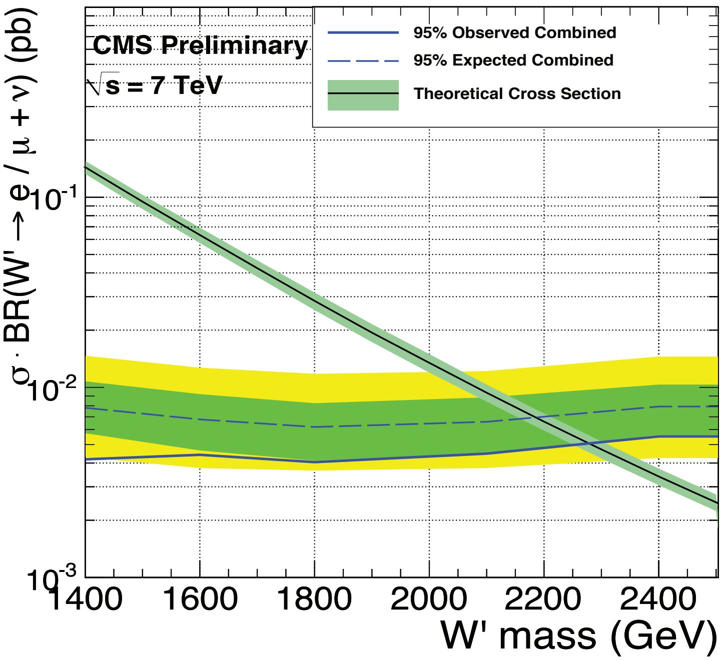

Figure 7.20.: Combined limit for the electron and muon channels with a statistics of 1.13 fb^{-1}.

7.11 ADDITIONAL MODELS AND FINAL STATES

As already mentioned in chapter 1, the Reference Model assumes that the process $\mathrm{W}' \to WZ$ is suppressed. However several extensions of the Standard Model [5, 7, 100–103], not discussed in this thesis, predict new heavy W′ bosons that decay into a pair of W and Z bosons. For example there are W′ models where the coupling to the leptons is suppressed, leading to a relative enhancement in the triple gauge couplings that could lead to a WZ final state. Other examples are models in which the W′ couples to new fermions where the decay to new fermion pairs would be suppressed if their masses are larger than the W′ mass, leading to dominance of decays into vector bosons [104]. Therefore, the search of the W′ decaying into a bosonic final state has been performed by the CMS collaboration and considered as complementary to the searches in the leptonic channels. The final state with three leptons and $E_{\mathrm{T}}^{\mathrm{miss}}$ is used to build the WZ invariant mass spectrum and the tail of the distribution is searched for excesses with respect to the SM background expectation. Also in this case, more stringent limits on the existence of the W′ have been obtained with respect to previous results from the Tevatron experiments. Assuming the Reference Model coupling, the analysis of 1.17 fb^{-1} of data excludes W′ bosons with masses below 784 GeV [105].

A comprehensive approach will be adopted in the early future to cover all the W′ decay channels. A common framework is being set up to share as many code and tools as possible and search for the W′ in the leptonic final state ($e+\nu$, $\mu+\nu$), bosonic final state (WZ, $W\gamma$) and hadronic final state ($t\bar{b}$).

Conclusions and prospects

A search for the production of heavy charged gauge bosons W' and the subsequent decay into electron and neutrino has been performed. The new bosons are predicted in many extensions of the Standard Model. In this analysis a general approach (Reference Model, Altarelli et al.) is considered, where the W' boson appears as a heavy copy of the Standard Model W boson. It is assumed that the couplings of the W' boson to quarks, leptons and gauge bosons of the electroweak interaction are identical to the Standard Model couplings, and that new decay channels (like $W' \to WZ$) are suppressed. These assumptions are realized within the Manifest Left-Right Symmetric Model if the W' boson is right-handed, and the right-handed neutrinos emerging from the decay are light.

Proton-proton collisions at a center-of-mass energy of $\sqrt{s} = 7$ TeV recorded with the CMS detector have been analyzed. The first half of the 2011 dataset corresponding to an integrated luminosity of about 1.13 fb^{-1} is investigated for deviations from the Standard Model prediction, but no significant excess is found. Moreover, an excellent agreement between data and background expectation can be stated. The tail of the transverse mass spectrum reconstructed from the electron and the missing transverse energy (neutrino) is analyzed for the statistical interpretation. A bayesian approach is chosen to set a lower limit on the invariant mass of the W'. In the context of the Reference Model additional charged gauge bosons with mass below 2.15 TeV can be excluded at the 95% confidence level. The limit grows up to 2.25 TeV if the electronic and muonic final states are combined. This result significantly improves the previous direct limits, and it is the most stringent to date. An updated result with the full statistics of 4.7 fb^{-1} collected during 2011 with the CMS detector will be published soon.

Since the final state under study involves mainly the electromagnetic calorimeter of CMS, the focus was set on the performance of the ECAL. Aspects related to the intercalibration of the individual channels of the ECAL and the stability in time of its response have been investigated. Moreover a new trigger path based on the use of the electron and the E_T^{miss} already at trigger level has been designed to record as many W events as possible and keep the event rate low at the same time. The trigger path was employed both in the W′ analysis, where the W Jacobian peak is exploited to validate the Monte Carlo and the data driven background estimate, and in the ECAL performance monitoring where the electrons coming from the decay of the W are used to monitor the calorimeter response by comparing the energy deposited in the ECAL with the track momentum measured with the tracker.

The CMS collaboration is collecting and analyzing data since the beginning of 2010 looking for new physics. If new heavy charged gauge bosons are realized within nature at the TeV scale, they should be discovered soon. For the 2012 run the LHC is expected to deliver 10-15 fb^{-1} with the same centre of mass energy as in 2011, or slightly increased to 8 TeV. This is expected to improve the sensitivity to the W′ search up to 3 TeV/c^2.

A further decisive gain in sensitivity will be possible only when LHC will provide collisions at its nominal centre of mass energy of 14 TeV, as expected to occur after the long shutdown planned for 2013-2014. At increased centre of mass energy, the on-shell production of the possible W′ would take place at larger masses. A naive scaling of figure 7.10 suggests that a larger centre of mass energy would reflect in an increased selection efficiency for larger W′ masses.

APPENDIX A

DATA-MC COMPARISON OF ECAL LOW LEVEL OBSERVABLES

A.1 INTRODUCTION: DATASETS AND SELECTIONS

For this analysis, collision events have been selected if triggered by a signal in any of the Beam Scintillators Counters (BSC), in coincidence with a signal from either of the two Beam Pick-up Timing experiment (BPTX) devices, indicating at least one bunch crossing the interaction point (IP).

The following requirements have been applied offline with the aim to select a sample with the largest possible acceptance while suppressing beam-related backgrounds:

- BPTX signals were required from both beams passing the IP in conjunction with a signal in either of the BSCs;
- beam-halo event candidates were rejected; these events have hits in the BSCs with timing consistent with that of a particle traversing horizontally the apparatus;
- a primary vertex was required with $|z| < 24$ cm and a transverse distance from the z axis smaller than 2 cm; it was also required the number of degrees of freedom used in the vertex fitting to be greater than 4;
- the fraction of high-quality tracks was required to be greater than 25%, for events with at least 10 reconstructed tracks. This cut aims at rejecting beam-scraping events, in which long horizontal sections of the pixel tracker are hit.

The data are compared to simulated minimum bias events obtained from the PYTHIA6 event generator processed through a simulation of the CMS detector response.

The detailed MC simulations of the CMS detector response are based on GEANT4.The position and width of the beam spot in the simulation were adjusted to those determined from the data. Simulated events were processed and reconstructed in the same manner as collision data.

In Section A.2, the analysis for an early 2010 run (run 132960) is presented for some basics variables (single channel energy spectra, pseudorapidity and azimuthal distributions). CMSSW version 3_5_8 was used for the reconstruction.

In Section A.3, the study has been updated using the full “Run2010A” dataset and extended including other observables. In this case, data and Monte Carlo are reconstructed with CMSSW3_9_7 and various Monte Carlo (MC) tunes have been added for the comparisons:

- Z2
- D6T
- P0
- CW

In the following comparisons, data and Monte Carlo distributions are normalized to the same number of minimum bias triggered events.

A.2 Early 2010 run comparisons

A.2.1 Single channel energy spectra

In figure A.1 the energy spectra of individual channels in the ECAL barrel and endcaps, again normalized to the number of minimum bias triggers in data, are shown.

Besides event quality selections, signal quality selections are applied to remove signals in data due to direct deposits in the readout APD, not yet simulated in MC. Anomalous energy deposits are removed using selections based on their topological characteristics: deposits in the ECAL barrel with transverse energy above 3 GeV and with the topological variable $(1 - E_4/E_1) > 0.95$ are rejected[1].

A.2.2 Pseudorapidity and azimuth distributions (max E)

The pseudorapidity distribution of the channel with the highest reconstructed energy in the barrel and in the two endcaps separately is presented in Fig. A.2. Each of the three histograms contains one entry per event.

[1] E_1 is the energy in the single crystal, E_4 is the summed energy in the four adiacent chennels in η, ϕ

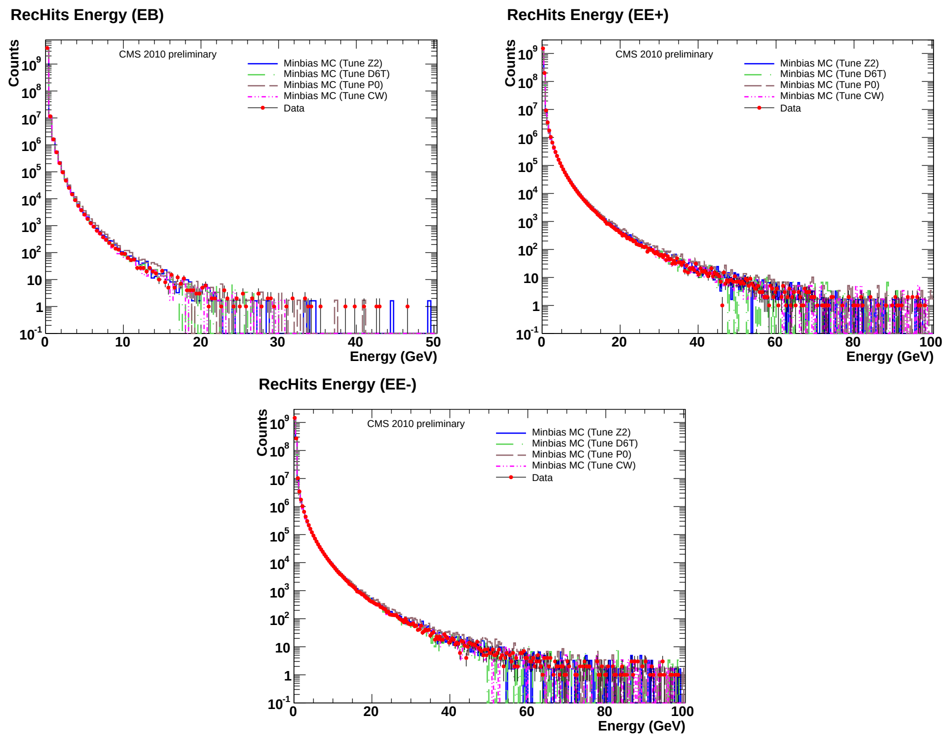

Figure A.1.: Energy spectra of the individual channels in EB (top), EE+ (center), EE- (bottom) in from 7 TeV minimum bias collision data.

The discontinuity at the transition between ECAL barrel and ECAL encaps ($\eta = \pm 1.5$) is an artifact of the selection, which was done to enhance the contribution of ECAL barrel events. A few channels with noise level higher than the average, not yet simulated in MC, are excluded from the comparison in the endcaps. The detailed simulation of the digitization step and of the energy equivalent noise in each channel explains the excellent agreement between data and Monte Carlo distributions. The difference between EE- and EE+ is due to the larger noise in EE-.

Figure A.3 shows the azimuthal distribution of the maximum energy channel in the barrel and in the endcaps. Variations as a function of ϕ are fairly reproduced in the MC simulation and reflect the modularity and the inhomogeneity of the energy equivalent noise in ECAL.

A.2.3 PSEUDORAPIDITY AND AZIMUTH DISTRIBUTIONS (MAX E_T)

The pseudorapidity distribution of the channel with the highest reconstructed transverse energy is presented in Fig. A.4. Each of the three histograms contains one entry per event. No lower threshold is applied to the maximum transverse energy considered.

Since the ECAL noise in ADC counts is roughly uniform across EB and EE and the

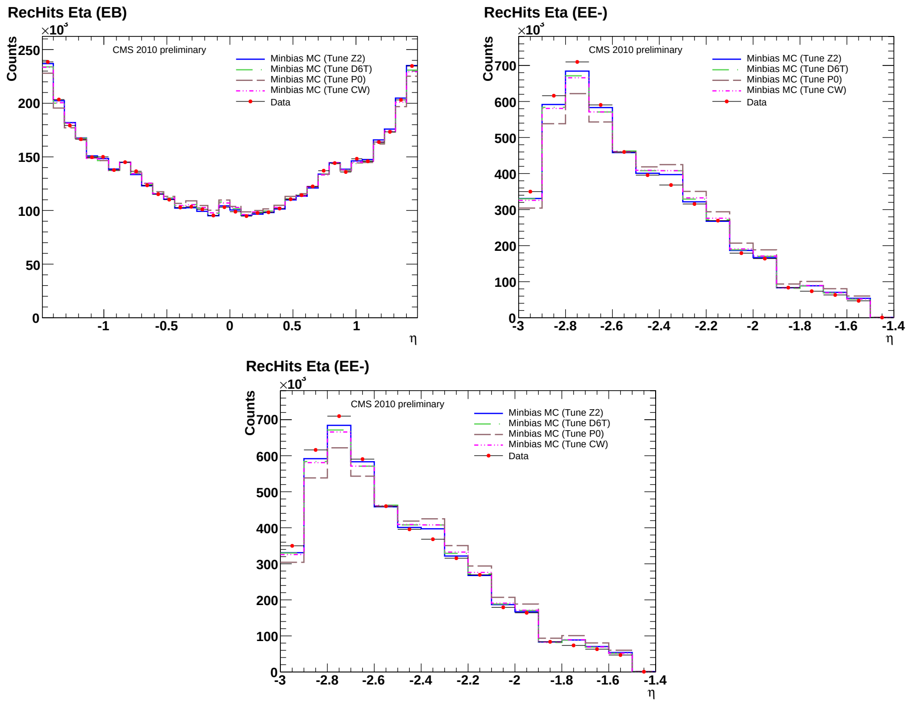

Figure A.2.: Pseudorapidity distributions of the channel with the highest reconstructed energy in minimum bias events at 7 TeV centre of mass energy for EE- (bottom-left), EB (top), EE+ (bottom-right).

energy distribution is mostly dominated by noise in minimum bias events, the pseudorapidity distribution tends to be more populated for lower values of pseudorapidity. In the endcaps, there is an additional effect related to the larger values of the intercalibration constants at smaller radii, i.e. at larger pseudorapidities.

Figure A.5 shows the azimuthal distribution of the maximum transverse energy channel in the barrel and in the two endcaps.

Variations as a function of ϕ are fairly reproduced in the Monte Carlo simulation. Two high occupancy regions around $\phi = \pm 2$ in EE- are visible. This reflects the fact that the distribution of the average intercalibration constants in EE- is not flat as function of ϕ. For the endcaps, the comparison excludes a few channels with noise level higher than the average, not yet simulated in MC, and two EE- supercrystals characterized by a light yield lower that the neighbours and, consequently, larger intercalibration constants.

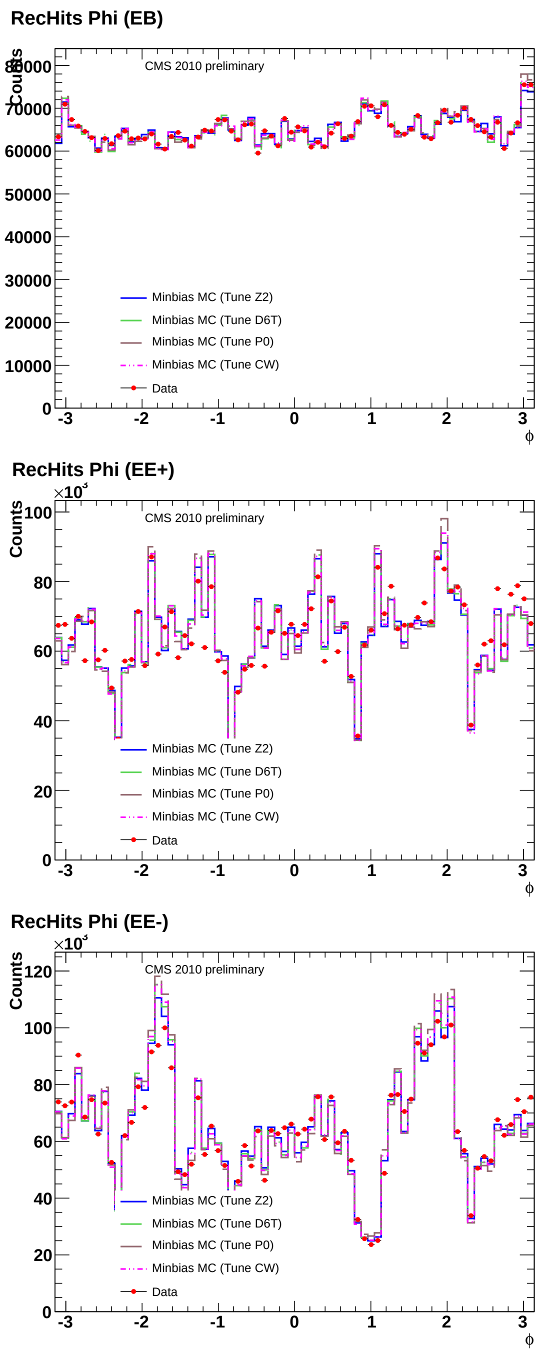

Figure A.3.: Azimuth distribution of the channel in EB(top), EE+ (center), EE- (bottom) with the highest reconstructed energy in minimum bias events at 7 TeV centre of mass energy.

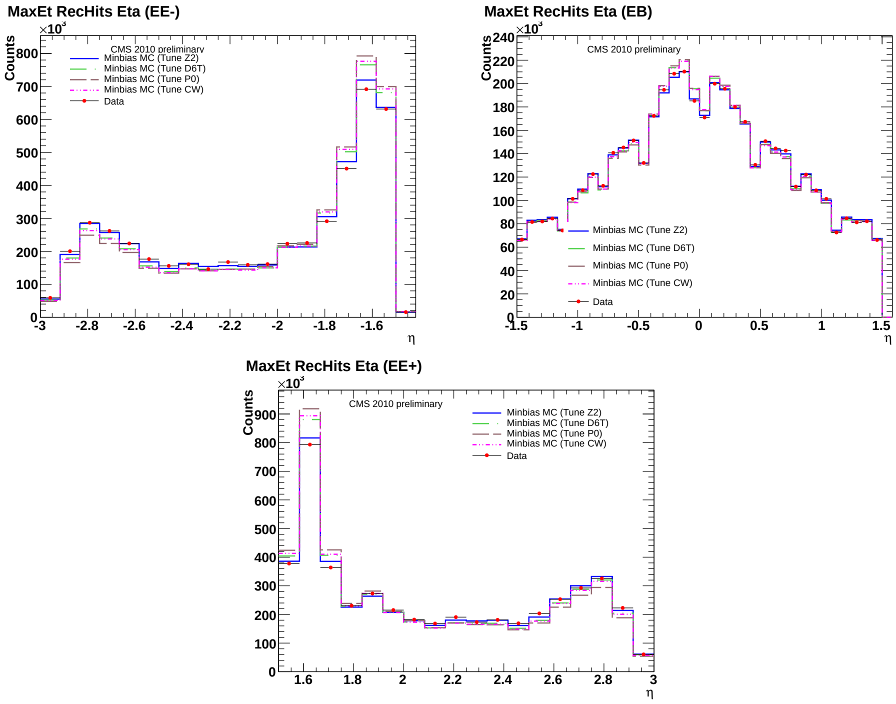

Figure A.4.: Pseudorapidity distributions of the channel with the highest reconstructed transverse energy in minimum bias events for EE- (bottom-left), EB (top), EE+ (bottom-right).

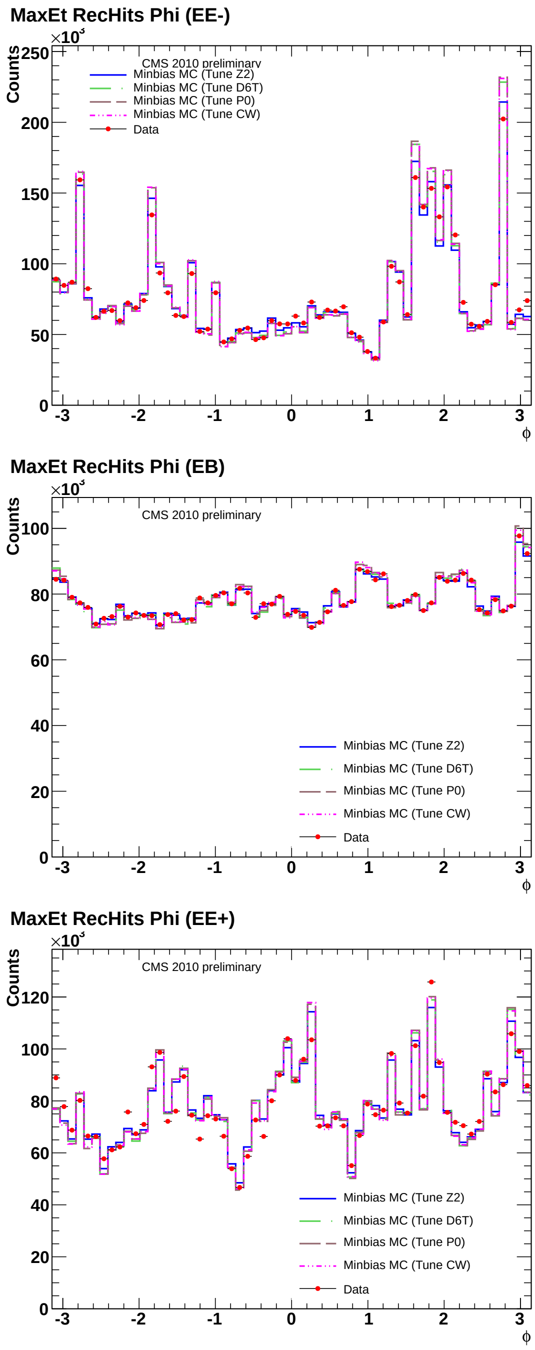

Figure A.5.: Azimuth distribution of the channel in ECAL barrel (top), EE+ (center) and EE-(bottom), with the highest reconstructed in minimum bias events.

A.3 Updated data-MC comparison

The following datasets are used in the comparisons:

· data: /MinimumBias/Run2010A-Dec22ReReco_v1/RECO

· Monte Carlo Tune Z2: /MinBias_TuneZ2_7TeV-pythia6/Winter10-START39_V8-v1/GEN-SIM-RECO

· Monte Carlo Tune P0: /MinBias_TuneP0_7TeV-pythia6/Winter10-START39_V8-v1/GEN-SIM-RECO

· Monte Carlo Tune D6: /MinBias_TuneD6_7TeV-pythia6/Winter10-START39_V8-v1/GEN-SIM-RECO

· Monte Carlo Tune CW: /MinBias_TuneCW_7TeV-pythia6/Winter10-START39_V8-v1/GEN-SIM-RECO

A.3.1 Channel occupancy

Figure A.6 shows the multiplicity of individual channels per event in the ECAL barrel and endcaps, normalized to the number of minimum bias triggers in data. The main peak is due to channels in low interest regions and above zero suppression threshold; secondary peaks at larger occupancies are due to high interest regions (E_T >2 GeV) where 225 crystals are readout without zero suppression.

A.3.2 Single channel energy spectra

In figure A.7 the energy spectra of individual channels in the ECAL barrel and endcaps, again normalized to the number of minimum bias triggers in data, are shown. The same signal quality selections described in Section A.2.1 are applied.

A.3.3 Pseudorapidity and azimuth distributions (max E)

The pseudorapidity distribution of the channel with the highest reconstructed energy in the barrel and in the two endcaps separately is presented in Fig. A.8. Each of the three histograms contains one entry per event.

A.3.4 Pseudorapidity and azimuth distributions (max E^T)

The pseudorapidity distribution of the channel with the highest reconstructed transverse energy is presented in Fig. A.9. Each of the three histograms contains one entry per event. No lower threshold is applied to the maximum transverse energy considered.

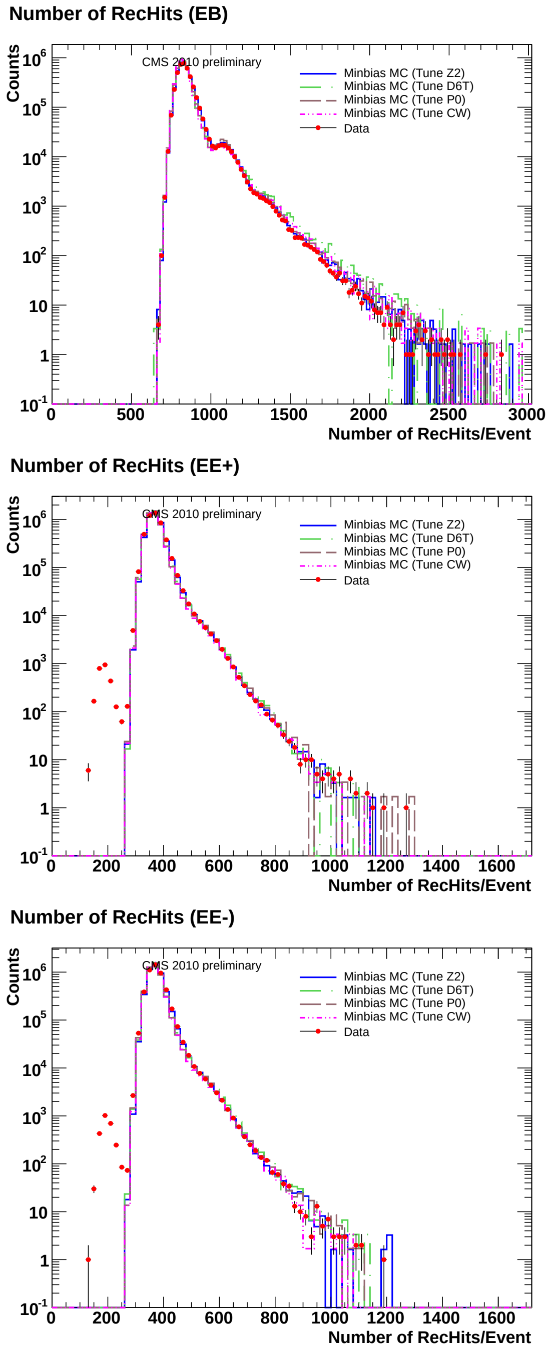

Figure A.6.: Individual channel multiplicity per event in EB (top), EE+ (centre) and EE- (bottom) in 7 TeV minimum bias collision data.

Figure A.10 shows the azimuthal distribution of the maximum transverse energy channel in the barrel and in the two endcaps.

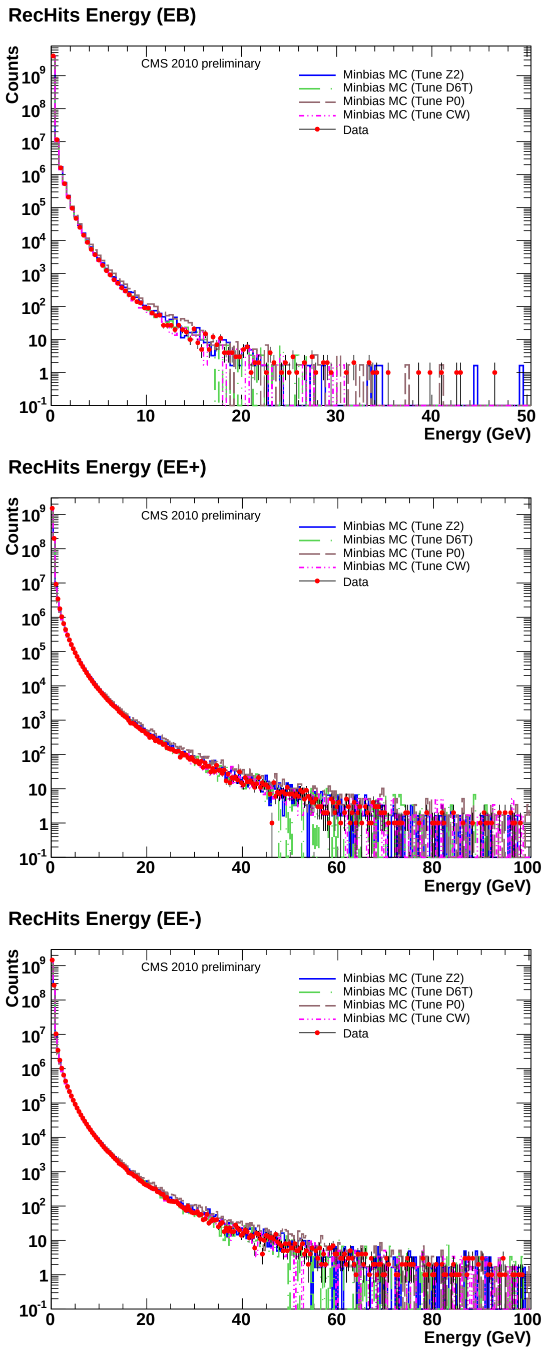

Figure A.7.: Energy spectra of the individual channels in EB (top), EE+ (center), EE- (bottom) in from 7 TeV minimum bias collision data.

A.3.5 Data-MC comparison of SuperClusters distributions

Figure A.11 shows the distribution of 'raw' transverse energy (meaning calculated from uncorrected energy) for superclusters in both barrel and endcaps. These distribu-

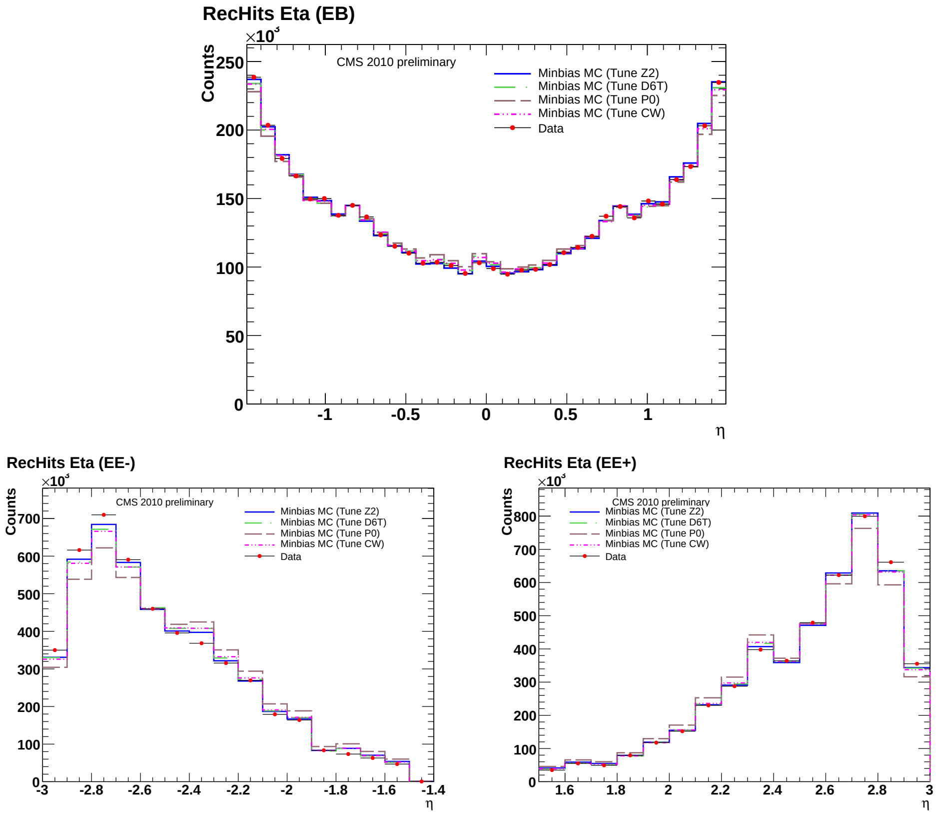

Figure A.8.: Pseudorapidity distributions of the channel with the highest reconstructed energy in minimum bias events at 7 TeV centre of mass energy for EE- (bottom-left), EB (top), EE+ (bottom-right).

tions show an overall good agreement between data and simulation, demonstrating the maturity of the understanding of the detector and reconstruction algorithms.

The pseudorapidity and azimuthal distributions of the superclusters are presented in Fig. A.12 and Fig. A.13 respectevely. They are normalized to the number of reconstruced superclusters in data to compare the shape of the distributions. The small discrepancy around $\phi = 1$ and η=2.7 between data and Monte Carlo is related to one supercrystal in EE- that was masked in the Monte Carlo reconstruction and not in the data.

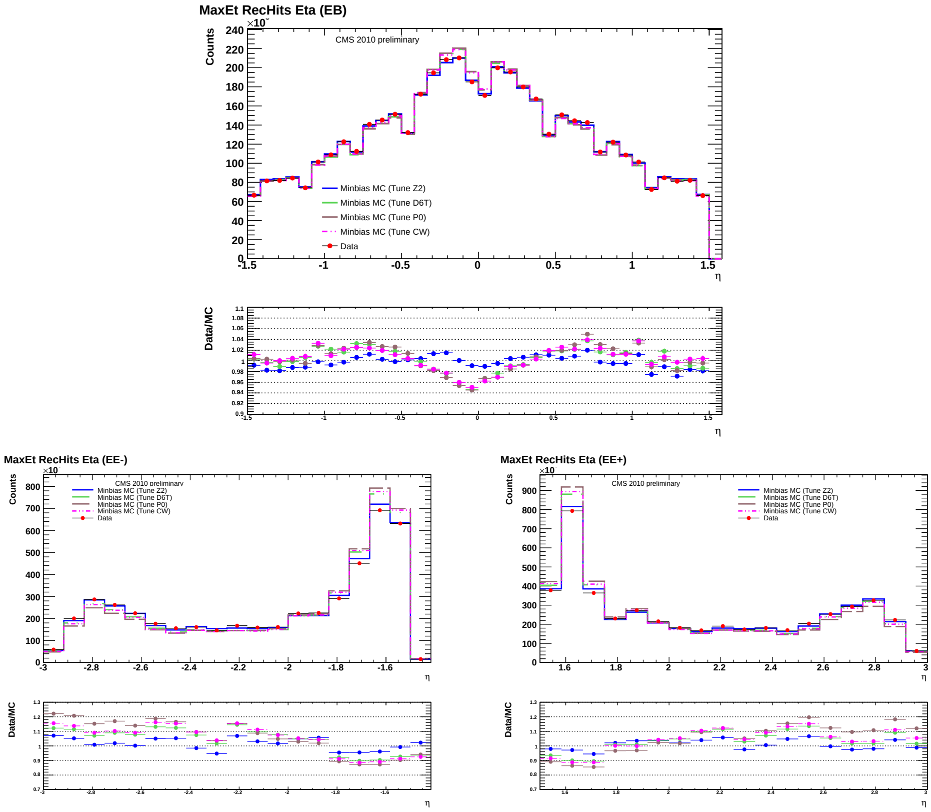

Figure A.9.: Pseudorapidity distributions of the channel with the highest reconstructed transverse energy in minimum bias events for EE- (bottom-left), EB (top), EE+ (bottom-right).

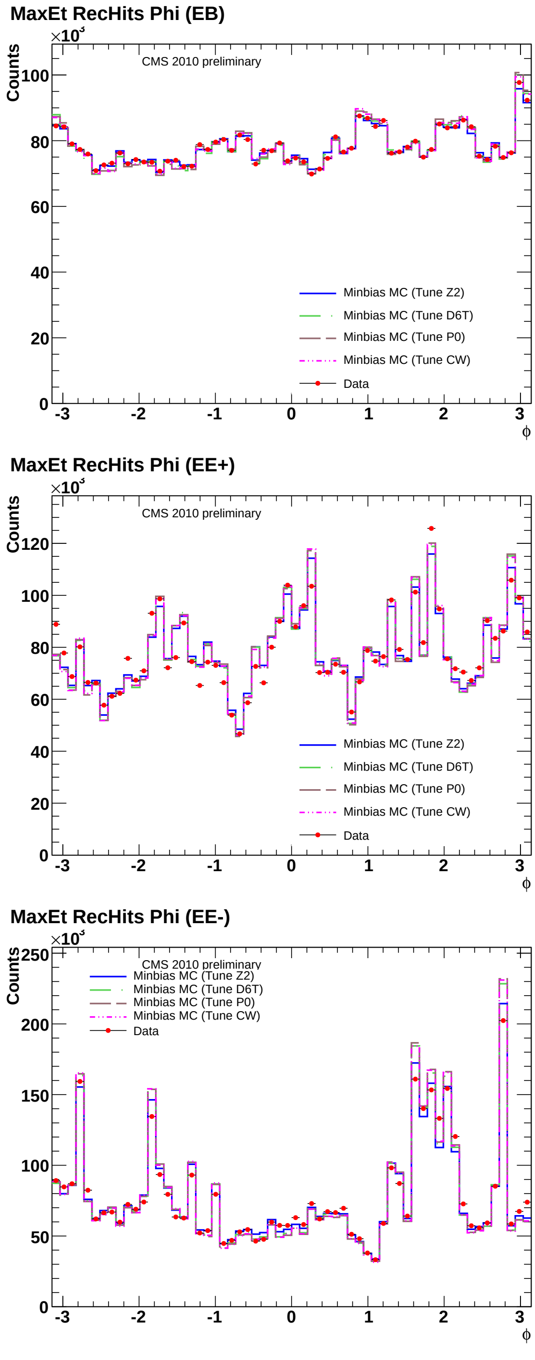

Figure A.10.: Azimuth distribution of the channel in ECAL barrel (top), EE+ (center) and EE-(bottom), with the highest reconstructed E^T in minimum bias events.

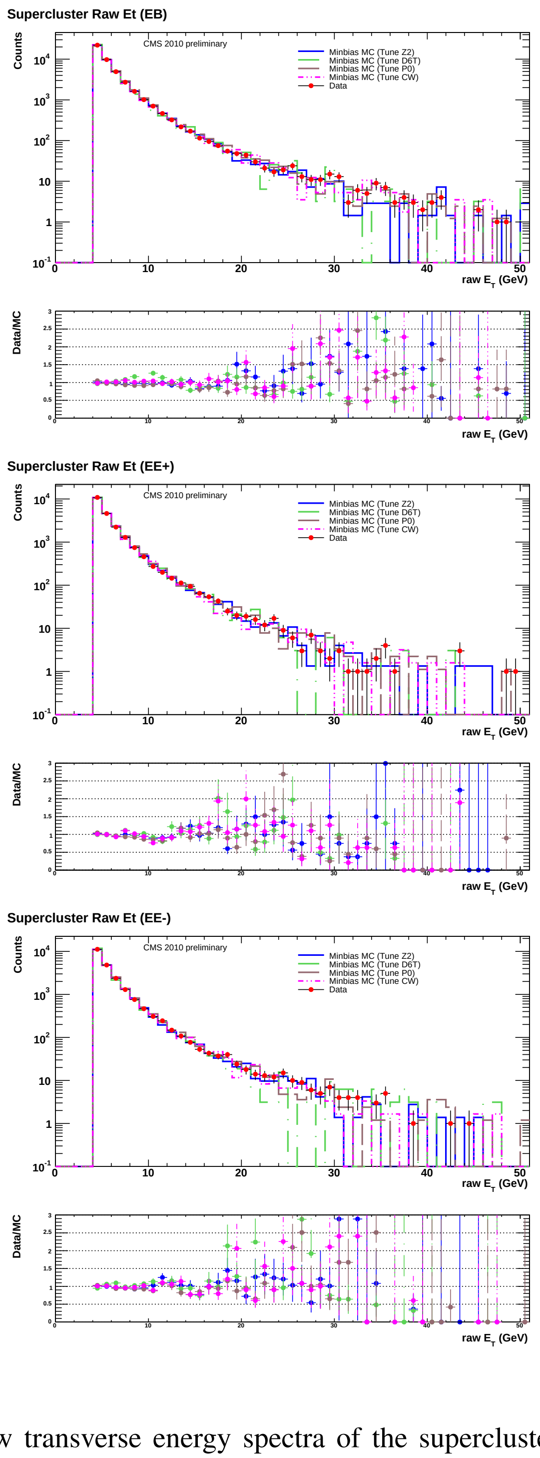

Figure A.11.: Raw transverse energy spectra of the superclusters in the barrel(top), EE+(center), EE-(bottom) in 7 TeV minimum bias collision data. The Data/MC ratio is shown at the bottom of each plot.

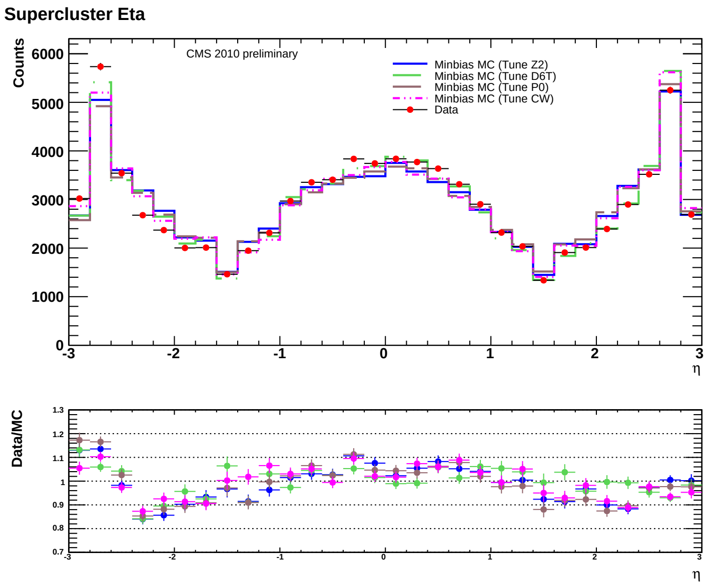

Figure A.12.: Pseudorapidity distribution of the ECAL superclusters in 7 TeV minimum bias collision data.

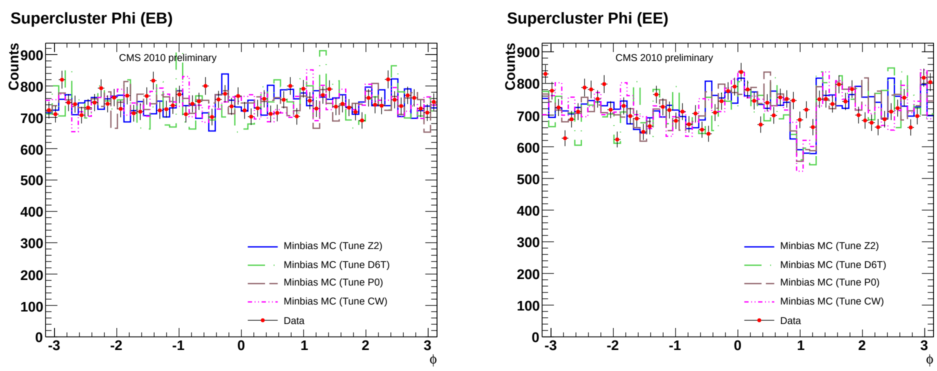

Figure A.13.: Azimutal distribution of the ECAL superclusters in the barrel (left) and in the endcaps (right) in 7 TeV minimum bias collision data.

APPENDIX B

W′ ANALYSIS DATASETS

Sample	Dataset Name
W $\rightarrow \mu\nu_\mu$	/WToMuNu_TuneZ2_7TeV-pythia6/Summer11-PU_S3_START42_V11-v2/AODSIM
	/WToMuNu_ptmin-100_7TeV-pythia6/Winter10-E7TeV_ProbDist_2010Data_BX156_START39_V8-v1/AODSIM
W $\rightarrow \tau\nu_\tau$	/WToTauNu_TuneZ2_7TeV-pythia6-tauola/Summer11-PU_S3_START42_V11-v2/AODSIM
Z $\rightarrow ee$	/DYToEE_M-20_TuneZ2_7TeV-pythia6/Summer11-PU_S3_START42_V11-v2/AODSIM
Z $\rightarrow \mu\mu$	/DYToMuMu_M-20_TuneZ2_7TeV-pythia6/Summer11-PU_S3_START42_V11-v2/AODSIM
Z $\rightarrow \tau\tau$	/DYToTauTau_M-20_TuneZ2_7TeV-pythia6-tauola/Summer11-PU_S3_START42_V11-v2/AODSIM
Z $\rightarrow ee, m_{\ell\ell} > 200$	/DYToEE_M-200_TuneZ2_7TeV-pythia6-tauola/Summer11-PU_S3_START42_V11-v2/AODSIM
Z $\rightarrow ee, m_{\ell\ell} > 500$	/DYToEE_M-500_TuneZ2_7TeV-pythia6-tauola/Summer11-PU_S3_START42_V11-v2/AODSIM
Z $\rightarrow ee, m_{\ell\ell} > 800$	/DYToEE_M-800_TuneZ2_7TeV-pythia6-tauola/Summer11-PU_S3_START42_V11-v2/AODSIM
Z $\rightarrow ee, m_{\ell\ell} > 1000$	/DYToEE_M-1000_TuneZ2_7TeV-pythia6-tauola/Summer11-PU_S3_START42_V11-v2/AODSIM
Z $\rightarrow \mu\mu, m_{\ell\ell} > 200$	/DYToMuMu_M-200_TuneZ2_7TeV-pythia6-tauola/Summer11-PU_S3_START42_V11-v2/AODSIM
Z $\rightarrow \mu\mu, m_{\ell\ell} > 500$	/DYToMuMu_M-500_TuneZ2_7TeV-pythia6-tauola/Summer11-PU_S3_START42_V11-v2/AODSIM
Z $\rightarrow \mu\mu, m_{\ell\ell} > 800$	/DYToMuMu_M-800_TuneZ2_7TeV-pythia6-tauola/Summer11-PU_S3_START42_V11-v2/AODSIM
Z $\rightarrow \mu\mu, m_{\ell\ell} > 1000$	/DYToMuMu_M-1000_TuneZ2_7TeV-pythia6-tauola/Summer11-PU_S3_START42_V11-v2/AODSIM
$t\bar{t}$	/TTJets_TuneZ2_7TeV-madgraph-tauola/Spring11-PU_S1_START311_V1G1-v1/AODSIM
Inclusive μ QCD	/QCD_Pt-20_MuEnrichedPt-15_TuneZ2_7TeV-pythia6/Spring11-PU_S1_START311_V1G1-v1/AODSIM
WW	/WWtoAnything_TuneZ2_7TeV-pythia6-tauola/Spring11-PU_S1_START311_V1G1-v1/AODSIM
WZ	/WZtoAnything_TuneZ2_7TeV-pythia6-tauola/Spring11-PU_S1_START311_V1G1-v1/AODSIM
ZZ	/ZZtoAnything_TuneZ2_7TeV-pythia6-tauola/Spring11-PU_S1_START311_V1G1-v1/AODSIM
W$^+ \rightarrow \mu^+\nu_\mu$	/WPlusToMuNu_CT10_TuneZ2_7TeV-powheg-pythia/Spring11-PU_S1_START311_V1G1-v1/AODSIM
W$^- \rightarrow \mu^-\nu_\mu$	/WMinusToMuNu_CT10_TuneZ2_7TeV-powheg-pythia/Spring11-PU_S1_START311_V1G1-v1/AODSIM
W $\rightarrow e\nu_e$	/WToENu_TuneZ2_7TeV-pythia6/Summer11-PU_S3_START42_V11-v2/AODSIM
	/WToENu_ptmin-100_TuneZ2_7TeV-pythia6/Summer11-PU_S4_START42_V11-v1/AODSIM
W $\rightarrow \tau\nu_\tau$	/WToTauNu_TuneZ2_7TeV-pythia6-tauola/Summer11-PU_S3_START42_V11-v2/AODSIM
W $\rightarrow \mu\nu_\mu$	/WToMuNu_TuneZ2_7TeV-pythia6/Summer11-PU_S3_START42_V11-v2/AODSIM
QCD EM enriched $20 < \hat{p}_T < 30$	QCD_Pt-20to30_EMEnriched_TuneZ2_7TeV-pythia6/Spring11-PU_S1_START311_V1G1-v1/AODSIM
QCD EM enriched $30 < \hat{p}_T < 80$	QCD_Pt-30to80_EMEnriched_TuneZ2_7TeV-pythia6/Spring11-PU_S1_START311_V1G1-v1/AODSIM
QCD EM enriched $80 < \hat{p}_T < 170$	QCD_Pt-80to170_EMEnriched_TuneZ2_7TeV-pythia6/Spring11-PU_S1_START311_V1G1-v1/AODSIM
WW	/WWtoAnything_TuneZ2_7TeV-pythia6-tauola/Spring11-PU_S1_START311_V1G1-v1/AODSIM
WZ	/WZtoAnything_TuneZ2_7TeV-pythia6-tauola/Spring11-PU_S1_START311_V1G1-v1/AODSIM
ZZ	/ZZtoAnything_TuneZ2_7TeV-pythia6-tauola/Spring11-PU_S1_START311_V1G1-v1/AODSIM
$t\bar{t}$	/TTJets_TuneZ2_7TeV-madgraph-tauola/Spring11-PU_S1_START311_V1G1-v1/AODSIM
$t \rightarrow bl\nu$ (s-Channel)	/TToBLNu_TuneZ2_s-channel_7TeV-madgraph/Spring11-PU_S1_START311_V1G1-v1/AODSIM
$t \rightarrow bl\nu$ (t-Channel)	/TToBLNu_TuneZ2_t-channel_7TeV-madgraph/Spring11-PU_S1_START311_V1G1-v1/AODSIM
$t \rightarrow bl\nu$ (tW-Channel)	/TToBLNu_TuneZ2_tW-channel_7TeV-madgraph/Spring11-PU_S1_START311_V1G1-v1/AODSIM
$\gamma + Jets, 0 < \hat{p}_T < 15$	/G_Pt_0to15_TuneZ2_7TeV_pythia6/Spring11-PU_S1_START311_V1G1-v1/AODSIM
$\gamma + Jets, 15 < \hat{p}_T < 30$	/G_Pt_15to30_TuneZ2_7TeV_pythia6/Spring11-PU_S1_START311_V1G1-v1/AODSIM
$\gamma + Jets, 30 < \hat{p}_T < 50$	/G_Pt_30to50_TuneZ2_7TeV_pythia6/Spring11-PU_S1_START311_V1G1-v1/AODSIM
$\gamma + Jets, 50 < \hat{p}_T < 80$	/G_Pt_50to80_TuneZ2_7TeV_pythia6/Spring11-PU_S1_START311_V1G1-v1/AODSIM
$\gamma + Jets, 80 < \hat{p}_T < 120$	/G_Pt_80to120_TuneZ2_7TeV_pythia6/Spring11-PU_S1_START311_V1G1-v1/AODSIM
$\gamma + Jets, 120 < \hat{p}_T < 170$	/G_Pt_120to170_TuneZ2_7TeV_pythia6/Spring11-PU_S1_START311_V1G1-v1/AODSIM
$\gamma + Jets, 170 < \hat{p}_T < 300$	/G_Pt_170to300_TuneZ2_7TeV_pythia6/Spring11-PU_S1_START311_V1G1-v1/AODSIM
$\gamma + Jets, 300 < \hat{p}_T < 470$	/G_Pt_300to470_TuneZ2_7TeV_pythia6/Spring11-PU_S1_START311_V1G1-v1/AODSIM
$\gamma + Jets, 470 < \hat{p}_T < 800$	/G_Pt_470to800_TuneZ2_7TeV_pythia6/Spring11-PU_S1_START311_V1G1-v1/AODSIM
$\gamma + Jets, 800 < \hat{p}_T < 1400$	/G_Pt_800to1400_TuneZ2_7TeV_pythia6/Spring11-PU_S1_START311_V1G1-v1/AODSIM
$\gamma + Jets, 1400 < \hat{p}_T < 1800$	/G_Pt_1400to1800_TuneZ2_7TeV_pythia6/Spring11-PU_S1_START311_V1G1-v1/AODSIM
$\gamma + Jets, \hat{p}_T > 1800$	/G_Pt_1800_TuneZ2_7TeV_pythia6/Spring11-PU_S1_START311_V1G1-v1/AODSIM

Table B.1.: Datasets correspoding to the analyzed background Monte Carlo samples.

Dataset	Trigger	Run Range	L(pb^{-1})
/SingleElectron/Run2011A-May10ReReco-v1/AOD	Ele27_CaloIdVT_CaloIsoT_TrkidT_TrkIsoT	160431-161176	5.9
	Ele32_CaloIdVT_CaloIsoT_TrkidT_TrkIsoT	161217- 163869	198.3
/SingleElectron/Run2011A-PromptReco-v4/AOD	Ele32_CaloIdVT_CaloIsoT_TrkidT_TrkIsoT	165088-165633	144.3
	HLT_Ele25_WP80_PFMT40_v1	165970-166967	537.1
	HLT_Ele27_WP80_PFMT50_v1	$\geq$167039	64.4

Table B.2.: List of the datasets used in the analysis and the corresponding run ranges.

BIBLIOGRAPHY

[1] Thomas Sven Pettersson and P Lefevre. The large hadron collider: conceptual design. oai:cds.cern.ch:291782. Technical Report CERN-AC-95-05 LHC, CERN, Geneva, Oct 1995.

[2] Rabindra N. Mohapatra and Goran Senjanovic. Neutrino mass and spontaneous parity nonconservation. *Phys. Rev. Lett.*, 44:912, 1980.

[3] G. Senjanovic and Rabindra N. Mohapatra. Exact Left-Right Symmetry and Spontaneous Violation of Parity. *Phys. Rev.*, D12:1502, 1975.

[4] Rabindra N. Mohapatra and Jogesh C. Pati. Left-Right Gauge Symmetry and an Isoconjugate Model of CP Violation. *Phys. Rev.*, D11:566–571, 1975.

[5] Jogesh C. Pati and Abdus Salam. Lepton Number as the Fourth Color. *Phys. Rev.*, D10:275–289, 1974.

[6] *CMS: the Compact Muon Solenoid technical proposal*. LHC Tech. Proposal. CERN, Geneva, 1994.

[7] Guido Altarelli, B. Mele, and M. Ruiz-Altaba. Searching for new heavy vector bosons in p $\bar{p}$ COLLIDERS. *Z. Phys.*, C45:109, 1989.

[8] K. Nakamura et al. Review of particle physics. *J.Phys.G*, G37:075021, 2010.

[9] G. Beall, Myron Bander, and A. Soni. Constraint on the mass scale of a left-right-symmetric electroweak theory from the $K_L - K_S$ mass difference. *Phys. Rev. Lett.*, 48:848–851, Mar 1982.

[10] M. Allet, K. Bodek, J. Camps, J. Deutsch, M. Ferro-Luzzi, F. Gimeno-Nogues, J. Govaerts, J. Lang, R. Maller, S. Navert, O. Naviliat-Cuncic, I. Pepe, R. Prieels, P. Quin, N. Severijns, J. Sromicki, E. Stephan, E. Thomas, and J. Zejma. Search for right-handed weak currents in the beta-asymmetry-polarization correlation from 12n decay. *Physics Letters B*, 383(2):139 – 144, 1996.

[11] Stephen P. Martin. A Supersymmetry Primer. *arXiv:hep-ph/9709356v5*, 2008.

[12] Howard Georgi and S. L. Glashow. Unity of all elementary-particle forces. *Phys. Rev. Lett.*, 32:438–441, Feb 1974.

[13] A.J. Buras, J. Ellis, M.K. Gaillard, and D.V. Nanopoulos. Aspects of the grand unification of strong, weak and electromagnetic interactions. *Nuclear Physics B*, 135(1):66 – 92, 1978.

[14] Nima Arkania Hamed, Savas Dimopoulos, and Gia Dvali. The hierarchy problem and new dimensions at a millimeter. *Physics Letters B*, 429:263 – 272, 1998.

[15] Ignatios Antoniadis, Nima Arkani-Hamed, Savas Dimopoulos, and Gia Dvali. New dimensions at a millimeter to a fermi and superstrings at a tev. *Physics Letters B*, 436:257 – 263, 1998.

[16] Hidezumi Terazawa, Masaki Yasua, Keiichi Akama, and Masaki Hayashi. Observable effects of the possible sub-structure of leptons and quarks. *Physics Letters B*, 112:387 – 392, 1982.

[17] The CMS Collaboration. CMS Exotica Public Physics Results.

[18] A. and Leike. The phenomenology of extra neutral gauge bosons. *Physics Reports*, 317:143 – 250, 1999.

[19] Lisa Randall and Raman Sundrum. An alternative to compactification. *Phys. Rev. Lett.*, 83:4690–4693, Dec 1999.

[20] Lisa Randall and Raman Sundrum. Large mass hierarchy from a small extra dimension. *Phys. Rev. Lett.*, 83:3370–3373, Oct 1999.

[21] The CMS Collaboration. Search for Resonances in the Dilepton Mass Distribution in pp Collisions at $\sqrt{s} = 7$ TeV.

[22] The CMS Collaboration. Search for signatures of extra dimensions in the diphoton mass spectrum at the Large Hadron Collider.

[23] Savas Dimopoulos and Leonard Susskind. Mass without scalars. *Nuclear Physics B*, 155(1):237 – 252, 1979.

[24] Savas and Dimopoulos. Technicoloured signatures. *Nuclear Physics B*, 168(1):69 – 92, 1980.

[25] Edward Farhi and Leonard Susskind. Technicolour. *Physics Reports*, 74(3):277 – 321, 1981.

[26] The CMS Collaboration. Search for pair production of first-generation scalar leptoquarks in pp collisions at $\sqrt{s} = 7$ TeV. *Phys. Rev. Lett.*, 106:201802, May 2011.

[27] The CMS Collaboration. Search for first generation scalar leptoquarks in the channel in pp collisions at $\sqrt{(s)}$=7 tev. *Physics Letters B*, 703(3):246 – 266, 2011.

[28] The CMS Collaboration. Search for Second Generation Scalar Leptoquarks.

[29] Luis A. Anchordoqui, Haim Goldberg, Dieter Lüst, Satoshi Nawata, Stephan Stieberger, and Tomasz R. Taylor. Dijet signals for low mass strings at the large hadron collider. *Phys. Rev. Lett.*, 101:241803, Dec 2008.

[30] Schuyler Cullen, Maxim Perelstein, and Michael E. Peskin. Tev strings and collider probes of large extra dimensions. *Phys. Rev. D*, 62:055012, Aug 2000.

[31] U. Baur et al. Excited quark production at large hadron colliders. 1987.

[32] Paul H. Frampton and Sheldon L. Glashow. Chiral color: An alternative to the standard model. *Physics Letters B*, 190:157 – 161, 1987.

[33] Elizabeth H. Simmons. Coloron phenomenology. *Phys. Rev. D*, 55:1678–1683, Feb 1997.

[34] JoAnne L. Hewett and Thomas G. Rizzo. Low-energy phenomenology of superstring-inspired e6 models. *Physics Reports*, 183:193 – 381, 1989.

[35] The CMS Collaboration. Search for resonances in the dijet mass spectrum from 7 tev pp collisions at cms. *Physics Letters B*, 704(3):123 – 142, 2011.

[36] P.Q. Hung and Chi Xiong. Dynamical electroweak symmetry breaking with a heavy fourth generation. *Nuclear Physics B*, 848(2):288 – 302, 2011.

[37] Gad Eilam, Bla ženka Melić, and Josip Trampetić. cp violation and the fourth generation. *Phys. Rev. D*, 80:116003, Dec 2009.

[38] Otto Eberhardt, Alexander Lenz, and Jürgen Rohrwild. Less space for a new family of fermions. *Phys. Rev. D*, 82:095006, Nov 2010.

[39] The CMS Collaboration. Inclusive search for a fourth generation of quarks with the CMS experiment.

[40] U. Baur, M. Spira, and P. M. Zerwas. Excited-quark and -lepton production at hadron colliders. *Phys. Rev. D*, 42:815–824, Aug 1990.

[41] The CMS Collaboration. A search for excited leptons in pp collisions at. *Physics Letters B*, 704(3):143 – 162, 2011.

[42] CMS Collaboration. Search for new physics in highly boosted z^0 decays to dimuons in pp collisions at $\sqrt{s} = 7$ tev. *CMS Physics Analysis Summary: EXO-10-025*, 2010.

[43] The CMS Collaboration. Search for Large Extra Dimensions in Dimuon Events in pp Collisions at $\sqrt{s} = 7$ TeV.

[44] Fairbairn Kraan Milstead et al. Stable massive particles at colliders. 2006.

[45] Particle Data Group. Large Electron-positron Collider - LEP. *web pages at:*, http://public.web.cern.ch/public/en/research/lep-en.html.

[46] *ATLAS: technical proposal for a general-purpose pp experiment at the Large Hadron Collider at CERN*. LHC Tech. Proposal. CERN, Geneva, 1994.

[47] *ALICE : Technical Proposal*. Tech. Proposal. CERN, Geneva, 2001.

[48] *LHCb : Technical Proposal*. Tech. Proposal. CERN, Geneva, 1998.

[49] V Karimaki. *The CMS tracker system project: Technical Design Report*. Technical Design Report CMS. CERN, Geneva, 1997.

[50] *The CMS electromagnetic calorimeter project: Technical Design Report*. Technical Design Report CMS. CERN, Geneva, 1997.

[51] CMS Collaboration. Search for a higgs boson decaying into two photons in the cms detector. *CMS Physics Analysis Summary: HIG-11-021*, 2011.

[52] *The CMS hadron calorimeter project: Technical Design Report*. Technical Design Report CMS. CERN, Geneva, 1997.

[53] *The CMS muon project: Technical Design Report*. Technical Design Report CMS. CERN, Geneva, 1997.

[54] Sergio Cittolin, Attila Racz, and Paris Sphicas. *CMS trigger and data-acquisition project: Technical Design Report*. Technical Design Report CMS. CERN, Geneva, 2002.

[55] C. Rovelli P. Meridiani. Clusters containment corrections using ecal position measurements at the 2006 h4 testbeam. *CMS detector note 2008-007*, 2008.

[56] Serguei Chatrchyan et al. Time Reconstruction and Performance of the CMS Electromagnetic Calorimeter. *JINST*, 5:T03011, 2010.

[57] M. Dejardine. Determination of the single pulse response of the cms-ecal electronics and application to the pulse shape reconstruction. *CMS detector note 2008-001*, 2008.

[58] https://cmsdoc.cern.ch/cms/cpt/software/html/general.

[59] The CMS Collaboration. CMS ECAL time calibration.

[60] M. Raymond et al. The mgpa electronic calorimeter readout chip for cms. *Proceeding of the 2003 LECC Conference*, 2003.

[61] B. Clerbaux et al. Tev electron and photon saturation studies. *CMS analysis note 2006-004*, 2006.

[62] P. Adzic et al. Intercalibration of the barrel electromagnetic calorimeter of the CMS experiment at start-up. *JINST*, 3:P10007, 2008.

[63] D. Futyan and C. Seez. Intercalibration of ecal crystals in phi using simmetry of energy deposition. *CMS note 2002-031*, 2002.

[64] D. Futyan. Intercalibration of the cms electromagnetic calorimeter using jet trigger events. *CMS note 2004-007*, 2004.

[65] L. Agostino et al. Intercalibration of the cms electromagnetic calorimeter with isolated electrons. *CMS note 2006-021*, 2006.

[66] P.Meridiani and R.Paramatti. Use of $z \to e^+e^-$ events for ecal calibration. *CMS note 2006-039*, 2006.

[67] Serguei Chatrchyan et al. Commissioning of the CMS Experiment and the Cosmic Run at Four Tesla. *JINST*, 5:T03001, 2010.

[68] N. V. Mokhova D. E. Groom and S. I. Striganov. Muon stopping power and range tables. *Atom. Data Nucl. Data*, pages 183–356, 2001.

[69] Particle Data Group. Atomic and Nuclear Properties of Materials. *web pages at:*, http://pdg.lbl.gov/2009/AtomicNuclearProperties/, 2009.

[70] Serguei Chatrchyan et al. Measurement of the Muon Stopping Power in Lead Tungstate. *JINST*, 5:P03007, 2010.

[71] The CMS Collaboration. Electromagnetic calorimeter commissioning and performance with 7 tev data. *CMS analysis note 2010-012*, 2010.

[72] CMS Collaboration. Cms physics technical design report, volume i: Detector performance and software. *CERN/LHCC 2006-001*, 2006.

[73] M. Anderson et al. Review of clustering algorithms and energy corrections in ecal. *CMS internal note 2010-008*, 2008.

[74] E. Meschi et al. Electron reconstruction in the cms electromagnetic calorimeter. *CMS internal note 2001-034*, 2001.

[75] R and Frahwirth. Track fitting with non-gaussian noise. *Computer Physics Communications*, 100(1-2):1 – 16, 1997.

[76] The CMS Collaboration. Electron Identification Based on Simple Cuts.

[77] The Electroweak worning group. Generic tag and probe tool for measuring efficiency at cms with early data. *CMS analysis note 2009-111*, 2009.

[78] The Electroweak working group. Updated measurements of the inclusive w and z cross sections at 7 tev. *CMS analysis note 2010-264*, 2010.

[79] CMS Collaboration. Missing et performance in cms. *CMS physics analysis summary*, 2007.

[80] CMS Collaboration. Track-corrected missing transverse energy in cms. *CMS physics analysis summary*, 2009.

[81] CMS Collaboration. Particle-flow event reconstruction in cms. *CMS Physics Analysis Summary: PFT-09-001*, 2009.

[82] CMS Collaboration. Cms met performance in events containing electroweak bosons from pp collisions at $\sqrt{(s)}$=7 tev. *CMS Physics Analysis Summary JME-10-005*, 2010.

[83] P. Skands T. Sjostrand, S. Mrenna. Pythia 6.4 physics and manual. *JHEP, 05:026*, 2006.

[84] S. Agostinelli et al. GEANT4: A simulation toolkit. *Nucl. Instrum. Meth.*, A506:250–303, 2003.

[85] J. Pumplin et al. Generation of parton distributions with uncertainties from global qcd analysis. *JHEP 0207, 012*, 2002.

[86] D. Stump et al. Inclusive jet production, parton distributions, and the search for new physics. *JHEP 0310, 046*, 2003.

[87] R. Gavin et al. Fewz 2.0: A code for hadronic z production at next-to-next-to-leading order. *arXiv:1011.3540v1*, 2010.

[88] DongHee Kim et al. Pdf uncertainties and k-factor for the w' search. *CMS analysis note 2011-273*, 2011.

[89] Simone Alioli et al. Nlo vector-boson production matched with shower in powheg. *JHEP, 07:060*, 2008.

[90] P. Nason. A new method for combining nlo qcd with shower monte carlo algorithms. *JHEP, 11:040*, 2004.

[91] C. Oleari S. Frixione, P. Nason. Matching nlo qcd computations with parton shower simulations: the powheg method. *JHEP, 11:070*, 2007.

[92] Johan Alwall et al. Madgraph/madevent v4: the new web generation. *JHEP, 09:028*, 2007.

[93] The CMS Collaboration. Standard Model Cross Sections for CMS at 7 TeV.

[94] G. Bauer et al. Modeling of $w \to l\nu E_{\mathrm{T}}^{\mathrm{miss}}$ with boson recoil. *CMS analysis note 2010-332*, 2010.

[95] N. Adam et al. Absolute calibration of luminosity measurement in cms. *CMS analysis note 2011-092*, 2011.

[96] The CMS Collaboration. Absolute luminosity normalization. *CMS DP-2011-002*, 2011.

[97] B. Clerbaux et al. Search for high-mass resonances decaying to electron pairs in the cms experiment. *CMS analysis note 2011-444*, 2011.

[98] S. Elgammal et al. Validation of ecal calibration at high energy using electrons in $\sqrt{(s)}$=7 tev data. *CMS analysis note 2011-085*, 2011.

[99] Wprime Group. Search for a heavy gauge boson w' in the leptonic final states in pp collisions at $\sqrt{(s)}$=7 tev. *CMS analysis note 2011-227*, 2011.

[100] Paul Langacker. The physics of heavy z' gauge bosons. *Rev. Mod. Phys.*, 81(3):1199–1228, Aug 2009.

[101] Maxim Perelstein. Little higgs models and their phenomenology. *Progress in Particle and Nuclear Physics*, 58(1):247 – 291, 2007.

[102] Estia Eichten and Kenneth Lane. Low-scale technicolor at the tevatron and lhc. *Physics Letters B*, 669(3-4):235 – 238, 2008.

[103] Kenneth Lane. Technihadron production and decay in low-scale technicolor. *Phys. Rev. D*, 60(7):075007, Sep 1999.

[104] K.S. Babu, X.G. He, and E. Ma. New supersymmetric left-right gauge model: Higgs-boson structure and neutral-current analysis. *Phys. Rev.*, D36:878, 1987.

[105] Wprime Group. Search for exotic wz resonances at cms. *CMS analysis note 2011-337*, 2011.